

DISSERTATION

CLIMATE AND HEALTH IMPACTS OF PARTICULATE MATTER FROM RESIDENTIAL
COMBUSTION SOURCES IN DEVELOPING COUNTRIES

Submitted by

John K. Kodros

Department of Atmospheric Science

In partial fulfillment of the requirements

For the Degree of Doctor of Philosophy

Colorado State University

Fort Collins, Colorado

Summer 2018

Doctoral Committee:

Advisor: Jeffrey R. Pierce

John Volckens

Sonia Kreidenweis

A.R. Ravishankara

Copyright by John K. Kodros 2018

All Rights Reserved

ABSTRACT

CLIMATE AND HEALTH IMPACTS OF PARTICULATE MATTER FROM RESIDENTIAL COMBUSTION SOURCES IN DEVELOPING COUNTRIES

Globally, close to 2.8 billion people lack access to clean cooking technology, while 1.8 billion people lack access to electricity altogether. As a means to generate energy for residential tasks, it is common in many developing countries to rely on combustion of solid fuels (wood, dung, charcoal, trash, etc.). Solid fuel use (SFU) can emit substantial amounts of fine particulate matter ($PM_{2.5}$), often in or in close proximity to residences, creating concerns for human health and climate; however, large uncertainties exist in indoor and outdoor concentrations and properties, limiting our ability to estimate these climate and health impacts. This work explores the uncertainty space in estimates of premature mortality attributed to exposure to $PM_{2.5}$ from residential SFU (e.g., cooking, heating, lighting) and makes the first estimates of health and radiative effects from combustion of domestic waste (i.e., trash burning). Next, we investigate key uncertain parameters (emission size distribution, black carbon mixing state, and size-resolved respiratory deposition) that drive uncertainties in health and radiative impacts from SFU, in order to improve model estimates of aerosol impacts from all sources.

In many developing regions, combustion of solid fuels for cooking and heating is not the only aerosol source impacting air quality and climate. While uncontrolled combustion of domestic waste has been observed in many countries, this aerosol source is not generally included in many global emissions inventories. Using a global chemical-transport model, we estimate exposure to ambient $PM_{2.5}$ from domestic-waste combustion to cause 270,000 (5th-95th percentile: 213,000 to 328,000) adult mortalities per year, most of which occur in developing countries. Regarding aerosol radiative effects, we estimate the globally averaged direct radiative effect (DRE) to range from -40 mW m^{-2} to $+4 \text{ mW m}^{-2}$ and the aerosol indirect effect (AIE) to range from -4 mW m^{-2} to -49 mW m^{-2} . In

some regions with significant waste combustion, such as India and China, the aerosol radiative effects exceed -0.4 W m^{-2} . The sign and magnitude of the global-mean DRE is strongly sensitive to assumptions on how black carbon (BC) is mixed with scattering particles, while the AIE is strongly sensitive to the emission size distribution.

To determine what factors dominate the uncertainty space in mortality estimates from SFU, we perform a variance-based sensitivity analysis on premature mortality attributed to the combined exposure to ambient and household $\text{PM}_{2.5}$ from SFU. We find that uncertainty in the percent of the population using solid fuels for energy contributes the most to the uncertainty in mortality (53-56% of uncertainty across Asia and South America) with the concentration-response function the next largest contributor (40-50%).

In the second half of this dissertation, we explore several key uncertainties in climate and health estimates of aerosol from residential sources in order to reduce overall model uncertainty of aerosol impacts from any source. To test the sensitivity of the AIE to treatment of aerosol size distributions in global models, we estimate the AIE due to anthropogenic emissions with prognostic sectional aerosol microphysics and compare this to the AIE calculated when the simulated aerosol mass of each species is remapped onto a prescribed size distribution. Simulations using the prognostic scheme yield a global mean anthropogenic AIE of -0.87 W m^{-2} , while the simulations with the prescribed scheme predict -0.66 W m^{-2} . These differences suggest that simulations with prescribed size-distribution mapping are unable to capture regional and temporal variability in size-resolved aerosol number and thus may lead to biases in estimates of the AIE.

ACKNOWLEDGEMENTS

Moving to Colorado for my graduate studies proved to be a momentous decision. My experience here will always be inextricably linked with the faculty, students, and staff, as well as the foothills, canyons, and rivers. I owe a huge debt of gratitude to my advisor, Jeff Pierce, who offered mentorship and an enthusiasm for science that turned every topic into an adventure. Jeff, thank you for your guidance through all of our projects, patience through all of my many mistakes, and freedom to explore all the many diversions and tangential questions I wanted to ask. Most importantly thank you for your belief and faith in me over the years. I do not think I would have thrived under any other advising. Working with you the past five years has been a fun and exciting experience with a lot of laughs, stories, and album recommendations.

In addition to Jeff, I have been fortunate to have many collaborators and mentors at CSU who contributed to this dissertation. Thank you to all the many co-authors who contributed to this research. I owe a big thank you to John Volckens who acted as additional mentor through the many meetings, emails, borrowed UPAS-es, and advice he offered the past few years. The opportunity John gave me to participate in the laboratory and field campaigns for the cookstove project greatly influenced my perspective of this field and future goals as a researcher. Thank you to my committee members, John Volckens, Sonia Kreidenweis, and Ravishankara for the support and feedback during this process. Many thanks to Christian L'Orange and Michael Johnson for helping me learn the intricacies of the cookstove world, and especially to Kelsey Bilsback for toughing out a few "bonus" days in India. My diversion into environmental health was made substantially easier with the aid of Sheryl Magzamen and Ellison Carter. A special thank you to Bonne Ford Hotmann who offered a huge amount of help ranging from science questions, to lending ski gear, to delicious baked treats. Many thanks to all the members of the Pierce Group for agreeing on Indian food for lunch and putting up with the worst of my jokes. Thank you to all of my friends for the adventures in rock climbing, skiing, yurting, eclipse hunting, music playing, and relaxing. Finally, a big thank you to my parents and sister for providing me this opportunity and the support to see it through.

TABLE OF CONTENTS

ABSTRACT	ii
ACKNOWLEDGEMENTS	iv
Chapter 1 Introduction	1
1.1 Motivation	1
1.2 Scope of dissertation	3
Chapter 2 The aerosol radiative effects of uncontrolled combustion of domestic waste	5
2.1 Introduction	5
2.2 Methods	9
2.2.1 Model overview	9
2.2.2 Aerosol optical depth (AOD) comparison	12
2.2.3 Direct radiative effect calculation	13
2.2.4 Cloud-albedo aerosol indirect effect calculation	14
2.3 Model results	14
2.3.1 Comparison to observations	14
2.3.2 Changes in mass concentrations from domestic-waste combustion	16
2.3.3 Changes to size-resolved number concentrations	18
2.3.4 Aerosol direct radiative effect	21
2.3.5 Cloud-albedo aerosol indirect effect	24
2.4 Conclusions	25
Chapter 3 Global burden of mortalities due to chronic exposure to ambient PM _{2.5} from open combustion of domestic waste	28
3.1 Introduction	29
3.2 Methods	32
3.2.1 Chemical-transport model overview	32
3.2.2 Calculation of premature mortality	33
3.3 Results	35
3.3.1 Model increases in PM _{2.5} due to waste-combustion emissions	35
3.3.2 Global and country-level mortality rates due to waste-combustion PM _{2.5}	35
3.3.3 Deaths averted due to removal of waste-combustion emissions	38
3.3.4 Sensitivity of mortality rates to emission mass and model resolution	38
3.4 Discussion and conclusions	41
Chapter 4 Quantifying the contribution to uncertainty in mortality attributed to household, ambient, and joint exposure to PM _{2.5} from residential solid-fuel use	44
4.1 Introduction	45
4.2 Methods	47
4.2.1 Uncertain parameters and data sources	47
4.2.2 Calculation of premature mortality from solid-fuel use	50

4.2.3	Variance-based sensitivity analysis	53
4.3	Results and discussion	55
4.3.1	Country-level mortality attributed to solid-fuel use	55
4.3.2	Sensitivity analysis	58
4.4	Conclusions	65
Chapter 5	Important global and regional differences in aerosol cloud-albedo effect estimates between simulations with and without prognostic aerosol microphysics	69
5.1	Introduction	70
5.2	Methods	73
5.2.1	GEOS-Chem model setup	73
5.2.2	Aerosol size distributions	74
5.2.3	Offline calculation of CDNC and aerosol cloud-albedo effect	78
5.2.4	Description of observations of aerosol size distributions	79
5.3	Results	79
5.3.1	Comparison to observations	79
5.3.2	Size-resolved particle number concentration and CDNC	81
5.3.3	Aerosol cloud-albedo effect	85
5.4	Conclusions	91
Chapter 6	Size-resolved mixing state of black carbon in the Canadian high Arctic and implications for simulated direct radiative effect	95
6.1	Introduction	96
6.2	Methods	99
6.2.1	Flight overview and sample locations	99
6.2.2	Measurement of refractory black carbon	101
6.2.3	Measurement of total aerosol size distributions	104
6.2.4	Determination of the fraction of total aerosols containing rBC vs aerosol diameter	104
6.2.5	Model overview	105
6.2.6	GEOS-Chem-TOMAS	105
6.3	Results	112
6.3.1	Measurements of coating thickness as a function of rBC core size and fraction of rBC-containing particles	112
6.3.2	Comparison to model simulations	114
6.3.3	Implications for the direct radiative effect	115
6.3.4	Study limitations	118
6.4	Conclusions	119
Chapter 7	The role of inter-regional variability in aerosol size distributions on respiratory deposition of particulate matter air pollution	121
7.1	Introduction	122
7.2	Methods	125
7.2.1	Modeling size-resolved particle deposition in the body	125
7.2.2	Simulating ambient aerosol size distributions	127
7.3	Results	128

7.3.1	Simulated annual PM _{2.5} concentration	128
7.3.2	Respiratory deposited PM mass and deposition ratio	130
7.3.3	Speciated size-dependent deposition	135
7.3.4	Deposition ratios based on number and surface area	140
7.3.5	Discussion and Conclusions	141
Chapter 8	Synthesis and future work	144
References	148
Appendix A	Supplemental to Global burden of mortalities due to chronic exposure to ambient PM _{2.5} from open combustion of domestic waste	204
A.1	Details of the GEOS-Chem chemical transport model	204
A.2	Total adult mortalities due to exposure to ambient PM _{2.5}	205
A.3	Waste-combustion emissions	205
A.4	Model evaluation	205
A.5	Country-level mortalities	206
A.6	Sensitivity simulations	207
A.7	Mortalities at different resolutions	207
Appendix B	Supporting Information for Quantifying the contribution to uncertainty in mortality attributed to household, ambient, and joint exposure to PM _{2.5} from residential solid-fuel use	216
B.1	GEOS-Chem model setup	216
B.2	Calculating lognormal parameters	216
B.3	Sensitivity analysis results with a lognormal uncertainty distribution and restricting input parameters to 2.5 to 97.5 percentile range	217
B.4	Sensitivity analysis results with uniform uncertainty distributions (where the end-points are the 2.5 to 97.5 percentiles)	217
Appendix C	Supplemental Material to Size-resolved mixing state of black carbon in the Canadian high Arctic and implications for simulated direct radiative effect	220
C.1	Bounding cases of coating thickness for rBC cores less than 140 nm and resulting direct radiative effect	220
C.2	April mean albedo	222
Appendix D	Supplemental Information for The role of inter-regional variability in aerosol size distributions on respiratory deposition of particulate matter	224
D.1	Sensitivity to particle dosimetry model: ICRP versus MPPD	224
D.2	Size-resolved particle growth due to water uptake in the lung	225

Chapter 1

Introduction

1.1 Motivation

Airborne particulate matter (PM), or aerosols, can significantly degrade air quality and alter global and regional climate. One of the largest sources of anthropogenic PM is carbonaceous aerosol emitted during combustion processes (Bond et al., 2013). Combustion as a source of energy is prevalent in every part of the world, ranging from diesel engines in trucks to biomass cookstoves in homes. While anthropogenic combustion emissions in developed countries are generally declining due to regulations and constantly improving technologies (e.g., McDonald et al., 2018), aerosol emissions from residential combustion sources in developing countries have increased over the past century due to a rapidly expanding population (Fernandes et al., 2007). Today, close to 2.8 billion people lack access to clean cooking technology, while 1.8 billion people lack access to electricity altogether (International Energy Agency, 2017).

Residential solid fuel use (SFU) most commonly refers to combustion of solid fuels (such as wood, dung, agricultural waste, coal, or charcoal) as a source of energy for domestic tasks such as cooking, heating, or lighting. In addition to this common definition, other emission sources, such as combustion of household trash as a means of waste management, are also prevalent in many of the same communities (e.g., Wiedinmyer et al., 2014). The reliance on residential SFU as a source of energy makes understanding the health and climate impacts essential; however, uncertainties in combustion aerosol emissions and their properties make the net health and climate impacts uncertain. A number of recent studies have suggested targeting residential SFU as a means of simultaneously improving public health and mitigating climate change caused by greenhouse gases (e.g., Grieshop et al., 2009, 2011; Shindell et al., 2012). Additionally, increasing access to electricity or clean energy alternatives has been suggested as a means of achieving various United Nations Millennium Development Goals such as overcoming poverty, child malnutrition, and gender inequality in

developing countries (Detchon and Leeuwen, 2011). While reducing combustion emissions through increasing access to cleaner technologies will likely have some positive health and social benefits, the magnitude of these health improvements and the overall sign of climate impacts is largely uncertain due to present-day uncertainties. Rapid changes to combustion technologies, populations, and demographics introduce substantial uncertainty as to the net effect of aerosols on climate and health in the near future. The lack of quantification of uncertainties limits our ability to assess air quality and climate change mitigation strategies.

Emissions from residential SFU can affect climate in a variety of ways. Greenhouse gas emissions from combustion processes, such as carbon dioxide and methane, are well mixed in the atmosphere due to long lifetimes (decades to centuries) and their first-order forcings are well understood (always positive) (Boucher et al., 2013). Conversely, aerosol emissions from residential SFU, mostly in the form of black carbon (BC) and organic aerosol (OA), have short lifetimes (days to weeks) and can lead to both positive and negative radiative effects (Bauer et al., 2010). Carbonaceous aerosol emissions from combustion sources can impact climate in a variety of ways. In this work, we focus on the direct radiative effect (scattering and absorption of incoming radiation) (Charlson et al., 1992) and the cloud-albedo aerosol indirect effect (altering cloud reflectivity) (Twomey, 1974). In our previous study (Kodros et al., 2015), we quantified the sensitivity of the direct radiative effect (DRE) and cloud-albedo aerosol indirect effect (AIE) from residential biofuel combustion to uncertainties in emissions and model processes. The sign and magnitude of the global-mean DRE (-20 to +60 mW m⁻²) is strongly sensitive to the black carbon to organic aerosol emission ratio, the absorptive properties of OA (termed “brown carbon”), and assumptions on how BC is mixed with scattering particles, while the AIE (+10 to -20 mW m⁻²) is strongly sensitive to the emission size distribution. This dissertation builds and expands upon our initial findings.

Exposure to PM with aerodynamic diameters less than 2.5 μm (PM_{2.5}) has been linked to an increased risk of mortality from cardiovascular and respiratory diseases (Dockery et al., 1993; Krewski et al., 2009; Pope et al., 2002). Research over the past several decades consistently suggests that the health burden from exposure to air pollutants from residential SFU is likely to be

substantial (e.g., Forouzanfar et al., 2016; Smith et al., 2014; World Health Organization, 2014). The Global Burden of Disease 2015 report (GBD2015) estimates that 2.85 (95% confidence interval: 2.18-3.59) million deaths in the year 2015 were due to exposure to household air pollution (i.e., emissions from cooking and heating), ranking it among the leading risk factors contributing to premature mortality (Forouzanfar et al., 2016). In addition, household air pollution from SFU has the potential to degrade ambient (i.e., outdoor) air quality (Butt et al., 2016; Chafe et al., 2014; Conibear et al., 2018; Lacey and Henze, 2015). However, to our knowledge, no work has yet tried to estimate premature mortality associated with SFU by an approach that jointly considers ambient and household exposures. Moreover, health impact assessments of “household air pollution” neglect similar emission sources of solid fuel use (such as combustion of household trash). Finally, estimates of mortality from exposure to $PM_{2.5}$ from SFU (including exposure to household and/or ambient air pollution from this source) rely on input data sources including country-level baseline mortality rates, $PM_{2.5}$ exposure levels, the magnitude and shape of concentration-response functions, and the number of people exposed to a specific concentration; however, no studies, to our knowledge, have investigated the sensitivity of mortality estimates to these input parameters.

Given the large uncertainty space surrounding the sign of aerosol radiative effects (potentially spanning both positive and negative forcings) and magnitude of aerosol health effects, targeted reductions of residential SFU may not yield climate and health “co-benefits”. Rather, research may instead need to focus on reducing overall model uncertainty to better communicate the potential benefits of improvement scenarios to policy makers. This dissertation is focused on improving the understanding of uncertainties in aerosol climate and health impacts from residential SFU and constraining key model parameters to improve estimates of health and climate impacts from all aerosol sources.

1.2 Scope of dissertation

This dissertation contains 6 chapters of research, all of which have either been published or submitted to relevant journals. The first 3 chapters focus on quantifying and probing the uncertainty

space of aerosol climate and health impacts from residential SFU. The last 3 chapters focus on constraining model uncertainties for aerosol from all emission sources (but regarding aerosol properties that are important for SFU climate and health effects).

In Chapter 2, we make first estimates of the aerosol radiative effects from uncontrolled combustion of domestic waste. This emission source has not been included in past global modeling studies. In addition to estimating the direct and indirect aerosol effects, we evaluate simulated aerosol optical depth with AERONET measurements.

Similarly, In Chapter 3, we make first estimates of premature adult mortality from chronic exposure to ambient $PM_{2.5}$ from uncontrolled combustion of domestic waste. We explore the sensitivity of estimates of mortality to different model resolutions.

In Chapter 4, we develop a new estimate of mortality attributable to exposure from household SFU and ambient $PM_{2.5}$ pollution from all sources. We then perform a variance-based sensitivity analysis on mortality attributed to the combined exposure to ambient and household $PM_{2.5}$ from SFU to determine what factors lead to uncertainties in mortality estimates.

Next, in Chapter 5, we explore the sensitivity of treatments of aerosol size distributions (a key parameter affecting estimates of aerosol indirect effect from residential SFU) to the cloud-albedo indirect effect from all anthropogenic aerosol emissions.

In Chapter 6, we combine airborne observations of the mixing state of black carbon (a key parameter affecting estimates of the direct radiative effect from residential SFU) with simulated aerosol number and mass concentrations to estimate the direct radiative impact in the springtime Arctic.

In Chapter 7, we explore size-resolved particle deposition in the lung, a possible source of variability in health response due to exposure to $PM_{2.5}$. We combine a size-resolved respiratory particle deposition model with a global size-resolved aerosol model to estimate the variability in particle deposition along the respiratory tract due to variability in ambient PM size distributions.

Finally, in Chapter 8, we present a summary of conclusions and implications of this dissertation. We also discuss future areas of research.

Chapter 2

The aerosol radiative effects of uncontrolled combustion of domestic waste¹

Open, uncontrolled combustion of domestic waste is a potentially significant source of aerosol; however, this aerosol source is not generally included in many global emissions inventories. To provide a first estimate of the aerosol radiative impacts from domestic-waste combustion, we incorporate the Wiedinmyer et al. (2014) emissions inventory into GEOS-Chem-TOMAS, a global chemical-transport model with online aerosol microphysics. We find domestic-waste combustion increases global-mean black carbon and organic aerosol concentrations by 8 and 6 %, respectively, and by greater than 40 % in some regions. Due to uncertainties regarding aerosol optical properties, we estimate the globally averaged aerosol direct radiative effect to range from -5 to -20 mW m^{-2} ; however, this range increases from -40 to $+4 \text{ mW m}^{-2}$ when we consider uncertainties in emission mass and size distribution. In some regions with significant waste combustion, such as India and China, the aerosol direct radiative effect may exceed -0.4 W m^{-2} . Similarly, we estimate a cloud-albedo aerosol indirect effect of -13 mW m^{-2} , with a range of -4 to -49 mW m^{-2} due to emission uncertainties. In the regions with significant waste combustion, the cloud-albedo aerosol indirect effect may exceed -0.4 W m^{-2} .

2.1 Introduction

Open, uncontrolled combustion of domestic waste occurs on a global scale, potentially emitting significant amounts of black carbon (BC) and organic aerosol (OA); however, this source is not commonly considered in modeling studies estimating aerosol radiative impacts (Christian et al., 2010; Mohr et al., 2009; Wiedinmyer et al., 2014). Uncontrolled combustion of domestic waste

¹This Chapter published as: Kodros, J. K., Cucinotta, R., Ridley, D. A., Wiedinmyer, C. and Pierce, J. R.: The aerosol radiative effects of uncontrolled combustion of domestic waste, *Atmos. Chem. Phys.*, 16(11), 6771-6784, doi:10.5194/acp-16-6771-2016, 2016.

refers to the intentional disposal of trash in an open fire either at home or at a dump (Wiedinmyer et al., 2014). This practice is common in developing countries in both rural and urban areas where municipal waste collection is insufficient; however, open combustion of domestic waste also occurs in rural developed countries (Christian et al., 2010; Wiedinmyer et al., 2014). The proximity of waste-combustion emissions to residences has created concerns for both air quality and climate. In a separate study, we estimate the global burden of mortalities due to chronic exposure of waste-combustion PM_{2.5} (Kodros et al., 2016b). Here we provide a first estimate of the aerosol radiative impacts of domestic-waste combustion.

Carbonaceous aerosol from combustion sources can impact climate in several ways; the best understood of these being the direct radiative effect (DRE) and cloud-albedo aerosol indirect effect (AIE) (Boucher et al., 2013). The DRE refers to scattering and absorption of incoming solar radiation by aerosols (Charlson et al., 1992). The magnitude and relative amount of scattering and absorption is dependent on particle composition and size, as well as the manner of mixing of different species within a single particle (Bond et al., 2006, 2013). BC has a strong absorbing component, while OA is either considered as completely scattering or having some absorbing component in the shorter visible and ultraviolet wavelengths (i.e., brown carbon) (Andreae and Gelencsér, 2006; Hammer et al., 2016; X. Wang et al., 2014), although these optical properties of organic aerosol are an open area of research. Additionally, scattering and absorption efficiencies of carbonaceous particles depend on the ratio of particle diameter to wavelength of radiation. For solar radiation, atmospheric aerosol typically have peak efficiencies between diameters of 100 nm to 1 μm , though this will vary with composition (Seinfeld and Pandis, 2012). Finally, absorption tends to increase in an internally mixed population (all particles in a size range contain an identical mixture of all chemical species) compared to an externally mixed population (different chemical species exist in separate particles) (Chung and Seinfeld, 2005; Jacobson, 2001). In this study, we assume spherical particles, which is not realistic for fresh combustion aerosol. Details of particle shape may alter optical properties.

The cloud-albedo AIE refers to altering the reflectivity of clouds by changing the cloud droplet number concentration (CDNC) (Twomey, 1974). The ability for OA and BC cloud condensation nuclei (CCN) to activate into cloud droplets is a strong function of particle size. In typical atmospheric conditions, OA and BC (when mixed with hydrophilic species) typically act as CCN when they have diameters larger than 40–100 nm (Petters and Kreidenweis, 2007). The number of particles in this size range is dependent on primary emissions as well as nucleation, condensation, and coagulation (Pierce and Adams, 2009). As these microphysical processes are often interconnected, the AIE response to an emission source may be nonlinear (e.g., additional primary emissions may reduce nucleation and condensation growth while increasing coagulation) (Bauer et al., 2010; Butt et al., 2016; D'Andrea et al., 2015). The AIE is also dependent on particle hygroscopicity (Petters and Kreidenweis, 2007). Particle hygroscopicity can be described with the hygroscopicity parameter, κ , which is the ratio of the number of moles of solute per dry volume to the moles of water per volume of pure water (Petters and Kreidenweis, 2007). While combustion aerosols tend to have lower hygroscopicity (κ for OA = ~ 0.1 and BC = 0.0), mixing with inorganic species, such as sulfate and sea salt, and chemical aging of the organics to more-hygroscopic species allows for activation at smaller diameters.

Waste combustion is an often-overlooked emission source, especially in developing countries (Christian et al., 2010). Wiedinmyer et al. (2014) provided a new global inventory for the uncontrolled combustion of domestic waste, estimating global BC and OC emissions of 0.6 and 5.1 Tg year⁻¹, respectively. This estimate is an order of magnitude greater than earlier estimates of emissions from uncontrolled waste combustion in Bond et al. (2004) (which focused on combustion-aerosol emissions in general, not just from waste combustion). Amount of annual waste burned was the largest difference between the inventories, where Bond et al. (2004) estimated a total of 33 Tg and Wiedinmyer et al. (2014) predicted 970 Tg. Further, Wiedinmyer et al. (2014) considered waste combustion in both rural and urban areas in developing and rural areas in developed countries. Many global inventories, including Emissions Database for Global Atmospheric Research (EDGAR), do not include estimates of uncontrolled waste-combustion emissions. In addition

to carbonaceous emissions, Wiedinmyer et al. (2014) estimated 0.5 Tg year^{-1} of sulfur dioxide (SO_2) and 1.1 Tg year^{-1} of ammonia (NH_3). These gas-phase species may increase nucleation and condensation rates, thereby increasing particle number and mass concentration through secondary aerosol formation.

There are several uncertainties related to emissions in the Wiedinmyer et al. (2014) inventory. First, the reported uncertainty in the Akagi et al. (2011) emission factors for BC and OC are 42 and 93 %, respectively. This is in addition to uncertainties in the mass of waste generated (i.e., estimates of fuel use). Second, the Wiedinmyer et al. (2014) inventory does not include information on emission size distribution. The emitted particle size distribution varies with fuel type and flaming condition and goes through rapid aging in the first few hours after emission on spatial scales not resolved in global models (Janhäll et al., 2010; Sakamoto et al., 2015). Finally, this inventory does not include information on the optical properties of organic aerosol. Absorptive OA (or brown carbon, BrC) has been observed in some wood and agricultural waste fuels, under certain flaming conditions (Chen and Bond, 2010; McMeeking et al., 2014; Saleh et al., 2013); however, we are not aware of studies determining these aerosol properties for domestic-waste combustion. In this paper, we explore uncertainties in total emission mass and size distribution (affecting both DRE and AIE) as well as optical properties (affecting just DRE).

To our knowledge, this is the first paper to quantify the global aerosol radiative impacts from uncontrolled combustion of domestic waste. In Sect. 2, we discuss the model set-up (Sect. 2.1), methods for model evaluation (Sect. 2.2), and calculation of radiative effects (Sects. 2.3–2.4). In Sect. 3, we show comparisons to ground observations of model simulations with and without waste-combustion emissions. In Sect. 4, we discuss changes in modeled aerosol mass (Sect. 4.1), size-resolved aerosol number concentration (Sect. 4.2), direct radiative effect (Sect. 4.3), and cloud-albedo aerosol indirect effect (Sect. 4.4). In Sect. 5, we share our conclusions.

Table 2.1: Description of simulations.

Simulation	GMD	Mass scale factor	Species
BASE	100 nm	1.0	primary and secondary
SIZE200	200 nm	1.0	primary and secondary
SIZE30	30 nm	1.0	primary and secondary
PRIMARY	100 nm	1.0	primary BC and OA only
HIGHMASS	100 nm	2.0	primary and secondary
LOWMASS	100 nm	0.5	primary and secondary
WASTE_OFF	N/A	0.0	none

2.2 Methods

2.2.1 Model overview

To calculate aerosol number, mass, and size distributions from domestic-waste combustion, we use the Goddard Earth Observing System global chemical-transport model (GEOS-Chem) version 10.01 coupled with Two Moment Aerosol Sectional (TOMAS) microphysics scheme (Adams and Seinfeld, 2002). We use GEOS-Chem with 47 vertical layers and a $4^\circ \times 5^\circ$ horizontal resolution. This version of TOMAS uses 15 size sections ranging from 3 nm to $10 \mu\text{m}$ with tracers for sulfate, sea salt, OA, BC, and dust (Lee and Adams, 2012; Y. H. Lee et al., 2013). GEOS-Chem is driven using reanalysis meteorology fields from GEOS5 (<http://gmao.gsfc.nasa.gov>). Since meteorology is prescribed, the addition of waste-combustion emissions does not feedback into weather patterns. All simulations are for the year 2010, with 1 month of model spinup that is not included in analysis.

We use a ternary nucleation scheme involving water, sulfuric acid, and ammonia following the parameterization of Napari et al. (2002), scaled with a global tuning factor of 10^{-5} (Jung et al., 2010; Westervelt et al., 2013). In addition, we use a binary nucleation scheme (sulfuric acid and water) when ammonia mixing ratios are less than 1 pptv (Vehkamäki, 2002). Secondary organic aerosol (SOA) sources include a biogenic monoterpene component of 19 Tg year^{-1} as well as an anthropogenically enhanced component of 100 Tg year^{-1} (we do not know if the anthropogenically enhanced SOA is due to anthropogenic volatile organic compounds or an enhancement of biogenic SOA due to anthropogenic influences on chemistry) (D’Andrea et al., 2013; Spracklen et al., 2011).

SOA is condensed irreversibly onto existing aerosol at the time of emission of the parent compounds using 10 % of monoterpene emissions for the biogenic component and 0.2 Tg SOA per Tg-CO for the anthropogenic component (CO emissions are used as a proxy for the spatial and temporal distribution of anthropogenically enhanced SOA).

In all simulations we use the following emission inputs. We use fossil-fuel combustion anthropogenic emissions from the Emissions Database for Global Atmospheric Research (EDGAR) version 4 (Janssens-Maenhout et al., 2011). EDGAR emissions are overwritten in the United States by the Environmental Protection Agency 2011 National Emissions Inventory (NEI2011; <http://www3.epa.gov/ttn/chief/>), in Canada by Criteria Air Contaminants (CAC; <http://www.ec.gc.ca/inrp-npri/>), in Mexico by Big Bend Regional Aerosol and Visibility Study (BRAVO) (Kuhns et al., 2005), in Europe by the Cooperative Programme for Monitoring and Evaluation of the Long-Range Transmission of Air Pollutants in Europe (EMEP) (Vestreng et al., 2009), and in Asia by the Streets inventory (Streets et al., 2003). Black and organic carbon (OC) emissions from biofuel and fossil-fuel combustion are from Bond et al. (2007) and biomass burning from Global Fire Emissions Database version 3 (GFED3) (Van Der Werf et al., 2010) with 3-hourly scale factors. Sea salt aerosol emissions follow the scheme of Jaeglé et al. (2011), while dust emissions are based on the DEAD scheme (Zender, 2003).

To estimate the impact of waste-combustion emissions, we include the Wiedinmyer et al. (2014) inventory to the above emissions set-up. Table 2.1 describes all simulations used in this study. Our BASE simulation uses total BC, OC, SO₂, and NH₃ mass as in Wiedinmyer et al. (2014). We emit 1 % of SO₂ as aerosol-phase sulfate (SO₄) and use a fixed OA to OC ratio of 1.8. We scale bulk BC and OA mass into size sections assuming a single lognormal mode with a geometric number-mean diameter (GMD) of 100 nm and a standard deviation of 2. We note that Wiedinmyer et al. (2014) do not include information on the emission size distribution, and this is a significant source of uncertainty (L. Lee et al., 2013). The spatial distribution of emissions is shown in Figure 2.1 for OA, BC, and NH₃. The emissions of SO₂ show a similar spatial pattern but with a factor of 2 lower in magnitude than NH₃. The regions with the largest particle emissions are eastern China,

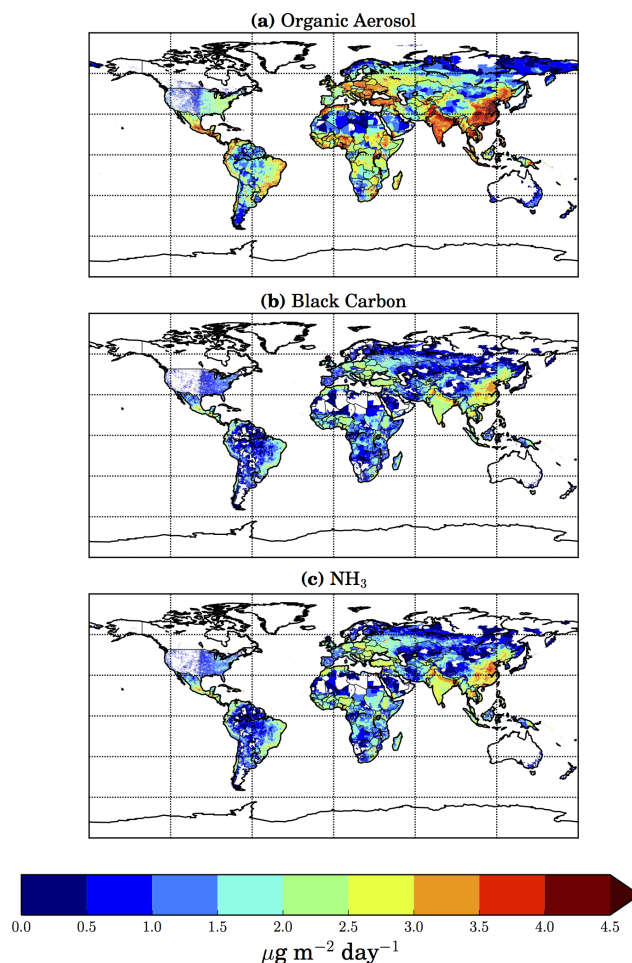


Figure 2.1: Emission fluxes from the open combustion of domestic waste for (a) organic aerosol, (b) black carbon, and (c) NH₃ from Wiedinmyer et al. (2014).

northern India, eastern Europe, and Mexico. To test the sensitivity of aerosol radiative effects to waste-combustion emission size distribution, we include two sensitivity simulations, SIZE200 and SIZE30. Here, we conserve total emission mass but increase the GMD from 100 to 200 nm and decrease the GMD from 100 to 30 nm, respectively. These distributions are chosen to reflect the range of reported values from fresh and aged fossil fuel and biomass burning (Ban-Weiss et al., 2010; Carrico et al., 2010; Janhäll et al., 2004; Sakamoto et al., 2015). In Kodros et al. (2015), we also tested the sensitivity of aerosol radiative effects to uncertainty in the standard deviation of the emission size distribution and found the results are qualitatively similar to uncertainties in the GMD (a narrowing of the emission size distribution has a similar effect as to decreasing the

value of the GMD, and visa versa), and so we do not include that here. In PRIMARY, we emit only aerosol-phase BC and OA waste combustion, and remove emissions of gas-phase SO₂ and NH₃, from this source. This simulation will test the contribution of nucleation and condensation from gas-phase species emitted from waste combustion. Finally, we test the sensitivity of aerosol effects to a factor of 2 uncertainty in total waste-combustion emission mass (HIGHMASS and LOWMASS). The factor of 2 uncertainty is similar to uncertainties listed in emission factors in Akagi et al. (2011). We compare these simulations to a control simulation with no waste-combustion emissions (WASTE_OFF).

2.2.2 Aerosol optical depth (AOD) comparison

We compare model aerosol optical depth with measurements made with the Aerosol Robotic Network (AERONET). AERONET is a network of ground-based remote sensing instruments aimed at providing global, long-term measurements of aerosol properties. AERONET uses a sun photometer to measure AOD at several wavelengths in 15 min intervals when the sun is not obscured by clouds (Holben et al., 1998).

To compare to AERONET measurements, we output GEOS-Chem-TOMAS size-resolved mass and number concentrations at 3 h intervals for the BASE and WASTE_OFF simulations. We calculate model AOD using refractive indices from the Global Aerosol Database and published Mie code (Bohren and Huffman, 1983). In this calculation, we only consider an external mixing-state assumption, though we note the extinction optical depth (what we are referring to as AOD) of an internal mixture is very similar (though the individual scattering and absorption optical depths are different). We average AERONET AOD into 3 h intervals and match measured time and locations with model AOD. We restrict observed AOD to contain greater than six measurements within each 3 h time period, thus removing intervals where measurements were limited due to clouds or instrument error. We also restrict our comparison to only include time periods when the observed AOD is greater than 0.01 to avoid detection-limit issues, as this is the uncertainty limit of AERONET

measurements (Holben et al., 1998). We then compare the time average of the co-sampled sites that match these criteria.

2.2.3 Direct radiative effect calculation

We calculate the all-sky DRE using GEOS-Chem-TOMAS monthly averaged aerosol mass and number concentrations and refractive indices from GADS. We calculate AOD, single scatter albedo, and asymmetry parameter using Mie code published in Bohren and Huffman (1983). We use these aerosol optical properties and monthly mean albedo and cloud fraction from GEOS5 as inputs to the offline version of the rapid radiative transfer model for global climate models (RRTMG) (Iacono et al., 2008), implemented in GEOS-Chem (Heald et al., 2014), that considers longwave and shortwave and treats clouds with the Monte Carlo independent column approximation (McICA) (Pincus et al., 2003).

We estimate the DRE for six different optical assumptions: a core–shell morphology with and without absorptive OA, an external mixture with a constant absorption enhancement factor of 1.5 (ext*1.5) with and without absorptive OA, a homogeneous internal mixture, and an external mixture. These optical assumptions are discussed in detail in Kodros et al. (2015) (see Table 1 in Kodros et al., 2015, and Table 2.3 in this paper) and are applied to all particles, regardless of emission source. In all cases, we assume the particles are spherical. Briefly, the homogeneous internal mixture assumes all particles in a size bin have the same composition and the refractive index of the particle is a volume-weighted average of the individual species. The core–shell mixture assumes black carbon forms a spherical core and the other hydrophilic species form a homogeneously mixed shell around the core. The external mixture assumes black carbon exists as a separate population from the other homogeneously mixed species. Finally, in ext*1.5 we simply multiply the absorption predicted in the external mixture by a constant enhancement factor of 1.5. This is done in some models to estimate the enhanced absorption observed in core–shell mixtures (such as X. Wang et al., 2014). In the BrC calculations, we estimate absorptive OA (or brown carbon) using the modeled OA to BC

ratio and the parameterization in Saleh et al. (2014). In all other calculations, we assume that OA is near-purely scattering throughout the visible spectrum.

We note several important limitations in our treatment of aerosol optics. First, mixing state may vary regionally and temporally, yet here we apply each mixing state globally and at all times. Second, it has been suggested that the optical properties of OA may change with photolysis, yet here our optical properties are held fixed (Lee et al., 2014; Zhao et al., 2015). Therefore, these mixing states should be considered as ideal cases. Finally, we use monthly mean concentrations and properties as well as monthly mean cloud properties. Despite these limitations, we feel this method is sufficient for a first estimate of the DRE from waste-combustion emissions.

2.2.4 Cloud-albedo aerosol indirect effect calculation

We use monthly mean GEOS-Chem-TOMAS mass and number concentrations and the activation parameterization of Abdul-Razzak and Ghan (2002) to calculate CDNCs. We assume a constant updraft velocity of 0.5 m s^{-1} . For the AIE, we assume aerosol species are mixed internally within each size bin and calculate κ , the hygroscopicity parameter, as a volume-weighted average of the individual species (Petters and Kreidenweis, 2007). As a control, we assume an effective cloud drop radii of $10 \mu\text{m}$ and then perturb this value by taking the ratio of CDNC with and without waste-combustion emissions to the one-third power (as in Rap et al., 2013; Scott et al., 2014). To simulate the change in the top-of-the-atmosphere radiative flux due to changes in effective cloud drop radii, we use RRTMG with monthly mean cloud fraction, temperature, pressure, and liquid water content from GEOS5. Again, we note that the use of monthly mean aerosol and meteorology fields is a limitation in this method, yet we feel it is sufficient for a first estimate.

2.3 Model results

2.3.1 Comparison to observations

Figure 2.2 shows comparisons of time-averaged model AOD with AERONET measured AOD at all available sites for the BASE (a–c) and WASTE_OFF (d–f) simulations at 380, 500, and 1020 nm

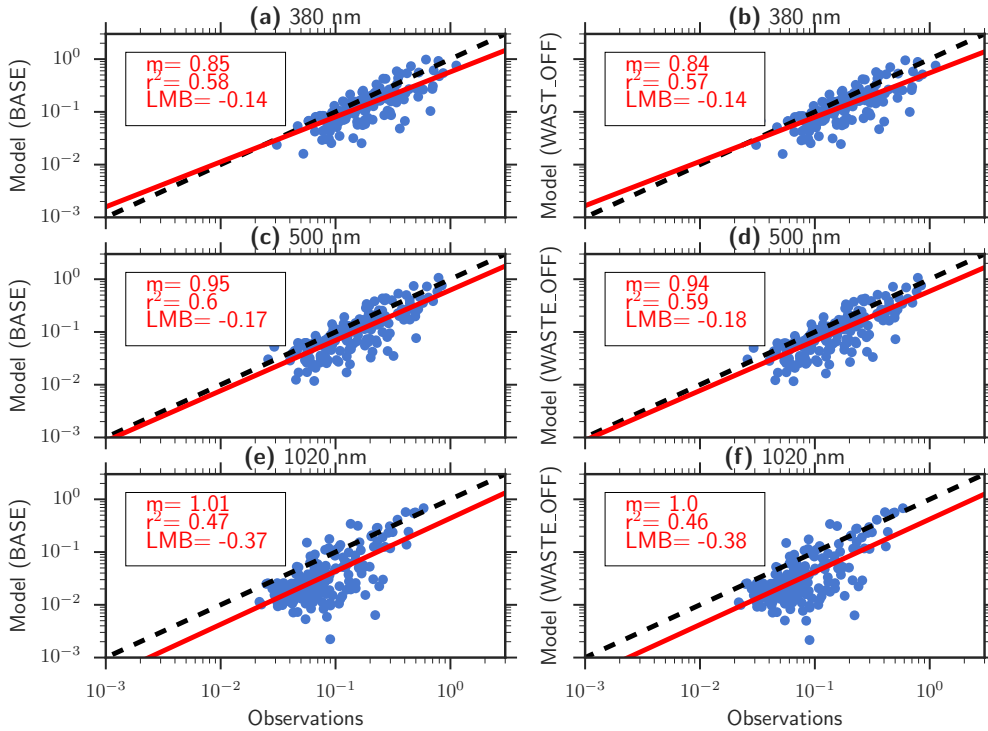


Figure 2.2: One-to-one plots of time-averaged AOD for BASE (a, c, e) and WASTE_OFF (b, d, f) compared to AERONET observations at 380 nm (a, b), 500 nm (c, d), and 1020 nm (e, f). The values in the box give the slope of the linear regression (m), the correlation (r^2), and the log-mean bias (LMB), while the black dashed line represents the 1 : 1 line and the red line is the result of the linear regression.

wavelengths (one dot for each site). After we apply the criteria described in Sect. 2.2, we have 173 sites at 380 nm, 193 sites at 500 nm, and 211 sites at 1020 nm. The model is generally capable of capturing the variability in measured AOD (in WASTE_OFF at 500 nm slope = 0.94 and log-mean bias = -0.18). Given the coarse spatial resolution of the model, the large variability is expected ($r^2 = 0.59$), as more- and less-polluted areas may exist within the same model grid box (~ 400 km length scale). Including waste-combustion emissions slightly improves the model comparison in all three metrics and at all wavelengths (with the exception of the slope at 1020 nm). While these changes are not statistically significant, we note that GEOS-Chem-TOMAS has some skill at reproducing observed aerosol optical properties, and including this inventory does not degrade model comparison.

Table 2.2: Percent change in global, annual-mean N10, N40, N80, N150, BC mass, and OA mass from domestic-waste combustion (i.e., relative to WASTE_OFF simulation).

Simulation	N10 (%)	N40 (%)	N80 (%)	N150 (%)	BC (%)	OA (%)
BASE	0.86	0.90	1.04	1.16	8.46	5.60
SIZE200	0.86	0.55	0.46	0.36	8.36	5.53
SIZE30	4.02	5.43	5.42	4.40	8.07	5.14
PRIMARY	-0.17	0.232	0.52	0.89	8.47	5.61
HIGHMASS	1.68	1.77	2.06	2.31	16.9	11.2
LOWMASS	0.44	0.45	0.53	0.59	4.23	2.80

Table 2.3: Global-mean all-sky direct radiative effect and cloud-albedo aerosol indirect effect relative to the WASTE_OFF simulation for all sensitivity simulations and mixing-state assumptions.

Simulation	Direct radiative effect (mW m^{-2})						AIE (mW m^{-2})
	Core-shell, BrC	Ext*1.5, BrC	Homog.	Core-shell	Ext*1.5	Ext.	
BASE	-5.0	-8.7	-11	-13	-17	-20	-13
SIZE200	+3.2	-6.0	-3.7	-8.7	-16	-18	-8.3
SIZE30	+4.1	+3.7	-1.5	-1.6	-2.3	-5.8	-49
PRIMARY	-5.7	-9.3	-12	-14	-17	-20	-4.0
HIGHMASS	-10	-17	-22	-26	-34	-40	-24
LOWMASS	-2.5	-4.3	-5.6	-6.5	-8.7	-10	-6.7

2.3.2 Changes in mass concentrations from domestic-waste combustion

Figure 2.3 shows the annual-mean percent change in boundary-layer OA, BC, NH_3 , and $\text{PM}_{2.5}$ in the BASE-WASTE_OFF simulations, and global-mean OA and BC changes are in Table 2.2. Combustion of domestic waste under the BASE emission assumptions increases BC and OA concentrations in the global mean by 8.5 and 5.6 %, respectively. Regionally, domestic-waste combustion increases surface BC concentrations by 10–20 % throughout much of Asia, northern Africa, and South and Central America. The largest increases in BC (greater than 40 %) occur in central Mexico (i.e., Mexico City), Turkey, northern Egypt (i.e., Cairo), Sri Lanka, and Papua New Guinea, as well as increases of 30–40 % in Pakistan, Morocco, and Central America. Despite greater OA emissions, the relative change of OA from domestic-waste combustion is generally less than BC due to large OA sources from biofuel combustion and secondary organic aerosol in waste-combustion regions. Waste combustion does increase OA concentrations by more than 40 %

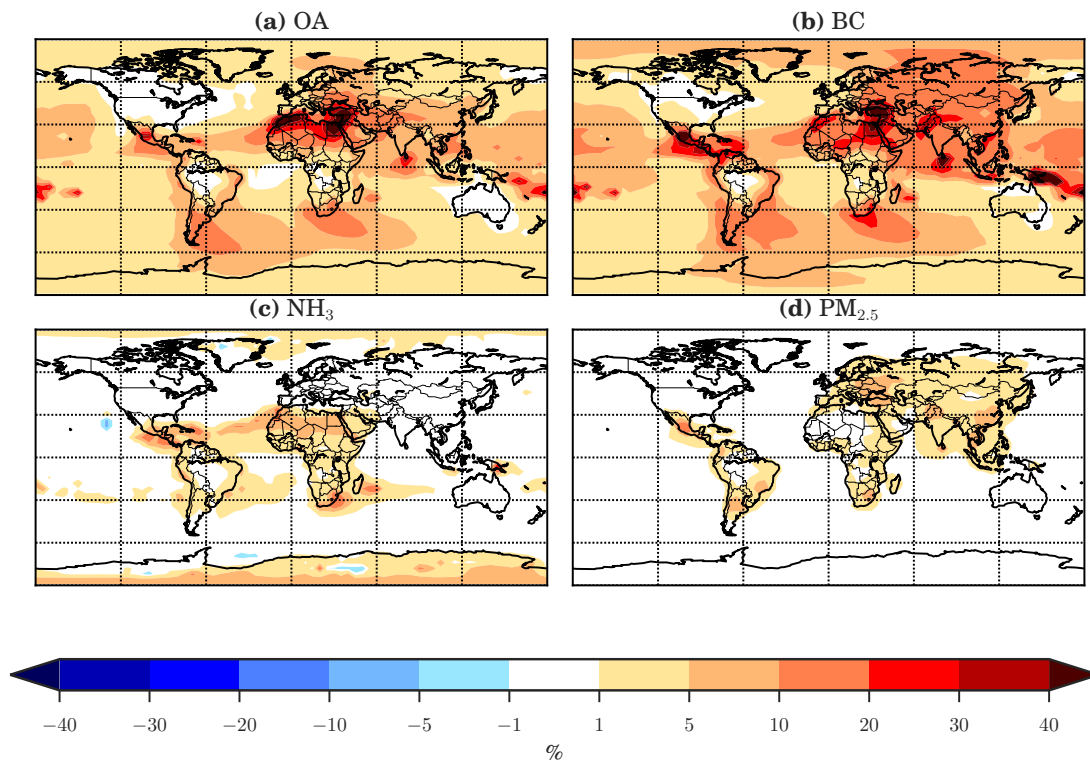


Figure 2.3: Percent changes in annually averaged boundary-layer (a) OA, (b) BC, (c) NH₃, and (d) PM_{2.5} mass due to domestic-waste combustion (BASE-WASTE_OFF).

in Morocco, Turkey, Egypt, and the eastern portions of the Middle East. Increases in BC and OA lead to increases in surface PM_{2.5} concentrations of 1–5 % over most land masses outside of North America and Australia and 5–10 % in source regions.

Figure 2.3 also shows the percent change in gas-phase NH₃. Waste combustion contributes increases in NH₃ of 1–10 % in Mexico, Central and South America, and Africa. These are regions of significantly lower NH₃ concentrations compared to Asia and Europe in our simulations, which have negligible relative changes to NH₃. In our model, NH₃ may contribute to particle nucleation and growth, which may alter particle size distributions (but have little effect on PM_{2.5} mass). These changes are discussed in the next section. Relative changes in SO₄ mass generally follow the spatial pattern of OA; however, these changes are less than 1 % and so are not shown.

Table 2.2 shows the global, annual-mean percent change in boundary-layer BC and OA mass for BASE and the sensitivity simulations compared to WASTE_OFF (thus isolating the contribution

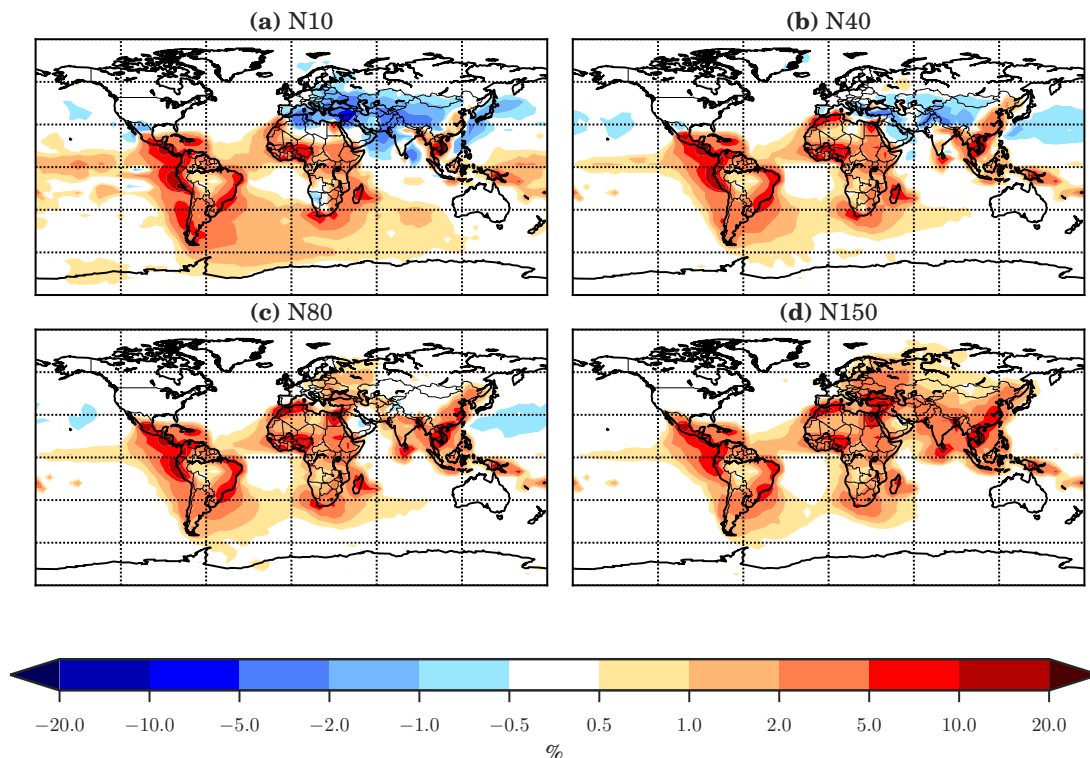


Figure 2.4: Annual-mean percent change in boundary-layer (a) N10, (b) N40, (c) N80, and (d) N150 for domestic-waste combustion (BASE-WASTE_OFF).

of domestic-waste combustion to BC and OA). The largest changes to modeled BC and OA mass come when emission BC and OA mass is doubled (HIGHMASS) and halved (LOWMASS). In these simulations, the model response to changes in emission mass is close to linear. In simulations PRIMARY, SIZE30, and SIZE200, total BC and OA emission mass is held constant. The BC and OA mass distributions in SIZE30 and SIZE200 are shifted to smaller and larger sizes, respectively, which may lead to changes in deposition rates; however, these changes prove to be minor (Table 2.2). The global-mean relative change in BC and OA mass from domestic-waste combustion ranges from 4.23 to 16.9 and 2.80 to 11.2 %, respectively, given the factor of 4 uncertainty in emission mass tested here.

2.3.3 Changes to size-resolved number concentrations

Modeled percent changes to annual-mean size-resolved number concentrations for the BASE-WASTE_OFF comparison are shown in Figure 2.4 and the global averages in Table 2.2. Here we

consider the following size classes: all particles with a diameter greater than 10 nm (N10), 40 nm (N40), 80 nm (N80), and 150 nm (N150). N40, N80, and N150 are proxies for climate-relevant particles. In the global mean for our BASE assumptions, waste combustion leads to a larger increase in N80 (1.04 %) and N150 (1.16 %) than in N10 (0.86 %) and N40 (0.90 %). This is due to particle emissions represented as a single lognormal mode centered around 100 nm as well as a microphysical feedback (discussed below).

Regionally, the sign and magnitude of changes to particle number concentration vary with size class. Waste combustion tends to increase particle number concentration in each size class in Mexico, Central and South America, and the Pacific Islands. Conversely, waste combustion decreases N10 and N40 in much of Europe and Asia. This discrepancy is caused by a feedback in aerosol microphysics (discussed in detail in Westervelt et al., 2014; Pierce and Adams et al., 2009; Kodros et al., 2015). Briefly, emitted primary accumulation-mode particles (in BASE this is centered around 100 nm) increase particle surface area, thus increasing the sink for condensation vapors (e.g., H_2SO_4 , NH_3 , organics). This increased condensation sink reduces nucleation rates, reduces growth rates, and increases coagulation scavenging of nucleation mode particles. This effect is predominant in Europe and Asia and for smaller size cutoffs (N10 and N40) with a significant contribution of nucleation mode particles (such that waste combustion emissions cannot compensate for the reduced nucleation and growth). The regions of Central and South America and Africa have lower concentrations of condensable vapor than Europe and Asia in WASTE_OFF, and so this feedback is less dominant. In addition, the Americas and Africa have a larger fractional increase in NH_3 concentrations, which aid in nucleation and growth (Figure 2.3).

Figure 2.5a shows the change in global-mean particle number distribution for each of the sensitivity simulations relative to WASTE_OFF. In the BASE-WASTE_OFF comparison, particle number concentration decreases for sizes less than 80 nm (due to the feedback described above) and increases for sizes greater than 80 nm (due to primary emissions) (see Table 2.2 for integrated values). The emission mass scale factor tends to scale the total waste combustion number distribution up or down, while maintaining the general shape of the distribution. The HIGHMASS simulation has a

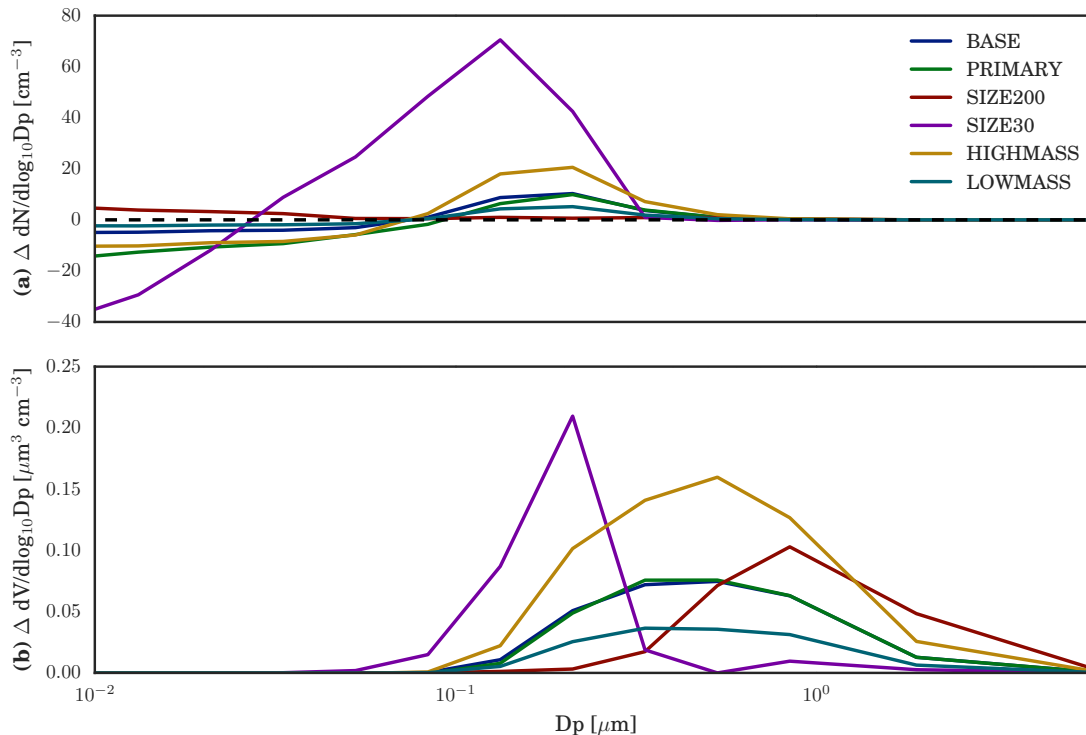


Figure 2.5: The change in global-mean (a) number distribution and (b) volume distribution for the different sensitivity studies relative to the WASTE-OFF simulation.

larger increase in accumulation-mode particles as well as a stronger suppression of nucleation/growth and thus a larger decrease in nucleation-mode particles relative to BASE. Meanwhile, LOWMASS scales in the opposite direction. In the PRIMARY simulation, we remove gas-phase NH_3 and SO_2 emissions from waste combustion, which contributes to particle nucleation and condensational growth. The removal of these condensable vapors results in a larger suppression of nucleation and growth relative to BASE, causing a larger decrease in sub-80 nm particles as well as fewer particles in the 80–200 nm range. When only primary BC and OA from waste combustion are emitted, the global-mean N10 decreases (-0.17% , Table 2.2). Nucleation and condensational growth is a less significant contributor to particles greater than 200 nm, and so PRIMARY and BASE have the same distribution at these larger sizes.

Altering the GMD of the emissions size distribution leads to the largest changes in modeled distributions. In SIZE200, we increase emission GMD while keeping total mass constant. As-

suming a constant density, this necessitates a smaller number flux of emitted particles (as larger particles have more mass). The reduced particle number concentration relative to BASE allows for nucleation through emitted NH_3 and SO_2 to increase the number of sub-80 nm particles; however, increases in global-mean particle number concentration are less than 1 % in all size classes (Table 2.2). Conversely, global-mean particle number concentration increases by greater than 4 % in all size classes in the SIZE30 simulation. The increased particle number concentration does lead to a stronger suppression of nucleation; however, as emission GMD is now 30 nm, particle number concentration changes become positive at 20 nm (compared to 80 nm for BASE). Across all simulations, our particle number concentration is most sensitive to decreasing the value of the GMD of the assumed size distribution. Thus, understanding near-source, sub-grid-scale aging, which takes primary combustion particles from diameters around 30 nm to larger sizes (e.g., Sakamoto et al., 2016), is very important in determining the size-distribution effects of waste combustion. Across all sensitivity simulations, we find a range in the global-mean particle number concentration changes due to waste combustion of -0.2 to 4.0 % for N10, 0.2 to 1.8 % in N40, 0.5 to 5.4 % in N80, and 0.4 to 4.4 % in N150.

2.3.4 Aerosol direct radiative effect

Table 2.3 and Figure 2.6 show the global-mean all-sky DRE from waste combustion for the six different mixing-state assumptions for the BASE-WASTE_OFF comparison as well as other sensitivity simulations. Under the BASE assumptions, the global-mean DRE is negative for all mixing states, ranging from -5 to -20 mW m^{-2} . Globally, the OA to BC ratio from waste-combustion emissions is around 14 to 1, leading to increased scattering and a predominantly negative or cooling DRE. The relative emission mass of OA and BC is a source of uncertainty in Wiedinmyer et al. (2014). In Kodros et al. (2015), we found that the sign of the DRE is sensitive to the OA to BC ratio, where increasing the relative amount of BC leads to more positive (less negative) DRE. As in previous studies, the DRE becomes more positive when BC is assumed to

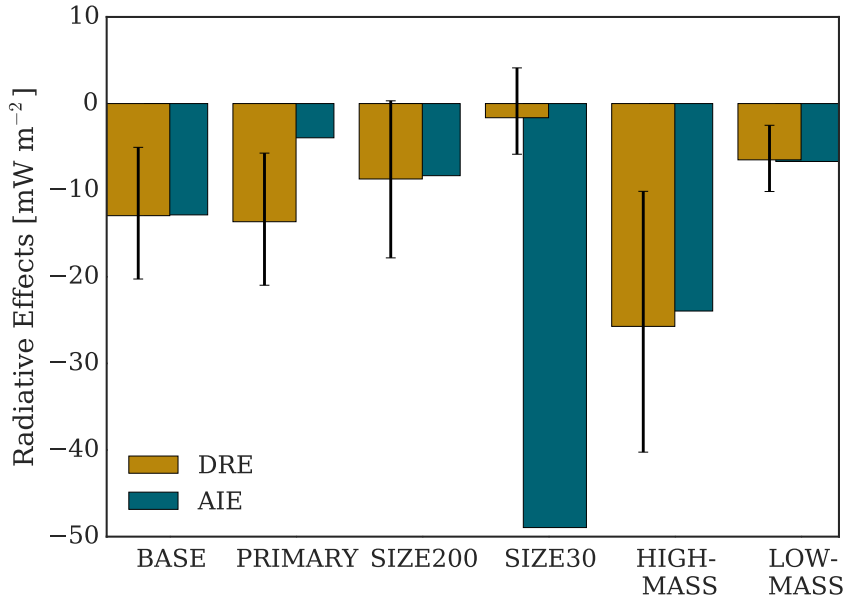


Figure 2.6: Global-mean all-sky direct radiative effect (DRE) and cloud-albedo aerosol indirect effect (AIE) for the baseline (BASE), aerosol-phase emissions only (PRIMARY), larger (SIZE200) and smaller (SIZE30) geometric mean diameter, and doubled (HIGHMASS) and halved (LOWMASS) emission mass relative to the WASTE_OFF simulation. The gold bars represent the DRE for the core-shell mixing state, while the error bars show the range due to the other optical assumptions.

be mixed internally (represented as core-shell, homogenous, and ext*1.5) as opposed to externally mixed and when OA is assumed to absorb as brown carbon.

Figure 2.7 shows maps of annual-mean all-sky DRE from waste combustion for all mixing states for BASE-WASTE_OFF. Waste combustion causes a largely negative DRE in much of Asia, Eastern Europe, and the Americas. In regions with bright surfaces (high albedo), such as the Sahara or Greenland ice sheet, the aerosol mixture has a high-enough absorbing component to decrease planetary albedo and cause a positive or warming DRE. The largest-magnitude DRE from waste combustion occurs in eastern China (ranging from -0.4 to -0.1 W m^{-2}), as well as northern India and Eastern Europe (-0.3 to -0.05 W m^{-2}).

Across all simulations and mixing-state combinations, the global-mean DRE from waste combustion ranges from -40 to $+4 \text{ mW m}^{-2}$ (Table 2.3). In simulations HIGHMASS and LOWMASS, the factor-of-2 uncertainty in emission mass leads to approximately a factor-of-2 scale in DRE. In PRIMARY, the removal of the emission gas-phase condensable vapors results in a reduction of

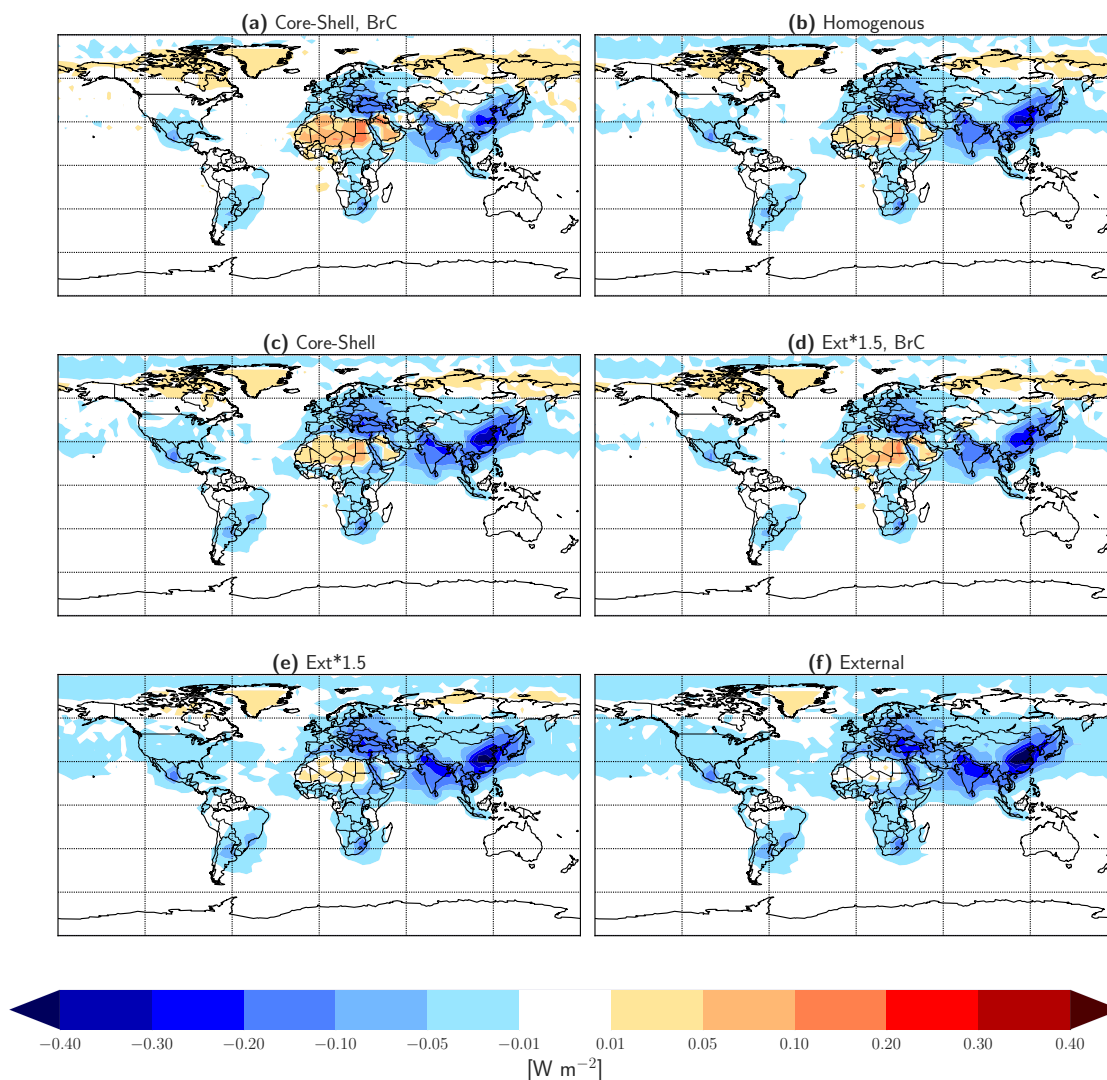


Figure 2.7: The all-sky direct radiative effect for domestic-waste combustion (BASE-WASTE_OFF) assuming a (a) core-shell with brown carbon, (b) homogenous internal, (c) core-shell, (d) external with brown carbon and an absorption enhancement factor of 1.5, (e) external with an absorption enhancement factor of 1.5, and (f) external mixing state.

sub-200 nm particles, which does not greatly affect the volume distribution (Figure 2.5b). As a result, the global-mean DRE in PRIMARY is similar to that in BASE. The slightly more negative DRE in the internal mixtures (core-shell and homogenous) may be a result of smaller shell diameters due to reduced condensation. Both SIZE200 and SIZE30 result in less negative DRE. In SIZE200, the mass distribution is moved to larger sizes, resulting in decreases in mass scattering and absorption efficiencies (the size distribution in the BASE simulation has nearly optimal mass scattering and

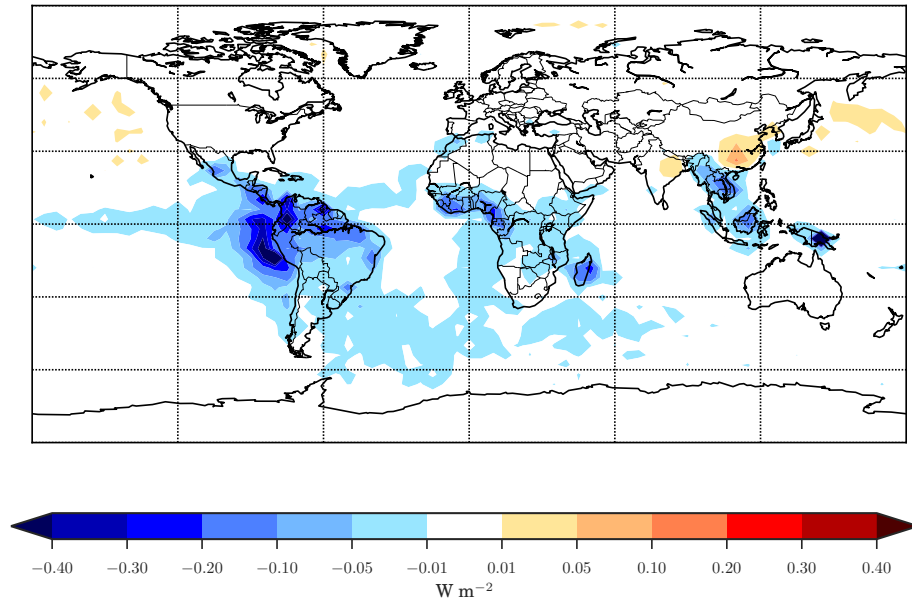


Figure 2.8: The cloud-albedo aerosol indirect effect difference between BASE-WASTE_OFF.

absorption efficiencies). However, the fractional decrease in scattering efficiency is greater than that for absorption, resulting in a lower single-scattering albedo and an overall decrease in the magnitude of cooling. In SIZE30, the mass distribution is shifted to smaller sizes, which again lowers mass scattering and absorption efficiencies with a greater decrease in scattering relative to absorption. Again, this lowers the single-scattering albedo and decreases the magnitude of cooling.

2.3.5 Cloud-albedo aerosol indirect effect

Figure 2.8 shows the cloud-albedo AIE from domestic-waste combustion in the BASE-WASTE_OFF simulation. Waste-combustion emissions increase CDNC, and thus cloud reflectivity leading to a negative AIE in Central and South America, Africa, and the Pacific Islands. These are regions where the microphysical feedback suppressing nucleation and growth is less dominant, and waste combustion leads to increases in N40 (Figure 2.4). Conversely, despite increases in aerosol mass from waste combustion in Asia and Europe, the AIE is 0 or slightly positive. This is caused by feedbacks in aerosol and cloud microphysics. The “suppression of nucleation and growth” feedback (described earlier) leads to decreases in N40 and thus CDNC. In addition, heavy anthropogenic

pollution in India and China results in a strong competition for water vapor. Increases in N80 and N150 (Figure 2.4) decrease the maximum supersaturation achieved in updrafts, which further limits droplet activation. As a result of the competing regional effects, the global-mean AIE for BASE-WASTE_OFF is -13 mW m^{-2} (Table 2.3).

The global, annual-mean AIE for all simulations is listed in Table 2.3 and plotted in Figure 2.6. In the global mean, the AIE ranges from -4 to -49 mW m^{-2} based on all emission uncertainties. In general, AIE is stronger in simulations with greater particle-number increases from waste combustion (SIZE30, HIGHMASS) and weakest in simulations with smaller particle-number increases (SIZE200, PRIMARY, LOWMASS). The largest-magnitude AIE occurs in the SIZE30 simulation (-49 mW m^{-2}) due to the large increase in particle number concentration (Table 2.2 and Figure 2.5). The lowest magnitude AIE occurs in the PRIMARY simulation, where condensable vapors from waste-combustion emissions are removed, leading to fewer particles in the 40–200 nm size range relative to BASE (Figure 2.5). This implies a non-trivial contribution of nucleation and growth to CCN concentrations from the NH_3 and SO_2 emissions from trash combustion.

2.4 Conclusions

In this paper, we use a global chemical-transport model to provide a first estimate of aerosol concentrations and radiative impacts from open, uncontrolled combustion of domestic waste. Using emissions from Wiedinmyer et al. (2014), we find increases in global-mean boundary-layer BC and OA mass of 8.5 and 5.6 %, with regional increases exceeding 40 %, relative to simulations without waste-combustion emissions. In our base simulations, we estimate that domestic-waste combustion emissions lead to a global-mean DRE ranging from -5 to -20 mW m^{-2} (range due to optical assumptions) and an AIE of -13 mW m^{-2} . In areas where open waste combustion occurs, the resulting aerosol radiative impacts can range from -0.1 to -0.4 W m^{-2} . On a global scale, we find minor improvements of model AOD compared to observed AERONET AOD when including waste-combustion emissions.

We include several sensitivity simulations to explore uncertainties in waste-combustion emission size distribution, gas-phase species (leading to secondary aerosol), and emitted particulate mass. In the global, annual mean, we estimate a range in the DRE of +4 to -40 mW m^{-2} and in the AIE of -4 to -49 mW m^{-2} . We find altering the waste-combustion emission size distribution while keeping total mass constant (SIZE200 and SIZE30) leads to substantial changes in the modeled size distribution, thus affecting the AIE (-8 to -49 mW m^{-2}) and to a lesser extent the DRE (+4 to -18 mW m^{-2}). In PRIMARY, we emit only primary BC and OA particles from waste combustion (and not particle-precursor gases). In this simulation, waste combustion leads to a stronger suppression of nucleation and growth, smaller increases in particle number concentration, and a lower magnitude AIE (-4 mW m^{-2}). Thus, the particle-precursor gases emitted from waste combustion are important contributors to new-particle formation and growth, and they contribute to the negative AIE from waste-combustion emissions. We introduce a factor of 2 uncertainty in emission mass in HIGHMASS and LOWMASS. We find this leads to a near-linear increase in BC and OA mass and DRE (-2.5 to -40 mW m^{-2}). Scaling emission mass up/down also increases/decreases emitted particle number concentration, leading to a range of AIE of -7 to -24 mW m^{-2} . There is little information on emission size distribution and optical properties from waste combustion. Better knowledge of these parameters along with continued validation of emission mass fluxes will reduce model uncertainty.

Our estimates for the aerosol radiative effects from waste combustion are relatively small compared to the total aerosol burden; however, they are of similar magnitude to recent estimates of radiative impacts from biofuel combustion (-0.06 to $+0.08 \text{ W m}^{-2}$ for the DRE and -0.05 to $+0.01 \text{ W m}^{-2}$ for the AIE), another emission source associated with developing countries (Bond et al., 2013; Butt et al., 2016; Kodros et al., 2015; Lacey et al., 2015). Based on our estimates, it appears that the aerosol radiative effects from waste combustion likely have an overall cooling effect.

In a separate study (Kodros et al., 2016), we estimated that this waste-combustion aerosol leads to 284 000 (95 % CI: 188 000–404 000) premature deaths globally each year. If waste-combustion

aerosol were reduced to protect human health, this may also lead to a positive radiative forcing (warming tendency) due to a reduction of the waste-combustion-aerosol cooling. A reduction in waste combustion would also lead to a change in greenhouse gases, although these greenhouse-gas estimates are out of the scope of this paper due to the complex nature of greenhouse-gas emissions from waste decomposition and/or recycling. The greenhouse-gas changes due to choice of waste-removal method are an important topic to be studied in the future.

Chapter 3

Global burden of mortalities due to chronic exposure to ambient PM_{2.5} from open combustion of domestic waste²

Uncontrolled combustion of domestic waste has been observed in many countries, creating concerns for air quality; however, emissions from these waste fires are not included in many inventories, and the health implications have not yet been quantified. In this study, we incorporate the Wiedinmyer et al. (2014) emissions inventory into the standard emission setup of the global chemical-transport model, GEOS-Chem, and provide a first estimate of premature adult mortalities from chronic exposure to ambient PM_{2.5} from open, uncontrolled combustion of domestic waste. Using the concentration-response functions (CRFs) of Burnett et al. (2014), we estimate that waste combustion emissions result in 270,000 (5th-95th: 213,000-328,000) premature adult mortalities per year, with a high spatial density of mortalities in urban centers in developing countries. The confidence interval results from the uncertainty in the CRFs. We acknowledge that this result is likely sensitive to the choice of chemical-transport model, CRFs, and emission inventories. Our central estimate equates to approximately 9% of adult mortalities from exposure to ambient PM_{2.5} reported in the Global Burden of Disease Study 2010. Exposure to PM_{2.5} from waste combustion increases the risk of premature mortality by more than 0.5% for greater than 50% of the population. Complete removal of waste combustion would only avoid 191,000 (5th-95th: 151,000-224,000) mortalities per year (smaller than the total contributed premature mortalities due to nonlinear CRFs). In addition to the statistical uncertainty in the CRFs, we consider sensitivity simulations to waste-combustion emission mass as well as model resolution. A factor-of-2 uncertainty in waste-

²This Chapter published as: Kodros, J. K., Wiedinmyer, C., Ford, B., Cucinotta, R., Gan, R., Magzamen, S. and Pierce, J. R.: Global burden of mortalities due to chronic exposure to ambient PM_{2.5} from open combustion of domestic waste, *Environ. Res. Lett.*, 11(12), 124022, doi:10.1088/1748-9326/11/12/124022, 2016.

combustion PM leads to a sub-linear mortality response (ranging from 138,000 to 518,000 mortalities per year for factors-of-2 reductions and increases, respectively, using the central estimates of the CRFs). In general, mortality rates decrease with decreasing model resolution. Decreasing model resolution from $2^\circ \times 2.5^\circ$ to $4^\circ \times 5^\circ$ results in 16% fewer mortalities attributed to waste-combustion $PM_{2.5}$, and similarly, over Asia, decreasing resolution from $0.5^\circ \times 0.667^\circ$ to $2^\circ \times 2.5^\circ$ results in 21% fewer mortalities attributed to waste-combustion $PM_{2.5}$. Owing to coarse model resolution, our global estimates of premature mortality from waste-combustion $PM_{2.5}$ are likely a lower bound. Furthermore, combustion of domestic waste may emit additional toxic gas- and particle-phase species that are not explicitly considered in this analysis.

3.1 Introduction

Open, uncontrolled combustion of domestic waste (i.e. trash burning) occurs on a global scale, emitting particulate matter (PM) and toxic gaseous and particulate compounds (Christian et al., 2010; Wiedinmyer et al., 2014). Domestic waste can include food and agricultural products, containers and packaging, and other sources of residential trash. Combustion occurs both in homes and at community waste sites (i.e. dumps), and both in developing and developed countries, though waste combustion is more widespread in developing countries (Wiedinmyer et al., 2014). While combustion of waste is ubiquitous in rural areas, there are also significant emissions in urban areas, potentially leading to pollution exposure of dense populations (Wiedinmyer et al., 2014).

Until recently, inventories of pollutant emissions from combustion processes either did not include emissions from uncontrolled domestic-waste combustion (e.g., Bond et al., 2007; Janssens-Maenhout et al., 2011), or the domestic-waste-combustion emissions were assumed to be low relative to other sources in all locations (Bond et al., 2004). However, Wiedinmyer et al. (2014) recently created an emissions inventory focused specifically on the emissions from the uncontrolled open combustion of domestic-waste products. The total estimated $PM_{2.5}$ emissions were 10 Tg yr^{-1} , globally, an order of magnitude higher than a previous estimate in Bond et al. (2004), and similar to the emissions from biofuel combustion in Bond et al. (2004). The more-recent estimates

were higher due to newer assumptions in waste production, fraction burned, and emission factors. The largest driver of the difference in emissions was the estimated amount of annual waste burned: Bond et al. (2004) estimated a total of 33 Tg, while Wiedinmyer et al. (2014) predict 970 Tg. This discrepancy is in part due to the assumption in Bond et al. (2004) that no waste combustion occurs in rural developing countries. Thus, ambient air quality particularly in developing countries may be substantially impacted by domestic-waste combustion.

PM air pollution is a major contributor to the global burden of disease, and the most important environmental contributor to morbidity and mortality in the world (Lim et al., 2012). Thus, exposure to ambient pollution from uncontrolled domestic-waste combustion may have serious health implications, yet these health effects have not been quantified. A number of past studies have linked exposure to ambient PM with aerodynamic diameters less than $2.5 \mu\text{m}$ ($\text{PM}_{2.5}$) to increased risk of mortality for adults from ischaemic heart disease (IHD), cerebrovascular disease (CeVD, or stroke), chronic obstructive pulmonary disease (COPD), and lung cancer (LC) (Burnett et al., 2014; Krewski et al., 2009; Laden et al., 2006; Pope et al., 2002). Using a combination of satellite and ground observations, and chemical-transport models to estimate $\text{PM}_{2.5}$ exposure from all sources, the Global Burden of Disease (GBD) Study 2010 estimated 3.1 million premature mortalities, globally, in 2010 (Lim et al., 2012).

For global/regional scale studies, chemical-transport models have been used to estimate surface-level ambient $\text{PM}_{2.5}$ exposure for use in health-impact assessments (e.g., Anenberg et al., 2010; Butt et al., 2016; Lelieveld et al., 2013, 2015). Despite uncertainties in emissions and atmospheric processes, models have an advantage over ground-based measurements in that they provide exposure estimates in regions where few surface measurements are available. In addition, models can provide source-specific $\text{PM}_{2.5}$ estimates, thereby allowing for policy-relevant mortality estimates from specific emission sectors (e.g., Butt et al., 2016; Corbett et al., 2007). Recently, Lelieveld et al. (2015) used the ECHAM model to estimate source-specific mortalities, finding dominant sources in Asia are from residential solid-fuel combustion and biomass burning; however, this study does not include emissions from open waste combustion.

One potential drawback of using chemical-transport models on a global scale is that computational efficiency often limits model spatial resolution. Lower-resolution global models average $PM_{2.5}$ concentrations over larger areas, limiting the ability to predict very-polluted regions and sharp gradients outside these regions. As emissions are often co-located with population, this may lead to a dependence of mortality estimates on model resolution. Pungler and West (2013) estimated ambient $PM_{2.5}$ mortalities in the United States using different model resolutions, and find substantially (~30%) lower estimates when scaling $PM_{2.5}$ to spatial scales representative of global models (>250 km) relative to 12 km. One method to correct for sub-grid scale gradients involves using satellite aerosol optical depth (AOD) at resolutions higher than the model (e.g. ~10 km vs. ~200 km) to interpolate $PM_{2.5}$ exposure fields at the resolution of the satellite AOD. However, this method relies on the ratio of modeled AOD to surface $PM_{2.5}$ (van Donkelaar et al., 2015). Ford and Heald (2016) estimated 20% uncertainty in mortality due to methodology in estimating surface $PM_{2.5}$ concentrations from satellite AOD. Additionally, while this method was used in several studies to estimate all-source $PM_{2.5}$ mortality (Evans et al., 2013; Lim et al., 2012), satellite observations cannot be used to isolate individual sources of $PM_{2.5}$; one would need to assume that spatial distribution of AOD from each individual source follows the spatial distribution of the total AOD.

In this study, we provide the first estimates of mortality due to chronic exposure to $PM_{2.5}$ from domestic-waste combustion. We include the recent Wiedinmyer et al. (2014) waste-combustion inventory into the global/regional chemical-transport model, GEOS-Chem. In Section 2, we discuss the model setup and methodology for estimating mortality. In Section 3.1, we present model results for waste-combustion $PM_{2.5}$ and in Section 3.2 we present the global and country-level attributed mortality. In Section 3.3, we estimate the deaths averted due to complete removal of emissions. In Section 3.4, we test the sensitivity of mortality rates to uncertainties in emission mass and model resolution. We share our conclusions in Section 4. In a separate study, Kodros et al. (2016a), we estimate the aerosol radiative impacts from domestic-waste combustion.

3.2 Methods

3.2.1 Chemical-transport model overview

To estimate $PM_{2.5}$ concentrations, we use the Goddard Earth Observing System chemical-transport model (GEOS-Chem) version 10.01. GEOS-Chem is driven by GEOS-5 assimilated meteorology fields (<http://gmao.gsfc.nasa.gov>), and includes PM tracers for black carbon, organic aerosol, dust, sea salt, sulfate, nitrate, and ammonium in addition to 52 gas-phase species. Globally, we use the EDGAR emissions inventory with regional overwrites as described in the Supplemental Material (Appendix A). Waste-combustion emissions are not included in these base GEOS-Chem emissions inventories. We incorporate to GEOS-Chem the waste-combustion inventory of Wiedinmyer et al. (2014), which estimates the mass of waste burned in urban and rural areas for developing countries, and rural areas for developed countries. The inventory primarily uses emission factors compiled in Akagi et al. (2011). Estimated waste-combustion emissions include 0.6 Tg yr^{-1} of black carbon and 5.1 Tg yr^{-1} of primary organic carbon, as well as more-minor contributions from gas-phase species including sulphur dioxide, ammonia, and nitrous oxides, which contribute to additional $PM_{2.5}$ (<10% of the total addition) through chemical reactions. Evaluation of the modeled aerosol burden with and without waste-combustion emissions is included in the Supplemental Material (Appendix A).

We perform GEOS-Chem simulations for year 2010 with a pair of simulations: one with emissions from all sources (including waste burning; 'WASTE_ON'), and another, otherwise-identical simulation but without waste-combustion emissions ('WASTE_OFF'). Comparison of these pairs of simulations allows us to isolate the impacts of waste combustion on $PM_{2.5}$ concentrations and mortality. In order to test the sensitivity of mortality rates to uncertainties in waste-combustion emission mass, we assume waste-combustion $PM_{2.5}$ scales linearly with PM emission mass and simply double ('HIGHMASS') and half ('LOWMASS') modeled waste-combustion $PM_{2.5}$ concentrations. The factor-of-2 uncertainty in emission mass is similar to uncertainties in waste-combustion emission factors reported in Akagi et al. (2011). In order to test the sensitivity of mortality rates to model resolution we repeat the WASTE_ON and WASTE_OFF simulations at three resolutions: $2^\circ \times 2.5^\circ$

(~200 km) and $4^\circ \times 5^\circ$ (~400 km) resolution globally, and a $0.5^\circ \times 0.666^\circ$ (~50 km) resolution over Asia.

3.2.2 Calculation of premature mortality

Our methodology to estimate mortalities from waste-combustion $PM_{2.5}$ is based on the methods used in the GBD 2010 to estimate ambient $PM_{2.5}$ mortalities. We discuss a number of uncertainties and limitations of this method in Section 4. We use year 2010 gridded population (from the NASA Socioeconomic Data and Application Center (SEDAC, <http://sedac.ciesin.columbia.edu/>) and baseline mortality rates compiled for the GBD 2013 for ischemic heart disease (IHD), cerebrovascular disease (CeVD), cardiopulmonary disease (COPD), and lung cancer (LC) for adults (ages greater than 25) (Naghavi et al., 2015). Baseline mortalities are reported at the country level, and we aggregate them to the model resolution assuming no sub-national gradients. Data on baseline mortality variability at a sub-national scale were not available.

The fraction of all premature mortalities due only to $PM_{2.5}$ is based on concentration-response functions (CRFs) that relate exposure to ambient $PM_{2.5}$ to increased risk of premature mortality from specific diseases. We calculate the relative risk (RR) from all $PM_{2.5}$ sources (RR_{total}) using the integrated CRFs of Burnett et al. (2014). We choose the Burnett et al. (2014) study as it uses smoking and household air pollution to constrain the risk at high $PM_{2.5}$ concentrations (such as ambient $PM_{2.5}$ found in India and China). The Burnett et al. (2014) study makes several assumptions relevant to this study: the toxicity of $PM_{2.5}$ is not dependent on composition, increased mortality risk is a result of long-term exposure, CRFs apply globally, there exists a minimum $PM_{2.5}$ threshold (modeled as a uniform distribution ranging from 5.8 - $8.8 \mu g m^{-3}$) below which no further negative health impacts are assumed to occur, and the relationship between relative risk of mortality and $PM_{2.5}$ exposure is nonlinear. We note that CRFs are an active area of research, and our results are likely sensitive to our choice of CRF. Burnett et al. (2014) fits coefficients using a Monte Carlo approach, reporting 1,000 sets of coefficients for each cause (and each age group for CeVD and IHD). We use these sets of coefficients to determine median, 5th, and 95th percentiles of mortality.

The attributable fraction of premature mortalities by $PM_{2.5}$ is then calculated from the RR by: $(RR_{total}-1)/RR_{total}$.

We estimate total premature adult mortality from $PM_{2.5}$ as the product of population, cause and age specific baseline mortality rates, and attributable fraction from all $PM_{2.5}$ sources in each model gridcell. We estimate 2.7 million premature adult mortalities from ambient $PM_{2.5}$ in the $2^\circ \times 2.5^\circ$ -resolution simulation (Figure A.1). This number is lower than estimates of 3.1 million from Lelieveld et al. (2015) and Lim et al. (2012); however, it is within the reported uncertainty ranges (2.5 to 3.7 million for Lim et al., 2012 and 1.5 to 4.6 million for Lelieveld et al., 2015). The coarser resolution of our global model likely contributes to the lower estimate.

To attribute the *number of mortalities owing to waste-combustion emissions*, we scale total mortalities from all $PM_{2.5}$ by the fraction of $PM_{2.5}$ from waste combustion (attribution method). This is represented by Equation 3.1:

$$M_{waste} = \frac{PM_{2.5,WASTE_ON} - PM_{2.5,WASTE_OFF}}{PM_{2.5,WASTE_ON}} \times M_{all(WASTE_ON)} \quad (3.1)$$

where M_{waste} is the premature mortalities due to waste combustion, $M_{all(WASTE_ON)}$ is the premature mortalities due to all sources in the WASTE_ON simulation, and $PM_{2.5,WASTE_ON}$ and $PM_{2.5,WASTE_OFF}$ are the modeled $PM_{2.5}$ concentrations in the WASTE_ON and WASTE_OFF simulations, respectively. Additionally, we estimate the *number of mortalities averted due to removal of waste-combustion emissions* by subtracting the total mortalities in the WASTE_OFF simulation from the total mortalities in the WASTE_ON simulation (subtraction method). This is represented by Equation 3.2:

$$M_{waste} = M_{all(WASTE_ON)} - M_{all(WASTE_OFF)} \quad (3.2)$$

where $M_{all(WASTE_OFF)}$ is the premature mortalities from all sources in the WASTE_OFF simulation. The subtraction method yields different results than the attribution method as the concentration-response function has strong nonlinearities (discussed below).

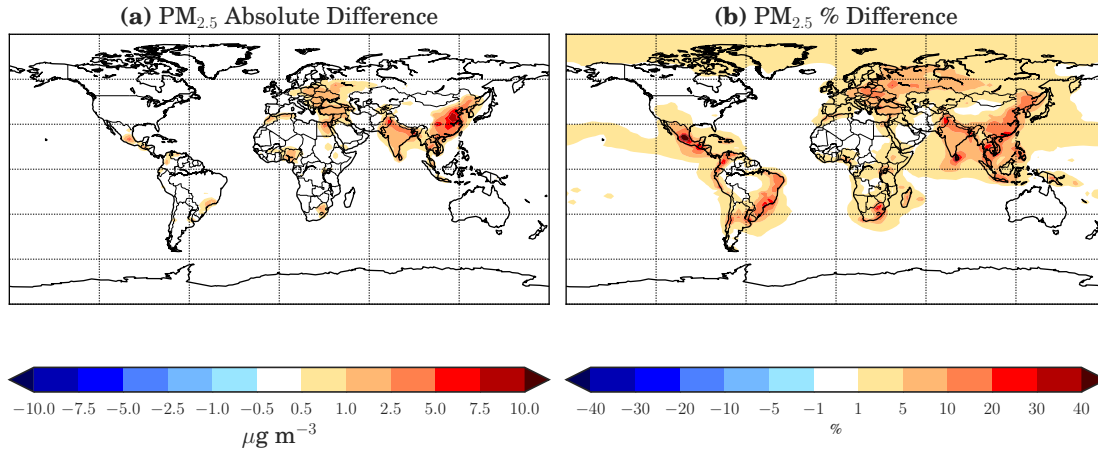


Figure 3.1: The (a) absolute difference and (b) percent difference in modeled boundary layer PM_{2.5} from including emissions from combustion of domestic waste in our simulations at 2°x2.5° resolution.

3.3 Results

3.3.1 Model increases in PM_{2.5} due to waste-combustion emissions

Figure 3.1 shows the absolute increase (panel a) and percent increase (panel b) in PM_{2.5} from waste-combustion emissions at 2°x2.5° model resolution. Waste-combustion emissions lead to over 10% increases in ambient PM_{2.5} concentrations in South and South-East Asia, Eastern Europe, Central America and Coastal South America. Notably, PM_{2.5} increases by more than 40% in Sri Lanka and central Mexico (e.g. Mexico City). The absolute increases in PM_{2.5} are greatest in eastern China and northern India, but there are anomalously large fractional increases in grid cells corresponding to large urban areas such as Johannesburg, Cairo, Moscow, and Mexico City.

3.3.2 Global and country-level mortality rates due to waste-combustion PM_{2.5}

The mortality rates per area associated with waste-combustion PM_{2.5} calculated through the attribution method are shown in Figure 3.2a, and global annual mortalities listed by cause of death are in Table 3.1. We attribute waste-combustion PM_{2.5} to 270,000 (5th-95th:213,000-328,000) adult mortalities per year (calculated as the sum of IHD, CeVD, COPD, and LC). The majority of these mortalities are caused by IHD (120,000, 5th-95th:106,000-136,000) and CeVD (108,000, 5th-95th:86,000-130,000). Spatially, the highest concentration of deaths occurs in eastern China

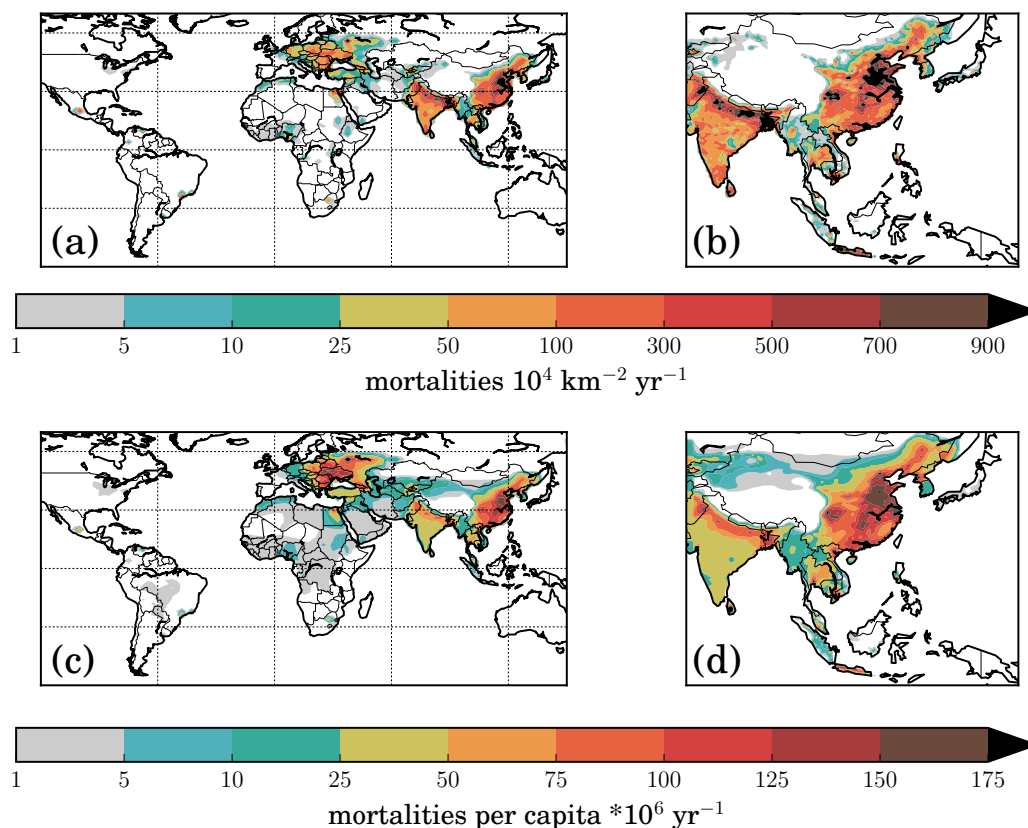


Figure 3.2: Annual mortalities from chronic exposure to ambient PM_{2.5} from waste combustion per 10⁴ km² in the (a) 2°x2.5° global domain and (b) in the 0.5°x0.666° Asian domain as well as per 10⁶ people in the (c) 2°x2.5° global domain and (d) in the 0.5°x0.666° Asian domain.

and northern India where mortality exceeds 900 deaths per 10⁴ km² (a 100x100 km box) per year. There is also a substantial number of mortalities in Eastern Europe. Significant increases in PM_{2.5} co-located with dense populations lead to greater than 300 deaths per 10⁴ km² in densely populated cities. Figure 3.2c shows the waste combustion mortality rate per 10⁶ people (in each grid cell). A combination of large relative PM_{2.5} increases and high baseline mortality rates in Eastern Europe and Russia lead to a similar mortality rate as in Asia. Figure 3.2c also shows more widespread health impacts in Africa and the Middle East, where lower population densities limit the total number of annual mortalities.

At the country level, the estimated premature mortality rates due to waste-burning PM_{2.5} (normalized either by population or area) varies by several orders of magnitude between regions and economic level. This mortality range is due to (1) differing amounts of waste generation (and hence

Table 3.1: Annual mortalities (thousands) by cause and model resolution for the global and Asian domains due to exposure to PM_{2.5} from combustion of domestic waste. The first number is the median estimate, and the 5th and 95th percentile confidence intervals are in parentheses. Abbreviations: IHD, ischaemic heart disease; CeVD, cerebrovascular disease; COPD, cardiopulmonary disease; LC, lung cancer.

	Resolution	IHD	CeVD	COPD	LC	Sum
Global Domain	4°x5°	103 (91-116)	89 (71-107)	23 (12-34)	12 (6-34)	227 (180-275)
	2°x2.5°	120 (106-136)	108 (86-130)	27 (14-40)	15 (7-21)	270 (213-328)
	2°x2.5°- HIGHMASS	229 (203-258)	208 (165-249)	52 (28-77)	30 (14-41)	518 (180-275)
	2°x2.5°- LOWMASS	62 (55-70)	55 (44-66)	13 (7-20)	7 (3-11)	138 (109-167)
	2°x2.5°- SUBTRACT	70 (63-80)	84 (67-98)	23 (14-30)	13 (8-17)	191 (151-224)
	4°x5°	76 (68-84)	76 (61-91)	21 (11-31)	11 (6-15)	184 (146-222)
	2°x2.5°	90 (81-101)	93 (74-110)	24 (13-36)	13 (6-19)	221 (174-266)
	0.5°x0.667°	113 (102-126)	120 (96-143)	29 (15-44)	16 (8-23)	279 (221-336)

emissions) and pollution transport leading to differing PM_{2.5} concentrations, (2) large variations in total number and density of the exposed population, and (3) differences in baseline mortality rates. In addition, non-waste-combustion PM_{2.5} plays an important role. In both WASTE_ON and WASTE_OFF, some countries are uniformly below the minimum concentration threshold set as the counterfactual in Burnett et al. (2014) for PM_{2.5} health effects (though, we note that the actual minimum concentration threshold has not been clearly identified in the literature). By aggregating mortalities to the country level, we find the countries with the largest total mortalities due to waste combustion are China, India, Pakistan, and Russia. These four countries amount to 78% of the global mortality. The countries with the highest mortalities per capita are Montenegro, Bulgaria, Moldova, and Ukraine. Normalizing by mass of waste generated, we find that the countries with the highest mortalities per mass of waste generated are Nepal, Montenegro, Uruguay, and Bulgaria. Supplemental Figure A.4 shows box-and-whisker plots of country-level generated waste per capita per year (a) (from Wiedinmyer et al. (2014)), mortality rates per capita (b), and mortality per mass

of waste generated (c) split between 4 economic strata: high income, upper-middle income, lower-middle income, and low income. While on average high-income countries generate two times more waste, only 10 people die for every Tg of waste generated compared to 82 deaths for every Tg of waste generated in low- to upper-middle-income countries. This difference is driven by a higher fraction of waste generated being burned in low- to upper-middle income countries compared to high-income countries.

3.3.3 Deaths averted due to removal of waste-combustion emissions

We estimate 191,000 (5th-95th:51,000-224,000) premature mortalities per year may be saved by eliminating waste combustion (subtraction method; see explanation in Section 2.2) (Table 3.1 and Figure A.6). Thus, removing waste combustion would reduce premature mortality rates by a smaller number than the mortality rate attributed to waste combustion. This is due to the nonlinear CRFs where the mortality response to PM_{2.5} saturates with increasing PM_{2.5} concentrations. This saturation effect is strongest in the heavily polluted regions of India and China (which lie on the sub-linear portion of the CRF). This saturation effect is partly balanced out by a larger number of mortalities avoided in cleaner regions where waste-combustion emissions elevates PM_{2.5} concentrations from below to above minimum-PM_{2.5}-threshold values.

3.3.4 Sensitivity of mortality rates to emission mass and model resolution

Wiedinmyer et al. (2014) acknowledge large uncertainties in PM_{2.5} emission mass. To test the sensitivity of mortality rates to uncertainties in emission mass, we introduce a factor-of-2 uncertainty in waste-combustion PM_{2.5} mass. Halving waste-combustion PM_{2.5} (LOWMASS) results in 138,000 (5th-95th:109,000-167,000) mortalities per year and doubling PM_{2.5} (HIGHMASS) results in 518,000 (5th-95th:410,000-626,000) through the attribution method (Table 3.1 and Figure A.5). The relationship between waste-combustion PM_{2.5} and mortality is sub-linear (additional PM_{2.5} impacts health less when PM_{2.5} concentrations are already high) because many of the waste-combustion source regions occur in already heavily polluted areas; thus, the waste-combustion emissions in these regions lead to fewer mortalities than if PM_{2.5} concentrations were lower.

In order to explore the dependence on estimated attributed mortality rates to model resolution, we use a coarser $4^\circ \times 5^\circ$ and finer $2^\circ \times 2.5^\circ$ global simulation and a $0.5^\circ \times 0.666^\circ$ simulation over Asia. The total number of annual mortalities in the global $4^\circ \times 5^\circ$ resolution simulation is 16% lower than the $2^\circ \times 2.5^\circ$ resolution simulation (Table 3.1 and Figure A.7). The decrease in mortality rates with coarser resolution is caused by two main factors. First, as grid-box area increases, ambient $PM_{2.5}$ is averaged over a larger area and may reduce concentrations below the minimum threshold for mortality (between 5.8 - $8.8 \mu g m^{-3}$) in some locations. Second, higher-resolution simulations are better able to co-locate dense urban populations with $PM_{2.5}$ increases from waste combustion. Figure 3.2b shows the annual mortality per $10^4 km^2$ and Figure 3.2d shows annual mortality per 10^6 people over Asia at $0.5^\circ \times 0.666^\circ$ resolution. In this domain, total mortalities increase from 184,000 (5th-95th:146,000-222,000) in the $4^\circ \times 5^\circ$, to 221,000 (5th-95th:174,000-266,000) in the $2^\circ \times 2.5^\circ$, to 279,000 (5th-95th:221,000-336,000) in the $0.5^\circ \times 0.666^\circ$ resolution simulation. The higher-resolution simulation predicts more mortalities just in the Asia domain than the $2^\circ \times 2.5^\circ$ simulation predicts globally, which highlights the importance of model resolution when using simulated $PM_{2.5}$ concentrations to estimate mortality rates.

Figure 3.3 shows the fractions of the population impacted by waste-combustion $PM_{2.5}$ and mortality risk. Figure 3.3a shows the complementary cumulative distribution functions (CCDF) of the percent of the global population exposed to different levels of $PM_{2.5}$ from domestic-waste combustion. In the global $2^\circ \times 2.5^\circ$ domain, 50% of the total population is exposed to a greater than $1.3 \mu g m^{-3}$ increase in $PM_{2.5}$ from waste combustion, while 10% is exposed to a greater than $5.3 \mu g m^{-3}$ increase. Increases in exposure due to waste-combustion $PM_{2.5}$ are generally smaller in the coarser $4^\circ \times 5^\circ$ domain due to dilution of emissions into larger grid cells. Figure 3.3b shows the corresponding CCDFs for the relative increase in $PM_{2.5}$ -mortality risk in the WASTE_ON compared to the WASTE_OFF simulation (The all-cause relative risk is the mean value of the relative risk of the four causes weighted by the proportion of each cause to the total baseline mortality). For the two global resolutions, more than 50% of the population has greater than a 0.5% increased risk of mortality by any cause due to waste-combustion emissions, while 10% of the population

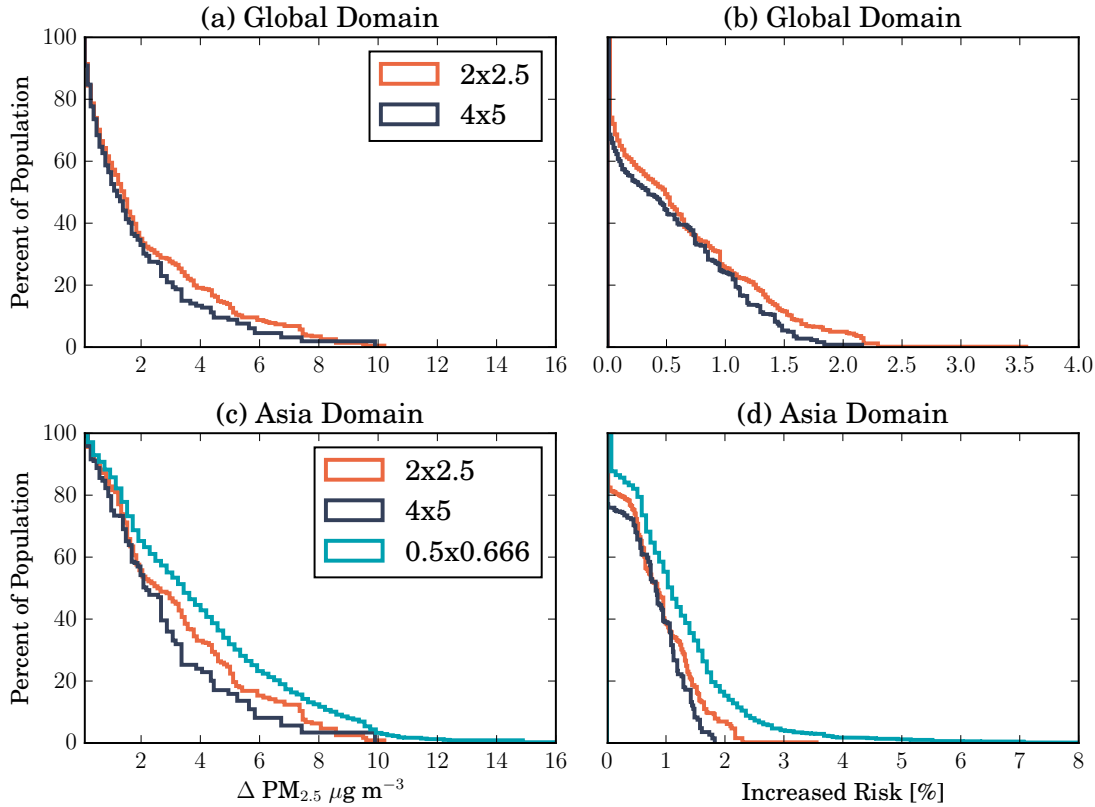


Figure 3.3: Complementary cumulative distribution functions weighted by percent of the population for (a) the change in $\text{PM}_{2.5}$ due to combustion of domestic waste for the global domain, (b) the increased risk for mortality due to combustion of domestic waste for the global domain, (c) the change in $\text{PM}_{2.5}$ for the Asia domain, and (d) the increased risk of mortality for the Asia domain.

has a greater than 1.5% increased risk of mortality. While in Figure 3.3a 91% of the population is exposed to at least a $0.1 \mu\text{g m}^{-3}$ increase in $\text{PM}_{2.5}$, only 75% of the population has a greater than 0.02% increased risk of mortality in Figure 3.3b (due to minimum $\text{PM}_{2.5}$ thresholds in the concentration-response function). Figures 3.3c and d show increased $\text{PM}_{2.5}$ and increased risk of mortality in the Asian domain for the three model resolutions. The majority of global mortalities occur in Asia (Table 3.1), where a larger fraction of the population is exposed to waste-combustion $\text{PM}_{2.5}$ and thus increased risk of mortality. All three resolutions show that nearly 99% of the population in Asia is exposed to at least a $0.1 \mu\text{g m}^{-3}$ increase in $\text{PM}_{2.5}$ and nearly 83% of the population have an greater than 0.02% increased risk of mortality from waste combustion. The $0.5 \times 0.666^\circ$ resolution simulation predicts that a higher fraction of the population is exposed to

larger increases in PM_{2.5} and mortality risk than the coarser resolutions due to the reasons discussed above.

3.4 Discussion and conclusions

As stated in the results, we estimate 270,000 (5th-95th:213,000-328,000) annual adult mortalities from waste combustion. Our estimate of mortality attributed to waste combustion is similar to recent estimates of mortalities due to PM_{2.5} from solid-fuel cookstoves (300,000-400,000 mortalities per year), another emission source associated with the developing world (Butt et al., 2016; Chafe et al., 2014). Waste-combustion emissions are approximately 10% of our total ambient PM_{2.5} mortalities and 9% of the total ambient PM_{2.5} mortalities estimated in the GBD2010. We note that our estimate of global mortalities from waste-combustion emissions are of a similar magnitude to the Lelieveld et al. (2015) estimate of mortalities from PM_{2.5} from biomass burning (~165,000), land traffic (~165,000), and industrial emissions (~231,000); however, we note that our total mortality estimate is 10% lower than Lelieveld et al. (2015).

Waste combustion has high mortality rates due to proximity of emissions to population. In developing countries, substantial amounts of waste combustion can occur in urban areas. We find high mortality densities (>300 deaths per 10⁴ km² yr⁻¹) in cities such as Mexico City, Moscow, Johannesburg, and Rio de Janeiro. Four countries (China, India, Pakistan, and Russia) account for slightly more than 2/3 of the global mortality burden due to waste combustion. Globally, more than half of the world's population is exposed to an additional 1.3 μg m⁻³ of PM_{2.5} due to waste combustion leading to a 0.5% increased risk of mortality each year just from waste-combustion emissions.

Due to a factor-of-2 uncertainty in PM_{2.5} emission mass, we estimate a range of mortalities per year of 138,000 to 518,000. We note that even on the low end of this range, waste combustion contributes to a substantial number (greater than 100,000) of mortalities per year. Additionally, we estimate that a complete removal of waste-combustion would avoid 191,000 mortalities per year (see explanation in Section 2.2). In these sensitivity simulations, the calculated decrease of

premature mortality is less than the proportional decrease in $PM_{2.5}$. The sub-linear nature of these sensitivity tests demonstrates that most of the mortalities from waste combustion occur in heavily polluted areas.

Our estimates of premature mortality from waste-combustion $PM_{2.5}$ are likely a lower bound due to the coarse resolution of the global model. Combustion of domestic waste often occurs near where people live and work, sometimes in streets or in front of homes, and none of our model simulations resolve this near-field pollution exposure. The $2^\circ \times 2.5^\circ$ resolution is unable to capture high $PM_{2.5}$ gradients, which are often co-located with dense populations. We include an additional simulation at $4^\circ \times 5^\circ$ and calculate 227,000 mortalities (16% lower than the estimate at $2^\circ \times 2.5^\circ$). This suggests increasing mortalities at progressively finer model resolutions. Due to the high mortality rates in Asia, we include a higher resolution $0.5^\circ \times 0.666^\circ$ simulation in this domain. We estimate 279,000 mortalities in Asia at this model resolution. The sensitivity of health-response estimates to model resolution has been explored in past studies (e.g., Pungler and West, 2013; Thompson and Selin, 2012).

The methods and data sources used here are similar to the GBD 2010 and several recent health-impact studies (e.g., Apte et al., 2015; Lelieveld et al., 2015; Lim et al., 2012); however, there are substantial uncertainties and limitations inherent in these methods. First, the Burnett et al. (2014) concentration-response function is largely based on epidemiologic studies that occur in the United States, and while there are age modification factors for CeVD and IHD, there are no modifications for other sociodemographic factors. We assume here that this function applies globally; however, as demographics and pollution sources vary regionally, this may not be a valid assumption. Second, we consider all species of $PM_{2.5}$ to be equally toxic; however, some studies have suggested that combustion particles may be more toxic (Krzyżanowski et al., 2005). Third, due to lack of data, baseline mortality rates used here are reported at the national or regional level; however, demographics often vary sub-nationally, and national and regional level mortality rates may introduce uncertainty. Chowdhury and Dey (2016) estimate 15% fewer premature mortalities from ambient $PM_{2.5}$ exposure in India when assuming a uniform country-level baseline mortality

rate as opposed to varying baseline mortality at the state level using gross domestic product as a proxy. The uncertainties listed here are in addition to uncertainties in emissions (Akagi et al., 2011; Wiedinmyer et al., 2014) and model processes.

In this study, we focus on mortality from chronic exposure to ambient $PM_{2.5}$, but we note that waste combustion also emits a number of gas- and particulate-phase toxins that may have additional significant health implications. While generally accepted that these toxins have negative health impacts, the concentration-response functions are less well-developed making it difficult to estimate a global health impact. Thus, because $PM_{2.5}$ response functions exist, it is common to use $PM_{2.5}$ estimates as a proxy for exposure to a broad array of toxic species. Therefore, the net health impacts from waste combustion could be greater than estimates for only $PM_{2.5}$.

Uncontrolled domestic-waste-combustion emissions are a potentially significant emission source that has been largely overlooked in past studies. Waste combustion creates health-effect disparities between high-income countries and lower-income countries, where high-income countries generate more waste but combust less, resulting in a factor of 8 fewer deaths per mass waste of generated than lower-income countries (Figure A.4). Due to the coarse model resolution and exclusion of gaseous toxic species, our estimate of mortalities from waste-combustion emissions is likely a lower bound. Despite this, we find a substantial burden of disease (9% of mortalities from all $PM_{2.5}$) that are on the same order of magnitude as modeling estimates of industry, land traffic, and biomass burning. Waste combustion also affects aerosol number concentrations and radiative impacts, and we explore this in a separate study (Kodros et al., 2016a).

Chapter 4

Quantifying the contribution to uncertainty in mortality attributed to household, ambient, and joint exposure to PM_{2.5} from residential solid-fuel use³

While there have been substantial efforts to quantify the health burden of exposure to PM_{2.5} from solid-fuel use (SFU), the sensitivity of mortality estimates to uncertainties in input parameters has not been quantified. Moreover, previous studies separate mortality from household and ambient air pollution. In this study, we develop a new estimate of mortality attributable to SFU due to the joint exposure from household and ambient PM_{2.5} pollution and perform a variance-based sensitivity analysis on mortality attributable to SFU. In the joint-exposure calculation, we estimate 2.81 (95% CI: 2.48-3.28) million premature deaths in 2015 attributed to PM_{2.5} from SFU, which is 580,000 (18%) fewer deaths than would be calculated by summing separate household and ambient mortality calculations. Regarding the sources of uncertainties in these estimates, in China, India, and Latin America, we find that 53-56% of the uncertainty in mortality attributable to SFU is due to uncertainty in the percent of the population using solid fuels and 42-50% from the concentration-response function. In sub-Saharan Africa, baseline mortality rate (72%) and the concentration-response function (33%) dominate the uncertainty space. Conversely, the sum of the variance contributed by ambient and household PM_{2.5} exposure ranges between 15-38% across all regions (the percentages do not sum to 100% as some uncertainty is shared between parameters). Our findings suggest that future studies should focus on more precise quantification of solid-fuel use and the concentration-response relationship to PM_{2.5}, as well as mortality rates in Africa.

³This Chapter published as: Kodros, J. K., Carter, E., Brauer, M., Volckens, J., Bilsback, K. R., L'Orange, C., Johnson, M. and Pierce, J. R.: Quantifying the Contribution to Uncertainty in Mortality Attributed to Household, Ambient, and Joint Exposure to PM_{2.5} From Residential Solid Fuel Use, *GeoHealth*, doi:10.1002/2017GH000115, 2018.

4.1 Introduction

Close to 40% of the world's population relies on combustion of solid fuels for residential cooking and heating (Bonjour et al., 2013). Incomplete combustion of these fuels emits substantial amounts of particulate matter (PM) that are harmful to human health (Brook et al., 2010; Naeher et al., 2007). While solid-fuel use (SFU) as a source of household energy is concentrated in developing regions of the world, high-income countries also burn biomass as a heating fuel (Rogalsky et al., 2014). Research over the past several decades consistently suggests the health burden from exposure to air pollutants from SFU is likely to be substantial (e.g., Forouzanfar et al., 2016; Smith et al., 2014; World Health Organization, 2014).

Exposure to PM with aerodynamic diameters less than $2.5 \mu\text{m}$ ($\text{PM}_{2.5}$) has been linked to an increased risk of mortality from cardiovascular and respiratory diseases. The Global Burden of Disease 2015 report (GBD2015) estimates that 2.85 (95% CI: 2.18-3.59) million deaths in the year 2015 were due to exposure to household air pollution from SFU (Forouzanfar et al., 2016). The GBD2015 ranks exposure to household air pollution from SFU among the leading risk factors contributing to premature mortality, globally (Forouzanfar et al., 2016). Using similar methods as GBD2015 but with different input data, the World Health Organization (WHO) estimates 4.3 million deaths from household air pollution from SFU in the year 2012 (World Health Organization, 2014). In addition, SFU has the potential to degrade ambient (i.e. outdoor) air quality. Estimates of mortality due to exposure to ambient $\text{PM}_{2.5}$ from SFU typically range from 0.3 to 0.5 million (Butt et al., 2016; Chafe et al., 2014; Lacey et al., 2017). However, to our knowledge, no work has yet tried to estimate premature mortality associated with SFU by an approach that jointly considers ambient and household exposures. Rather, estimates rely on separate calculations for household (indoor) air pollution and ambient air pollution (e.g., Anenberg et al., 2017; Forouzanfar et al., 2016; Smith et al., 2014).

Estimates of mortality from exposure to $\text{PM}_{2.5}$ from SFU (including exposure to household and/or ambient air pollution from this source) rely on input data sources including: country-level baseline mortality rates, $\text{PM}_{2.5}$ exposure levels, the magnitude and shape of concentration-response

functions, and the number of people exposed to a specific concentration. Each of these data sources contains an uncertainty range reflecting the degree of confidence of the estimate in a given region. As a result of the various sources of uncertainties in the input parameters, there is a large variance in estimates of mortality attributable to exposure to PM_{2.5} from SFU. To reduce the variance in estimated mortality, effort has focused on reducing uncertainty in the input parameters that contribute the most to the uncertainty in mortality. However, no studies, to our knowledge, have investigated the sensitivity of mortality estimates to these input parameters.

In this work, we perform a variance-based sensitivity analysis to quantify the contribution of uncertainty in mortality attributable to SFU to each of the following input parameters: baseline mortality rates, household and ambient PM_{2.5} exposure concentrations, concentration-response functions, and population exposed to household and ambient PM_{2.5} from SFU. A variance-based sensitivity analysis provides a framework to apportion uncertainty in model output (in this case mortality) to sources of uncertainty from model input (Saltelli et al., 2007). This approach involves calculating mortality tens of thousands of times based on random draws from the input parameter distributions. The end result of this analysis is a percent contribution of each input term to the overall variance (the quantified uncertainty) in the mortality estimate. This allows for selection of parameters that can be prioritized to reduce uncertainty in mortality estimates. This approach has been used for other environmental applications, recently for particulate matter in the context of cloud condensation nuclei and radiative forcing (Carslaw et al., 2013; Y. H. Lee et al., 2013) and simulated acetone budget (Brewer et al., 2017). A limitation of this approach is that we do not test the sensitivity to the major assumptions and uncertainties from GBD2015 that are not quantifiable (e.g., equal toxicity of PM_{2.5} regardless of source or composition, lack of direct evidence of mortality caused by cardiovascular disease from household air pollution, application of a single exposure-response function across diverse populations).

The objectives of this study are to evaluate the sensitivity of mortality estimates attributable to SFU to the five aforementioned data input sources with quantified uncertainty bounds. In addition, we present a new calculation to quantify the joint effect of exposure to household and ambient PM_{2.5}

pollution. In Section 2.1, we describe the input parameters used in mortality estimates. In Section 2.2, we describe the calculation of mortality from household, ambient, and the joint exposure to $PM_{2.5}$. In Section 2.3, we describe the variance-based sensitivity analysis. In Section 3.1, we compare the mortality attributed to $PM_{2.5}$ exposure from SFU in the joint exposure calculation to the mortality attributed to $PM_{2.5}$ exposure from SFU through separate calculations for household and ambient exposures. We present the results of the sensitivity analysis in Section 3.2 and share our conclusions in Section 4.

4.2 Methods

4.2.1 Uncertain parameters and data sources

We briefly describe the nomenclature, uncertain input parameters, and relevant citations here. In Sections 2.2 and 2.3, we present how these data are used in estimating mortality from SFU and the resulting sensitivity analysis.

Nomenclature:

- *H-SFU* refers to household $PM_{2.5}$ pollution from solid-fuel use. The H-SFU mortality calculation uses similar assumptions and methods as the GBD “household air pollution” calculation.
- *A-SFU* refers to ambient $PM_{2.5}$ pollution from solid-fuel use. The A-SFU mortality calculation uses similar assumptions and methods as the GBD “ambient air pollution” calculation.
- *J-SFU* refers to the joint effect of ambient and household $PM_{2.5}$ pollution from solid-fuel use. The J-SFU mortality calculation is a new estimate of mortality described in this study.

Uncertain Factors

- *Baseline mortality rates (BMR)*: Reported country-level and age-specific mortality rates for ischemic heart disease (IHD), stroke, lower respiratory infections (LRI), chronic obstructive pulmonary disease (COPD), and lung cancer (LC). Baseline mortality rates were compiled

for GBD2015 and include published 95% confidence intervals (<http://ghdx.healthdata.org/gbd-results-tool>).

- *Concentration-response functions (CRF)*: Functions relating $PM_{2.5}$ exposure to a relative risk of mortality from IHD, stroke, LRI, COPD, and LC. Age-specific adjustments are included for IHD and stroke. The concentration-response functions are based on the integrated exposure-response function of Burnett et al. (2014) with updates as described in Cohen et al. (2017). The integrated exposure-response function published in Cohen et al. (2017) includes 1,000 sets of coefficients fit to the health data.
- PM_{Amb} : Ambient $PM_{2.5}$ exposure concentration from all sources (available from: <https://www.stateofglobalair.org/>) presented as an annual, population-weighted mean at the country level. Mean $PM_{2.5}$ and 95% confidence levels (also country level) about the mean are included in Cohen et al. (2017) and based on methods described in Shaddick et al. (2017). Following the assumptions in Cohen et al. (2017), the ambient $PM_{2.5}$ concentrations are assumed to represent exposure.
- $\%PM_{A-SFU}$: Percent of the PM_{Amb} originating from SFU emissions. Mean, country-level $PM_{2.5}$ concentrations with and without residential emissions are simulated with the GEOS-Chem chemical-transport model for this work (described in Appendix B). 95% confidence intervals are estimated as a factor of 2 about the mean, following uncertainty estimates in the emission inventory described in Bond et al. (2007).
- $\%SFU$: The percent of a country's population using solid fuels (coal, wood, charcoal, dung, and agricultural residues). Estimates of household SFU (and 95% confidence levels) are based on Bonjour et al. (2013) and updated in Forouzanfar et al. (2016). Upcoming iterations of the GBD assume low (<5%) solid-fuel use in high-income countries.
- PM_{H-SFU} : 24-hour average household exposure to $PM_{2.5}$ originating from SFU. The household $PM_{2.5}$ exposure concentrations are taken from GBD2015. These exposure concentrations

are based on the ratio of indoor PM_{2.5} concentrations and personal exposures measured in India from Balakrishnan et al. (2013) with added exposure studies across several countries and a mixed effect model to estimate region specific concentrations as described in World Bank (2016) and Forouzanfar et al. (2016). Exposure concentrations are reported at the regional level. Uncertainty intervals are taken from 95% confidence levels of indoor kitchen concentrations from Balakrishnan et al. (2013), resulting in a factor of 1.4 in both directions about the central estimate. In this study, we average exposure concentrations across reported values for men, women, and children. Household exposure to PM_{2.5} from solid-fuel use is assumed to be zero in high-income countries. Quantifying the variability in this parameter is an open area of research and the sensitivity analysis results are likely sensitive to the assumed confidence bounds.

The input parameters listed here, with the exception of the concentration-response functions, are published reporting mean or median values with 95% confidence intervals. We assume the underlying uncertainty is lognormally distributed and discuss calculating the parameters that describe the lognormal distribution in the Supplemental Information (SI; Appendix B). Also in the SI, we present results assuming a uniform distribution, and we find that this assumption does not greatly impact our conclusions. For the concentration-response functions, we interpolate between the 1,000 sets of coefficients to include a smooth distribution of relative risk at each PM_{2.5} concentration. In addition, there are separate uncertainty distributions for each of the five disease outcomes for baseline mortality rate and the concentration-response functions. We treat each disease outcome as a separate uncertain parameter.

Counting five unique baseline mortality rate parameters, five unique concentration-response function parameters, three measures of PM_{2.5} exposure, and the parameter estimating the percent of a country's population using solid fuels, we consider 14 uncertain parameters. In addition, there are a number of major uncertainties and assumptions that are made in PM_{2.5}-mortality calculations that cannot be quantified. We follow the major assumptions inherent in the GBD concentration-response

functions, including a globally applicable function and equal toxicity regardless of PM source. The implications of these assumptions are discussed below.

4.2.2 Calculation of premature mortality from solid-fuel use

We estimate mortality from SFU under three different PM_{2.5} exposure scenarios. To help explain the implications of the different assumptions, we include a schematic illustrating the differing approaches to calculating PM_{2.5} exposure and associated health response (Figure 4.1). Figure 4.1 contains a representative concentration-response function (IHD age group 65-70) with PM_{2.5} exposure concentration on the x-axis and relative risk of disease on the y-axis. For this schematic, we use relative risk as a proxy for health burden. The green bars represent PM_{2.5} or relative risk associated with SFU, while the orange bars represent all other PM_{2.5} sources.

Mortality calculation for exposure to household PM_{2.5} pollution from SFU: We calculate deaths attributable to exposure to household PM_{2.5} pollution from SFU (H-SFU) for the year 2015 following the methods and assumptions in GBD2015 for the “household air pollution” calculation (Forouzanfar et al., 2016; Smith et al., 2014). For a given country, health outcome, and age group, the number of premature deaths from H-SFU can be described as:

$$M_{H-SFU} = P \times BMR \times \%SFU \times \frac{RR(\text{PM}_{H-SFU}) - 1}{RR(\text{PM}_{H-SFU})}$$

where M_{H-SFU} is the premature mortality from household solid-fuel use, P is the country-level population, RR is the relative risk, and the other parameters are as described in Section 2.1. The relative risk quantifies the increased risk of mortality due to exposure to the given PM_{2.5} concentration. The relationship between relative risk and exposure is given by the concentration-response function (or the CRF parameter defined in the previous section). The H-SFU calculation assumes the total PM_{2.5} exposure for the SFU population originates from H-SFU (with negligible impacts from other PM_{2.5} sources). This assumption is qualitatively described in Figure 4.1a. In this example, the PM_{2.5} exposure is 250 $\mu\text{g m}^{-3}$ (approximately the median value for India) resulting in a relative risk of 1.5. Since the H-SFU calculation assumes all of the PM_{2.5} exposure is from

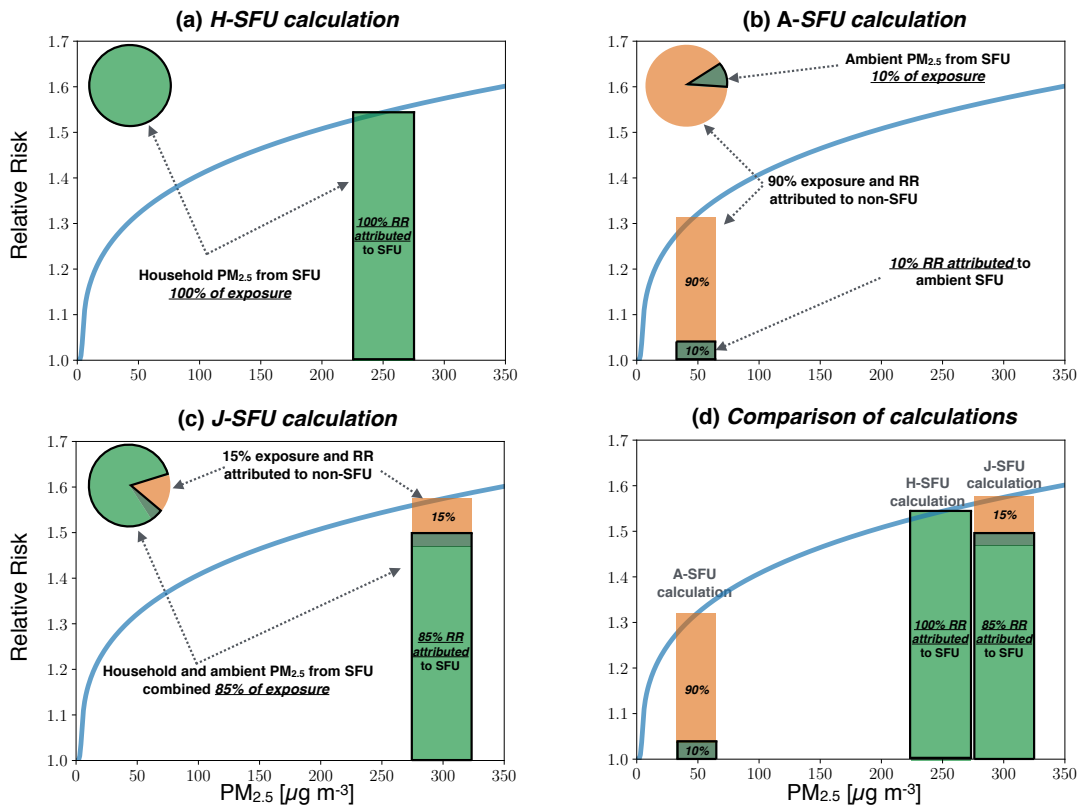


Figure 4.1: Schematic showing the calculation of relative risk (RR) from SFU and ambient sources in (a) the H-SFU calculation, (b) A-SFU calculation, and (c) the J-SFU calculation for a given disease (IHD) and population group (65-70 year olds). To apportion mortality attributed to exposure to PM_{2.5} from a specific source (in this case SFU), we assume the total health risk from exposure to PM_{2.5} from all sources scales proportionally with the percent of exposure from only SFU (following the discussions in GBD MAPS Working Group, 2016). The benefit of this method is that the apportionment of health risk does not depend on the order of the source contribution to exposure. In the H-SFU calculation (a), the GBD Comparative Risk Assessment assumes 100% of the PM_{2.5} exposure concentration (in this example 250 $\mu\text{g m}^{-3}$) is from SFU, and thus 100% of the health risk is apportioned to SFU. In the A-SFU calculation (b), the total PM_{2.5} exposure concentration is composed of emissions from SFU and non-SFU sources. In this example, the total PM_{2.5} exposure concentration is 50 $\mu\text{g m}^{-3}$, of which 10% (or 5 $\mu\text{g m}^{-3}$) is from SFU. Using the proportionality assumption, we thus assume 10% of the health risk is apportioned to SFU and the remaining 90% from non-SFU sources. For the J-SFU calculation (c), we assume that the total PM_{2.5} exposure concentration (300 $\mu\text{g m}^{-3}$) is the sum of PM_{2.5} concentrations associated with household SFU (250 $\mu\text{g m}^{-3}$), ambient SFU (5 $\mu\text{g m}^{-3}$), and all other ambient sources (45 $\mu\text{g m}^{-3}$). As SFU sources account for 85% of the total PM_{2.5} exposure in this example (255 $\mu\text{g m}^{-3}$ divided by 300 $\mu\text{g m}^{-3}$), we apportion 85% of the health risk to SFU. Panel (d) compares the attributed relative risk (RR) using the three calculation approaches. In the J-SFU calculation, the total PM_{2.5} exposure concentration is higher than in the H-SFU calculation; however, a lower percent of the total exposure is associated with SFU. As this concentration-response function is sublinear in this range and assuming PM_{2.5} source-specific mortality scales proportionally with exposure concentration, less of the health risk is thus apportioned to SFU.

H-SFU, all of the relative risk (or health burden) is attributed to SFU. Following the definitions of GBD2015, the H-SFU calculation does not include household exposure to wood heating in high-income countries (for instance, %SFU is assumed to be zero in Canada).

Mortality calculation for the contribution of SFU to exposure to ambient PM_{2.5} pollution: The number of deaths from A-SFU, for a given country, health outcome, and age group, can be described by:

$$M_{A-SFU} = P \times BMR \times \frac{RR(\text{PM}_{\text{Amb}}) - 1}{RR(\text{PM}_{\text{Amb}})} \times \%PM_{A-SFU}$$

In the calculation of mortality from A-SFU, we assume the total PM_{2.5} exposure for the entire population is characterized by PM_{Amb}; however, only a fraction of this exposure originates from SFU. To estimate mortality associated with ambient exposure to PM_{2.5} from SFU emissions only (M_{A-SFU}), we assume the mortality attributed to exposure to PM_{2.5} from all sources scales proportionally with the fraction of PM_{2.5} from SFU emissions to the total ambient PM_{2.5} concentration (following the discussion in GBD MAPS Working Group, 2016). This proportionality assumption yields a different estimate of mortality than subtracting the estimated number of deaths with and without PM_{2.5} from SFU (e.g., Kodros et al., 2016b). The proportionality assumption is qualitatively described in Figure 4.1b. In this example, the total PM_{2.5} exposure is 50 $\mu\text{g m}^{-3}$. Of this concentration, approximately 10% of the PM_{2.5} concentration (5 $\mu\text{g m}^{-3}$) is apportioned to emissions of SFU, while the remaining 90% is apportioned to emissions of other sources. As a result, only 10% of the relative risk is attributed to SFU. In this study, %PM_{A-SFU} includes emissions of SFU from residential heating in high-income countries in addition to residential cooking and heating emissions in all other countries.

Mortality calculation for joint exposure to household and ambient PM_{2.5} pollution from SFU: To further investigate mortality from SFU, we present a new estimate of the joint effect of exposure to household and ambient PM_{2.5} from SFU. This calculation is not included in GBD2015. We estimate the number of deaths from J-SFU for a given country, health outcome, and age group by:

$$M_{J-SFU} = P \times BMR \times \%SFU \times \frac{RR(\text{PM}_{H-SFU} + \text{PM}_{\text{Amb}}) - 1}{RR(\text{PM}_{H-SFU} + \text{PM}_{\text{Amb}})} \times$$

$$\frac{\text{PM}_{H-SFU} + \text{PM}_{\text{Amb}} \times \% \text{PM}_{A-SFU}}{\text{PM}_{H-SFU} + \text{PM}_{\text{Amb}}} + P \times \text{BMR} \times (1 - \% \text{SFU}) \times \frac{\text{RR}(\text{PM}_{\text{Amb}}) - 1}{\text{RR}(\text{PM}_{\text{Amb}})} \times \% \text{PM}_{A-SFU}$$

In the J-SFU calculation, we assume that the population using solid fuels ($P * \% \text{SFU}$) is exposed to both PM_{H-SFU} and PM_{Amb} . This is a result of 2 assumptions. First, PM_{H-SFU} is defined, following the definition in Forouzanfar et al. (2016), as the exposure concentration only to $\text{PM}_{2.5}$ originating from household solid-fuel use. Second, we assume that ambient $\text{PM}_{2.5}$ concentration also exists indoors (for instance, in the absence of any local emissions from household solid-fuel the household $\text{PM}_{2.5}$ concentration would equal PM_{Amb}). In contrast to the H-SFU calculation, we do not assume that all of this exposure (and thus all of the health risk) originates from SFU. Similar to the A-SFU calculation, we assume that the mortality attributed to exposure to $\text{PM}_{2.5}$ from all sources scales proportionally with the fraction of $\text{PM}_{2.5}$ originating from just SFU emissions. This assumption is depicted qualitatively in Figure 4.1c. In this figure, the total $\text{PM}_{2.5}$ exposure for the population using solid fuels is $300 \mu\text{g m}^{-3}$. This is a sum of PM_{H-SFU} (assumed to be only from SFU) along with PM_{Amb} (of which only $\% \text{PM}_{A-SFU}$ is from SFU and the rest from other sources). In this example, PM_{H-SFU} is $250 \mu\text{g m}^{-3}$, PM_{Amb} is $50 \mu\text{g m}^{-3}$, and $\% \text{PM}_{A-SFU}$ is 10% (or $5 \mu\text{g m}^{-3}$). This results in 85% of the total $\text{PM}_{2.5}$ exposure apportioned to SFU ($255 \mu\text{g m}^{-3}$ divided by $300 \mu\text{g m}^{-3}$). Using the proportionality assumption for source-specific mortality, only 85% of the relative risk is assumed to be from SFU. The remaining population not using solid fuels (described by $1 - \% \text{SFU}$) is still exposed to ambient $\text{PM}_{2.5}$ as in the A-SFU calculation. We acknowledge that we follow the same assumption as in Burnett et al. (2014), Smith et al. (2014), and Forouzanfar et al. (2016) that health risk from exposure to ambient and household $\text{PM}_{2.5}$ pollution is estimated using a single (integrated) exposure-response curve.

4.2.3 Variance-based sensitivity analysis

We use the Fourier Amplitude Sensitivity Test (FAST) (Saltelli et al., 1999) to attribute the fraction of total variance in mortality from SFU to each uncertain input parameter. The FAST

algorithm selects sets of input parameters across the uncertainty space to develop the output distribution. FAST then apportions the variance in the output distribution to the contribution by each input parameter. The result of this analysis is to quantify the *main effect index* and *total effect index* for each parameter. Following the descriptions in Saltelli et al. (2010), the main effect (or first-order or additive effect) of a parameter describes the expected reduction in output variance if that parameter alone were held fixed (e.g., what is the expected reduction of uncertainty in our mortality calculation if the concentration-response function were perfectly known?). The total effect index of a parameter includes the main effect index plus the variance contributed by interactions of that parameter with all other parameters. The total effect thus describes the expected remaining variance if all other parameters were held fixed (e.g. what is the expected amount of remaining uncertainty in our mortality calculation if all parameters except the concentration-response function were perfectly known?). In the absence of interactions between parameters, the main effect index would equal the total effect index.

We perform a variance-based sensitivity analysis on the H-SFU, A-SFU, and J-SFU mortality calculations separately. For each calculation, the number of random draws is set to be equal to the number of uncertain parameters times 10,000. As discussed in Section 2.1, we assume the underlying uncertainty follows a lognormal distribution for each parameter except for the concentration-response function, where the uncertainty space follows the interpolation of the 1,000 parameter fits. In the SI, we test an underlying uniform distribution and find this does not greatly impact our results. In the case of baseline mortality rate and concentration-response function, each disease is treated as a separate uncertain parameter; however, age group is not treated as an independent parameter. Instead, we assume a z-score to apply across all age groups. Mortality calculations and the resulting sensitivity analysis are done at the country level.

4.3 Results and discussion

4.3.1 Country-level mortality attributed to solid-fuel use

4.3.1.1 Premature mortality from H-SFU and A-SFU

We estimate 2.76 (95% CI: 2.37-3.31) million deaths from H-SFU and 0.66 million (95% CI: 0.52-1.0 million) deaths from A-SFU in 2015. The deaths attributable to A-SFU represent approximately 17% of the total mortality burden attributed to exposure to ambient PM_{2.5} from all sources. The countries with the largest mortality from H-SFU are: India (0.86 million; 95% CI: 0.58-1.26 million), China (0.63 million; 95% CI: 0.43-0.92 million), Bangladesh (0.12 million; 95% CI: 0.09-0.15), and Pakistan (0.11 million; 95% CI: 0.08-0.16 million). The countries with the largest mortality from A-SFU are: India (0.29 million; 95% CI: 0.14-0.60 million), China (0.14 million 95% CI: 0.07-0.30 million), Bangladesh (0.04 million; 95% CI: 0.02 - 0.08 million), and Pakistan (0.02 million 95% CI: 0.01-0.04 million). The mortality attributable to A-SFU in these countries represents 30%, 14%, 38%, and 18%, respectively, of mortality attributable to ambient exposure to PM_{2.5} from all sources. Mortality estimates for each calculation and for all countries are included in the SI.

Our estimate of mortality from H-SFU is slightly less than the estimate of 2.85 (95% CI: 2.18-3.59) million from GBD2015 household air pollution (“HAP”) calculation for several possible reasons. First, estimates of the percent of the population using solid-fuel have been updated slightly since GBD2015 (to assume no household solid-fuel use exposure in high income countries). Second, due to data limitations, we do not separate exposure by gender. Third, due to computational limitations, we do all calculations at the country-level. Finally, in this calculation we assume the uncertain parameters follow a lognormal distribution. A different assumption of underlying mortality distribution may impact the uncertainty range. Despite this, we note that our calculation of mortality from H-SFU are within 3% of the household air pollution calculation from GBD2015 and thus we do not plot them here. Similarly, our estimates of mortality in the A-SFU calculation for India and China compare well with estimates made by the GBD Major Air Pollution Sources working group (Group, 2016).

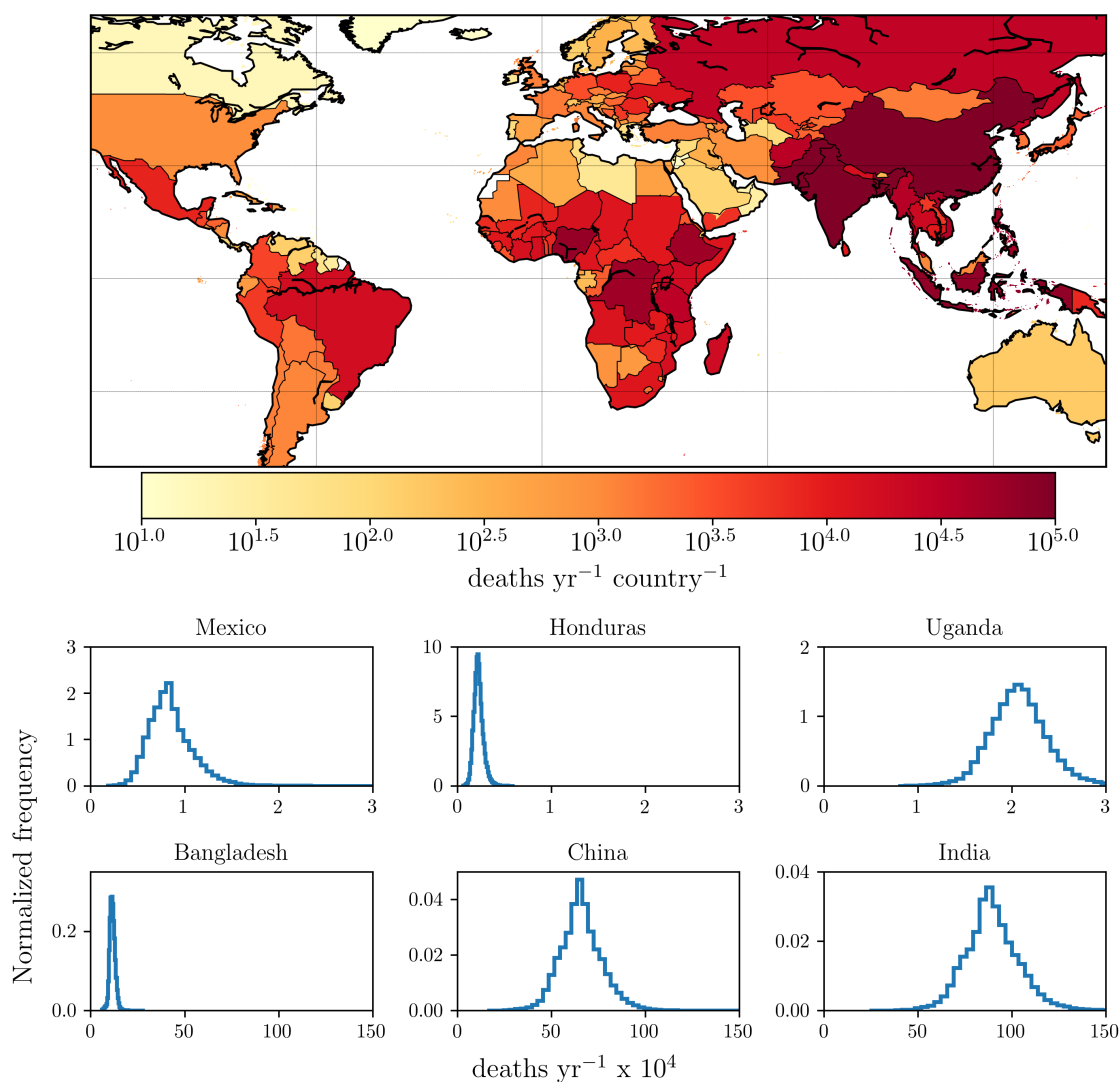


Figure 4.2: Annual mortalities by country due to the joint effect from indoor and outdoor exposure to PM_{2.5} in 2015. Map colors represent the median of each country’s mortality distribution; the normalized probability distributions of six representative countries are also shown. The mortality distributions are different for each country, reflecting differences in model uncertainties for each country’s input data.

4.3.1.2 Premature mortality from J-SFU

Figure 4.2 presents a map of the median estimated mortality in 2015 from J-SFU along with normalized probability distributions of 6 representative countries. The mortality distributions are different for each country, reflecting differences in uncertainties in input data sources. Our sensitivity analysis (Section 3.2) further investigates the factors contributing to variance in these mortality distributions. We estimate 2.81 (95% CI: 2.48-3.28) million premature deaths from J-SFU, with

the largest contributing countries similar to the ranking for H-SFU (India, China, Pakistan, and Bangladesh).

Globally, we estimate 0.58 million fewer deaths in the J-SFU calculation than would result from summing of our H-SFU and A-SFU calculations. When considering only the population using solid fuels, the J-SFU calculation predicts 0.26 million fewer deaths than in the H-SFU calculation. The reason for the fewer deaths in the population using solid fuels for the J-SFU calculation is qualitatively depicted in Figure 4.1d. In the H-SFU calculation, we assume all of the $PM_{2.5}$ exposure (PM_{H-SFU}), and thus all the increased health risk, is from SFU emissions. In the J-SFU calculation, we assume the $PM_{2.5}$ exposure for the same population (i.e. solid fuel users) is the sum of PM_{H-SFU} and PM_{Amb} . This increases the exposure concentration (in the example in Figure 4.1d from $250 \mu g m^{-3}$ to $300 \mu g m^{-3}$, which is roughly representative of India and China) and thus the relative risk; however, as PM_{Amb} includes non-SFU sources, we only attribute a fraction of the relative risk to SFU (in this example approximately 85%). As the concentration-response function is sublinear in this range for IHD and stroke, the increase in relative risk does not scale proportionately to the increase in $PM_{2.5}$ exposure, resulting in lower SFU-attributable health risk for the population using solid fuels in the J-SFU approach than in the H-SFU approach. In the J-SFU calculation, we also account for exposure to ambient $PM_{2.5}$ from SFU ($\%PM_{A-SFU}$) in the population not using solid fuels, calculated as $(1 - \%SFU)$.

Shown in Figure 4.3 are the percent difference in mortality calculated with the J-SFU and sum of the H-SFU and A-SFU calculations. It is not recommended to add deaths from H-SFU and A-SFU exposure, as this does not account for a nonlinear health response to exposure; however, we show this difference to demonstrate the impact of considering joint exposure to ambient and household $PM_{2.5}$, as in the J-SFU calculation. Since the high-income countries only have mortality attributed to A-SFU, the difference between mortality estimates using the J-SFU calculation and the sum of independent mortality estimates from H-SFU and A-SFU is negligible (it is non-zero due to the stochastic sampling of input parameters). For most countries, we estimate fewer deaths using our J-SFU calculation than would be estimated by summing mortality estimates from the

independent H-SFU and A-SFU calculations. This is because the J-SFU calculation no longer attributes all of the household exposure to SFU. Countries in South Asia and sub-Saharan Africa where a substantial (i.e. greater than ~50%) of the population uses solid fuels are more impacted by the change in assumptions regarding exposure (Figure 4.1d), and thus show a larger reduction in mortality attributed to SFU. In India and Pakistan, a large percent of the population using solid fuels combined with a substantial concentration of $PM_{2.5}$ from non-SFU sources results in a greater than 20% reduction in mortality in the J-SFU calculation. In sub-Saharan Africa, smaller absolute concentrations of ambient $PM_{2.5}$ from non-SFU sources limits this reduction in mortality to between 7-15% despite greater than 90% of the population using solid fuels in many countries in this region.

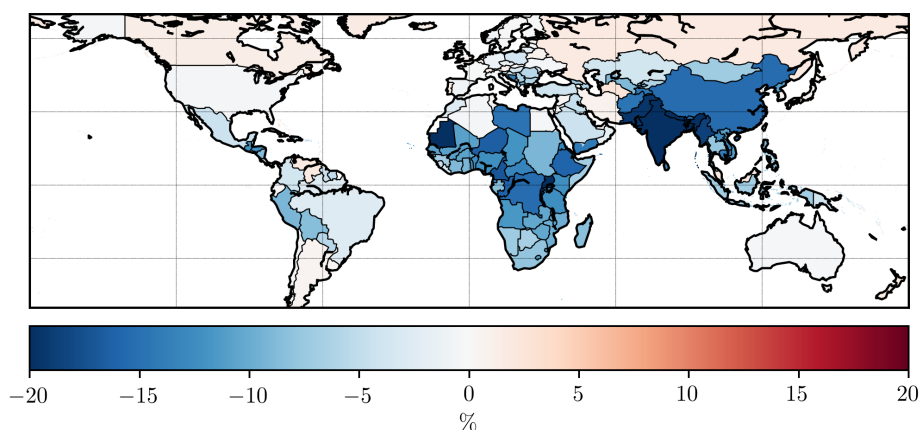


Figure 4.3: Percent difference in estimated country-level mortalities in 2015 using J-SFU relative to mortalities determined using the sum of the H-SFU and A-SFU calculations.

4.3.2 Sensitivity analysis

The results of the variance-based sensitivity analysis for (a) China, (b) India, (c) Latin America, and (d) sub-Saharan Africa are presented in Figures 4.4-4.6 for the H-SFU, A-SFU, and J-SFU mortality calculations, respectively. These representative regions are selected due to their high rates of solid-fuel use (notably sub-Saharan Africa) and high estimated air pollution-related mortality (notably India and China). The bar plots for Latin America and sub-Saharan Africa are averages

over the sensitivity indices of each country in the region weighted by that country's SFU mortality. The y-axis quantifies the percent of the variance in the mortality distribution in each country/region contributed by each input parameter outlined on the x-axis. As discussed in Section 2.3, we present the main effect and total effect indices for each parameter. The total effect index is represented by the total height of the bar with the interaction term represented in grey. The non-grey portion of the bar represents the main effect index. The contributed variance for baseline mortality rate and concentration-response function are separated by disease outcome (represented by the different colors), while the remaining parameters are not dependent on disease. Sensitivity analysis results for all countries are provided in the SI.

4.3.2.1 Sensitivity Analysis for the H-SFU calculation

Shown in Figure 4.4 are the H-SFU sensitivity analysis results. Considering only the main effect index, the percent of the population using solid fuels (%SFU) dominates the uncertainty in H-SFU mortality (contributing greater than 70%) in China, India, and Latin America. This implies that learning this parameter precisely would reduce the variance in the H-SFU mortality distribution in these regions by approximately 70%. In terms of absolute numbers, the variance in mortality would be reduced by 0.44, 0.63, 0.03 million deaths in China, India, and Latin America, respectively. Conversely, in sub-Saharan Africa, the percent of the population using solid fuels contributes only 8% to the variance (or 0.04 million deaths). In sub-Saharan Africa, the percent of the population using solid fuels in many countries is greater than 90% with a small relative uncertainty. The small relative uncertainty in this parameter is reflected in the small contribution to variance in the H-SFU mortality distribution in this region. Baseline mortality rate contributes the most uncertainty in sub-Saharan Africa (close to 70%), specifically from lower respiratory infections. The large contribution to overall variance from lower respiratory infections is caused by the combined impact of their large contribution to H-SFU mortality and a large relative uncertainty range on this contribution, as opposed to lung cancer, which also has a large uncertainty range but contributes only a small number of deaths to H-SFU.

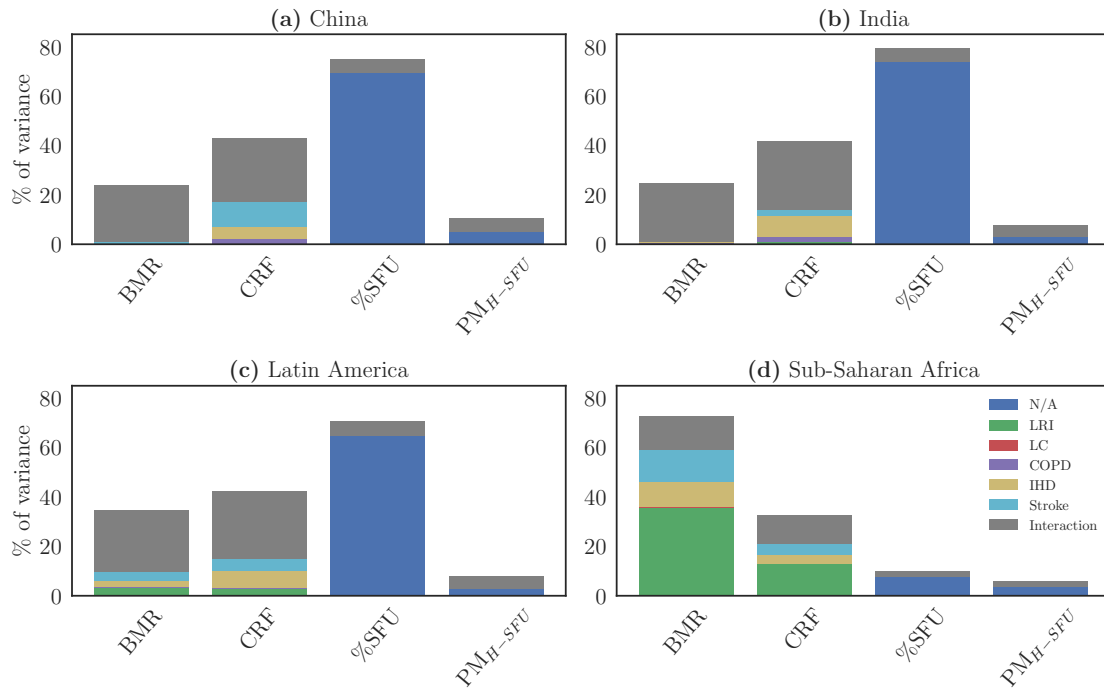


Figure 4.4: Contribution to variance in mortality attributed to H-SFU by each parameter for China (a) and India (b) as well as regional averages weighted by cookstove mortalities for countries in Latin America (c) and Sub-Saharan Africa (d). Acronyms on the x-axis are as defined in Section 2.1 (BMR: baseline mortality rate; CRF: concentration-response function; % SFU: percent of the population using solid fuel; PM_{H-SFU}: exposure to PM_{2.5} from household solid fuel use). Acronyms in the legend refer to: LRI: lower respiratory infection; LC: lung cancer; COPD: chronic obstructive pulmonary disease; IHD: ischemic heart disease; STROKE: ischemic and hemorrhagic stroke; N/A: not applicable (referring to input parameters that do not depend on disease)

The main effect index combined with the interaction term (represented by the grey bars in Figure 4.4) yields the total effect index (the percent of the variance we would expect to remain if all other parameters were known). The total effect for the four parameters sums to 125-154% across these four regions, indicating a fair amount of interaction between terms. The high degree of interaction shared between baseline mortality rate, concentration-response function, and PM_{H-SFU} is likely a result of the FAST sampling algorithm selecting extreme values (in the upper and lower 10th percentiles).

In all four regions, PM_{H-SFU} contributes only a minor amount to the total variance. This is in part due to the relatively flat response of the concentration-response function for IHD and stroke at high PM_{2.5} concentrations. While there are large uncertainties in estimates of PM_{H-SFU}, the relative risk

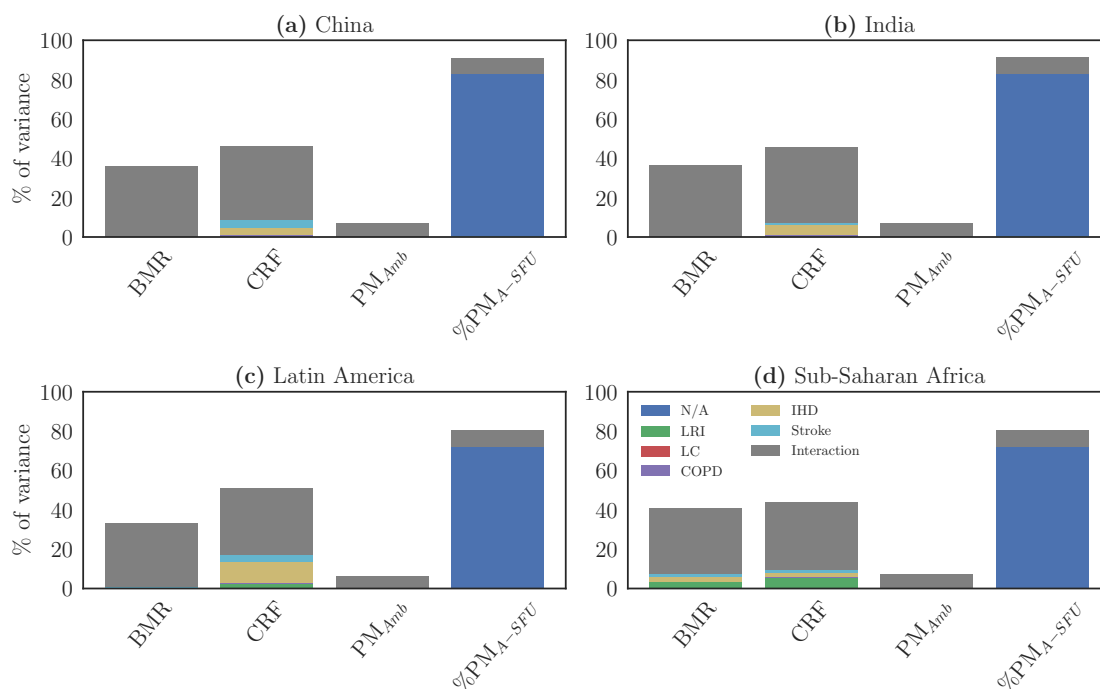


Figure 4.5: Contribution to overall variance in mortality attributable to A-SFU by each parameter for China (a) and India (b) as well as regional averages weighted by cookstove mortalities for countries in Latin America (c) and Sub-Saharan Africa (d). Acronyms are as defined in Section 2.1 (BMR: baseline mortality rate; CRF: concentration-response function; PM_{Amb}: Exposure to ambient PM_{2.5} from all sources; %PM_{A-SFU}: exposure to ambient PM_{2.5} from solid fuel use). Acronyms in the legend refer to: LRI: lower respiratory infection; LC: lung cancer; COPD: chronic obstructive pulmonary disease; IHD: ischemic heart disease; STROKE: ischemic and hemorrhagic stroke.

changes by a small amount relative to the large uncertainties present in the concentration-response function. Thus, in the PM_{2.5} concentration range typical of household solid-fuel use, the uncertainty in the concentration-response function dominates over uncertainty in PM_{2.5}; however, we note that some of the uncertainty in the concentration-response function is shared with PM_{H-SFU} (indicated by the grey portion of the PM_{H-SFU} bar).

4.3.2.2 Sensitivity Analysis for the A-SFU calculation

Figure 4.5 presents the sensitivity analysis results for the A-SFU mortality calculation. In all regions, the total effect index for %PM_{A-SFU} dominates the variance in A-SFU mortality (approximately 80%), reflecting the large uncertainty bounds on this parameter (Section 2.1). This implies that if all other parameters except %PM_{A-SFU} were known, an uncertainty range of 0.13, 0.26, 0.01,

0.03 million deaths would remain in China, India, Latin America, and Africa. A majority of the uncertainty in $\%PM_{A-SFU}$ comes from the main effect index. In contrast, PM_{Amb} contributes less than 9% of the variance, with most of this contribution resulting from the interaction term. The difference in the contribution to variance from the two $PM_{2.5}$ parameters can be attributed to two main factors. First, the relative uncertainty ranges for PM_{Amb} and $\%PM_{A-SFU}$ are very different. Satellite retrievals and surface observations provide constraints on the uncertainty range for PM_{Amb} . Conversely, the uncertainty range for $\%PM_{A-SFU}$ (estimated here as a factor of 2 about the mean) is a result of estimates of uncertainty from emission factors (e.g., Johnson et al., 2008, 2011) and fuel use (e.g., Fernandes et al., 2007), and are much wider than for PM_{Amb} . Second, PM_{Amb} is the exposure concentration included in the concentration-response function. The concentration-response function for IHD and stroke is sublinear, so the changes in relative risk due to different selections of PM_{Amb} are dampened in regions with high PM_{Amb} . Similar to the H-SFU calculation, there are large interaction terms shared between baseline mortality rate, concentration-response function, and PM_{Amb} that are likely caused by sampling from extreme values in the uncertainty distribution.

4.3.2.3 Sensitivity Analysis for the J-SFU calculation

The sensitivity analysis results for the J-SFU calculation are presented in Figure 4.6. In the 4 representative regions, the relative order of parameters in the variance contributions in the J-SFU calculation closely follow the H-SFU calculation. This is because most of the mortality in the J-SFU calculation come from the population using solid fuels, and so the results are more similar to the results for H-SFU. Conversely, in countries where a very low percent of the population uses solid fuels and the mortality burden is primarily from A-SFU (such as in Canada or Algeria), the variance contributions in the J-SFU calculation follow the A-SFU calculation. In China, India, and Latin America, the largest contributions to the variance (in the total effect index) come from the percent of the population using solid fuels (53-56% or 0.03-0.49 million deaths) followed by concentration-response function (42-50% or 0.03-0.42 million deaths). In sub-Saharan Africa, baseline mortality rate (72%) and concentration-response function (33%) dominate the uncertainty space. While $\%PM_{A-SFU}$ dominates the variance in all 4 regions in the A-SFU calculation, this term

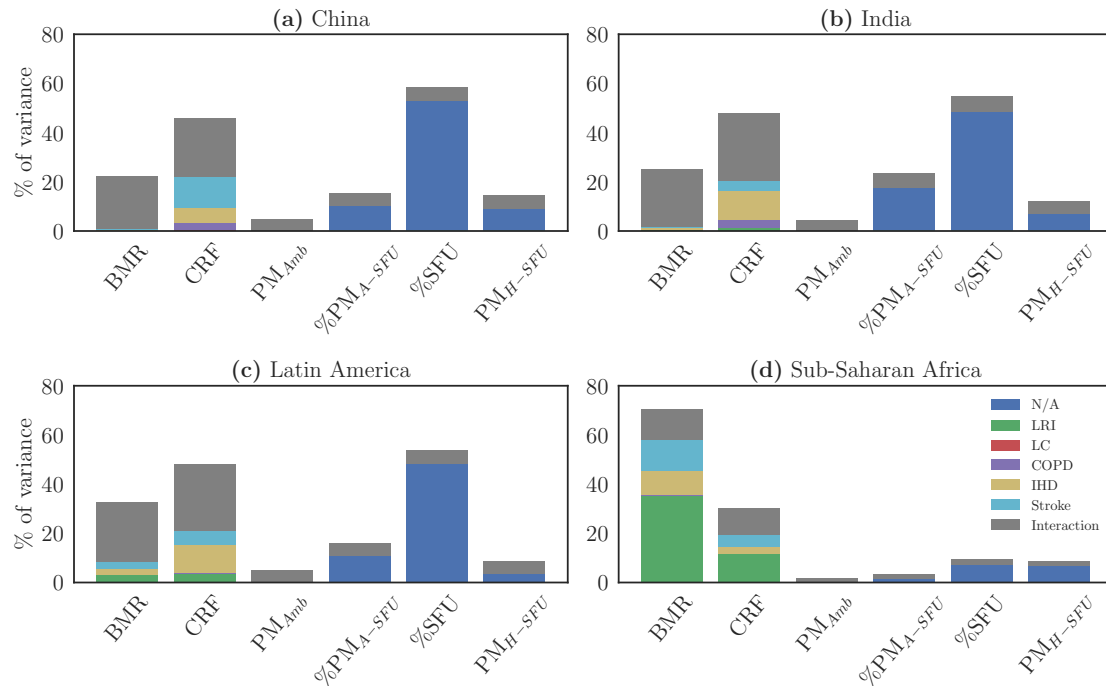


Figure 4.6: Contribution to overall variance by each parameter to the uncertainty in the joint-effect mortality calculation in China (a) and India (b) as well as regional averages weighted by cookstove mortalities for countries in Latin America (c) and Sub-Saharan Africa (d). Acronyms are as defined in Section 2.1 (BMR: baseline mortality rate; CRF: concentration-response function; PM_{Amb} : Exposure to ambient $PM_{2.5}$ from all sources; $\%PM_{A-SFU}$: exposure to ambient $PM_{2.5}$ from solid fuel use; $\%SFU$: percent of the population using solid fuel; PM_{H-SFU} : exposure to $PM_{2.5}$ from household solid fuel use). Acronyms in the legend refer to: LRI: lower respiratory infection; LC: lung cancer; COPD: chronic obstructive pulmonary disease; IHD: ischemic heart disease; STROKE: ischemic and hemorrhagic stroke.

contributes only a small amount of variance in the J-SFU calculation (15-23% in China, India, and Latin America, but less than 5% in sub-Saharan Africa). As A-SFU has only a minor contribution to the total mortality in J-SFU calculation, this parameter contributes a much smaller amount of the variance in the J-SFU calculation compared to the A-SFU calculation. In all four regions, the three $PM_{2.5}$ concentrations (PM_{Amb} , $\%PM_{A-SFU}$, PM_{H-SFU}) combined account for 15-38% of the variance in the total effect index; however, some of the interaction term in concentration-response function is shared between the $PM_{2.5}$ terms. With the exception of sub-Saharan Africa, most of the variance in mortality apportioned to the three $PM_{2.5}$ parameters comes from the percent of ambient $PM_{2.5}$ originating from SFU rather than the total ambient and household concentrations themselves. In sub-Saharan Africa, PM_{H-SFU} is the most important $PM_{2.5}$ factor due to the very high

percent of the population using solid fuels. The low contribution of $PM_{2.5}$ concentrations to the mortality uncertainty suggests that much of the uncertainty in mortality estimates are from the health inputs (baseline mortality rate and concentration-response function) and percent of the population using solid fuels as opposed to the $PM_{2.5}$ exposure. In the SI, we present results truncating the uncertainty distributions at the 95% CI. This reduces the summed total effect to 118-130% across all four regions. Sampling from a uniform distribution (which also truncates at the 95% CI), as opposed to a lognormal distribution, reduces the interaction term to 108-110% (see Appendix B). The nonlinear interactions between the various input terms increase when sampling from the tails of the uncertainty distributions.

4.3.2.4 Limitations of this work

We acknowledge a number of limitations in the sensitivity analysis in this study. In addition to the factors with quantifiable uncertainty ranges described above, there are several major assumptions in which a specific quantified confidence range cannot be applied due to limitations in our current knowledge. Mortality estimates from SFU have required applying and extrapolating epidemiological evidence from studies of outdoor air pollution conducted in high-income countries (mainly the United States and Europe) along with studies of secondhand smoke exposure and tobacco smoke exposure to developing countries with typically higher exposure concentrations (Burnett et al., 2014); whether this extrapolation holds between countries is unclear. In addition, we assume an equal toxicity of different chemical composition of $PM_{2.5}$ (Burnett et al., 2014). Further, while there is limited emerging evidence of links between measures of cardiovascular health with household air pollution (e.g., Agarwal et al., 2017; Mitter et al., 2016), direct evidence of exposure to household air pollution contributing to increased risk of mortality through cardiovascular diseases was not included in the Burnett et al. (2014) concentration-response function (though evidence of cigarette smoking and of ambient air pollution contributing to this health outcome was included). The sensitivity analysis presented here describes the apportioned uncertainty in mortality from input parameters with quantified uncertainty ranges, and thus additional uncertainty in mortality should be considered from the major assumptions of the concentration-response function in addition to what

is considered here. For instance, IHD and stroke contribute substantially to uncertainty in mortality due to exposure to household air pollution in all regions; however, there is additional uncertainty beyond what we quantified here for parameters related to IHD and stroke because of the lack of direct evidence relating exposure to household air pollution and cardiovascular disease outcomes (i.e. events such as stroke). An additional limitation is that the sensitivity analysis used here is itself sensitive to the uncertainty range provided for each data input source. For example, measurements of personal $PM_{2.5}$ exposure are limited, and several studies (e.g., Baumgartner et al., 2011; Ni et al., 2016) report personal exposures with a different uncertainty distribution including portions of the distribution outside the published range used in this study. To test this limitation, we increased the 95% uncertainty levels for the PM_{H-SFU} parameter from a factor of 1.4 to 2 in both directions around the central estimate. In the H-SFU calculation, this increased the percent contribution in the total effect index of the parameter from 6-10% to 15-20% (across the four regions). Despite these limitations, the sensitivity analysis in this study provides valuable information on the sources of uncertainty in mortality calculations attributed to SFU.

4.4 Conclusions

The large health burden attributed to SFU has motivated interventions aimed at replacing traditional cookstoves with cleaner-burning fuels and combustion devices (e.g., M. Clark et al., 2010, 2013; S. Clark et al., 2017; Mortimer et al., 2016; Piedrahita et al., 2016; Ruiz-Mercado et al., 2011); however, there are large uncertainties in the number of deaths attributed to exposure to $PM_{2.5}$ from SFU. These uncertainties originate from uncertain input parameters as well as the contribution of health risk from other ambient $PM_{2.5}$ sources. There is currently no framework to estimate mortality from SFU while accounting for $PM_{2.5}$ from other sources. In this study, we estimate 2.81 (95% CI: 2.48-3.28) million deaths in 2015 from the joint exposure to household and ambient $PM_{2.5}$ from SFU using the J-SFU calculation. This estimate has 580,000 (18%) fewer deaths than the sum of the H-SFU and A-SFU calculations, and 260,000 fewer deaths among the population using solid fuel in the J-SFU calculation than in the H-SFU calculation alone. This indicates that treating

household and ambient pollution as independent risk factors leads to overestimates of mortality attributed to SFU, particularly in regions with high ambient $PM_{2.5}$ concentrations. Health and epidemiology studies taking place in areas (such as periurban areas) with high $PM_{2.5}$ concentrations from sources other than SFU may expect a smaller health response due to decreases in $PM_{2.5}$ from SFU.

We performed a variance-based sensitivity analysis on each mortality calculation to apportion the variance in mortality attributed to SFU to each uncertain input parameter. In the H-SFU calculation, the percent of the population using solid fuels and the concentration-response function contribute the most uncertainty in SFU mortality except in regions where greater than 90% of the population uses solid fuels and the uncertainty range is small. The $PM_{2.5}$ exposure estimates contribute a relatively small amount of uncertainty in mortality because the range of exposures associated with household solid fuel use extends across a flatter part of the concentration-response function for dominant causes of death (IHD and stroke). While the percent of the population using solid fuels has a smaller relative uncertainty than the $PM_{2.5}$ exposure, it contributes a much larger percent of the uncertainty in mortality. We note that the results of this study do not rank input parameters by their precision, but rather, by how the uncertainty in each input parameter affects the uncertainty in model output.

In the A-SFU calculation, the contribution of SFU emissions to ambient $PM_{2.5}$ concentration dominates the uncertainty space. This is a result of large uncertainties in SFU emission inventories, which are a result of the combination of uncertainties in emission factors and fuel use. This is also a reflection of the difficulty of atmospheric models to attribute the fraction of ambient $PM_{2.5}$ to a specific source (even though the total ambient $PM_{2.5}$ can be constrained with surface observations and satellite retrievals).

The sensitivity analysis on our J-SFU calculation reflects a combination of the contributed uncertainty in mortality from the H-SFU calculation and the A-SFU calculation. In the J-SFU calculation, a majority of the total deaths occur in the population using solid fuels (and are thus exposed to higher indoor concentrations). As a result, the sensitivity analysis results are more similar

to the results from the H-SFU calculation. In China, India, and Latin America, the parameters that contribute the most uncertainty to mortality attributed to PM_{2.5} exposure from SFU are the percent of the population using solid fuels (53-56%) and the concentration-response function (42-50%). The three PM_{2.5} exposure concentrations contribute between 15-38% of the variance in mortality distributions. Our findings suggest that future research focused on constraining the health response of exposure to PM_{2.5} and estimates of solid fuel use could measurably reduce uncertainty in premature mortality estimates associated with solid fuel use. Improving solid fuel use estimates would reduce uncertainty in both the H-SFU calculation (where the leading contribution to mortality is from the population using solid fuels) and the A-SFU calculation (where the large uncertainties in ambient PM_{2.5} from SFU emissions are linked to uncertainty in solid-fuel use). In sub-Saharan Africa, where the percent of the population using solid fuels is relatively well constrained, our results suggest that future work should focus on reducing the uncertainty in baseline mortality rates.

It is important to note that while our sensitivity analysis shows a relatively small contribution from PM_{2.5} exposure to uncertainty in J-SFU mortality estimates, this by no means implies that PM_{2.5} exposure is unimportant for estimating premature mortality from SFU. Fundamentally, there must be exposure to PM_{2.5} from SFU in order to have mortality from PM_{2.5} attributable to SFU. This analysis only estimates the contribution to variance in SFU mortality. It is not meant to indicate which factors contribute the most to the estimated magnitude of mortality from SFU. As such, our results do not indicate that reducing exposure to PM_{2.5} from SFU would not have a health benefit; we mean to suggest that the uncertainty in the magnitude of the health benefit is largely from uncertainties in the population using solid fuels and the concentration-response function. Additionally, improving concentration-response functions (one of the largest contributors to uncertainty identified here) necessitates accurate measurements of PM_{2.5} exposure in the epidemiological studies used to generate the concentration-response functions.

The estimated health burden attributed to SFU is substantial both in terms of mortality, disability adjusted life years, years of life lost, and willingness to pay losses (Cohen et al., 2017; World Bank, 2016; World Health Organization, 2014). Future studies may seek to quantify uncertainty

in mortality from SFU in different years or with different data inputs (such as those compiled by the World Health Organization). To gain a better understanding of the expected benefits of SFU interventions, future research should also focus on more accurate and precise estimates of populations using solid fuels, exposure-response relationships, and mortality rates in sub-Saharan Africa.

Chapter 5

Important global and regional differences in aerosol cloud-albedo effect estimates between simulations with and without prognostic aerosol microphysics⁴

Aerosol-cloud interactions are among the most uncertain climate forcings, in part due to the strong sensitivity of cloud droplet number concentration (CDNC) to changes in the size distribution of potential cloud condensation nuclei (CCN). Despite this sensitivity of simulated aerosol-cloud interactions to variations in size-resolved aerosol concentrations being well established, many chemistry-climate and chemical-transport models do not include explicit treatment of the aerosol size distribution. We use a global chemical-transport model to estimate the aerosol cloud-albedo effect (CAE) due to anthropogenic emissions with prognostic sectional aerosol microphysics and compare this to the CAE calculated when the simulated aerosol mass of each species is re-mapped onto a prescribed size distribution. We find that, although both the prescribed and prognostic methods compare similarly well with present-day size-distribution observations, there are substantial differences in the relative CDNC and CAE due to anthropogenic emissions. When using the prognostic size-distribution method, anthropogenic emissions yield a 25-75% larger increase in CDNC over most land masses but a 50-75% smaller increase in some remote-marine regions than in the prescribed size-distribution methods. Simulations using the prognostic scheme yield a global-mean anthropogenic CAE of -0.87 W m^{-2} , while the simulations with the prescribed scheme predict -0.66 W m^{-2} . In South America and South Asia, differences in the CAE exceed 3.0 W m^{-2} . These differences suggest that simulations with prescribed size-distribution mapping are

⁴This Chapter published as: Kodros, J. K. and Pierce, J. R.: Important global and regional differences in aerosol cloud-albedo effect estimates between simulations with and without prognostic aerosol microphysics, *J. Geophys. Res. Atmos.*, doi:10.1002/2016JD025886, 2017.

unable to capture regional and temporal variability in size-resolved aerosol number, and thus may lead to biases in estimates of the CAE.

5.1 Introduction

The radiative forcing due to the impact of anthropogenic changes in aerosol particles on clouds is the most uncertain climate forcing of those quantified in the IPCC 5th assessment report (Boucher et al., 2013). Estimates of the global-mean aerosol-cloud-interaction (ACI) effective radiative forcing in the IPCC report range from -1.2 to 0.0 W m^{-2} , compared to the CO_2 effective radiative forcing of $+1.33$ to $+2.03 \text{ W m}^{-2}$. Given the opposing sign of the aerosol-cloud-interaction and CO_2 forcings, the ACI forcing may be masking a significant portion of the temperature increase from CO_2 (Andreae et al., 2005). There is therefore a strong motivation to reduce the uncertainty in the ACI forcing in order to better constrain the climate response to future greenhouse-gas emissions.

The range in ACI forcing estimates includes uncertainties in rapid adjustments to cloud properties; however, a substantial portion includes uncertainties in the cloud-albedo, or 1st, aerosol indirect effect (Boucher et al., 2013). The aerosol cloud-albedo effect (CAE) refers to altering the reflectivity of clouds through changing the number of cloud drops while holding the liquid water content of the cloud constant (Twomey, 1974). In the liquid-phase region of the cloud, increasing the cloud droplet number concentration (CDNC) increases cloud albedo; however, the relationship between cloud reflectivity and CDNC, known as "cloud susceptibility," is nonlinear (Twomey, 1991). In addition to cloud susceptibility, particle activation to CDNC is also nonlinear, as high concentrations of cloud condensation nuclei (CCN) limit in-cloud water supersaturation (Seinfeld and Pandis, 2012) and lower the fraction of particles that activate to become cloud droplets. As a result of these nonlinear relationships, Carslaw et al. (2013) found that the CAE is most sensitive to uncertainties in the processes and emissions during the cleaner pre-industrial state with lower aerosol concentrations than in the present day.

Particle activation into CDNC (at a given supersaturation) is a strong function of particle size as well as chemical composition (Petters and Kreidenweis, 2007). The composition, as

relevant to particle activation, is often quantified by the hygroscopicity parameter, κ (Petters and Kreidenweis, 2007); however, (Dusek et al., 2006) finds that the primary factor determining activation is particle diameter, with particle composition being a secondary effect. For typical cloud conditions, particles with diameters larger than 40-100 nm will activate, the exact value of this lower-diameter limit depends on the cloud updraft velocity, aerosol size distribution and hygroscopicity (Abdul-Razzak and Ghan, 2002; Nenes and Seinfeld, 2003). It is therefore likely important (in terms of predicted aerosol-cloud interactions) to not only know the particle number concentration but the size distribution as well.

A common approach to modeling aerosol microphysics is to refer to the CCN concentration at a particular supersaturation, thereby specifically referring to the subset of soluble particles that would activate to cloud droplets (typically larger than 40 to 100 nm in diameter, depending on the supersaturation). The number of particles in the CCN size range is determined by primary aerosol emissions as well as secondary chemical and physical formation processes (L. Lee et al., 2013). Some of these secondary processes are a source or sink for particle number (e.g. nucleation, coagulation, deposition), while others shift the particle size distribution by adding mass while conserving number (e.g., condensation). Thus, the aerosol size distribution varies in time and space due to changes in species concentrations and the dominant chemical and physical processes.

Aerosol schemes range in complexity. Bulk schemes only track the total mass of each species and do not predict an aerosol size distribution (Collins et al., 2011; Donner et al., 2011; Lamarque et al., 2012, e.g.). These bulk schemes thus do not consider how aerosol microphysics (nucleation, condensation, coagulation) shape the size distribution. Aerosol microphysics schemes require more computational complexity than bulk schemes and have several variants: fixed modal schemes where the total mass of each species is tracked in modes of different size or populations (e.g., Bellouin et al., 2011), two-moment modal or moment schemes that track number and the mass of each species in sizes and/or populations (e.g., Bauer et al., 2008; Binkowski and Shankar, 1995; Ghan et al., 2001; Mann et al., 2010; Whitby, 1978), and sectional schemes that track the number and/or mass of each species within a large number of size sections and/or populations (e.g., Adams and

Seinfeld, 2002; Gong, 2003; Spracklen et al., 2005). The modal, moment, and sectional schemes track a dynamic size distribution and are commonly referred to as aerosol microphysics schemes, which stand in contrast to the bulk schemes that do not predict dynamic size distributions. The sectional approach does not assume an underlying size-distribution shape, and so tends to be more flexible and realistic than the other schemes; however, computational limitations necessitate using a relatively small number of bins or a degradation in spatial resolution.

Despite the number of independently developed microphysical models, computational resource considerations have, until recently, tended to discourage their use in climate models. Of the 10 models in the Atmospheric Chemistry and Climate Model Intercomparison Project (ACCMIP) (Lamarque et al., 2013; Shindell et al., 2013b) that include aerosols (8 of these participated in CMIP5), only 3 included online size-resolved aerosol microphysics (and only 2 of those participated in CMIP5) (Liu et al., 2012; Szopa et al., 2013). The remaining models use a bulk aerosol scheme and rely on prescribed mappings or correlations with satellite observations to obtain information on size-resolved aerosol properties (such as CDNC) (Collins et al., 2011; Donner et al., 2011; Lamarque et al., 2012; Rotstayn et al., 2012; Shindell et al., 2013a; Skeie et al., 2011; Watanabe et al., 2011). A common prescribed mapping involves mapping the mass of each bulk aerosol species into 1 to 3 lognormal modes (Collins et al., 2011; Croft et al., 2005; Donner et al., 2011; He et al., 2016; Karydis et al., 2011, 2012; Lamarque et al., 2012; Watanabe et al., 2011). This method relies on keeping size-distribution parameters (such as number median diameter and geometric standard deviation) constant at typical values for the different types derived from measurements of the particle size distribution. A substantial drawback of this method is that the parameters in a prescribed mapping are held fixed spatially and temporally, in spite of observations that show variations in aerosol size distributions from processes such as transport (Dentener et al., 2006; Sakamoto et al., 2016; Westphal and Toon, 1991), in-cloud aqueous oxidation (Hoppel and Frick, 1990), new-particle formation events (Merikanto et al., 2009; Westervelt et al., 2014), and production and evaporation of secondary aerosol (D'Andrea et al., 2013). As a result, aerosol size distributions vary seasonally and regionally, leading to variations in CDNC (e.g., Pringle et al., 2009). It is

therefore highly likely that size distributions of specific aerosol types (such as sulfate) will have changed markedly since pre-industrial times.

The purpose of this study is to explore possible differences in size-resolved aerosol number concentration and CAE when using a prognostic aerosol microphysics model as opposed to an assumed size distribution for each aerosol species. Differences between various microphysical schemes (modal, moment and sectional) have been investigated elsewhere (e.g., Bellouin et al., 2013; Ghan et al., 2001; Liu, 2005; Mann et al., 2012; Y. Zhang et al., 2002). In this study, we use a sectional scheme to represent aerosol microphysics schemes and take the total mass summed across the sectional bins to represent the "bulk" scheme. We are therefore isolating the effect on the CAE of the offline mass-to-number conversion using prescribed species-specific size distributions as opposed to online representations of chemical and physical processes. While we focus on a sectional scheme here, we expect modal and moment schemes to yield similar findings as to our approach with the sectional scheme as these schemes also allow for size shifts in the aerosol size distribution. In Section 2, we discuss the chemical-transport-model setup, the aerosol microphysics scheme, and the assumed prescribed aerosol size distributions. In Section 3.1, we compare the prognostic and prescribed modeled size distributions to observations. Differences in size-resolved aerosol number concentrations are discussed in Sections 3.2. The resulting differences in CAE are discussed in Section 3.3. In Section 4, we share our conclusions and recommendations.

5.2 Methods

5.2.1 GEOS-Chem model setup

To simulate the transport of gas- and aerosol-phase species, we use the Goddard Earth Observing System chemical-transport model, GEOS-Chem, version 10.01. We simulate the year 2010, driving the model with re-analysis meteorology from GEOS-5 (<http://gmao.gsfc.nasa.gov>). This version of GEOS-Chem includes 47 vertical layers and a horizontal resolution of 4° latitude and 5° longitude. GEOS-Chem includes tracers for 52 gas-phase species.

Table 5.1: Description of size-distribution schemes.

Size Distribution	Description
TOMAS	Online 2-moment sectional aerosol microphysics model incorporated into GEOS-Chem. TOMAS explicitly tracks total particle number and speciated particle mass.
LOGNORMAL	Particle-size re-mapping of total aerosol mass by species into lognormal distributions. Mass is converted to particle number using an assumed density and assuming spherical particles. Mapping parameters are reported in Table 5.2.
AVG-TOMAS	Particle-size re-mapping of total aerosol mass using the normalized global- and annual-mean TOMAS mass distribution for each species. Mass is converted to particle number using the global-mean mass-to-number ratio from TOMAS.

Standard emission setup is described in (Kodros et al., 2016a). To explore the dependence of anthropogenic CAE on assumed aerosol size-distribution shape, we include two simulations: one with all standard emissions (*anth_on*) and one with anthropogenic emissions turned off (*anth_off*). Comparing these simulations isolates the aerosol burden from anthropogenic emissions. We note that our *anth_off* simulation is separate from a "pre-industrial" simulation in several ways: we do not include land- use changes that may lead to an anthropogenic component to dust or biomass-burning emissions, we do not alter the spatial distribution of biofuel emissions, and all natural emissions are held constant for the year 2010. This comparison represents an illustrative change in emissions rather than an exact representation of any pre-industrial period. Therefore, our radiative calculations represent the total cloud-albedo radiative "effect" from select aerosol sources rather than a cloud-albedo radiative "forcing" over a specified time period.

5.2.2 Aerosol size distributions

Table 5.1 describes the aerosol size-distribution methods used in this study. The first size distribution method is an online, prognostic microphysics simulation using the microphysics package, Two Moment Aerosol Sectional (TOMAS) (Adams and Seinfeld, 2002), integrated into GEOS-Chem (known as 'GEOS-Chem-TOMAS'). Detailed descriptions of TOMAS can be found in (Adams and Seinfeld, 2002; Lee and Adams, 2012; Y. H. Lee et al., 2013). Briefly, TOMAS

discretizes the aerosol size distribution into sections ("bins") and tracks 2 moments within each bin: total number and speciated particle mass. This version of TOMAS includes 40 size bins, with equivalent particle diameters ranging from approximately 1 nm in the lowest bin to 10 μm in the largest bin. The exact diameter is dependent on particle density. Aerosol species include: sulfate, hydrophilic and hydrophobic organic aerosol, black carbon, sea salt, and dust. TOMAS includes a prognostic 40-bin size distribution for each species. Primary sulfate is emitted into the model assuming 2 lognormal modes: 15% of the mass in a first mode with a number median diameter (NMD) of 10 nm and geometric standard deviation (GSD) of 1.6, and the remainder in a second mode with a NMD of 70 nm and GSD of 2 (Adams and Seinfeld, 2003). Carbonaceous particle emissions are separated by emission source: those produced by fossil fuel have an NMD of 30 nm and GSD of 2, while biofuel and biomass-burning particles are emitted with an NMD of 100 nm and a GSD of 2 (Pierce et al., 2007). TOMAS includes separate size distributions for externally mixed black carbon and internally mixed species, including black carbon that has mixed into this population. Black carbon converts from the "externally mixed" to "internally mixed" population with a fixed conversion time scale of 1.15 days. Sea-salt aerosol emissions follow the scheme of Jaeglé et al. (2011), while dust emissions are based on the DEAD scheme (Zender, 2003). Nucleation in TOMAS follows a ternary scheme involving water, sulfuric acid, and ammonia following the parameterization of Napari et al. (2002), which has its nucleation rates scaled down by 5 orders of magnitude to better match observations (Westervelt et al., 2013). When ammonia mixing ratios are less than 1 pptv, TOMAS defaults to a binary nucleation scheme (sulfuric acid and water) (Vehkamäki, 2002). In addition to nucleation, TOMAS explicitly simulates condensation, coagulation, wet and dry deposition, and cloud processing. These processes have been evaluated against observations (D'Andrea et al., 2013; Kodros et al., 2016a; Westervelt et al., 2013).

The second size-distribution method used in this study is a prescribed mapping of bulk species mass to lognormal distributions (referred to as "LOGNORMAL", see Table 5.1). The purpose of the LOGNORMAL method is to represent the method of estimating aerosol number concentrations used in several mass-only (i.e. bulk) aerosol schemes. Here, the total particle mass for each species

is converted to a size distribution offline assuming lognormal distributions with either one mode (sulfate, OA, BC), two modes (sea salt), or three modes (dust). We assume an NMD, GSD, and density for each aerosol species for each mode and spread the mass across a size distribution. We calculate the total (bulk) aerosol mass for each species by summing over all TOMAS bins; thus, the total aerosol mass is conserved between the prognostic and prescribed size distributions considered here. Hence, the LOGNORMAL method described here is representative of bulk mass-only schemes in the offline comparison of monthly-mean particle number concentration, CDNC, and CAE, but does not represent bulk schemes in online microphysical processes. We take this approach to isolate the effect on CAE of mapping total mass of each species into number size distributions as opposed to the effect on microphysical processes in models. This size-distribution prescribed-mapping method is used in a number of studies (e.g., Collins et al., 2011; Croft et al., 2005; Donner et al., 2011; He et al., 2016; Karydis et al., 2011, 2012; Lamarque et al., 2012; Watanabe et al., 2011) to obtain size-resolved particle information (though we note not all of these studies are estimating the anthropogenic CAE). The specific parameters for the LOGNORMAL distribution method used in this study are listed in Table 5.2. Each species is mapped into a separate lognormal distribution and are then summed together to estimate total size-resolved particle number concentration. The mapping parameters are held fixed globally and across all simulations; however, variations (either spatially or across simulations) in the relative mass of each species allows for variations in the summed size distribution. The parameters listed in Table 5.2 are based on parameters listed in GEOS-Chem for photolysis calculations, which in turn are based on size distributions from the Global Aerosol Dataset (GADS) (Koepke et al., 1997). GADS is a compilation of measurement and modeling studies, providing average microphysical and optical parameters for 10 aerosol types.

The third size-distribution method is another prescribed-mapping method, but uses a fundamentally different underlying distribution than a lognormal distribution. In the "AVG- TOMAS" method, we use the normalized global- and annual-mean mass distributions from the TOMAS *anth_on* simulation as the mapping parameters. Thus, in each gridcell the normalized mass distribution of each species is identical to the normalized global and annual mean mass distribution from TOMAS

Table 5.2: Size-distribution parameters applied to the total mass of each species to create lognormal distributions.

Aerosol Species	Density [g cm ⁻³]	Number median diameter [μm]	Geometric standard deviation	Mode mass fraction (dust) or cutoff size (sea salt)
Sulfate	1.77	0.14	1.6	1.0
Organic Aerosol	1.40	0.14	1.6	1.0
Black Carbon	2.00	0.04	1.6	1.0
Sea Salt	2.00	0.18	1.5	0.001-0.5 μm
		0.8	1.8	0.5 - 11 μm
Dust	1.50	0.16	2.1	0.035
		1.4	1.9	0.958
		10.0	1.6	0.005

for that species (but will be scaled up or down depending on the total aerosol mass of each species). This approach is similar to that of LOGNORMAL in that the mapping parameters (in this case the fractional mass-per-bin of the average TOMAS distribution) are held fixed globally and across simulations for each species, though differences in relative mass of the species will allow in variations in summed number distribution. The purpose of using the simulated global- and annual-mean TOMAS size distribution as the mapping parameters is to explore the differences in the estimated CAE when using a fundamentally different set mapping parameters that are more similar to TOMAS in the global and annual mean (i.e. we take the global- and annual-mean distributions as "typical" size distributions in the ambient atmosphere). This approach enables us to test how sensitive our results are to the chosen LOGNORMAL mapping parameters.

In the LOGNORMAL and AVG-TOMAS methods, the aerosol mass of each species in *anth_off* is mapped using the same distribution parameters as in *anth_on*, which is consistent with previous studies that assumed prescribed size distributions. This assumes that the microphysical process responsible for "aging" particles to the assumed average size have the same magnitude in the *anth_off* simulation. We note, however, that perturbing the relative mass of each species will weight the mapping parameters in the summed number distribution differently, thereby enabling variations in the total size distribution for the prescribed methods. Conversely, in the prognostic online TOMAS model, changing gas and aerosol concentrations feedback into changing strengths of

microphysical processes leading to fundamentally different size distributions. This is an important assumption motivating this paper.

5.2.3 Offline calculation of CDNC and aerosol cloud-albedo effect

We use monthly mean size-resolved aerosol mass and number concentrations as inputs to the activation parameterization of Abdul-Razzak and Ghan (2002) to calculate CDNC. We assume a constant updraft velocity of 0.5 m s^{-1} and calculate κ , the hygroscopicity parameter, in each bin using a volume weighted average of the individual species (Petters and Kreidenweis, 2007). CDNC and resulting CAE are sensitive to assumptions regarding updraft velocity (L. Lee et al., 2013). We tested this sensitivity using updraft velocities of 0.1 m s^{-1} and 1.0 m s^{-1} , but find no qualitative differences in calculated CAE and do not include that analysis here. We assume a control liquid cloud drop radii of $10 \mu\text{m}$, and, for vertical levels below 600 hPa, perturb this value based on the ratio of the calculated CDNC in *anth_off* to *anth_on* to the one-third power (following Rap et al., 2013; Scott et al., 2014). We calculate the change in top-of-the-atmosphere flux from the perturbed and control fields using an offline version of the Rapid Radiative Transfer Model for GCMs (RRTMG) (Iacono et al., 2008), implemented in GEOS-Chem (Heald et al., 2014), that treats clouds with the Monte Carlo independent column approximation (McICA) (Pincus et al., 2003). Cloud fraction, temperature, pressure, and liquid water content are taken from monthly mean GEOS5 fields. While the use of monthly mean aerosol and meteorology fields likely introduces some errors, our main purpose here is in exploring the differences between assumed size distributions.

In this study, we explore changes to the aerosol cloud-albedo effect (also referred to as the cloud-albedo aerosol indirect effect or 1st aerosol indirect effect). As GEOS-Chem uses fixed re-analysis meteorology fields, changes in aerosol concentrations do not feedback into changes to cloud properties or circulation. We assume fixed cloud liquid water and cloud fractions across all simulations. We are therefore restricted to assessing the sensitivity of cloud albedo to size-resolved aerosol number concentration in the absence of the "rapid adjustments" in composition, dynamics, and clouds (Boucher et al., 2013; Myhre et al., 2013). In addition, we focus solely on changes

to cloud albedo in the context of the addition/removal of anthropogenic emissions under fixed meteorology. These simplifications are made to explore how sensitive simulated CDNC changes and the CAE are to assumptions regarding the aerosol size distribution.

5.2.4 Description of observations of aerosol size distributions

We use observations of aerosol size distributions from 21 field sites in Europe and North America. This dataset is described in detail in D'Andrea et al. (2013) (see map of site locations in Figure 1 in D'Andrea et al. (2013)) and used again in Pierce et al. (2015). Size distribution measurements were made using either a Scanning Mobility Particle Sizer (SMPS) (Wang and Flagan, 1990) or a Differential Mobility Particle Sizer (DMPS) (Aalto et al., 2001). All observations are long-term (1 year or longer) and located in rural continental regions to avoid sharp spatial gradients (such as in urban areas) that the coarse model resolution cannot capture. While this dataset has limitations with regard to number of datapoints and temporal and spatial scope, the purpose of this dataset is to test whether the simulated size distributions predict realistic values.

5.3 Results

5.3.1 Comparison to observations

Figure 5.1 shows one-to-one comparisons of the simulated number of particles with dry diameters greater than 10 nm (N10), 40 nm (N40), 80 nm (N80), and 150 nm (N150) at the 21 observation sites for the TOMAS and LOGNORMAL size-distribution methods. The TOMAS distribution is able to explain more of the variance (R^2) in each size range compared to the LOGNORMAL distribution method. The slope of the linear regression line is closer to unity for each size range except N10 ($m=0.9$ for TOMAS and 0.91 for LOGNORMAL). Notably, the slope of the regression line for TOMAS is 0.96 for N40, the size range representing "climate relevant" particle sizes. Both the TOMAS and LOGNORMAL methods exhibit a low bias relative to observations in all size ranges. Care should be taken in interpreting these results as observation sites are few in number ($N=21$), and we consider only long-term averages at remote continental sites. The main objective

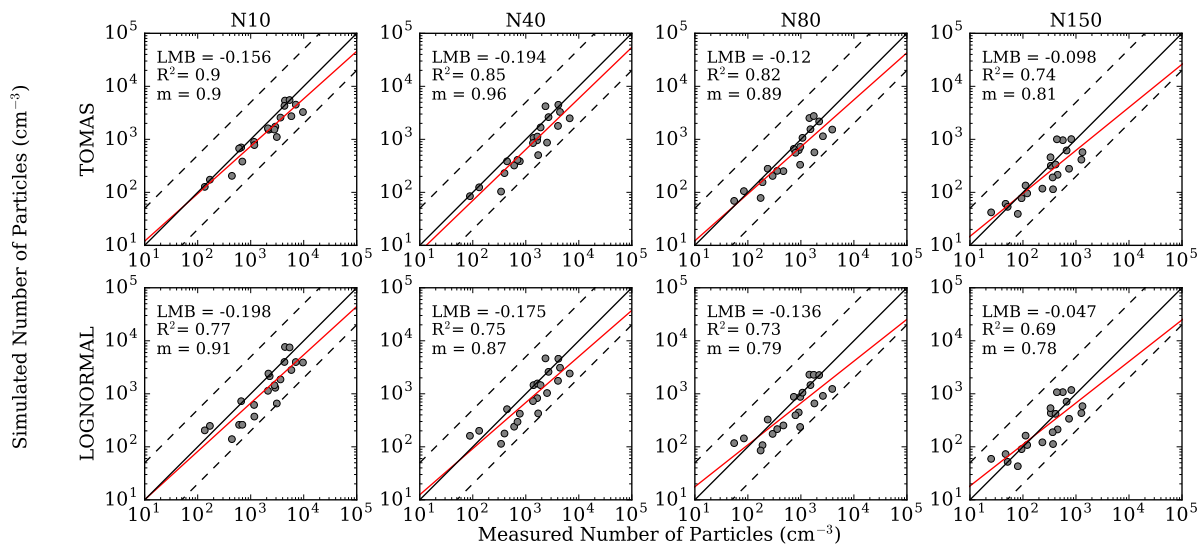


Figure 5.1: One-to-one plots of the simulated N10, N40, N80, and N150 for the *anth_on* simulation using the TOMAS (top) and LOGNORMAL (bottom) size-distributions schemes compared to 21 measurement sites described in D’Andrea et al. (2013). The dashed black lines represent the 1:5 and 5:1 lines, while the red line represents the results of the linear regression. The printed values give the slope (m), correlation (R^2), and log mean bias (LMB).

here is to demonstrate that both simulated number distributions produce reasonable comparisons to observations, particularly in the CCN relevant size ranges (for N40 $m=0.87$ and $m=0.96$ for LOGNORMAL and TOMAS, respectively).

Figure 5.2 shows the temporally averaged observed size distributions at each site along with the TOMAS and LOGNORMAL distribution methods. Each size-distribution location plotted here corresponds to a point in Figure 5.1. Again, both size distributions are able to produce reasonable number concentrations at each site (see the quantitative regression metrics in Figure 5.1). In some cases, such as Hyytiala and Pallas, the LOGNORMAL distribution method appears more representative of the observed distribution, while in other locations, such as Puszta and Alert, the TOMAS distribution is more representative. In general, the prognostic TOMAS microphysics predicts a more diverse range of size distributions than is possible in the prescribed LOGNORMAL distribution method.

Similar comparisons were made in D’Andrea et al. (2013) and Pierce et al. (2015). We attribute differences in the GEOS-Chem-TOMAS comparisons between the studies to number of bins used

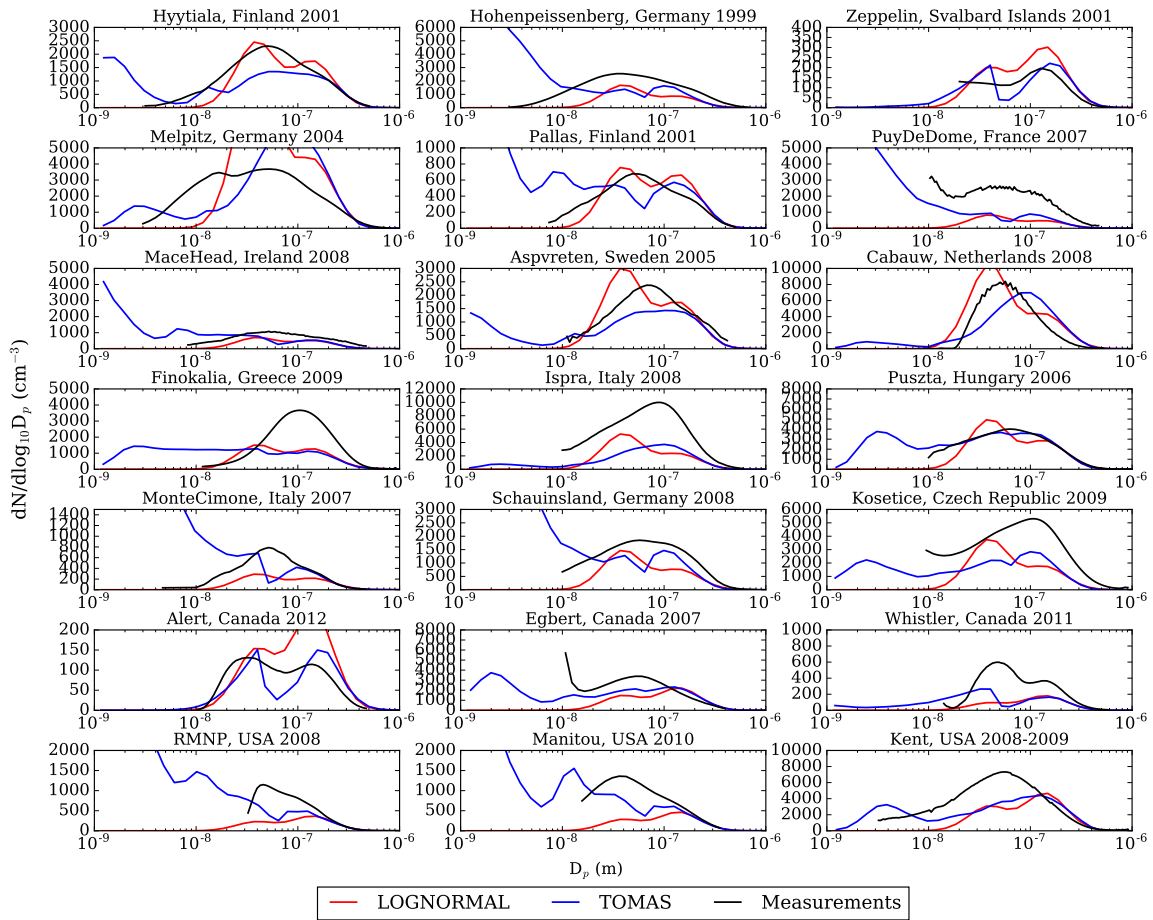


Figure 5.2: Observed and simulated (TOMAS and LOGNORMAL) aerosol number distributions for the sites described in D’Andrea et al. (2013) and Pierce et al. (2015).

(Pierce et al. (2015) uses a 15-bin versions), GEOS-Chem model updates (D’Andrea et al. (2013) uses version 8.02), and recently updated emissions inventories.

5.3.2 Size-resolved particle number concentration and CDNC

Figure 5.3a shows the simulated global- and annual-mean number size distributions for the *anth_on* and *anth_off* simulations using the three different size- distributions methods. The purpose of including both LOGNORMAL and AVG-TOMAS is to test if the modeled aerosol size distributions are more sensitive to the assumed mapping parameters or to the choice of the prognostic versus prescribed size-distribution approach. The LOGNORMAL distribution method predicts

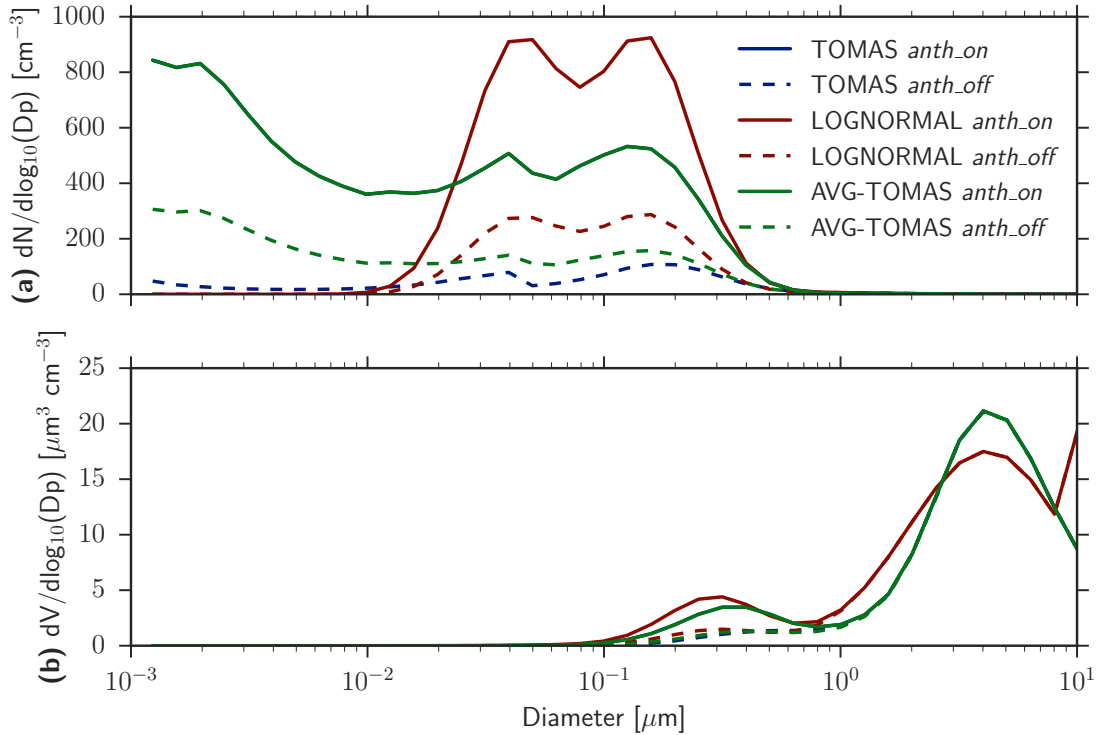


Figure 5.3: Global-mean number and volume size distributions for the simulation with anthropogenic emissions (solid lines) and without anthropogenic emissions (dashed line). The global- and annual-mean AVG-TOMAS *anth_on* simulation is, by definition, identical to the TOMAS distribution, and so lies on top of it.

the most accumulation- mode particles (diameters 20 nm - 150 nm) in both *anth_on* and *anth_off*. By definition, the global- and annual-mean AVG-TOMAS distribution is identical to the TOMAS distribution for *anth_on*; however, the *anth_off* distributions are quite different. In the *anth_off* simulation, we turn off aerosol and gas-phase anthropogenic emissions. The resulting decrease in aerosol sources from nucleation and carbonaceous fossil-fuel emissions (emitted at 30 nm compared to 100 nm for biomass-burning emissions) leads to an increase in the median diameter for accumulation-mode particles in TOMAS in *anth_off* compared to *anth_on*. The shift in median diameter between *anth_on* and *anth_off* is not captured in LOGNORMAL or AVG-TOMAS. The decreased nucleation-mode particle number concentration in TOMAS when anthropogenic emissions are removed demonstrates a substantial contribution of aerosol precursors from anthropogenic emissions; however, this result is likely sensitive to the representation of nucleation in the model

(Section 2). Figure 5.3b shows the corresponding volume distributions for each distribution method. While there are some differences between the magnitude of accumulation and coarse mode volume, the total volume and mass across the size range for all distribution methods is conserved.

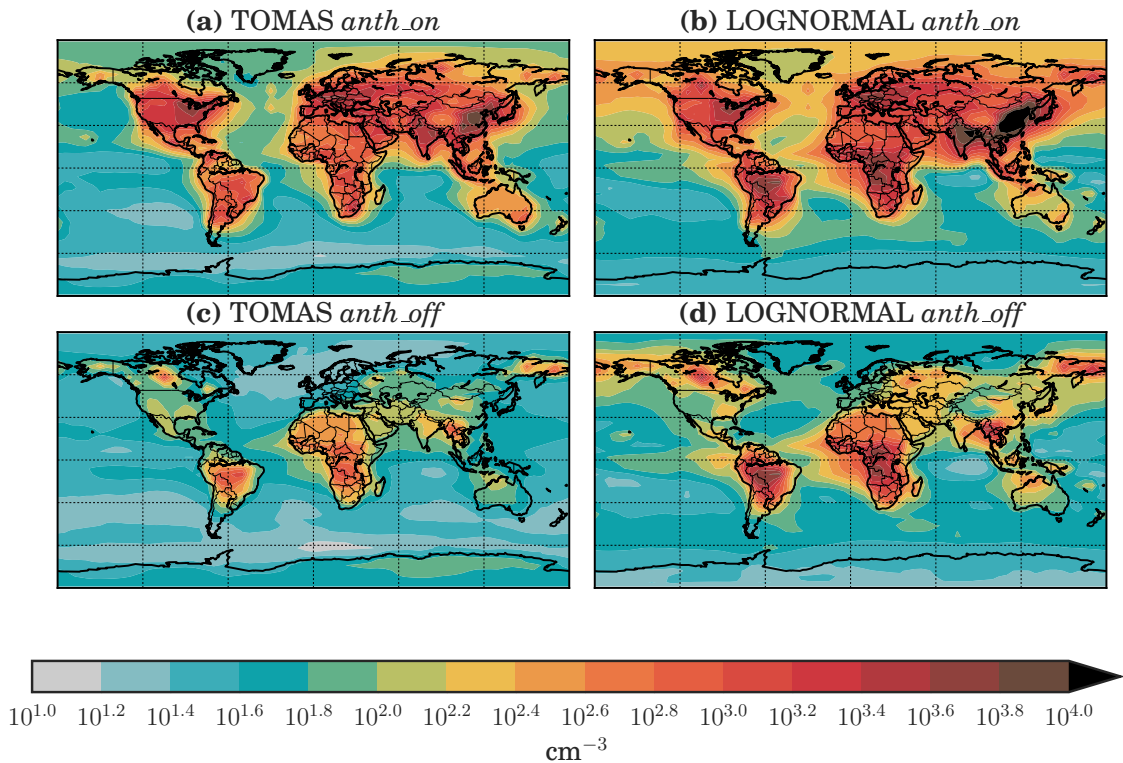


Figure 5.4: Annual mean N40 from the (a) TOMAS *anth_on*, (b) LOGNORMAL *anth_on*, (c) TOMAS *anth_off*, (d) LOGNORMAL *anth_off* simulations.

Maps of N40 concentration for the *anth_on* and *anth_off* simulations using the TOMAS and LOGNORMAL distribution methods are plotted in Figure 5.4. In both size-distribution methods, anthropogenic emissions increase N40 by 1-3 orders of magnitude over most continental regions. The largest increase in N40 occurs in the Northeast United States, Europe, East Asia, and India where anthropogenic emissions dominate particle number concentration. In general, the LOGNORMAL distribution method predicts higher particle number concentrations in the *anth_off* simulation, especially in biomass-burning regions of central South America and Africa, and the boreal regions of Canada and Russia. The reason for this is the larger average particle size in the accumulation

mode in the TOMAS *anth_off* simulation relative LOGNORMAL (see Figure 5.3a). For the same total aerosol mass, the larger accumulation-mode median diameter results in fewer particles. We note that the AVG-TOMAS method also predicts a smaller accumulation-mode median diameter in *anth_off* in the global-mean compared to the TOMAS size distribution (Figure 5.3a).

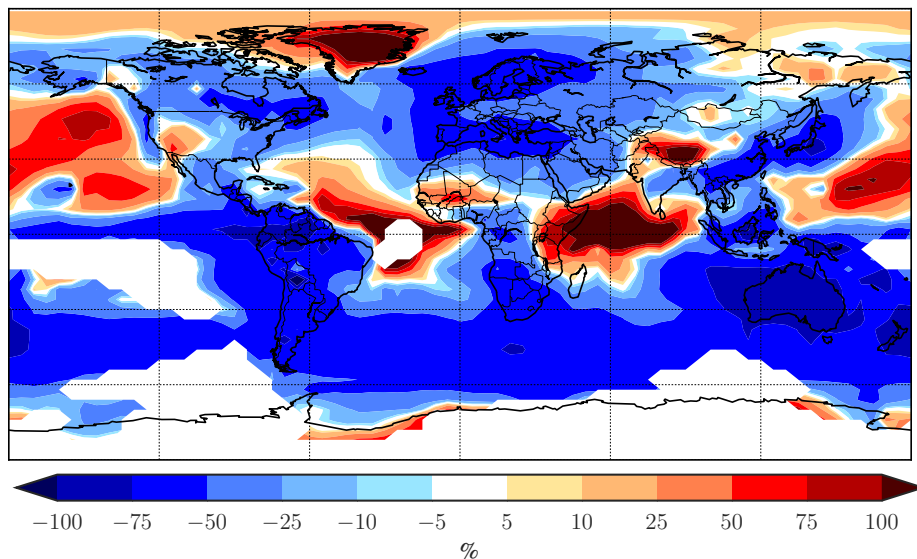


Figure 5.5: The percent change in the relative increase of CDNC from anthropogenic emissions between LOGNORMAL and TOMAS schemes. Red colors show locations where the CDNC increase due to anthropogenic emissions was larger in LOGNORMAL than TOMAS.

The order-of-magnitude increase in N40 due to anthropogenic emissions, results in large CDNC increases, notably over northern-hemisphere land masses where anthropogenic emissions dominate particle number concentration. Figure 5.5 shows the percent difference in relative increase in CDNC ($anth_{on} - anth_{off}$ relative $anth_{off}$) between LOGNORMAL and TOMAS distribution methods. Put differently, this is the percent difference between LOGNORMAL and TOMAS in the relative change in CDNC from anthropogenic sources. Despite generally higher accumulation-mode particle concentrations (Figure 5.3) and N40 concentrations (Figure 5.4), the LOGNORMAL distribution method tends to predict a smaller relative increase in CDNC from anthropogenic sources than TOMAS over most land masses. This is a result of lower baseline (*anth_off*) CDNC in TOMAS

leading to a larger percent increase in CDNC when anthropogenic emissions are included. In Europe, South and East Asia, and South America, the LOGNORMAL distribution method predicts 50 to 75% smaller relative changes in CDNC from anthropogenic aerosols than TOMAS. The LOGNORMAL distribution method predicts relatively more CDNC in the Pacific ocean, equatorial Atlantic ocean, Indian ocean, and Himalayan region. We discuss the cause of these differences in the next section.

5.3.3 Aerosol cloud-albedo effect

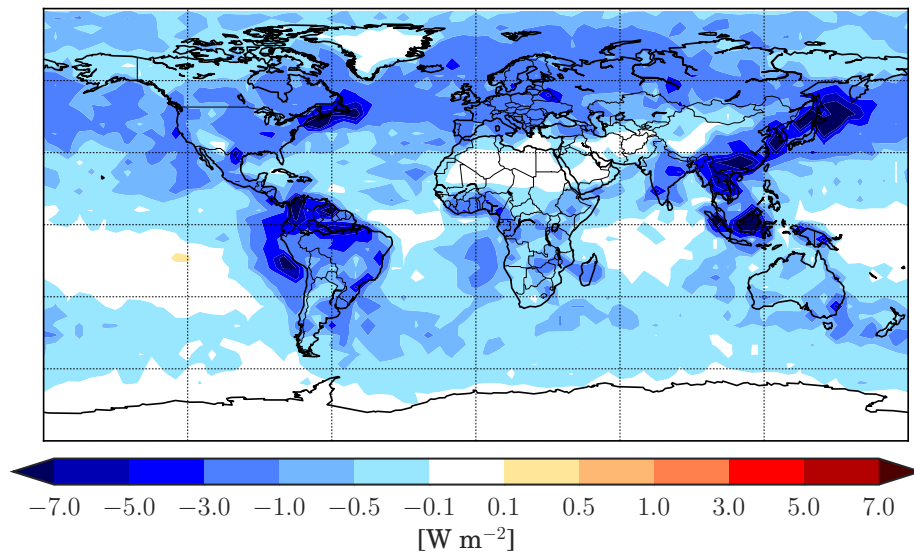


Figure 5.6: Annual mean aerosol cloud-albedo effect due to anthropogenic emissions in the TOMAS scheme.

Figure 5.6 shows the annual-mean CAE from anthropogenic emissions using the TOMAS size-distribution method. We estimate the global-mean CAE from anthropogenic emissions to be -0.87 W m^{-2} . This estimate is within the range of estimates of the cloud-albedo radiative forcing (relative to a pre-industrial time period) reported in the IPCC 4th assessment report (-0.4 to -1.8 W m^{-2}) (Forster et al., 2007). Though, we note again that we are estimating the radiative effect from anthropogenic emissions not the radiative forcing relative to a specific time period, and so there

are important differences between our estimates and those reported. In the heavily polluted regions of East and South Asia, South America, and Northeast United States the CAE exceeds -7 W m^{-2} . Throughout much of Europe, Russia, and North America the anthropogenic CAE is between -1.0 to -3.0 W m^{-2} . The magnitude of the CAE is generally lower in the Southern Hemisphere due to a lower magnitude of anthropogenic emissions (and relatively higher contribution of natural sources to the total aerosol burden).

Table 5.3: Summary of the CAE from the three size-distribution schemes.

Simulation	Global-mean CAE [W m^{-2}]	Absolute difference (Simulation-TOMAS) [W m^{-2}]	Root Mean Square Difference [W m^{-2}]
TOMAS	-0.87	–	–
LOGNORMAL	-0.66	+0.21	0.80
AVG-TOMAS	-0.66	+0.21	0.69

The global-mean anthropogenic CAE from TOMAS (-0.87 W m^{-2}), LOGNORMAL (-0.66 W m^{-2}), and AVG-TOMAS (-0.66 W m^{-2}) are reported in Table 5.3 along with the absolute difference and root-mean-square difference between the two prescribed-distribution schemes and TOMAS. Both the LOGNORMAL and AVG-TOMAS size-distribution methods predict an anthropogenic CAE 0.21 W m^{-2} more positive (less cooling tendency) in the global mean than the TOMAS size-distribution method. Figure 5.7 shows maps of the absolute difference between the anthropogenic CAE calculated with the **(a)** LOGNORMAL and **(b)** AVG-TOMAS size-distribution methods relative the full TOMAS size-distribution method. While in the global mean the TOMAS CAE is more negative than the prescribed-distribution methods, this difference is not consistent regionally. However, the spatial differences between the two prescribed-distribution schemes and TOMAS are very similar to each other even though the prescribed distributions were different between these schemes. This is caused by microphysical processes in TOMAS altering the average size of accumulation-mode particles, leading to large relative differences in CDNC (see Figure 5.5) that are not represented in the LOGNORMAL and AVG-TOMAS methods (discussed in more detail below). The root-mean-square (RMS) reflects the average difference accounting for both the positive and

negative directions. The RMS is greater than the global arithmetic mean radiative effect in both prescribed-distribution methods. The larger RMS for the LOGNORMAL distribution method (0.8 W m^{-2}) demonstrates a larger deviation (accounting for both the positive and negative directions) from TOMAS than the AVG-TOMAS distribution method (0.69 W m^{-2}).

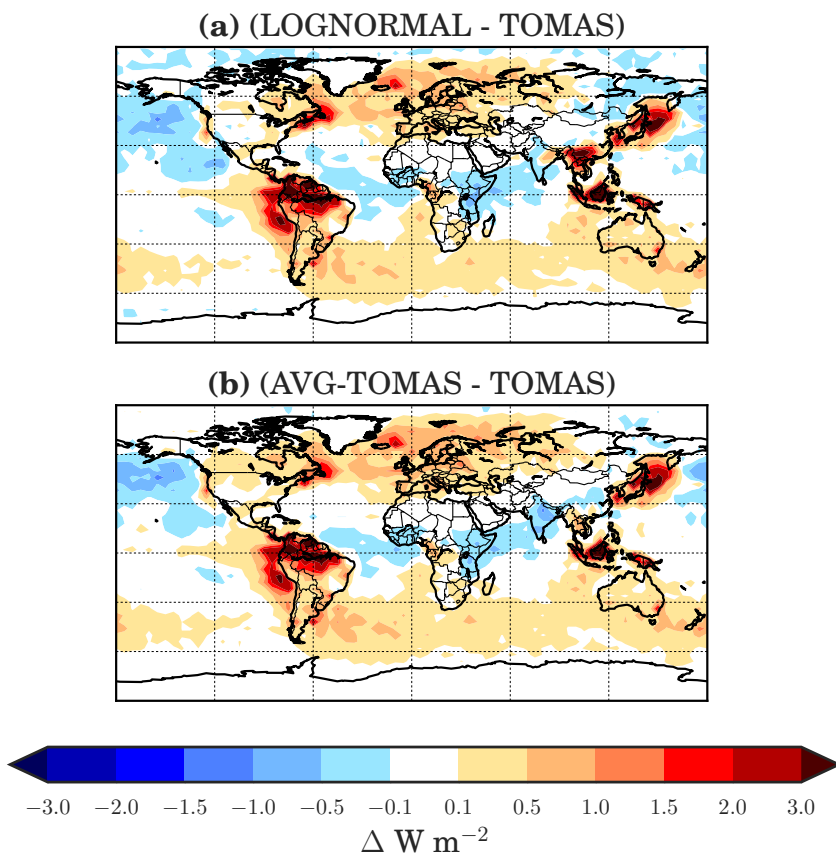


Figure 5.7: Absolute difference in estimated CAE from anthropogenic emissions using the LOGNORMAL scheme (top) and AVG-TOMAS scheme (bottom) relative the TOMAS scheme.

The CAE calculated using the prescribed size-distribution methods is greater than 2 W m^{-2} more positive in South (50-75%) and East Asia (10-25%), South America (50-75%), and the Northeast United States (10-25%) than the CAE calculated using the TOMAS method. The prescribed size-distribution methods also predict a more positive CAE over much of Europe. Conversely, the prescribed size-distribution methods predict a more negative CAE in the north Pacific, equatorial

Atlantic, and over India. The sign of the differences in CAE generally follows the sign of the relative difference in the CDNC changes (Figure 5.5).

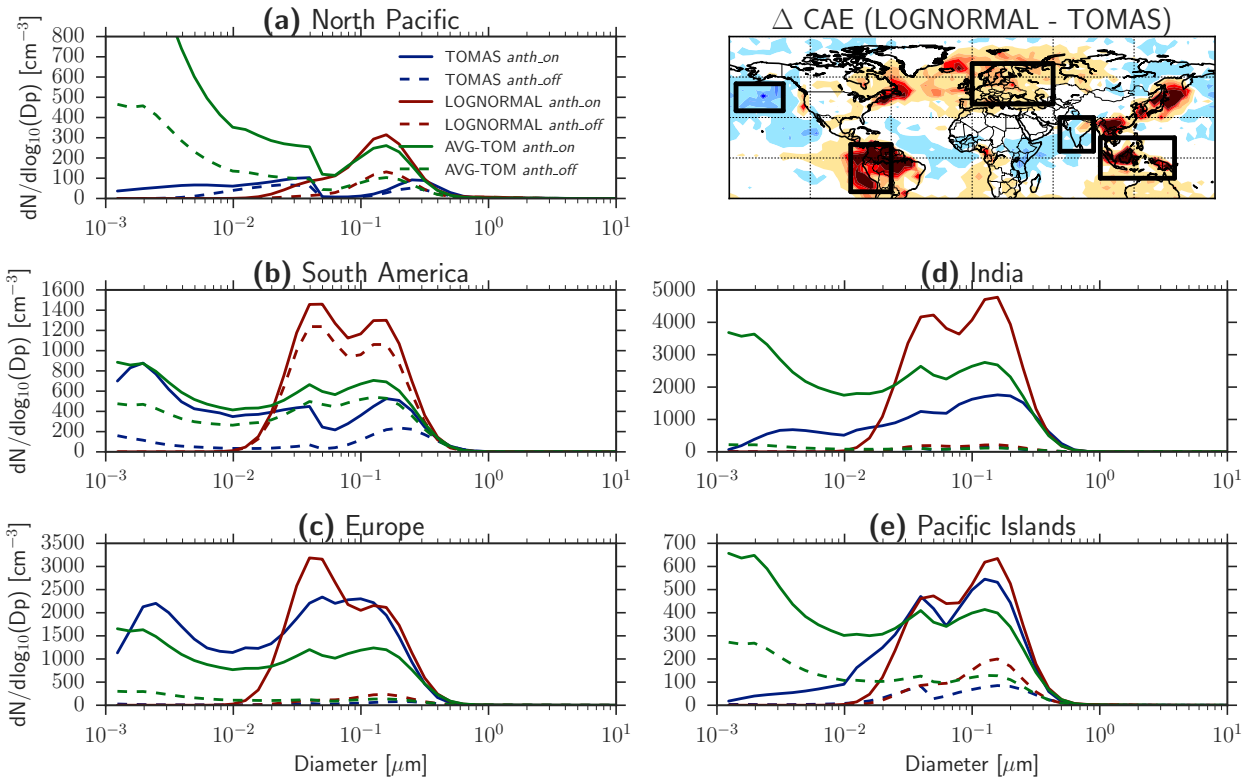


Figure 5.8: Regional size distributions for the *anth_on* (solid lines) and *anth_off* (dashed lines) from the TOMAS, LOGNORMAL, and AVG-TOMAS simulations. Also plotted is a reproduction of the difference in CAE between LOGNORMAL and TOMAS (Figure 5.7) with boxes indicating each respective region that is averaged over to create the size distributions.

To explain the magnitude and sign of regional differences in CAE between the prognostic and prescribed size-distribution methods (Figure 5.8), we plot regional number distributions for *anth_on* (solid) and *anth_off* (dashed) lines for the (a) North Pacific, (b) South America, (c) Europe, (d) India, and (e) Pacific Islands. We also re-plot the difference in LOGNORMAL and TOMAS CAE, adding boxes that define these regions. In the following paragraphs, we discuss the size distributions in each region to explain the simulated differences in CAE. The various emissions and size-dependent processes that dominate in these various regions highlight how assuming prescribed size-distribution shapes can miss potentially important regional changes in CAE.

North Pacific: The TOMAS *anth_on* number distribution produces the "Hoppel gap," characterized by a larger accumulation mode centered around a median diameter of 250 nm, a minimum in the 40-80 nm sizes, and a smaller aitken/nucleation mode (Hoppel et al., 1986). This minimum is a result of in-cloud aqueous SO₄ production shifting particle mass into larger sizes. In the TOMAS scheme, the SO₄ mass from aqueous oxidation results in a larger accumulation-mode median diameter while conserving particle number. Thus, for the *anth_on* simulations, the accumulation mode in the TOMAS simulation has a larger median diameter than the two prescribed size-distribution simulations, LOGNORMAL and AVG-TOMAS.

There is an increase in aerosol mass between going from *anth_off* to *anth_on*, and this increase in mass is the same regardless of size-distribution scheme. On the other hand, the fractional change in aerosol number is not the same between the prognostic TOMAS scheme and the two prescribed size-distribution schemes. For the two prescribed size-distribution simulations, the fractional increase in aerosol number is identical to the fractional increase in aerosol mass as the size of the particles do not change. This is because the change in aerosol composition between the two simulations does not substantially alter its size distribution (the median diameter for each individual species is still held constant). By contrast, for the TOMAS simulations, the increased SO₂ emissions from anthropogenic sources lead to a larger accumulation-mode median diameter in the *anth_on* simulation than in the *anth_off* simulation. Because of this increase in accumulation-mode diameter, the fractional increase in the number of CCN-sized particles between the *anth_on* and *anth_off* simulations is smaller than the fractional increase in mass between *anth_on* and *anth_off* (see Figure 5.5). Thus, the fractional increase in CCN number between *anth_on* and *anth_off* is smaller for the TOMAS simulations than for the two sets of prescribed size-distribution simulations, and this leads to a weaker CAE cooling effect when using the prognostic TOMAS microphysics relative to the prescribed size distributions. The shift in the average size of the CCN-sized particles between *anth_on* and *anth_off* is the key parameter driving the differences between the size-distribution schemes: prescribed size distributions cannot capture this size shift.

South America: Despite lower N40 concentrations in both *anth_on* and *anth_off*, the prognostic TOMAS distribution method has a much larger magnitude (exceeding 3 W m^{-2}) CAE response resulting from a larger relative increase in CDNC than the prescribed size-distribution methods (see Figure 5.4 and Figure 5.5). As in the case for the North Pacific region (above), the change in particle number from anthropogenic emissions in LOGNORMAL and AVG-TOMAS is proportional to the change in aerosol mass between *anth_on* and *anth_off*. However, in the size distributions simulated by TOMAS, particle number increases not only from increased mass from anthropogenic emissions, but also from a decrease in the average particle diameter (the opposite of the North Pacific case). Anthropogenic SO₂ emissions lead to enhanced new-particle formation in TOMAS (evidenced by the mode at 2 nm) in this region, leading to smaller but more numerous particles. In addition, fossil-fuel-combustion sources are emitted in GEOS-Chem-TOMAS at a smaller median diameter (30 nm) than biomass-burning emissions (100 nm), further decreasing the accumulation-mode median diameter simulated by TOMAS in *anth_on* compared to *anth_off* (where biomass burning is an important source). The net result is a larger relative increase in CDNC and thus CAE in TOMAS for the same increase in aerosol mass compared to LOGNORMAL and AVG-TOMAS. We note, however, that this result may be sensitive to nucleation schemes involving organics (shown to be important in equatorial South America in Tröstl et al. (2016)), which are not currently included in GEOS-Chem- TOMAS.

Europe: Despite substantial differences in the nucleation mode, the TOMAS and LOGNORMAL distribution methods predict a similar N40 concentration in the *anth_on* simulation; however, the TOMAS method predicts fewer N40 in *anth_off* due to a reduced contribution of nucleation and condensational growth (also see Figure 5.4). Similar to South America, in TOMAS, the increased nucleation and fossil-fuel-combustion sources in *anth_on* decrease the accumulation-mode median diameter compared to *anth_off*. The lower accumulation-mode median diameter due to anthropogenic emissions in TOMAS leads to a larger relative increase in CDNC and CAE for the same increase in aerosol mass compared to LOGNORMAL and AVG-TOMAS. This same effect drives the difference in CAE in the outflow off the Northeast United States and East Asia.

India: Conversely, over India, the relative increase in CDNC is greater in the LOGNORMAL and AVG-TOMAS schemes (with the exception of central India in the LOGNORMAL scheme), resulting in a stronger anthropogenic CAE. In TOMAS, anthropogenic emissions increase the accumulation-mode median diameter. While anthropogenic emissions do increase new-particle formation, the increase in average particle diameter is likely caused by a large contribution from biofuel emissions, emitted at 100 nm (Kodros et al., 2015), as well as coagulation scavenging of small particles by the large coagulation sink in *anth_on* in this region.

Pacific Islands: Similar to the cases in South America and Europe, the TOMAS distribution method exhibits a smaller accumulation-mode median diameter in *anth_on* compared to *anth_off*, resulting in a larger relative increase in CDNC for the TOMAS simulations than LOGNORMAL and AVG-TOMAS (Figure 5.5). The TOMAS *anth_off* simulation has lower N40 concentrations than LOGNORMAL (Figure 5.4) for the same aerosol mass due to the larger accumulation-mode median diameter (likely caused by aqueous oxidation). As the CAE response to CDNC is nonlinear, with a steeper slope in clean conditions, the low CCN concentration in the TOMAS *anth_off* leads to a strong CAE response compared to the prescribed size distributions.

Each of the regions described differ in how the various size-dependent processes shape the aerosol size distributions in the *anth_off* and *anth_on* simulations. While we are unable to determine if the prognostic TOMAS simulations are predicting these size-dependent processes accurately, especially in the *anth_off* cases, this work highlights that we expect size-dependent processes to behave differently in various regions and under different emissions scenarios, thus leading to diversity in size distributions. Simulations where the size-distribution shape is held fixed (even when different species are allowed to have different size-distribution shapes) fail to capture this diversity, resulting in possible biases in regional and global-mean CAE estimates.

5.4 Conclusions

We explore the sensitivity of the simulated aerosol cloud-albedo effect to different methods of simulating the aerosol size distribution, including a prognostic, sectional aerosol-microphysics

package, TOMAS, and two prescribed size-distribution methods: a mapping based on lognormal modes (LOGNORMAL) and a mapping based on the global- and annual-mean TOMAS distribution (AVG-TOMAS). The prescribed size-distribution methods are representative of methods used in models that track only bulk aerosol mass (and so do not predict aerosol size). We compare the prescribed size-distribution methods to the prognostic TOMAS scheme in order to explore the differences in the CAE that arise in models that track only bulk aerosol mass and prescribe the shape of the aerosol size distribution as opposed to a microphysical model where the median diameter of aerosol species is not held fixed. While the LOGNORMAL method is used in several past studies, we include the AVG-TOMAS method to explore how sensitive the CAE is to the shape of the prescribed aerosol size distribution. We find that the prognostic TOMAS distribution method predicts a larger increase in cloud albedo due to anthropogenic emissions than the prescribed size-distribution methods. The global-mean absolute difference in CAE between the prognostic and prescribed distribution methods is 0.2 W m^{-2} ; however, regional differences can exceed 3.0 W m^{-2} , notably in South Asia and South America.

The driver of these differences are changes in the average size of CCN-sized particles caused by changes to emissions and microphysical processes between the *anth_off* and *anth_on* simulations. The size-distribution changes are explicitly simulated in TOMAS, but cannot be captured in the simulations with assumed size distributions (LOGNORMAL, AVG-TOMAS). While it is possible for the average size of CCN particles to shift in the prescribed size-distribution methods due to changes in simulated aerosol composition (because the mapping parameters differ for each species), the change in composition between *anth_on* and *anth_off* did not result in a substantial shift in the median diameter of the total number distribution. Over most land masses, the prognostic TOMAS method predicts a decrease in the median diameter of accumulation-mode particles between *anth_on* and *anth_off* as a result of increased anthropogenic combustion sources and increased nucleation rates. This leads to a fractional increase in CCN-sized particles between *anth_on* and *anth_off* that is greater than that in the prescribed size-distribution methods. As in Mann et al. (2012) and Bellouin et al. (2013), discrepancies in representation of aqueous oxidation lead to substantial

differences in aerosol number concentrations in oceanic regions. Over the Pacific Ocean, the TOMAS method predicts an increase in particle size in *anth_on* compared to *anth_off* as a result of aqueous oxidation, and thus the opposite effect. Altering accumulation-mode median diameter is especially important in the *anth_off* simulations. As the response of cloud reflectivity to CDNC (cloud susceptibility) is strongly nonlinear, the CAE is perhaps more sensitive to changes in the baseline (*anth_off*) simulation. This result generally agrees with past studies showing a strong sensitivity of the cloud-aerosol forcing to pre-industrial aerosol concentrations (e.g., Carslaw et al., 2013; Hoose et al., 2009).

While the prognostic TOMAS size-distribution method generally agrees better with present-day aerosol size-distribution observations than the LOGNORMAL method, our comparison is limited both spatially and temporally, and it should not be considered a full model evaluation. Our main purpose in making this comparison is to demonstrate that both the prognostic and prescribed size-distribution methods predict realistic present-day concentrations of CCN sized particles (N40 in Figure 5.1); however, the shape of the aerosol size distributions may be different between *anth_on* and *anth_off* simulations with prognostic microphysical processes, resulting in large discrepancies in the change in CDNC and CAE. While present-day aerosol size-distribution parameters can be tuned to generally match aerosol-number observations, fundamental changes to the size distribution by processes such as nucleation, wet deposition, aqueous oxidation, condensation, and coagulation in non-present-day simulations cannot be constrained by observations and therefore require a model to simulate.

A common feature in the past several IPCC reports is the large uncertainty range in the aerosol indirect forcing. While complex aerosol microphysics models increase computational burden and add more uncertain parameters, they are necessary to capturing physical and chemical processes that alter particle number concentration. Our work highlights that size-dependent aerosol processes lead to regional variations in size distributions that simple, prescribed size-distribution assumptions (even allowing for diversity in size distributions between species) do not capture. Furthermore, size-dependent aerosol processes may change in time as aerosol-precursor and primary-aerosol

emissions change, which leads to differences in cloud-albedo CAE estimates between simulations with prognostic aerosol size distributions compared to simulations with prescribed size-distribution shapes. Thus, while adding aerosol microphysics to climate models adds complexity, lack of aerosol microphysics in climate models may lead to substantial errors and biases in estimating aerosol cloud forcings.

In this study, we focus on regional differences between prognostic and globally prescribed aerosol size distributions and the CAE from anthropogenic emissions. One possible area of future study is to map aerosol mass onto regional GEOS-Chem-TOMAS size distributions (as opposed to global-mean size distributions), thus further isolating the impacts of perturbed emissions and microphysical processes from regional variations in the aerosol size distribution.

Chapter 6

Size-resolved mixing state of black carbon in the Canadian high Arctic and implications for simulated direct radiative effect⁵

Transport of anthropogenic aerosol into the Arctic in the spring months has the potential to affect regional climate; however, modeling estimates of the aerosol direct radiative effect (DRE) are sensitive to uncertainties in the mixing state of black carbon (BC). A common approach in previous modeling studies is to assume an entirely external mixture (all primarily scattering species are in separate particles from BC) or internal mixture (all primarily scattering species are mixed in the same particles as BC). To provide constraints on the size-resolved mixing state of BC, we use airborne Single Particle Soot Photometer (SP2) and Ultra-High Sensitivity Aerosol Spectrometer (UHSAS) measurements from the Alfred Wegener Institute (AWI) POLAR6 flights from the NETCARE/PAMARCMIP2015 campaign to estimate coating thickness as a function of refractory BC (rBC) core diameter as well as the fraction of particles containing rBC in the springtime Canadian high Arctic. For rBC core diameters in the range of 140 to 220 nm, we find average coating thicknesses of approximately 45 to 40 nm, respectively, resulting in ratios of total particle diameter to rBC core diameters ranging from 1.6 to 1.4. For total particle diameters ranging from 175 to 730 nm, rBC-containing particle number fractions range from 16 to 3%, respectively. We combine the observed mixing-state constraints with simulated size-resolved aerosol mass and number distributions from GEOS-Chem-TOMAS to estimate the DRE with observed bounds on mixing state as opposed to assuming an entirely external or internal mixture. We find that the pan-Arctic average springtime DRE ranges from -1.65 W m^{-2} to -1.34 W m^{-2} when assuming

⁵This Chapter is in review as: Kodros, J. K., Hanna, S., Bertram, A., Leaitch, W. R., Schulz, H., Herber, A., Zanatta, M., Burkart, J., Willis, M., Abbatt, J. P. D. and Pierce, J. R.: Size-resolved mixing state of black carbon in the Canadian high Arctic and implications for simulated direct radiative effect, *Atmos. Chem. Phys. Discuss.*, 1-32, doi:10.5194/acp-2018-171, 2018.

entirely externally or internally mixed BC. Using the observed mixing-state constraints, we find the DRE is 0.05 W m^{-2} and 0.19 W m^{-2} less negative than the external mixing-state assumption when constraining by coating thickness of the mixed particles and by BC-containing particle number fraction, respectively. The difference between these methods is due to an underestimation of BC mass fraction in the springtime Arctic in GEOS-Chem-TOMAS compared to POLAR6 observations. Measurements of mixing state provide important constraints for model estimates of DRE.

6.1 Introduction

Over the last several decades, the Arctic has warmed at near twice the rate of the global mean (Boucher et al., 2013). In addition to CO_2 , short-lived climate forcers (such as black carbon and methane) may contribute to this increased rate of warming (Arctic Monitoring and Assessment Programme, 2015). Black carbon (BC), in particular, may be an efficient warming agent in the Arctic as its potential to decrease planetary albedo is magnified when BC is above a white surface, such as snow (e.g., Bond et al., 2013). BC can affect climate through aerosol-radiation interactions (e.g. the direct radiative effect, semi-direct radiative effect) or through aerosol-cloud interactions (e.g. the cloud-albedo indirect effect) (Boucher et al., 2013). The magnitude to which BC warms an atmospheric column through aerosol-radiation interactions is strongly sensitive to atmospheric concentration, altitude, and chemical mixing state (Bond et al., 2013). In this work, we focus on the mixing state of BC.

The population (or chemical) mixing state of BC refers to the degree in which BC particles are mixed with other aerosol species. In global and regional models where population mixing state is not explicitly tracked, BC is commonly represented as completely externally mixed (separate from other aerosol species) or a completely internally mixed (mixed together with other aerosol species). For BC mass in a given particle size range, the external mixture assumes the BC mass is divided up into particles of the same size as the non-BC particles. Conversely, in the internal mixture, the same BC mass is divided up into a relatively larger number of particles with smaller BC diameters such that the total mixed particle has the representative diameter of the size range. In a full internal

mixture, BC mass is spread among all particles. For a given BC mass, the internal mixing-state assumption will produce more absorption as the BC mass is spread amongst more particles giving rise to greater surface area and thicker coatings (Bond and Bergstrom, 2006; Seinfeld and Pandis, 2012). However, in the atmosphere, BC is often not mixed entirely as an internal or external mixture. For instance, Massoli et al. (2015) found that 35% of the total non-refractory submicrometer mass is associated with BC-containing particles in coastal California during the CALNEX campaign, and recent studies of the Arctic aerosol suggest a smaller percentage of the aerosol particles contain BC (e.g., Raatikainen et al., 2015; Sharma et al., 2017). Thus, the assumption in aerosol models of a full internal or external mixture may lead to over- or under-estimates of BC absorption.

A second component of BC mixing state is the morphological mixing state. The morphological mixing state refers to the distribution of chemical species within a particle, as well as the shape and location of BC within the aerosol particle. A common assumption for the morphological mixing state of BC is that the BC mass forms the core of a particle and the hydrophilic aerosol mass forms a shell around the particle (Bond et al., 2006; Lack and Cappa, 2010). The scattering component of the shell acts as a lens to focus more photons onto the core, thus increasing absorption (Bohren and Huffman, 1983; Bond et al., 2006). However, the degree of absorption enhancement is a strong function of the core diameter and shell thickness. Theoretical calculations (known as “core-shell Mie theory”) and laboratory studies have estimated enhancements in absorption for a given BC mass of a factor of 1.3 to 2 (Schnaiter et al., 2003, 2005; R. Zhang et al., 2008). Based on these findings, Bond et al. (2006) recommends scaling BC absorption by a factor of 1.5 to account for the “lensing” effect in models that do not assume internal aerosol mixtures. However, field campaigns have found a wider variation of absorption enhancements. While finding that 20-30% of BC particles had acquired a thick coating, McMeeking et al. (2011) and Subramanian et al. (2010) did not find a dependence of mass absorption cross section with coating. Similarly, Cappa et al. (2012) found an absorption enhancement of only 6%, and speculated that the BC may not be at the exact center of the particle. Conversely, Q. Wang et al. (2014) found an absorption enhancement of 1.8 in China, similar to laboratory findings. In addition, Sharma et al. (2017) found values of mass absorption

cross section to increase with coating thickness with a steeper slope than theoretical calculations. Thus, accurate model estimates of BC absorption must rely on an understanding of sources of BC as well as all other aerosol components.

Aerosol number and mass concentrations in the Arctic have a strong seasonal cycle, with contributions from anthropogenic sources leading to a peak in accumulation-mode aerosol mass in the winter and spring (e.g., Croft et al., 2016b; Quinn et al., 2007). Efficient wet removal in the summer results in conditions that favor new particle formation and nucleation-mode aerosol (e.g., Browse et al., 2012; Croft et al., 2016a,b; Garrett et al., 2011; Leaitch et al., 2013; Tunved et al., 2013; Willis et al., 2016). As there is little or no solar irradiance in the Arctic winter, it is essential to accurately simulate aerosol optical properties in the spring. Sources of BC in the Arctic include gas flaring and biomass burning; however, much of the atmospheric BC concentration is transported from lower latitudes (Xu et al., 2017, Schulz et al., in prep). Using a combination of observations and a chemical transport model, (Xu et al., 2017) found that in the Arctic spring much of the BC concentrations at higher elevations arrived from South Asia, while at lower elevations BC concentrations were transported from Asia and Eastern Europe. Sources of non-BC particles to the Arctic include direct marine sources, new particle formation from natural or possibly anthropogenic precursors, and transport from lower latitudes (e.g., Croft et al., 2016b; Wentworth et al., 2016; Willis et al., 2016).

Despite the dependence of aerosol absorption on BC mixing state, measurements of mixing state in the Arctic are limited. The Single Particle Soot Photometer (SP2) provides direct measurements of size-resolved refractory BC (rBC) mass for particle diameters in the range of approximately 75-700 nm. In addition, by the leading-edge fit method (Gao et al., 2007), the SP2 can provide estimates of coating thickness on rBC particles. Combining the size-resolved coated rBC measurements with a total aerosol size distribution provides information on the fraction of total aerosol number containing rBC, thus providing a constraint on the population mixing state of rBC. Raatikainen et al. (2015) measured rBC mixing state properties with an SP2 in the Finnish Arctic winter, finding 24% of particles contain rBC with an average total particle to refractory rBC core diameter of 2.

Similarly, Liu et al. (2015) found an average total particle to rBC core diameter of 2.25 (1.7 - 2.8) during aircraft campaign in the European Arctic in March. For biomass burning plumes, Kondo et al. (2011) measured a ratio of 1.3-1.6 during aircraft flights in the spring and summer in the Canadian Arctic. Finally, Sharma et al. (2017) found a ratio of 1.4-1.25 at the Alert ground station in spring of 2012.

In this study, we present measurements of BC mixing state aboard the Alfred Wegener Institute (AWI) POLAR6 flights, as part of the Network on Climate and Aerosols: Addressing Key Uncertainties in Remote Canadian Environments (NETCARE) and Polar Airborne Measurements and Arctic Regional Climate Model Simulation Project (PAMARCMiP). We use these measurements as constraints on simulated aerosol mass and number concentrations to estimate the direct radiative effect (DRE) in the springtime Arctic, and compare these estimates to the DRE calculated using bounding cases of completely external or internal mixing state-assumptions. While this study focuses on the DRE, we note that other aerosol-radiation interaction processes, such as the semi-direct effect, may also depend on BC mixing state. In Sections 2.1-2.3, we present the POLAR6 flight paths and size-resolved aerosol measurement setup. In Section 2.4, we discuss the chemical-transport model and assumptions in the calculation of the DRE. In Section 3, we present observations of BC mixing state and implications for simulated DRE. We share our conclusions and study limitations in Section 4.

6.2 Methods

6.2.1 Flight overview and sample locations

As part of the Network on Climate and Aerosols: Addressing Key Uncertainties in Remote Canadian Environments project (NETCARE, <http://www.netcare-project.ca>), and in collaboration with the Polar Airborne Measurements and Arctic Regional Climate Model Simulation Project (PAMARCMiP) (Herber et al., 2012), measurements of aerosol, trace gases and meteorological parameters were made in High Arctic spring aboard the Alfred Wegener Institute (AWI) Polar 6 aircraft, a DC-3 aircraft converted to a Basler BT-67 (Herber et al., 2008). Measurements on

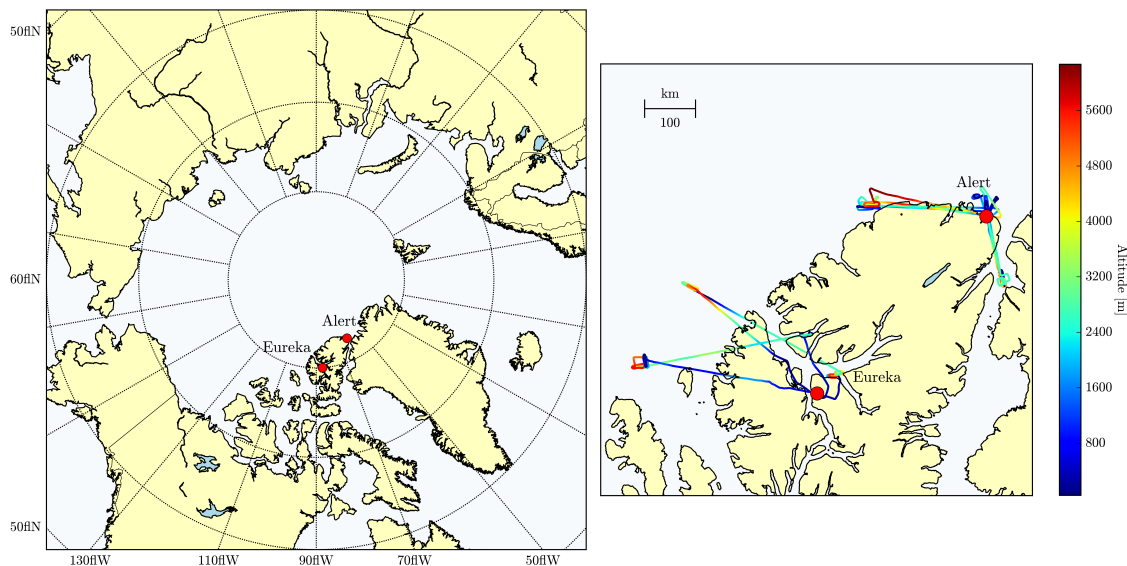


Figure 6.1: Map showing the location of Alert and Eureka as well as the flight paths for the six flights in the Canadian High Arctic portion of the POLAR6 campaign. The flights were undertaken between the 7th and 13th of April 2015.

a total of 10 flights took place from 4 – 22 April 2015 based at four stations: Longyearbyen, Svalbard (78.2°N, 15.6°E); Alert, Nunavut, Canada (82.5°N, 62.3°W); Eureka, Nunavut, Canada (80.0°N, 85.9°W); and Inuvik, Northwest Territories, Canada (68.4°N, 133.7°W). Polar 6 allowed measurements from 60 – 6000 m, with a survey speed of $\sim 75 \text{ m s}^{-1}$ ($\sim 270 \text{ km h}^{-1}$) with ascent and descent rates of $\sim 150 \text{ m min}^{-1}$. This study uses observations from flights conducted at Alert and Eureka, between 7 – 13 April 2015. Table 6.1 presents the date, departure location, and total flight time for the six flights used here. Flight tracks are shown in the map in Figure 6.1.

Aerosol was sampled near-isokinetically through a stainless steel shrouded diffuser inlet, located ahead of the engines. The inlet provided near unity transmission of particles 20 nm to $\sim 1 \mu\text{m}$ in diameter at typical survey airspeeds, corresponding to a total flow rate of $\sim 55 \text{ L min}^{-1}$. Bypass lines off the main inlet, at angles less than 90° , carried aerosol to various instruments described in Section 2.2 and 2.3. Aerosol was not actively dried prior to sampling; however, the temperature in the inlet line within the aircraft cabin was $>15 \text{ }^\circ\text{C}$ warmer than the ambient temperature so that the relative humidity decreased significantly.

Table 6.1: Time, location, and duration of the portion of POLAR6 flights used in this study and shown in Figure 6.1.

Period	Flight	Date	Takeoff/Landing location	Takeoff (UTC)	Landing (UTC)	Flight Time
Spring, 2015	2	7.4.2015	Alert (82.5° N, 62.3° W)	16:31:57	20:48:12	4:16:15
	3	8.4.2015	Alert (82.5° N, 62.3° W)	13:51:19	16:43:44	2:52:25
	4	8.4.2015	Alert (82.5° N, 62.3° W)	17:53:04	21:22:43	3:29:39
	5	9.4.2015	Alert (82.5° N, 62.3° W)	13:50:12	17:47:34	3:57:22
	6	11.4.2015	Eureka (80.0° N, 85.9° W)	15:57:28	21:16:05	5:18:37
	7	13.4.2015	Eureka (80.0° N, 85.9° W)	15:14:27	20:52:05	5:37:38

Periods when the aircraft was in-cloud were determined using data from a Forward Scattering Spectrometer Cloud Probe (FSSP-100, Droplet Measurement Technologies, Inc). The FSSP is an optical particle counter that detects droplets in the range of 2-50 μm in diameter. Any periods where a signal above noise was registered by the FSSP were determined to be in-cloud times and were removed from the dataset. In total the aircraft was in-cloud for $\sim 0.3\%$ of the flight time.

6.2.2 Measurement of refractory black carbon

6.2.2.1 rBC number vs rBC core diameter

Measurements of refractory black carbon (following the definition in Petzold et al., 2013) were made with a single particle soot photometer (SP2, Droplet Measurement Technologies Inc). The SP2 detects individual particles using an intra-cavity Nd:YAG laser operating at 1064 nm. As particles pass through the laser beam, those that contain a strongly absorbing component at 1064 nm (such as black carbon) are heated to incandescence. Light emitted by the incandescing fraction of the particle is detected by a pair of photomultiplier tubes. The peak amplitude of the thermal radiation emitted by the incandescing particle is proportional to the mass of refractory material in the particle (Moteki and Kondo, 2007; Slowik et al., 2007). In this work, size-selected Aquadag particles (Acheson Industries) were used as an external standard for mass calibration of the SP2. Measured Aquadag mobility diameters were converted to rBC (refractory black carbon) mass using the size-dependent effective densities reported by Gysel et al. (2011). Recent studies have shown that the SP2 is more

sensitive to Aquadag than it is to ambient rBC (Laborde et al., 2012; Moteki et al., 2010). In order to account for this, we have scaled the slopes of the Aquadag-derived calibration curves by a factor of 0.70 ± 0.05 . This scaling factor was derived from Figure 5 in Laborde et al. (2012) which shows the response of the SP2 to Aquadag as well as the response of the SP2 to rBC from diesel exhaust, wood smoke, and ambient particles.

Two single particles soot photometers (referred to as SP2#1 and SP2#2) were used in this study. SP2#1 had a detection range of 0.40 - 323 fg rBC (equivalent to spherical diameters ranging from 75 to 700 nm at an rBC density of 1.8 g cm^{-3} Bond and Bergstrom (2006)), while SP2#2 had a detection range of 0.40 - 9.37 fg rBC (equivalent to spherical diameters ranging from 75 to 220 nm at an rBC density of 1.8 g cm^{-3} Bond and Bergstrom (2006)). SP2#1 was used to measure rBC number, since it had a wider size detection range than SP2#2. SP2#2 was used to determine coating thicknesses as a function of rBC core diameter due to a misalignment of an optical detector needed for coating analysis in SP2#1.

6.2.2.2 rBC coating thickness vs rBC core diameter

As particles pass through the laser beam in the SP2 they elastically scatter light at 1064 nm. For particles that contain rBC, the particle may be heated and begin to vaporize before the scattering intensity reaches the peak value that an unperturbed particle would have reached. In this case, the unperturbed scattering amplitude can be retrieved by fitting the leading edge of the particle's scattering signal as described by Gao et al. (2007). In the leading edge fit method, the center position and width of a Gaussian (which reflects the laser beam profile) are fixed from the scattering profiles of non-incandescing particles collected during the preceding and following hour. The unperturbed peak scattering amplitude for an incandescing particle is then determined by fitting the measured scattering profile up to 5% of the peak scattering intensity using the fixed width and center position and allowing only the amplitude to vary. Fitting the profile only up to 5% of peak elastic scattering intensity allows the unperturbed peak amplitude to be retrieved. For an individual particle the uncertainty in reproducing the unperturbed amplitude is ~70% (~20% uncertainty in optical size) but since this uncertainty is random it does not systematically impact our results.

With the scattering amplitude determined by the leading-edge technique, and the measured rBC core diameter, a core-shell Mie model can be used to determine the optical diameter of the rBC-containing particles. In the Mie model we used a refractive index of $2.26-1.26i$ for rBC (Moteki et al., 2010) and a refractive index of $1.5-0.0i$ for the coating species. The value of $1.5-0.0i$ is appropriate for dry sulfate and sodium chloride (Schwarz et al., 2008a,b).

Although the SP2 can measure individual particle rBC mass down to 0.40 fg (~75 nm VED) the elastic scattering optical detectors can only measure scattering from bare rBC particles with volume-equivalent diameters of ~120 nm or greater. As a result, when rBC cores have a diameter smaller than 120 nm only those cores with significant coatings will produce a measurable elastic scattering signal. Additionally, in practice fewer than 90% of particles with a rBC core diameter of less than 140 nm are successfully assigned a coating. This is because the leading edge fit method uses two detectors to accurately determine the coating thickness. One of these is a two element scattering detector used to determine the position of a particle in the laser beam. With this two element detector, the scattering signal from a particle passing through the laser has a clear notch when it passes the gap between detecting elements and this notch position is used to locate the particle in the beam. In some cases, rBC containing particles may evaporate prior to crossing the notch position and, as a result, their coating thickness cannot be determined. This happens more frequently for smaller particles. As a result of the two caveats discussed above, there is a bias toward thicker coatings for rBC cores < 140 nm. To account for this bias, we calculate minimum, median, and maximum bounding cases for coating thickness for rBC core diameters less than 140 nm. A detailed discussion of the estimation of each case and the resulting impact on the DRE is included in the Supplemental Information (SI, Appendix C). As we do not see a substantial difference in the DRE across the three bounding cases, we focus on the median value for the remainder of this text. The median estimate of coating thickness for rBC core diameters less than 140 nm is taken as the overall median coating thickness across core diameters 140 to 220 nm.

6.2.3 Measurement of total aerosol size distributions

Total aerosol size distributions for particles with diameters in the range of 85 - 1000 nm were measured by an Ultra High Sensitivity Aerosol Spectrometer (UHSAS, Droplet Measurement Technology Inc). The UHSAS is a laser-based aerosol spectrometer in which particles intercept the beam of a Solid-state Nd³⁺:Y LiF₄ laser operating at ~1054 nm. Two sets of Mangin mirrors focus light scattered by the particles onto two detectors; one a high gain avalanche photodiode for detecting particles smaller than 250 nm and the other a low-gain PIN photodiode for detection particles larger than 250 nm. Counting efficiency for the UHSAS is >95% for particle concentrations < 3000 cm⁻³. Further details of the instrument operating principles can be found in Cai et al. (2008). The UHSAS was calibrated in during operations using polystyrene latex spheres (PSLs). Details of the calibration and comparison with other in-flight measurements can be found in Leaitch et al. (2016) as well as Willis et al. (2016) and Burkart et al. (2017). One potential issue with using the UHSAS aboard an aircraft is that, as the pressure changes during ascent and descent, the sample flow at the inlet of the chamber can deviate from the measured and regulated flow at the outlet of the chamber (Brock et al., 2011; Kupc et al., 2018) which can results in inaccurate particle concentration measurements. Brock et al. (2011) saw particle number deviations from a reference counter of ~10-15% on ascent and descent. In this study, comparison to counts of non-incandescent particles from the SP2, which was on the same inlet line, suggest that particle counts deviated by <5%.

6.2.4 Determination of the fraction of total aerosols containing rBC vs aerosol diameter

To determine the fraction of total aerosol particles containing rBC as a function of size, we first determined the size distribution of the rBC-containing particles, this time accounting for both the rBC core diameter and the thickness of any coating material. This was done by taking the coating thicknesses as a function of rBC core size for each flight and applying those coating thicknesses to the measured rBC core sizes from SP2#1. Once the coating thickness were applied to the rBC cores

measured by SP2#1, the particles were then binned according to their total size (core diameter plus 2 times the coating thickness) to give the number distribution for rBC containing particles. The bin increments were set to match the increments from the UHSAS and the fraction of rBC containing particles was calculated for each bin by dividing the number of rBC-containing particles by the number of total aerosols. As with the coating analysis, this process was carried out separately for each flight and the average of all flights were combined with GEOS-Chem-TOMAS simulations.

6.2.5 Model overview

6.2.6 GEOS-Chem-TOMAS

To simulate aerosol concentrations in the Arctic, we use the Goddard Earth Observing System chemical-transport model, GEOS-Chem, version 10.01. We simulate April 2015 with 2 months of spin-up not included in the analysis. Transport in GEOS-Chem is driven by MERRA re-analysis meteorology fields. This version of GEOS-Chem uses a horizontal resolution of 4° latitude by 5° longitude with 47 vertical layers.

Aerosol microphysics is simulated using Two Moment Aerosol Sectional (TOMAS) microphysics scheme (Adams and Seinfeld, 2002) coupled with GEOS-Chem (known as “GEOS-Chem-TOMAS”). The version of TOMAS used in this study includes 40 size bins ranging from diameters of approximately 1 nm to 10 μm (the exact diameter depends on the density of the aerosol). TOMAS includes tracers for sulfate, BC, organic aerosol, sea salt, dust, and aerosol water. In this work, we will use the term “BC” when referring to simulated mass concentration and “rBC” when referring to measurements made with the SP2. Description of aerosol microphysics in TOMAS has been included in Adams and Seinfeld (2002), Y. H. Lee et al. (2013), and Lee and Adams (2012). Croft et al. (2016b) compares aerosol size distributions simulated by GEOS-Chem-TOMAS to observations at Alert, Nunavut and Mt. Zeppelin, Svalbard and includes a description of the settings used here.

Global anthropogenic emissions are derived from The Emissions Database for Global Atmospheric Research (EDGAR) Hemispheric Transport of Air Pollution (HTAP) version 2.2 (Janssens-

Maenhout et al., 2015). Following the recommendation in Xu et al. (2017), we include BC and organic carbon emissions from gas flaring derived from the Evaluating the Climate and Air Quality Impacts of short Lived Pollutants (ECLIPSE) emission inventory (Klimont et al., 2017). Biomass burning emissions are from the The Fire Inventory from NCAR (FINN) for the year 2015 (Wiedinmyer et al., 2011). Dust aerosol emissions follow the DEAD scheme (Zender, 2003), while sea-salt aerosol emissions are based on the scheme of Jaeglé et al. (2011).

6.2.6.1 Direct radiative effect calculation

The all-sky direct radiative effect is estimated using an offline version of the Rapid Radiative Transfer Model for GCMs (RRTMG) (Iacono et al., 2008), following the online version implemented in GEOS-Chem (Heald et al., 2014). RRTMG treats clouds using the Monte Carlo independent column approximation (McICA) (Pincus et al., 2003). Aerosol optical properties are calculated using monthly averaged aerosol mass and number concentrations with refractive indices from the Global Aerosol Dataset (GADS). We use Mie code published in (Bohren and Huffman, 1983) to calculate aerosol optical depth, single scattering albedo, and asymmetry parameter. Available code includes Mie calculations for 2 concentric spheres (for use in core-shell morphologies). The use of monthly mean aerosol and cloud properties is a limitation of this study; however, we feel this is sufficient to explore the impacts of different BC mixing-state assumptions on the DRE.

6.2.6.2 Description of aerosol mixing states

We calculate the DRE with 5 BC mixing states, outlined in Table 6.2. Figure 6.2 is a schematic of the mixing states. We discuss a numerical example at the end of this section that follows Figure 6.2. In the “*external*” mixing state, all BC exists as a separate particle from the other aerosol species (Figure 6.2a). The “*external*1.5*” mixing state multiplies the BC absorption in the “*external*” mixing state by a factor of 1.5 to simulate absorption when BC is mixed internally, following the recommendation in Bond et al. (2006). As the “*external*1.5*” mixing state only modifies the absorption from the “*external*” mixing state, we do not explicitly animate it in Figure 6.2. Conversely to the “*external*” mixing state, the “*allCoreShell*” assumption treats all BC mass in

Table 6.2: Description of BC mixing states.

Mixing State	Description
<i>external</i>	All BC mass in a size range forms a separate particle from the other aerosol species with the same diameter. This mixing-state assumption provides a lower bound on absorption due to altering chemical mixing state.
<i>r_{shell}-constrained</i>	All BC mass in a size range forms the core of a mixed particle with measured rBC volume-equivalent diameter from the SP2. Hydrophilic scattering mass forms a shell around the core with measured shell thickness. Any remaining scattering mass forms a separate particle.
<i>external*1.5</i>	Identical to the <i>external</i> mixing-state assumption, but with BC absorption multiplied by a constant factor of 1.5 to simulate enhanced absorption in an external mixture, following the recommendation in Bond et al. (2006). This mixing-state assumption serves as an approximate “mid” point.
<i>fBC-constrained</i>	Simulated mass and number concentrations in a size range are split into a BC-containing and BC-free particle populations based on the measured rBC-containing particle fraction from the SP2 and UHSAS instruments. In the BC-containing population, core-shell morphologies are formed with diameters calculated based on the average BC mass or scattering mass per particle (calculated from the mass-to-number ratio).
<i>allCoreShell</i>	All BC mass in a size range forms the core of a particle with a concentric scattering shell. The total particle diameter is the sum of the core plus twice the shell thickness (and thus the BC diameter is less than the total diameter). This mixing-state assumption provides an upper bound on absorption due to altering chemical mixing state.

TOMAS output (250 nm size bin):
 0.06 $\mu\text{g m}^{-3}$ of BC mass;
 1.4 $\mu\text{g m}^{-3}$ total aerosol mass
 100 particles cm^{-3}

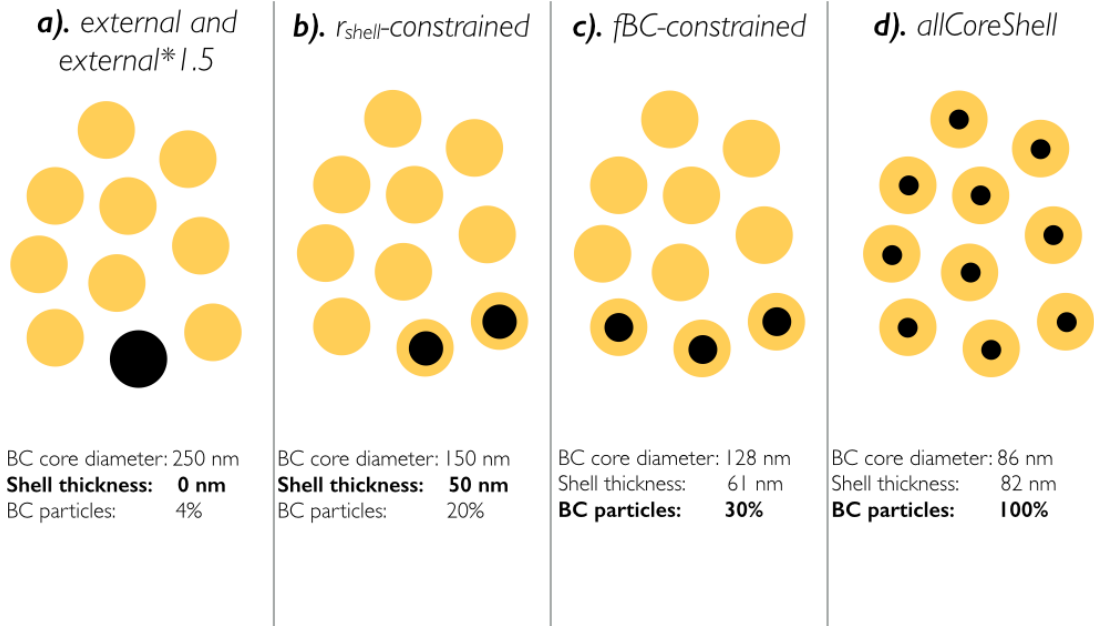


Figure 6.2: Schematic presenting the different BC mixing states for the TOMAS size bin corresponding to particle diameters of 250 nm. The bold text shows the parameter being constrained in each mixing state. In this example, GEOS-Chem-TOMAS simulates 4% BC mass fraction and a particle number concentration of 100 cm^{-3} . In the *external* mixing-state assumption, all BC mass forms separate particles (rounded to 1 particle out of 10 for convenience), while in the *allCoreShell* mixing-state assumption, all BC mass is spread among all particles. The r_{shell} -constrained mixing state uses SP2 measurements of BC core diameter and shell thickness to constrain BC mass. The f_{BC} -constrained mixing state uses BC-containing particle fractions from the SP2 and UHAS as the constraint on mixing state.

each size bin as the core with other hydrophilic species forming a shell around the BC core (Figure 6.2d). The *external* and *allCoreShell* mixing states are bounding cases, assuming that 0 and 100%, respectively, of BC particles are mixed with the other aerosol components. The *external*1.5* mixing state is included as a reference point in between the two bounding cases.

We compare these assumed mixing states to two mixing states based on the measurements described in Sections 2.2-2.3. The “ r_{shell} -constrained” mixing state uses measurements from the SP2 of shell thickness as a function of core diameter to constrain BC mixing state (Figure 6.2b). Across the SP2 size range, we take the total BC mass in a given size bin simulated by TOMAS, and

form BC cores with diameters given by the SP2 measurements. We then take the total scattering mass simulated by TOMAS in the same size bin and form concentric surrounding shells based on the thickness measured by the SP2. Any remaining scattering aerosol mass forms a separate particle with no BC included. Outside of the SP2 size range, we retain the ratio of rBC core diameter to total particle diameter at the lower/upper edge of the SP2 range and apply that to estimate core and shell diameters for the remaining TOMAS size bins. Using the measured rBC core diameter and shell thickness from the SP2, the resulting fraction of BC-containing particles for a given size range can be described by Equation 6.1:

$$f_{BC} = \frac{\left(\frac{M_{BC}}{M_{tot}}\right)}{\left(\frac{\rho_{BC} \frac{4}{3} \pi r_{core}^3}{\rho_{shell} \frac{4}{3} \pi r_{shell}^3 + \rho_{BC} \frac{4}{3} \pi r_{core}^3}\right)} \quad (6.1)$$

Where ρ_{shell} is the density of the shell, r_{shell} is the shell thickness, ρ_{BC} is the density of the BC core, r_{core} is the radius of the core, M_{tot} is the total aerosol mass, and M_{BC} is the mass of BC. The numerator in Equation 6.1 describes the BC mass fraction of the aerosol population for a given size range, while the denominator describes the BC mass fraction for a single aerosol particle. The resulting fraction of BC-containing particles is thus a function of the BC mass fraction as well as the ratio of the BC radius to the total particle radius. In our approach, values for r_{shell} and r_{core} are taken from the SP2 measurements while M_{BC} and M_{tot} are simulated by GEOS-Chem-TOMAS. The *r_{shell}-constrained* BC mixing state will not reproduce the measured fraction of rBC-containing particles unless the ratio of BC and scattering mass is similar to observed with the SP2 and UHSAS.

The second measurement-constrained mixing state, “*f_{BC}-constrained*”, uses the size-dependent fraction of all particles containing rBC as the measurement constraint (Figure 6.2c). In a given size range, we separate total aerosol mass and number (simulated by TOMAS) into a population containing BC and a population not containing BC based on the measured fraction of particles containing BC. We then form BC cores and scattering shells based on the simulated mass-to-number ratio and assumed density for each species. Using the fraction of rBC containing particles measured

with the SP2 and UHSAS, the resulting BC core diameter and shell thickness can be calculated by Equation 6.2 and 6.3:

$$d_{\text{core}} = \left[\frac{M_{\text{BC}}}{f_{\text{BC}} \times N \times \rho_{\text{BC}} \times \frac{\pi}{6}} \right]^{\frac{1}{3}} \quad (6.2)$$

$$r_{\text{shell}} = \frac{d_{\text{tot}} - d_{\text{core}}}{2} \quad (6.3)$$

Where d_{core} is the BC core diameter, f_{BC} is the fraction of BC-containing particles measured with the SP2 and UHSAS, N is the total particle number, and d_{tot} is the total particle diameter in the given TOMAS size bin. Similarly, this method will not produce the measured rBC core diameter and shell thickness unless TOMAS simulates a similar ratio of BC to scattering mass as is observed. For both *r_{shell}-constrained* and *f_{BC}-constrained*, we use the median measured values across all flights (see Appendix C for explanation), and we compare results of the minimum, median, and maximum cases based on the uncertainties in SP2 measurements in the 100-140 nm diameter size range range in the Supplemental Information (Appendix C).

The different mixing states are depicted schematically in Figure 6.2 with the bold text highlighting the parameter being constrained in each case. As an example, we depict the TOMAS size bin for 250 nm diameter particles where GEOS-Chem-TOMAS simulates a particle number concentration of 100 cm⁻³ and a ratio of BC to total-aerosol mass of 4%. In the *external* mixing-state assumption (Figure 6.2a), the 0.06 μg m⁻³ of BC mass is used to form pure BC particles with diameters of 250 nm (by definition, a shell thickness of 0 nm). This results in 4% of the particle number concentration being pure BC particles, while the remaining particles are composed of non-BC species also with diameters of 250 nm (for convenience, 1 out of 10 particles in the schematic depiction of *external* is pure BC). In the *r_{shell}-constrained* mixing state (Figure 6.2b), we use the observed rBC core diameter and corresponding shell thickness from the SP2 measurements (in this example a core of 150 nm and a shell thickness of 50 nm) to allocate the same 0.06 μg m⁻³ BC mass into mixed particles with total diameter 250 nm. As the BC diameter is now only 150 nm, the resulting BC

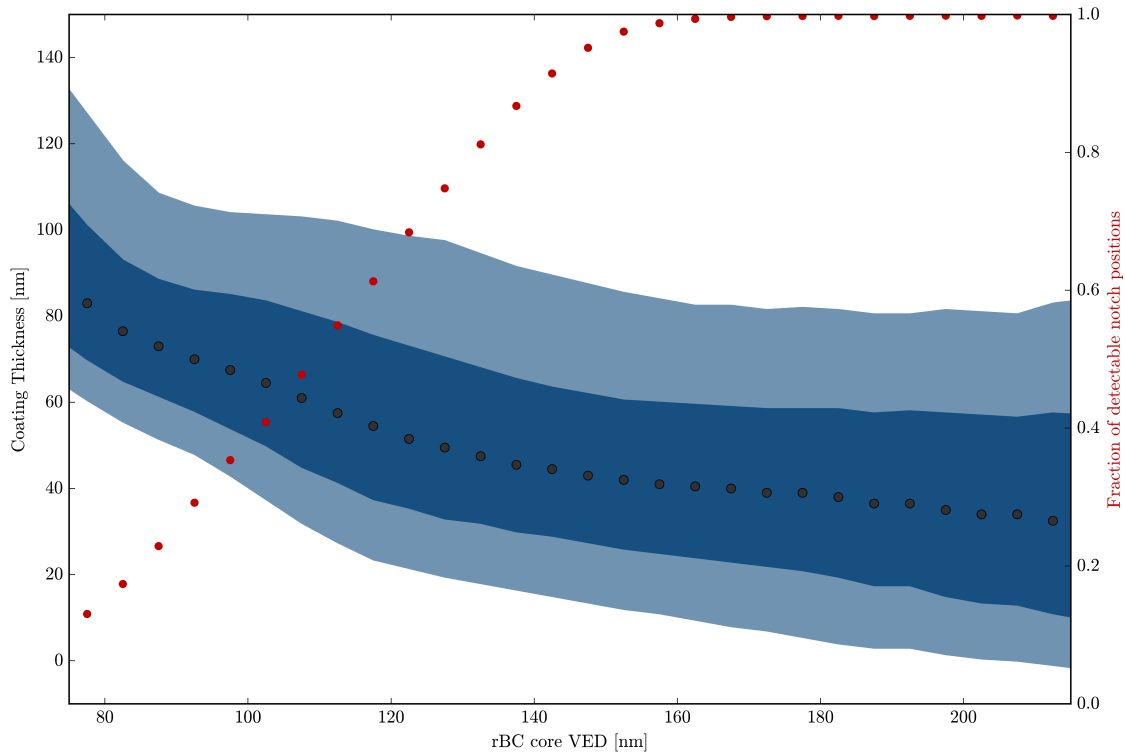


Figure 6.3: Coating thickness as a function of rBC core diameter. Grey markers are the median, dark shaded area is the 25th-75 percentile, lighter shaded area is the 10-90th percentile of coating thicknesses for each bin.

containing particle number fraction is 20%. In the *fBC-constrained* mixing state (Figure 6.2c), we instead constrain by the fraction of rBC-containing particles measured with the SP2 and UHSAS (30% in this example). To allocate the same BC mass onto 30% of particles, the BC core diameter has to equal 128 nm resulting in a shell thickness of 61 nm (to create a particle with total diameter of 250 nm). Finally, to allocate the same BC mass onto all particles in the *allCoreShell* mixing-state assumption (Figure 6.2d), the BC core diameter is further reduced to 86 nm and the shell thickness increased to 82 nm.

6.3 Results

6.3.1 Measurements of coating thickness as a function of rBC core size and fraction of rBC-containing particles

Figure 6.3 shows measured coating thickness as a function of the volume-equivalent diameter (VED) of the rBC cores (both the rBC cores and the coating are assumed to be spherical). The alternate axis gives the fraction of detectable notch positions (see Section 2.2.4 for details). The black dots represent the median and the shaded regions represent the interquartile range and 10th-90th percentile range of measurements for all particles across the different flights and altitudes. For rBC core diameters ranging from 140-220 nm (the region with greater than 90% successful fits), the median measured coating thickness decreases slightly from 45 nm to 40 nm (with an interquartile range of: 30-70 nm to 17-65 nm). This results in total particle to rBC core diameter ratios ranging from 1.6 (IQR: 1.4-2.0) for rBC cores at 140 nm to 1.4 (IQR: 1.2-1.6) for rBC cores at 220 nm. This range is similar to measurements in the Canadian Arctic by Kondo et al. (2011). When combining with model results, we use only the measured core and shell thicknesses in the range with greater than 90% detectable notch positions (i.e. core diameters larger than 140 nm), and use minimum and maximum bounding assumptions in the region 70-140 nm. Figure C.1 shows the minimum and maximum shell thickness across the range 70-700 nm. A detailed examination of vertical variability in rBC measurements from this campaign is included in Schulz et al. (in prep).

Figure 6.4a shows the measured number distributions for uncoated rBC, coated rBC, and total particle number, with sets of symbols representing the average across an individual flight. The diameters of the coated rBC particles represent a sum of the rBC core diameter and twice the shell thickness. The total aerosol size distribution has a mode centered at near 150 nm, similar to measured accumulation-mode particles in the Arctic spring reported in Croft et al. (2016b). The bare rBC size distribution peaks below the 70 nm size limit of the SP2. To estimate the size-resolved fraction of particles containing rBC, we take the ratio of the SP2-coated rBC particles and the UHSAS total particle size distribution (Figure 6.3b). In the median across all flights, we find that

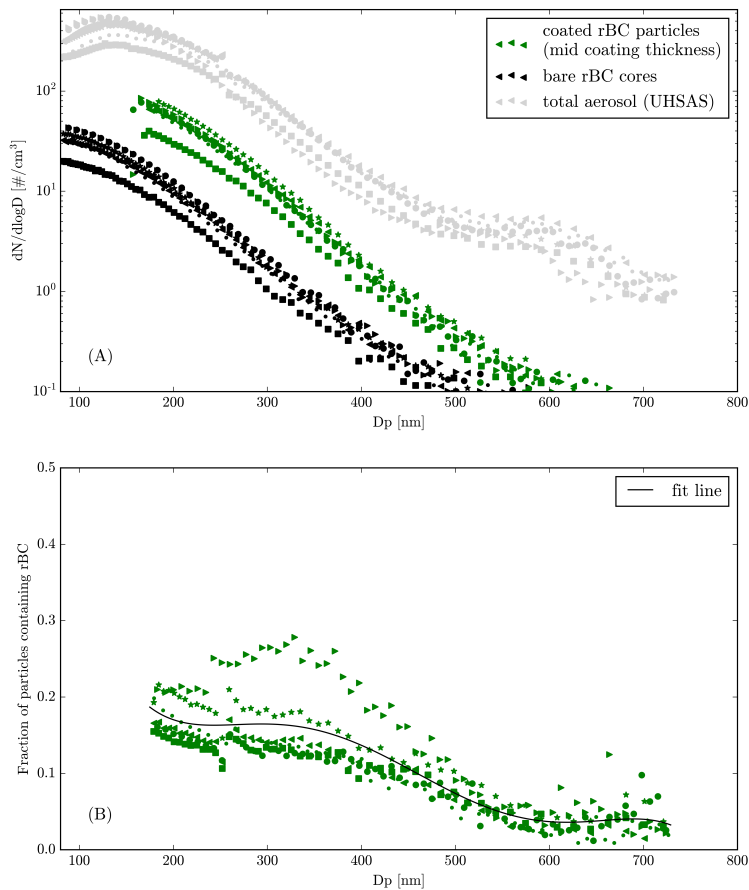


Figure 6.4: Number distributions for the bare rBC cores (black), the coated rBC-containing particles (green), and the total aerosol as detected by the UHSAS (grey) for the median coating thickness scenario. Shown in the bottom panel is the distribution of the fraction of the total aerosol containing rBC in the median coating scenario.

16% of particles in the 175-330 nm diameter size range contain rBC, with values ranging from 10-29%. For particles with diameters ranging between 550-730 nm, this fraction decreases to 3%. This result is similar in magnitude with surface measurements of rBC-containing particle fractions from Sharma et al. (2017) from Alert, Canada. In general, we expect chemically aged plumes to be more internally mixed (through condensation and coagulation). The relatively low fractions of rBC-containing particles measured here may suggest local sources of non-BC accumulation-mode particles, such as sea salt, which is common in April at Alert (e.g., Leaitch et al., 2017), or slow coagulation timescales.

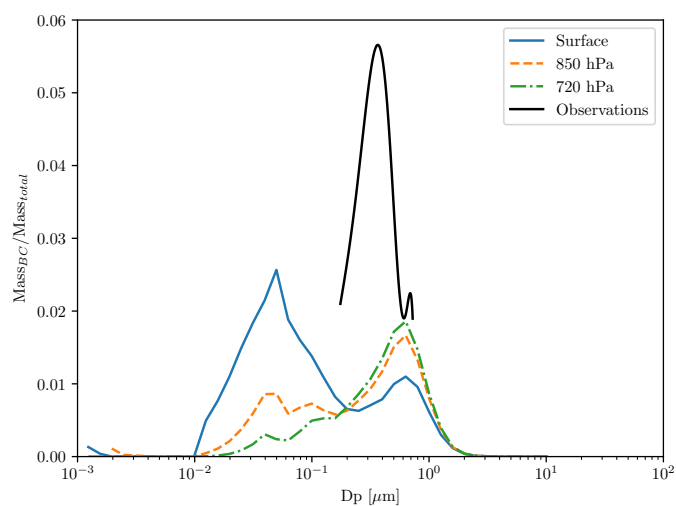


Figure 6.5: The fraction of BC aerosol mass relative total aerosol mass at each size bin in GEOS-Chem-TOMAS at three vertical levels along with the fraction determined from the SP2 and UHSAS observations.

6.3.2 Comparison to model simulations

Figure 6.5 shows the size-resolved fraction of BC mass relative to total aerosol mass based on the ratio of the SP2 to UHSAS compared to GEOS-Chem-TOMAS simulations. Due to instrument constraints, the measured size range is restricted to diameters of 175-730 nm compared to the TOMAS size range of 1 nm to 10 μm . Across the measurement size range, TOMAS predicts a lower BC mass fraction relative to total aerosol mass except at higher altitudes (~ 720 hPa) for diameters of 700 nm. The lower BC mass fraction is a result of both lower BC mass concentrations (consistent with previous studies, e.g., Xu et al., 2017) and higher non-BC mass simulated in GEOS-Chem-TOMAS than observed in the SP2 and UHSAS. In TOMAS, BC mass fraction is greatest at the surface for sub-200 nm diameter particles with a second peak at higher altitudes for particle diameters around 700 nm.

As the ratio of BC mass to total aerosol mass in TOMAS is lower than in measurements, the two different mixing-state constraints ($r_{shell-constrained}$ and $f_{BC-constrained}$) do not converge with the measurements. The effect of this is shown in Figure 6.6. In Figure 6.6a (left panel), we constrain all gridcells in the Arctic to have the measured fraction of BC-containing particles (shown in Figure

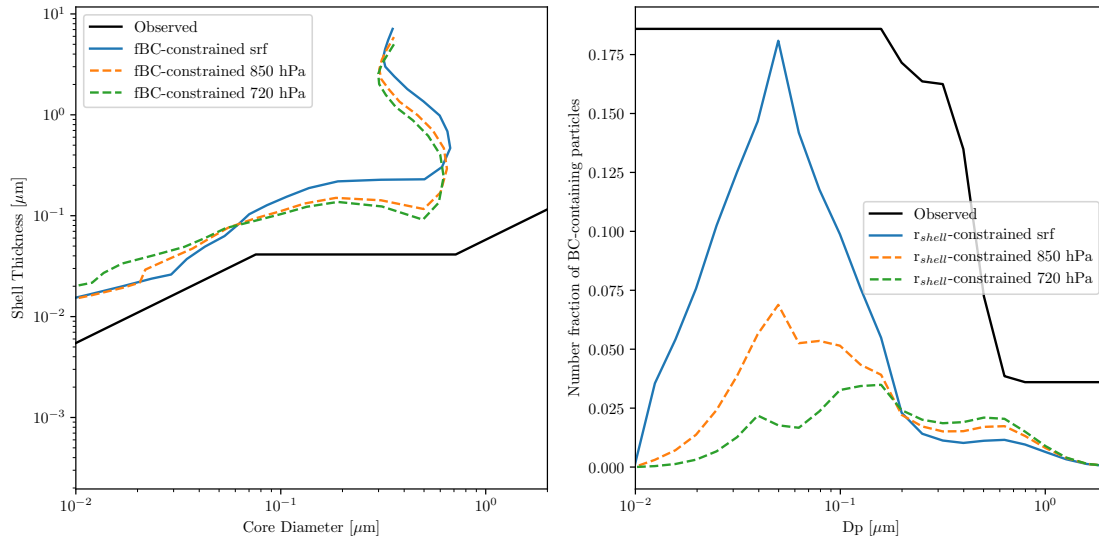


Figure 6.6: The simulated pan-Arctic mean shell thickness as a function of BC core diameter when the number fraction of BC is constrained by observations (left), and the simulated number fraction of BC when shell thickness as a function of core diameter is constrained by observations (right).

6.4b and re-binned to the TOMAS size bins in the black line in Figure 6.6b), and calculate the resulting BC core diameter and shell thickness. The black line in Figure 6.6a presents the measured core diameter and shell thickness for comparison. As the relative BC mass to total aerosol mass in TOMAS is less than observed (Figure 6.5), this results in smaller BC core diameters and larger shell thicknesses. Similarly, in Figure 6.6b, we constrain TOMAS aerosol mass to have the measured BC core diameters and shell thickness (shown in Figure 6.3 and re-binned to TOMAS sizes in the black line in Figure 6.6a), and calculate the resulting fraction of BC-containing particles. The resulting fraction of BC-containing particles for diameters of 200 nm using the *r_{shell}-constrained* method is a factor of 6 less than observed.

6.3.3 Implications for the direct radiative effect

To explore the impact of mixing state on DRE in the Arctic spring, we calculate the DRE due to all aerosol with the bounding mixing-state assumptions and the measurement constraints on mixing state. Figure 6.7 shows the net DRE over the Arctic for April assuming all BC is externally mixed. The pan-Arctic average DRE is -1.65 W m^{-2} , but locally there are regions of opposing sign. Regions

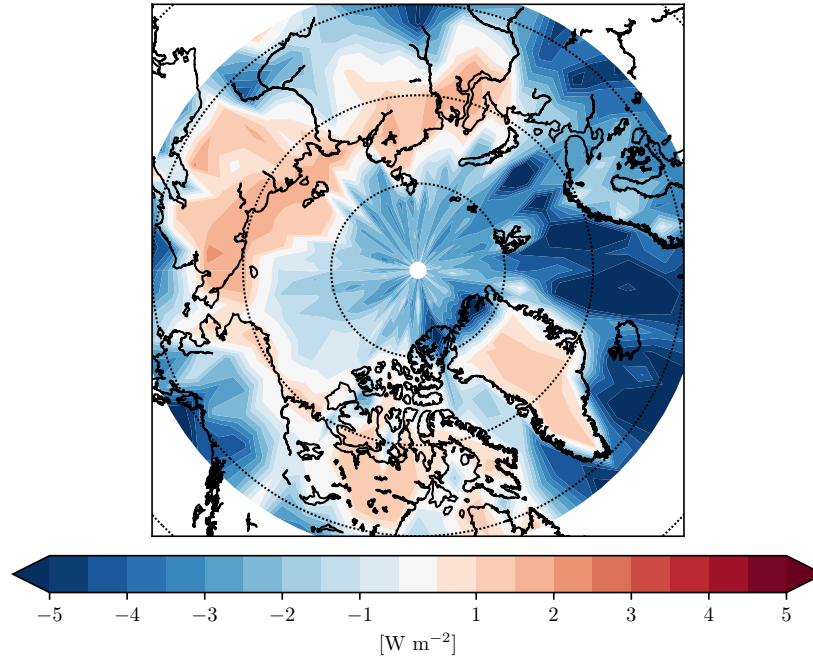


Figure 6.7: The net direct radiative effect over the Arctic in April assuming externally mixed particles.

Table 6.3: The net direct radiative effect (DRE) calculated using each mixing state averaged over the Arctic for April.

Mixing-state assumption	Net DRE (W m^{-2})
<i>external</i>	-1.65
<i>r_{shell}-constrained</i>	-1.59
<i>external*1.5</i>	-1.52
<i>fBC-constrained</i>	-1.45
<i>allCoreShell</i>	-1.34

with a slight positive DRE are over areas where the aerosol mixture is darker than the underlying albedo. This occurs mostly over snow-covered land surfaces as opposed to oceans where the water and sea-ice has a lower albedo and the aerosol mixture is more reflective than the surface. We include a map of monthly mean albedo for the Arctic in April in the SI. We note that this result is likely sensitive to monthly average albedo estimates.

Table 6.3 presents the April, pan-Arctic mean DRE from all aerosol for the 5 different mixing-state assumptions. As expected, the DRE calculated with the *external* mixing-state assumption produces the most negative DRE (-1.65 W m^{-2}), while the *allCoreShell* assumption produces the

more positive DRE (-1.34 W m^{-2}). The *external*1.5* assumption, included as a reference, is close to halfway (-1.52 W m^{-2}) between the two bounding assumptions. The *fBC-constrained* mixing state is less negative (-1.45 W m^{-2}) than the *r_{shell}-constrained* mixing state (-1.59 W m^{-2}). This is because constraining by the fraction of BC-containing particles results in smaller BC cores with larger shell thickness in TOMAS (Figure 6.6a) that leads to a larger amount of absorption.

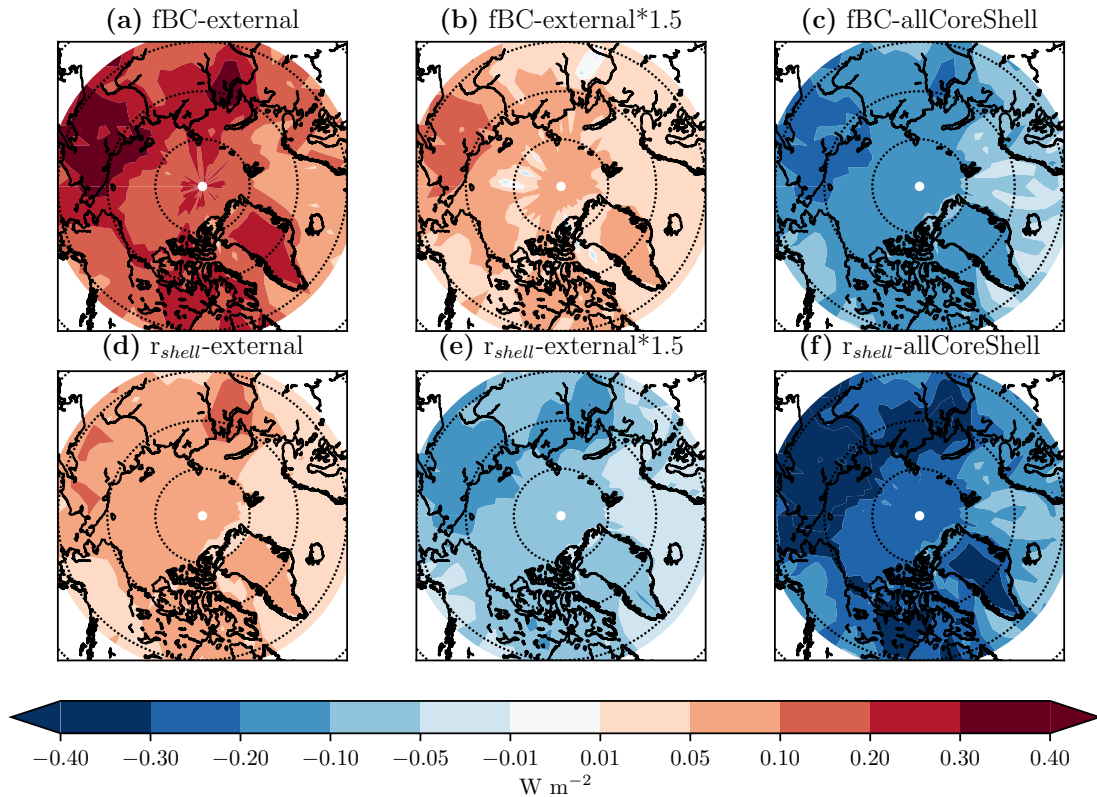


Figure 6.8: The difference in DRE between *fBC-constrained* (a,b,c) and *r_{shell}-constrained* (d,e,f) compared to the bounding mixing-state assumptions.

The difference in the DRE between the measurement-constrained mixing states (*fBC-constrained* and *r_{shell}-constrained*) and the bounding mixing states (*external*, *external*1.5*, and *allCoreShell*) are plotted in Figure 6.8. Both the measurement-constrained mixing states are more positive than completely externally mixed BC. While less than 15% of particles contain BC, the *fBC-constrained* mixing state is 0.19 W m^{-2} more positive than the *external* mixing-state assumption (or 58% of the difference between *external* and *allCoreShell*) and 0.05 W m^{-2} more positive than the *external*1.5*

mixing-state assumption (but 0.11 W m^{-2} more negative than *allCoreShell* mixing-state assumption). Conversely, the *r_{shell}-constrained* mixing state is only 0.06 W m^{-2} more positive than the *external* mixing-state assumption (or 20% of the difference between *external* and *allCoreShell*) and 0.07 W m^{-2} less negative than the *external*1.5* mixing-state assumption (but 0.25 W m^{-2} more negative than the *allCoreShell* mixing-state assumption). Regionally the areas with the largest differences between mixing states are over the areas with a slight positive net DRE in Figure 6.8 (Greenland, the Canadian high Arctic, and Russia). This further underscores the sensitivity to underlying surface albedo. In these regions, the *fBC-constrained* DRE is $0.3\text{-}0.4 \text{ W m}^{-2}$ more positive than the *external*1.5* mixing-state assumption, while the *r_{shell}-constrained* mixing state is $0.3\text{-}0.4 \text{ W m}^{-2}$ more negative.

Table C.1 presents the pan-Arctic mean DRE for the *r_{shell}-constrained* and *fBC-constrained* mixing states using the minimum and maximum estimates for coating thickness for rBC core diameters less than 140 nm. In the pan-Arctic mean, the difference in DRE is less than 1% across the minimum and maximum bounding assumptions. This is likely caused by an overall minor contribution to optical extinction in particle sizes less than 140 nm.

6.3.4 Study limitations

We acknowledge several limitations in understanding the difference in DRE when using measurement constraints (instrument limitations are discussed in Section 2). First, we assume a core-shell morphology with BC at the exact center of the particle. Several studies have suggested this may not always be representative of atmospheric aerosol (e.g., Cappa et al., 2012). We note that as we assume BC is always at the center of a mixed particle, BC absorption in this work is therefore an upper bound. Second, we assume all BC particles are coated (though sometimes with very thin coats as in the minimum coating assumption, see Appendix C). Some studies show that plumes may have a combination of coated and uncoated BC, with increasing in coated BC fraction increasing with chemical age of the plume (e.g., Subramanian et al., 2010). Third, we use averages of measurements across flights and altitudes for BC size distribution and coating information. A separate paper,

Schulz et al. (in prep), will examine spatial and vertical variability of BC measurements made in this campaign. Finally, the measurements used here are limited spatially and temporally. Future work may expand on the measurements reported here for other months and a larger spatial domain.

6.4 Conclusions

In this study, we present measurements of BC mixing state in the springtime Canadian high Arctic. Using an SP2 aboard the POLAR6 flights, we find that on average for rBC core diameters in the range of 140-220 nm, median coating thickness decreases from 45-40 nm (with an interquartile range of 30-70 nm to 17-65 nm). The ratio of total particle to rBC core diameter in this study (1.6-1.4) is comparable to measurements in the springtime Canadian Arctic by Kondo et al. (2011) and Sharma et al. (2017), as well as measurements in the European Arctic from Raatikainen et al. (2015) and Liu et al. (2015). Combining the SP2 size-resolved rBC measurements with total aerosol size distributions from the UHSAS instrument, we estimate approximately 16% of particles contain rBC in the 175-330 nm diameter range, and 3% of particles contain rBC in the 550-730 nm diameter range. We use these measurements separately as constraints on BC mixing state simulated in TOMAS. When constraining TOMAS mass and number concentrations with the shell thickness as a function of rBC core diameter (*r_{shell}-constrained*), we calculate only 5% of 200 nm particles contain BC (compared to 16% from the SP2 and UHSAS observations). Conversely, constraining by the fraction of particles containing rBC (*fBC-constrained*), we find the ratio of total particle to core diameter range from 2.6-2.7 across the SP2 size range (compared to 1.6 to 1.4). The reason these constraints do not converge towards the measurements is that GEOS-Chem-TOMAS simulates a lower BC mass concentration and higher non-BC mass concentration than measured by the SP2 and UHSAS, resulting in smaller BC mass to total aerosol mass ratio.

We estimate the Arctic DRE in April 2015 using bounding mixing-state assumptions of entirely externally mixed and internally mixed BC and compare this to the DRE estimate using the measurement-constrained mixing states. We find that the *fBC-constrained* mixing state is 0.19 W m⁻² less negative than the completely external mixing-state assumption (and 0.11 more negative

than the completely internal assumption), while the *r_{shell}-constrained* mixing state is 0.06 W m⁻² less negative than the completely external mixing-state assumption (and 0.25 W m⁻² more negative than the completely internal assumption). As the BC mass fraction in TOMAS is lower than observed, constraining by the fraction of BC-containing particles results in smaller BC cores with larger shell thickness. Over regions of bright underlying surface albedo the differences can be greater than 0.4 W m⁻². The difference in the calculated DRE between *r_{shell}-constrained* and *f_{BC}-constrained* highlight the importance of accurately simulating all aerosol components in order to represent the chemical mixing state. As the focus of this study was on the Arctic, we recommend future work to focus on using this approach globally.

Chapter 7

The role of inter-regional variability in aerosol size distributions on respiratory deposition of particulate matter air pollution⁶

Human exposure to airborne particulate matter (PM) increases the risk of negative health outcomes; however, substantial uncertainty remains in quantifying these exposure-response relationships. In particular, relating increased risk of premature mortality to exposure to PM with diameters smaller than $2.5 \mu\text{m}$ ($\text{PM}_{2.5}$) neglects variability in the underlying size distribution of $\text{PM}_{2.5}$ exposure. As particle deposition along the respiratory tract exhibits a strong size dependence, the fraction of PM mass that deposits is a function of ambient particle size distributions. In this study, we combine a size-resolved respiratory particle-deposition model with a global size-resolved aerosol model to estimate the variability in particle deposition along the respiratory tract due to variability in ambient PM size distributions. Globally, we find that the ratio of deposited PM mass in the tracheobronchial and alveolar regions per unit ambient $\text{PM}_{2.5}$ exposure (deposition ration, $\text{DR}_{\text{TB+AV}}$) varies by 20-30% between highly populated regions (e.g., Eastern US vs. India) due to variability in ambient PM size distributions. Furthermore, $\text{DR}_{\text{TB+AV}}$ can vary by as high as a factor of 5 between the minima in the fossil-fuel-dominated emissions regions of the Eastern US and Europe and the maximum in the desert-dominated emissions region of North Africa. Some of this variability in $\text{DR}_{\text{TB+AV}}$ is driven by coarse mode particles that are larger than $2.5 \mu\text{m}$ but still deposit in the tracheobronchial and alveolar regions. When considering individual PM species, such as sulfate or organic matter, we still find geographic variability in the $\text{DR}_{\text{TB+AV}}$ on the order of 30% due to regional variability in the size distribution. Hence, even if the toxicity of PM can be attributed to

⁶ This Chapter submitted as: Kodros, J. K., Volckens, J., Jathar, S. H., Pierce, J. R.: The role of inter-regional variability in aerosol size distributions on respiratory deposition of particulate matter air pollution, submitted to *GeoHealth*, 2018

specific species, one still may need to consider variability in the ambient size distribution. Finally, the spatial distribution of DR_{TB+AV} based on number or surface area are substantially different than the deposition ratio based on mass, further motivating the need to understand the underlying mechanisms controlling the dose from inhaled PM. The results of this study suggest that regional variability in ambient aerosol size distributions drive variability in PM deposition in the body, which may lead to variability in the health response from exposure to $PM_{2.5}$ from one region to the next.

7.1 Introduction

Exposure to particulate matter (PM) air pollution increases the risk of cardiovascular and respiratory disease. In particular, long-term exposure to the mass of PM with aerodynamic diameters less than $2.5 \mu\text{m}$ ($PM_{2.5}$) has been shown to have a causal association with an increased risk of mortality from cardiovascular and respiratory diseases (Dockery et al., 1993; Krewski et al., 2009; Pope and Dockery, 2006; Pope et al., 2002). Over 4 million deaths were estimated to be attributed to chronic exposure to ambient $PM_{2.5}$ pollution in 2015, making it one of the leading risk factors contributing to premature mortality Cohen et al. (2017). In addition, a number of studies have shown correlations between short-term exposure to $PM_{2.5}$ and negative health consequences (Gan et al., 2017; Ostro et al., 2006; Pope and Dockery, 2006). Despite numerous associations between $PM_{2.5}$ exposure and increased risks of negative health effects, substantial uncertainty remains in quantifying the magnitude and shape of these exposure-response relationships.

As the exact mechanisms that relate exposure to $PM_{2.5}$ to increased risk of negative health outcomes (such as premature mortality) are unclear, health impact assessments (such as the widely cited Global Burden of Disease Study) rely on integrated exposure-response functions to estimate population-level health impacts for a given level of $PM_{2.5}$ exposure (e.g., Burnett et al., 2014). These integrated exposure-response functions are synthesized from available epidemiologic data. The $2.5 \mu\text{m}$ diameter cutoff is frequently used as a proxy for airborne PM that, upon inhalation, can penetrate to and deposit within the lower respiratory region of the lung. In addition, as ambient particle mass size distributions (when weighted according to PM mass) tend to feature a local minima around

2.5 μm in diameter, this size cutoff separates fine particles (formed from combustion processes and secondary aerosol formation) and coarse particles (emitted mostly from mechanical emissions; e.g. dust and sea spray) (Seinfeld and Pandis, 2012). Long-term ambient $\text{PM}_{2.5}$ measurement networks have existed in recent decades in the United States, Europe, and Canada. As a result, most of the epidemiology studies that relate exposure to ambient $\text{PM}_{2.5}$ are based in the North America and Europe (e.g., Beelen et al., 2008; Brauer et al., 2002; Carey et al., 2013; Cesaroni et al., 2013; Chen et al., 2005; Crouse et al., 2012; Gan et al., 2013; Hertz-Picciotto et al., 2007; Hystad et al., 2013; Karr et al., 2007, 2009; Lepeule et al., 2012; Lipsett et al., 2011; Miller et al., 2007; Pinault et al., 2016; Puett et al., 2009; Thurston et al., 2016; Villeneuve et al., 2015). Very few studies used in generating health-response functions have been done in low- and middle-income countries in Asia, sub-Saharan Africa, or South America, yet these regions bear the majority of the health burden due to air pollution exposure (Cohen et al., 2017).

The GBD 2015 study acknowledges that applying these exposure-response functions generated in limited regions to all regions of the world is a major source of uncertainty (Burnett et al., 2014; Cohen et al., 2017). Possible sources of variability in published exposure-response relationships include demographic factors (a population in a certain region is more or less susceptible to exposure) or differential toxicity of different chemical components present in $\text{PM}_{2.5}$ (such as the sulfate or organic aerosol mass fraction) (e.g., Bates et al., 2015; Bell et al., 2007; Fang et al., 2017; Verma et al., 2015). Variability in the chemical composition of ambient $\text{PM}_{2.5}$ may reflect differing contributions from local emission sources, transport processes, or chemical and physical processes in the atmosphere. In addition to variability in demographics and the chemical composition of ambient $\text{PM}_{2.5}$, this work motivates that variability in ambient PM size distributions may also lead to variability in health responses following $\text{PM}_{2.5}$ exposure.

Ambient particle size distributions exhibit strong regional variability, reflecting local/regional differences in emission sources, transport, and ambient chemical/physical processes (e.g., Jaenicke, 1993). Different emission sources may emit particles at different sizes. For instance, combustion processes tend to emit particle mass in the 100-300 nm diameter range (Ban-Weiss et al., 2010;

Janhäll et al., 2010; Sakamoto et al., 2015; Winijkul et al., 2015) while dust and sea-spray emissions tend to be greater than $1 \mu\text{m}$ (Jaeglé et al., 2011; Kok, 2011; Mahowald et al., 2014). This results in urban regions having a strong contribution of accumulation-mode mass to $\text{PM}_{2.5}$ concentration, and desert regions having a substantial contribution to coarse-mode mass. In addition to local emissions, observations show variability in particle size distributions and chemical composition due to transport of PM (e.g., Dunlea et al., 2009; Xu et al., 2017). Finally, observations and modeling studies show that microphysical processes such as new-particle formation events (e.g., Hodshire et al., 2016; Merikanto et al., 2009; Westervelt et al., 2014), condensation to and evaporation of particles (e.g., Bian et al., 2017; Bougiatioti et al., 2014; D'Andrea et al., 2013), in-cloud aqueous oxidation (e.g., Hoppel and Frick, 1990), coagulation (e.g., Sakamoto et al., 2016; Westphal and Toon, 1991), wet deposition (e.g., Croft et al., 2012; Dentener et al., 2006), and dry deposition (e.g., Sehmel, 1980; L. Zhang et al., 2001) substantially influence particle number and mass distributions (Croft et al., 2016b; Kodros and Pierce, 2017).

Particle deposition along the respiratory tract exhibits a strong size and shape dependence (Hussein et al., 2013; Löndahl et al., 2007; Löndahl et al., 2009), and thus, the extent of particle deposition may depend on the inhaled particle size distribution. Mechanisms of deposition of particles in specific regions of the respiratory tract (e.g. head/nose, tracheobronchial, or alveolar) are complex. The fraction of particles deposited to different locations in the airways depends on particle size, shape, and density as well as airway geometry and breathing pattern (affecting flow rate and residence time). Briefly, Brownian diffusion, inertial impaction, and gravitational settling are the dominant processes governing particle deposition in the body (Hinds, 1982). Ultrafine particles (with diameters smaller than approximately 100 nm) deposit primarily through Brownian diffusion, lacking enough inertia to deposit through impaction or gravitational settling at relevant timescales. Coarse-mode particles (greater than $2.5 \mu\text{m}$) primarily deposit through inertial impaction or gravitational settling. There exists a minimum in deposition efficiency at diameters approximately $200\text{-}700 \text{ nm}$, where particles neither diffuse nor impact/settle with sufficient magnitude to deposit efficiently. Thus, the mechanics governing particle deposition have many size-dependent features

that are not accurately represented by a simple $2.5 \mu\text{m}$ cutoff measurement. Knowledge of the total particle size distribution is necessary to translate an exposure measurement into an estimate of PM mass deposited along the respiratory tract. A number of dosimetry models have been developed to estimate the fraction of particles that deposit in specific regions in the body. Such models include the empirical model of the International Commission on Radiological Protection (ICRP) (International Commission on Radiological Protection, 1994) and the Multiple Path Particle Dosimetry (MPPD) model (Miller et al., 2016).

In this study, we combine simulated ambient aerosol size distributions with size-resolved particle deposition models to estimate the geographic variability in deposited particle mass. We use this to motivate the idea that variability in $\text{PM}_{2.5}$ exposure response may be partly explained by variability in ambient particle size distributions affecting deposition mass of PM in the body. In Section 2, we our methods of using particle deposition models and a chemical-transport model with online aerosol microphysics. In Section 3.1-3.3, we present simulations of ambient $\text{PM}_{2.5}$ mass concentration along with deposited PM mass in the body. In Section 3.4, we explore geographic variability in species-specific PM size distribution and deposition. In Section 3.5, we present geographic variability in particle number and surface-area deposition. We share our conclusions in Section 4.

7.2 Methods

7.2.1 Modeling size-resolved particle deposition in the body

To estimate the mass of PM that deposits at region-specific sites in the body, we use the International Commission on Radiological Protection particle deposition model (International Commission on Radiological Protection, 1994). We use equations fit to measured deposition fractions as a function of particle diameter from the ICRP model averaged for various breathing conditions by Hinds (1982). Particle deposition fractions are shown in Figure 7.1 for all regions in the body, including the head/nose region, tracheobronchial region, alveolar region, and the sum of the tracheobronchial and alveolar regions. In later sections, we focus on the sum of deposition to the tracheobronchial and alveolar regions. Newer particle deposition models generally agree with the results of the ICRP

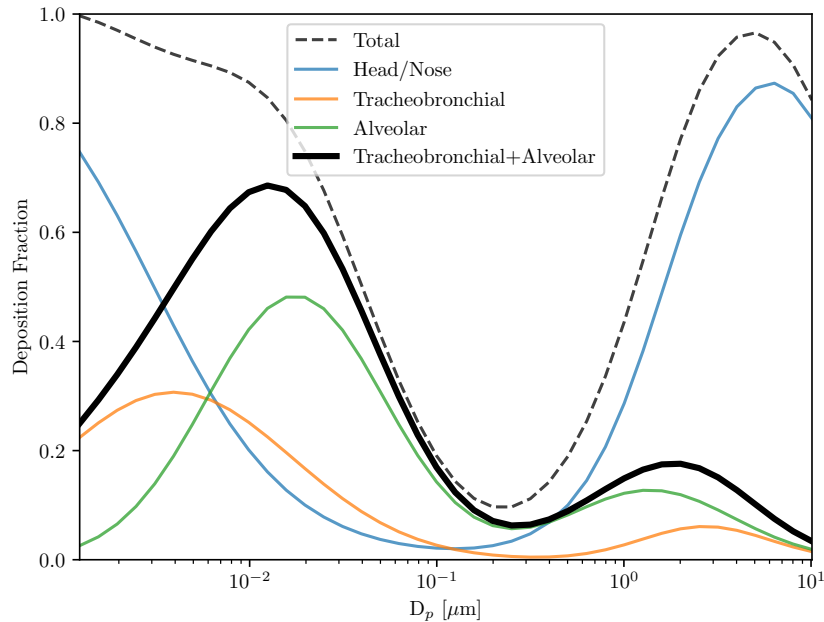


Figure 7.1: Deposition curves based on the ICRP model with fitted equations from Hinds (1982) for total deposition in the body as well as regional deposition in the head/nose, tracheobronchial, alveolar, and sum of the tracheobronchial and alveolar region. In later sections, we focus on the sum of deposition in the tracheobronchial and alveolar region.

model. To test the sensitivity to deposition model, we also consider regional deposition curves from the Multiple Path Particle Dosimetry (MPPD) model (Miller et al., 2016). In the Supplemental Information (SI; Appendix D), deposition fractions from the MPPD model to the ICRP model are compared Figures D.1-D.3.

We account for swelling of aerosol particles due to water uptake in the lung assuming that air in the lung and associated airways has a relative humidity of 99.5% and a temperature of 37° C (Anselm et al., 1990). The SI (Appendix D contains a detailed description of our treatment of aerosol water uptake in the lung. Briefly, we approximate growth to equilibrium sizes based on the total hygroscopicity of the particle in a given size range (assuming all particles in the size range are internally mixed). We test the sensitivity of this treatment in Figure D.4 by assuming no particle growth in the lung and growth based on lung relative humidities of 98% and 99.5%.

7.2.2 Simulating ambient aerosol size distributions

To simulate the transport of gas- and particle-phase species, we use the chemical-transport model, GEOS-Chem (Bey et al., 2001), version 10.01. GEOS-Chem is driven by reanalysis metrology fields by GEOS-FP. We run simulations of GEOS-Chem with 47 vertical levels and horizontal resolutions of $4\times 5^\circ$ and $2\times 2.5^\circ$ for the full global domain, and we perform nested simulations at $0.5\times 0.666^\circ$ over North America and eastern Asia. The standard setup of GEOS-Chem includes tracers for 52 gas-phase species. All simulations are for the year 2010 with a 1-month spin-up not included in analysis.

To simulate size-resolved aerosol mass and number concentrations, GEOS-Chem is coupled online to the Two Moment Aerosol Sectional (TOMAS) microphysical model (Adams and Seinfeld, 2002). TOMAS includes tracers for size-resolved particle number along with size-resolved mass for sulfate (SO_4), sea salt, organic aerosol (OA), black carbon (BC), and dust. We use versions of TOMAS with 15-bin and 40-bin size sections both simulating dry diameters from approximately 1 nm to 10 μm (Lee and Adams, 2012; Y. H. Lee et al., 2013). Due to computational limitations, we use the 40-bin TOMAS only with the GEOS-Chem $4\times 5^\circ$ horizontal resolution and the 15-bin TOMAS with the GEOS-Chem $2\times 2.5^\circ$ and $0.5\times 0.666^\circ$ horizontal resolutions. We use the 40-bin version of TOMAS at the coarse spatial resolution to inform an interpolation of aerosol size distributions with the 15-bin version at finer spatial resolution. This is done to optimize computational expense. All results shown here use interpolated 40-bin aerosol size distributions at $2\times 2.5^\circ$ or $0.5\times 0.666^\circ$ resolution.

Detailed descriptions of microphysical processes in TOMAS have been described in detail elsewhere (Adams and Seinfeld, 2002; Lee and Adams, 2012; Y. H. Lee et al., 2013). TOMAS explicitly accounts for size-resolved aerosol emissions, coagulation, condensation, wet and dry deposition, aqueous oxidation, and new-particle formation. Emissions of primary SO_4 include 2 lognormal size modes: the first mode contains 15% of the mass with a mass median diameter (MMD) of 19 nm and geometric standard deviation (GSD) of 1.6 and the remainder in a second mode with a MMD of 296 nm and GSD of 2 (Adams and Seinfeld, 2003). BC and OA emissions

are separated by emission source. Fossil fuel OA and BC is emitted into the model with an MMD of 126 nm and GSD of 2, while biofuel and biomass burning particles are emitted with an MMD of 422 nm and a GSD of 2 (Pierce et al., 2007). Dust emissions follow the DEAD scheme (Zender, 2003), while sea salt emissions are based on the scheme of Jaeglé et al. (2011). TOMAS includes a ternary nucleation scheme involving water, sulfuric acid, and ammonia following the parameterization of Napari et al. (2002), with nucleation rates scaled down by 5 orders of magnitude to better match observations (Westervelt et al., 2013, following). When ammonia mixing ratios are less than 1 parts per thousand by volume, TOMAS defaults to a binary nucleation scheme (sulfuric acid and water) (Vehkamäki, 2002). In addition to nucleation, TOMAS explicitly simulates condensation, coagulation, wet and dry deposition, and cloud processing.

Simulations using GEOS-Chem-TOMAS have been evaluated against observations of long-term size-resolved number concentrations (Croft et al., 2016b; D'Andrea et al., 2013; Kodros and Pierce, 2017; Westervelt et al., 2013) and aerosol optical depth (Kodros et al., 2016a). While GEOS-Chem-TOMAS has shown skill at reproducing variability in size-resolved aerosol concentrations, we acknowledge measurements of aerosol size distributions (and thus model evaluations) are limited. As such, we are unable to fully determine the accuracy of the simulated aerosol size distributions in GEOS-Chem-TOMAS; however, as we know particle size distributions exhibit regional variability (e.g., Jaenicke, 1993), TOMAS provides a reasonable option to explore how diversity in size distributions may affect respiratory PM deposition.

7.3 Results

7.3.1 Simulated annual PM_{2.5} concentration

In this study, we define PM_{2.5} as the dry particle mass concentration contained in particles with wet aerodynamic diameters smaller than 2.5 μm . We use this definition so that our simulated PM_{2.5} is directly comparable to PM_{2.5} networks that use a gravimetric cyclone to size-select particles with a wet aerodynamic diameter smaller than 2.5 μm , where these particles are then dried at ~35% RH, which removes most of the aerosol water. The annual-average PM_{2.5} mass simulated with

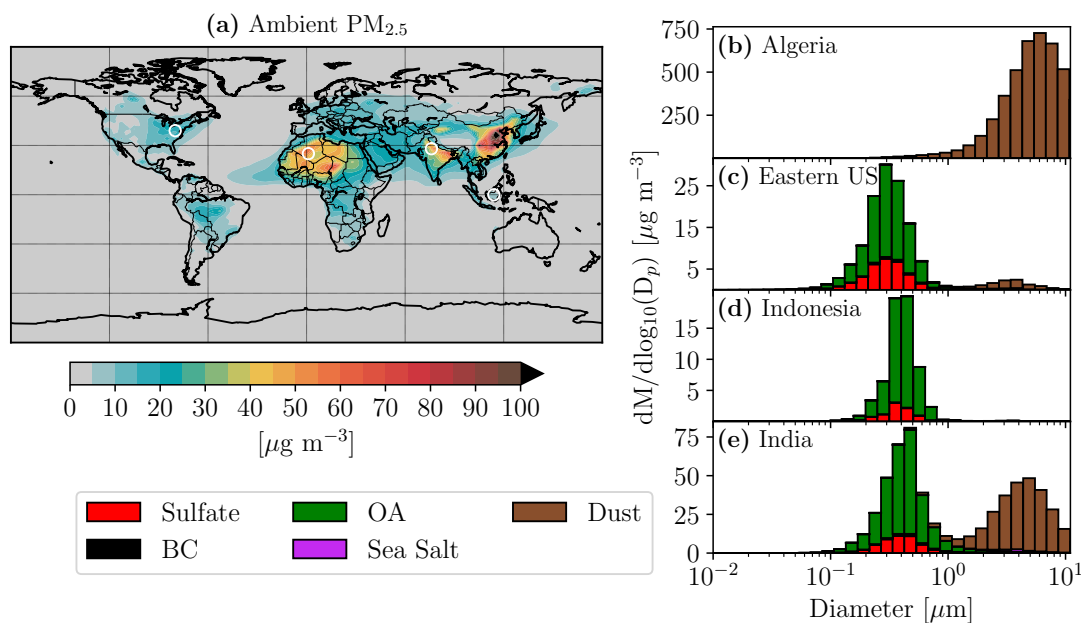


Figure 7.2: Central figure: (a) Annually averaged dry surface PM_{2.5} mass simulated with GEOS-Chem-TOMAS. **Outside figures:** Ambient dry mass distributions at wet aerodynamic diameters showing particle composition for a gridcell in the (b) Eastern United States, (c) Algeria, (d) Indonesia, and (e) Northern India.

GEOS-Chem-TOMAS is plotted in Figure 7.2a. There is substantial geographic variability in PM_{2.5} concentrations, ranging from 10-20 $\mu\text{g m}^{-3}$ in the Eastern US to 80-100 $\mu\text{g m}^{-3}$ in Eastern China. Regions with the highest concentration of PM_{2.5} include the Sahara, Eastern China, and Northern India. Evaluation of simulated PM_{2.5} by GEOS-Chem has been done in several previous studies (Park et al., 2006; van Donkelaar et al., 2010), and so we do not include this here.

In addition to geographic variability in total PM_{2.5} mass concentration, there is also substantial variability in the underlying mass distributions and chemical composition by size. In Figure 7.2b-e, we show dry mass distributions at wet aerodynamic diameters showing particle composition for a gridcell in the Eastern United States, Algeria, Indonesia, and Northern India. These four representative regions were chosen to demonstrate the variability in size distribution and composition. We refer to these regions throughout this section. The mass distributions in the Eastern US, Northern India, and Indonesia have a substantial contribution of accumulation-mode particles to PM_{2.5} mass. The accumulation-mode particles are primarily composed of OA (primary and secondary) along with SO₄ and trace amounts of BC. The Eastern US and India also have a contribution from coarse-mode

particles to $PM_{2.5}$ mass concentration; however, much of the coarse-mode mass is larger than a wet ambient diameter of $2.5 \mu m$, and hence would not be captured by a $PM_{2.5}$ monitor. Conversely, the $PM_{2.5}$ mass concentration in Algeria is composed almost entirely of dust even though the $PM_{2.5}$ dust is only a small fraction of the total dust in this location.

Differences in regional emissions sources explain much of the differences in particle size and composition, while chemical and physical processing (coagulation, condensation, cloud processing) in the atmosphere (discussed later) explains the rest. PM emissions in the Eastern US are largely derived from fossil-fuel combustion (e.g. road transportation, industry, power generation), resulting in PM composed mainly of SO_4 , OA, and BC. In GEOS-Chem-TOMAS, OA and BC from fossil fuel are emitted with smaller mass median diameters (MMD of 126 nm) than OA and BC from biomass burning emissions (MMD of 422 nm). The large contribution from fossil-fuel emissions in the Eastern US (such as from road transport) results in an accumulation-mode MMD between 250-300 nm, indicating particle growth from emission of MMD of approximately 130 nm likely through coagulation and condensation of sulfuric acid and organics. India and Indonesia have substantial PM emissions from biomass combustion (including residential, agricultural, and wildfire). This results in a relatively larger OA contribution to accumulation-mode PM mass than in the Eastern US. The large contribution from biomass combustion in India and Indonesia results in accumulation-mode MMD between 400-500 nm. Finally, local dust emissions in North Africa are predominantly emitted into the coarse mode resulting in a mass median diameter of $6 \mu m$ in Algeria.

7.3.2 Respiratory deposited PM mass and deposition ratio

To estimate geographic variability in the respiratory deposition of PM mass, we multiply the size-dependent ICRP deposition fraction to the simulated aerosol mass distributions from GEOS-Chem-TOMAS. This product results in deposited PM mass per volume of inhaled air (units of μg PM deposited in lung, written here as μg_{dep} , per m^3 of inhaled air, written here as $m_{inhaled}^{-3}$). In Figure 7.3a, we show the geographic distribution of total deposited PM mass in the body. Similar to the spatial distribution of $PM_{2.5}$ mass concentrations, the desert regions (the Sahara, Middle

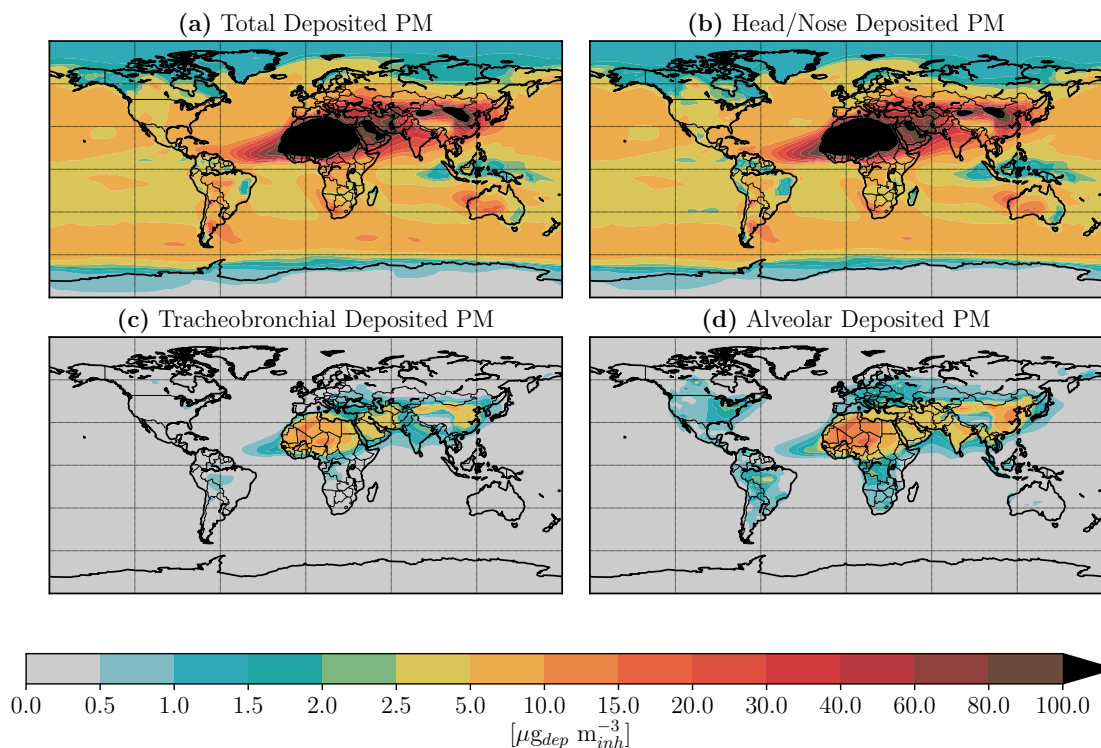


Figure 7.3: Deposited PM mass (integrating from 1 nm to 10 μm) in (a) all regions, (b) head/nose region, (c) tracheobronchial region, and (d) alveolar region.

East, and Gobi deserts) have the highest deposited PM mass concentration (larger than 50-100 $\mu\text{g}_{\text{dep}} \text{m}_{\text{inhaled}}^{-3}$). India and Eastern China also have high concentrations of deposited PM mass (35-50 $\mu\text{g}_{\text{dep}} \text{m}_{\text{inhaled}}^{-3}$). In addition to geographic variability, there is also variability in magnitude of deposition mass in each region of the body. We show maps of deposition in the (b) head/nose region, (c) tracheobronchial region, and (d) alveolar region in Figure 7.3. Most of the deposited PM mass deposits in the head/nose region; however, concentrations ranging from 0.5 to 30 $\mu\text{g}_{\text{dep}} \text{m}_{\text{inhaled}}^{-3}$ deposit in the tracheobronchial and alveolar regions.

Much of the geographic variability in deposited PM mass in Figure 7.3 arises from the magnitude of ambient PM mass. To remove this influence and understand the role of ambient particle size distributions in determining PM deposition in the tracheobronchial and alveolar regions (TB+AV), we normalize TB+AV deposited PM mass concentration ($\text{PM}_{\text{TB+AV}}$) by the ambient $\text{PM}_{2.5}$ concentration. We define the “deposition ratio” in the tracheobronchial and alveolar regions ($\text{DR}_{\text{TB+AV}}$) as the ratio of $\text{PM}_{\text{TB+AV}}$ per unit ambient $\text{PM}_{2.5}$ mass concentration. This ratio is meant to demon-

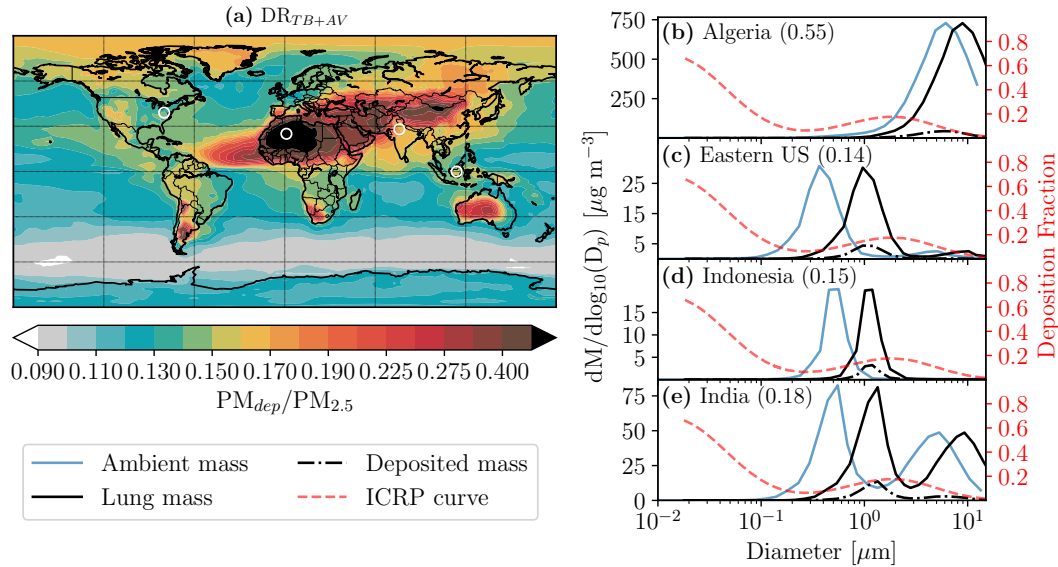


Figure 7.4: Central figure: (a) Map showing DR_{TB+AV} . **Outside figures:** The dry mass distribution at ambient wet aerodynamic diameters (light blue), the dry mass distribution at wet aerodynamic diameters for the RH of the lung (solid black line), the deposited mass at each size (dot-dashed black line) in the gridcell (denoted by the white circles) corresponding to (b) Eastern US, (c) Algeria, (d) Indonesia, and (e) India.

strate the variability of PM mass that deposits compared to what would be measured as ambient $PM_{2.5}$. Here, we focus on the lower-respiratory regions (the tracheobronchial and alveolar regions), as cardiovascular and respiratory diseases may be most sensitive to particle deposition in these respiratory regions; however, this is a simplifying assumption and the exact mechanisms relating particle deposition to effective dose are unclear. DR_{TB+AV} is plotted in Figure 7.4a (central map). Globally, the DR_{TB+AV} varies by 20-30% between the highly populated geographic regions (e.g. eastern US vs. India), but can be as high as a factor of 5. Regions with the highest DR_{TB+AV} are desert regions (e.g. the Sahara, Middle East, Gobi, Southwest US), while continental regions with the lowest DR_{TB+AV} include fossil-fuel-dominated regions of the Eastern US and Western Europe (and even lower in the Southern Ocean).

The cause of the variability in the DR_{TB+AV} comes from the underlying PM mass size distribution. In Figures 7.4b-e, we show the mass distribution at ambient conditions (light blue line), the mass distribution accounting for hygroscopic growth due to the RH of the lung (black solid line), the deposited mass concentration for each size (black dashed line), and the ICRP fractional deposition

curve (red line, left axis) for comparison. In the Eastern US (Figure 7.4b), the ambient mass distribution has a large contribution from accumulation-mode particles with mass median diameter between 250-300 nm. These particles are, to some degree, hygroscopic, and grow in the high RH of the lung to a median diameter of 1 μm . This growth increases PM deposition as it moves more particles out of the deposition minimum (centered at 250 nm). The Eastern US has some coarse-mode mass at sizes larger than 2.5 μm , which contributes to $\text{PM}_{\text{TB+AV}}$ but not the $\text{PM}_{2.5}$ concentration. The net result is a $\text{DR}_{\text{TB+AV}}$ of 0.14. Conversely, in Algeria, most of the mass at ambient conditions is coarse-mode dust (see Figure 7.2). Dust particles are modeled here as hydrophobic (a kappa value of 0.01; see Appendix D), resulting in less growth in the lung. Even though most coarse-mode mass is deposited in the head/nose region and not counted here (Figures 7.1 and 7.3), the ICRP model still estimates deposition fractions in tracheobronchial and alveolar region of 10% at 2.5 μm decreasing to near 0% at 10 μm . Much of this (TB+AV)-deposited mass is not included in the $\text{PM}_{2.5}$ cutoff. The net result is a $\text{DR}_{\text{TB+AV}}$ of 0.55. The ambient mass distribution in Indonesia is representative of a region with substantial emissions contribution from biomass burning. The ambient mass concentration is dominated by accumulation-mode particles with a mass median diameter between 400-500 nm. Similar to the Eastern US, these particles are partly hygroscopic and grow in the lung to a mass median diameter between 1-1.5 μm . The ambient mass distribution in Northern India contains both an accumulation mode (likely from residential solid fuel use and fossil-fuel combustion) as well as a coarse-mode mass from dust. The accumulation-mode particles are partly hygroscopic and grow to larger sizes, while the coarse mode is hydrophobic with slower condensational growth timescales. The larger contribution of coarse-mode particles to deposition mass results in a higher $\text{DR}_{\text{TB+AV}}$ in India (0.18) than Indonesia (0.15).

To further investigate the geographic variability of TB+AV particle deposition at continental scales, we include nested simulations at finer horizontal resolutions of $0.5 \times 0.666^\circ$ degrees over a domain centered on North American and a domain centered on Asia. In Figure 7.5, we show predicted $\text{DR}_{\text{TB+AV}}$ for the North American and Asian domains. In the finer-resolution North America domain the variability $\text{DR}_{\text{TB+AV}}$ increases to 50-60%, ranging from a maximum in the

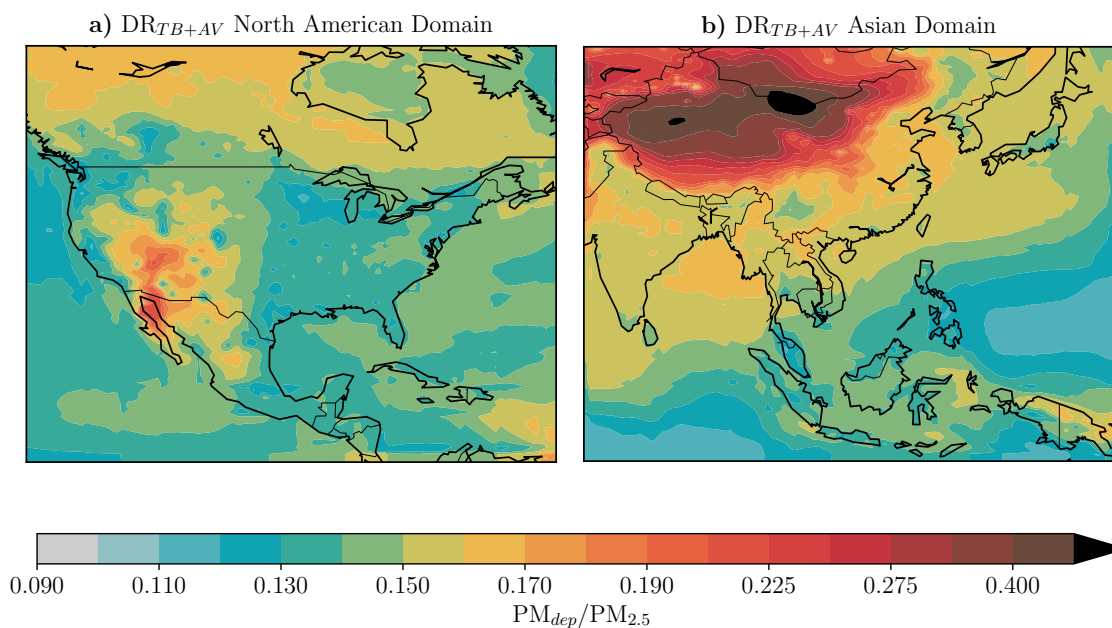


Figure 7.5: DR_{TB+AV} using a high-resolution simulation for the North American (left) and Asian (right) domains.

desert Southwest US to a minimum in areas more influenced by fossil-fuel combustion and secondary aerosol formation. The higher-resolution simulation for North America shows increased spatial variability compared to the global simulation with deposition minima in the populated areas of California, Pacific Northwest, Salt Lake City, Denver, Calgary and Mexico City. The primary reason for the lower DR_{TB+AV} in more populated areas relative rural areas is the higher hydrophobic particle fraction (mainly hydrophobic OA) emitted in urban areas. Downwind of urban areas, hydrophobic OA (and externally BC) undergoes atmospheric processing and converts to hydrophilic OA (and internally-mixed BC). Meanwhile, sulfur dioxide is oxidized and may form sulfate aerosol on a timescale of ~ 2 days. The net result is increased SO_4 and hydrophilic OA outside of urban areas (similar to results in Jimenez et al., 2009; Philip et al., 2014). The more hydrophilic particles are able to grow to larger diameters in the high RH of the lung, thus moving further out of the minimum in particle deposition (centered at 250 nm, see Figure 7.1). In the Asian domain, there exists a strong gradient in DR_{TB+AV} from the Gobi desert region to the more urban areas of Eastern China

and Northern India. Conversely to the North American domain, the spatial gradient of DR_{TB+AV} in Asia seems less influenced by urban areas. This is likely a result of high aerosol and precursor concentrations in this region leading larger accumulation mode diameters through condensation and coagulation. These larger-sized particles have higher deposition efficiencies in the TB+AV (Figure 7.1).

The spatial distribution of DR_{TB+AV} is sensitive to our assumptions regarding particle growth in the lung. In Figure D.4, we show DR_{TB+AV} with no particle growth, particle growth based on an RH of 98%, and particle growth based on an RH of 99.5%. The spatial variability between urban regions and desert regions of DR_{TB+AV} decreases with increasing particle growth in the lung. This is due to accumulation-mode particles growing out of the minimum in the deposition fraction of the ICRP model (Figure 7.1) thus depositing more efficiently, while coarse-mode particles grow to sizes that deposit less efficiently. Assuming particle growth based on a lung RH of 99.5% thus may provide a lower limit on the spatial variability of 99.5%.

7.3.3 Speciated size-dependent deposition

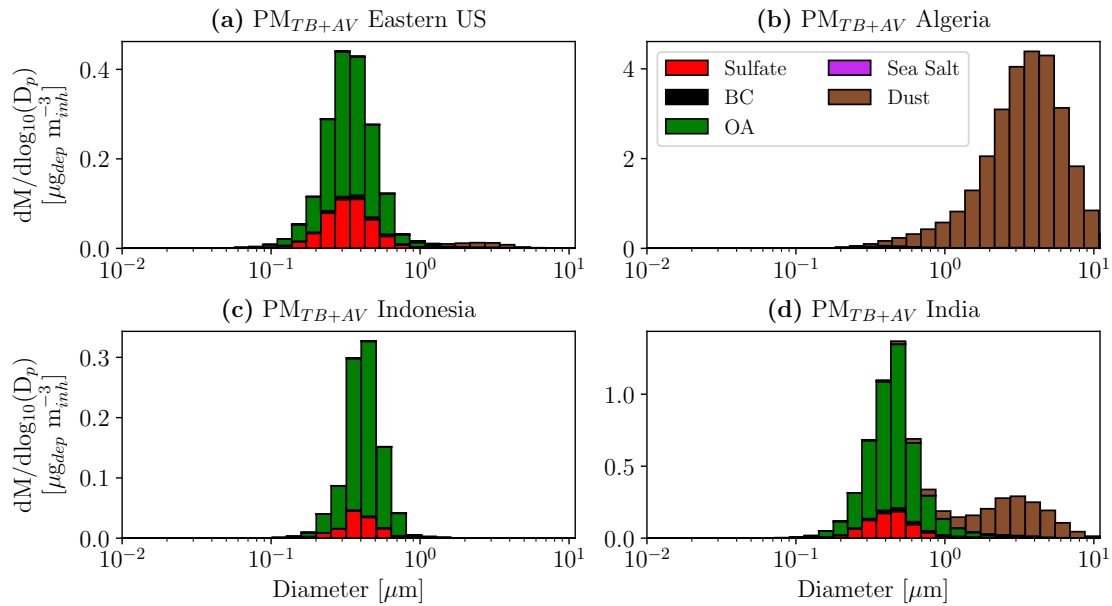


Figure 7.6: Speciated distribution of PM_{TB+AV} at each size interval for the region representing the (a) Eastern US, (b) Algeria, (c) Indonesia, and (d) India.

A current focus of much recent research is the possibility that regional variability in the health response to $PM_{2.5}$ exposure may be partly influenced by differential toxicity of different PM species. To some degree, differences in size distributions reflect changes in composition of PM. Figure 7.6 shows speciated distributions of PM_{TB+AV} (units of $\mu g_{dep} m_{inhaled}^{-3}$). These plots are analogous to the ambient mass distributions in Figure 7.2; however, they now show the TB+AV deposited particle mass concentrations at each size interval. Across the four representative regions shown here, there is variability not just in PM_{TB+AV} , but in the composition of particles that deposit. In the Eastern US and India, much of the PM_{TB+AV} is OA, SO_4 , and dust with trace contributions from BC. The relative contribution of dust to PM_{TB+AV} is increased relative the contribution of dust to ambient PM mass. Conversely, the PM_{TB+AV} in Algeria is almost entirely dust, reflecting the dominant particle emission source in this region. Due to the large contribution of biomass burning to the local PM burden in Indonesia, accumulation-mode OA makes up much of the PM_{TB+AV} in this region. The variability in composition of PM_{TB+AV} further motivates understanding the differential toxicity of different PM species.

To some degree, variability in size distributions and variability in particle composition are connected. Much of the accumulation-mode mass is made up of OA, SO_4 , and BC, while the coarse-mode mass is made up of dust and sea salt. To test if variability in the respiratory deposition of PM mass could be resolved by focusing only on variability in chemical species, Figure 7.7 shows the DR for specific chemical species of PM. In Figures 7.7a and c, we show deposited PM mass of SO_4 per unit ambient $PM_{2.5}$ mass of SO_4 in all body regions (DR_{total}) and DR_{TB+AV} , respectively. In Figures 7.7b and d, we show the same ratios for OA. When focusing on a specific PM species, there still exists potentially significant geographic variability in DR_{total} . For deposition in any region of the body, the DR_{total} of SO_4 deposited mass to ambient SO_4 $PM_{2.5}$ mass varies by 40-50%, ranging from minima in South America, sub-Saharan Africa, and Western Europe to maxima in the desert Sahara and Middle East. The maxima in desert regions is likely caused by mixing of SO_4 mass into the coarse mode via coagulation with and condensation onto dust particles. The DR_{total} for OA has a similar range of variability, but with a different geographic distribution. The OA DR_{total}

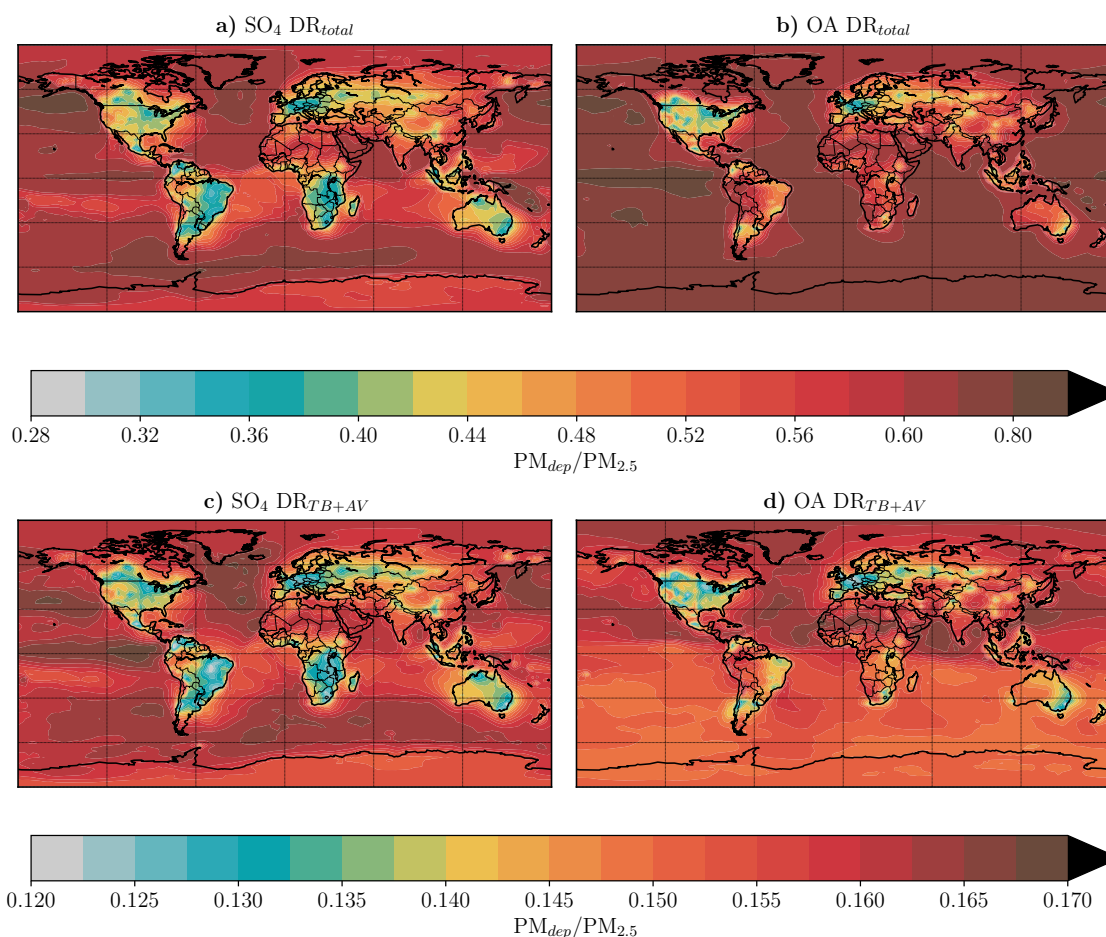


Figure 7.7: Geographic variability of (a, c) sulfate DR_{total} and DR_{TB+AV} and (b,d) organic aerosol DR_{total} and DR_{TB+AV} per unit ambient sulfate and OA $PM_{2.5}$ mass, respectively.

has a maximum in South America and all of Africa and the Middle East with minima in North America and Europe. The maxima in South America and central Africa are likely caused by the larger emission MMD of biomass burning particles, as well as condensation of secondary OA onto a relatively low number concentration (relative the Eastern US) allowing for particle growth to larger diameters with higher TB+AV deposition efficiency. Similar to SO_4 , the maxima in the desert regions of North Africa and the Middle east is likely caused by coagulation with coarse-mode dust particles. The minima in DR_{total} in North America and Europe is due to primary OA emitted at

diameters similar to the minimum in the ICRP deposition fraction curve (Figure 7.1). The DR_{TB+AV} for SO_4 and OA varies by up to 25%, similar to when considering DR_{TB+AV} from all PM species. The DR_{TB+AV} for SO_4 and OA differ in South America and sub-Saharan Africa, showing minima for SO_4 but maxima for OA. Conversely, both show lower DR_{TB+AV} for the United States and Europe relative India and China. These results show that even if the health effects of PM can be attributed to specific PM species, we may still need to consider variability in the size distributions of these species.

We show the DR_{TB+AV} for SO_4 and OA for the finer-resolution simulations in the North American and Asian domains in Figure 7.8. In North America, the spatial variability in DR_{TB+AV} for both SO_4 and OA follows a strong urban versus rural split. The minima in DR_{TB+AV} are limited to urban areas such as Minneapolis, Denver, Houston, coastal California, Calgary, and Mexico City. Similar to DR_{TB+AV} based on all-species PM respiratory deposition, this occurs due to a larger hydrophobic particle fraction in urban areas (more hydrophobic OA and less SO_4) leading to less particle growth in the airways. While the deposited mass in Figures 7.7-7.8 are only from SO_4 and OA, the water uptake in the lung is based on the total particle hygroscopicity in a given size range (i.e., we assume internally mixed particles). Particle sizes in urban areas tend to be closer to the minimum in deposition fraction (Figure 7.1) than rural regions, where increased atmospheric processing increases hydrophilic OA and SO_4 concentrations thus increasing overall hygroscopicity and particle growth to sizes with more efficient deposition in the TB+AV. Thus, contributions from non- SO_4 and OA species still influence the particle size distributions. Conversely, this urban/rural split is less apparent in India and China due to the larger ambient accumulation-mode median diameters in these regions. Biomass burning leads to a lower DR_{TB+AV} than fossil-fuel-emission regions in both the North American domain (wildfires in Northern and Eastern Canada) and the Asian domain (in Indonesia and the Philippines) due to larger emitted particle diameters and higher hygroscopic particle fractions than fossil-fuel emissions.

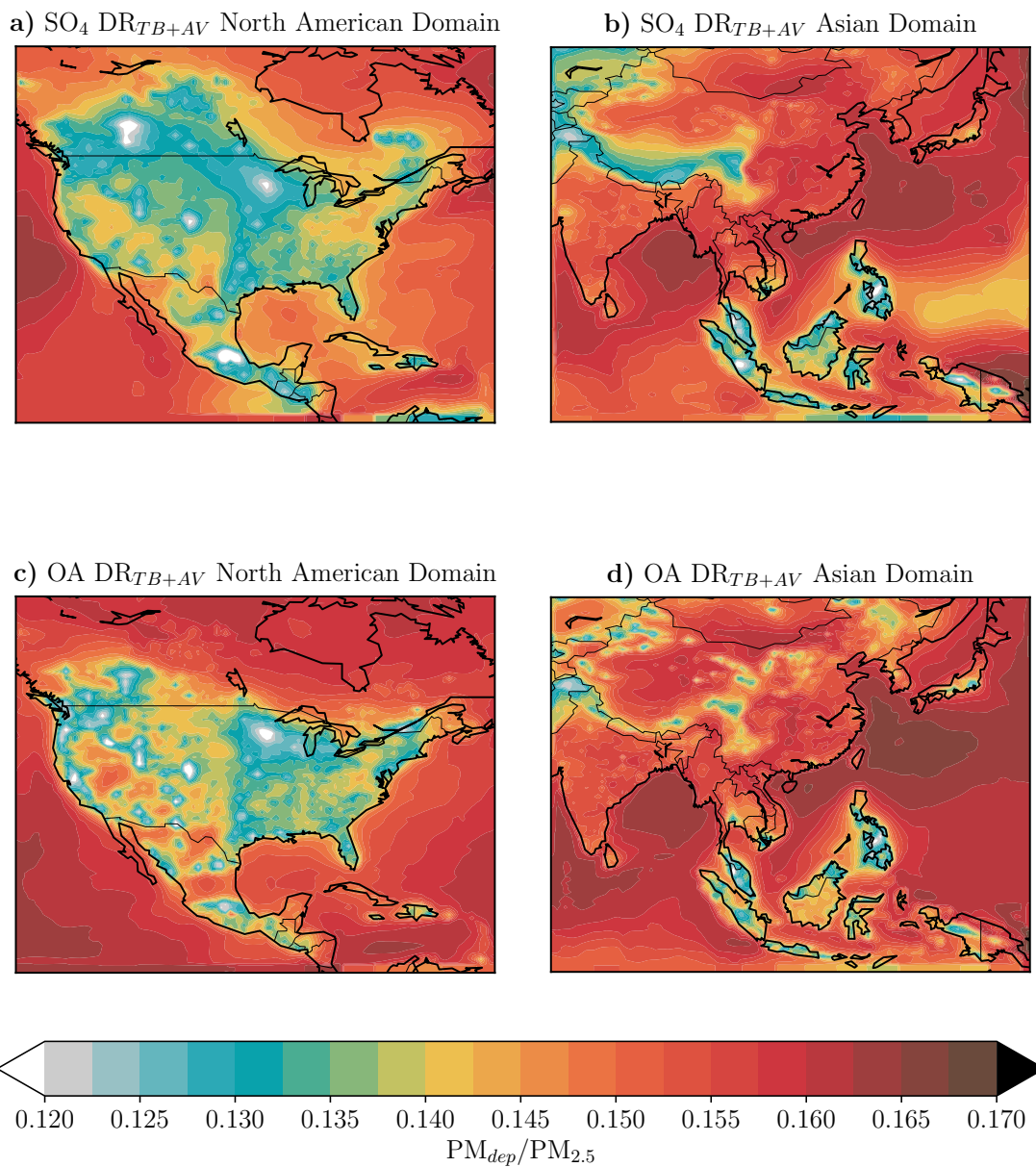


Figure 7.8: The $\text{DR}_{\text{TB}+\text{AV}}$ based on (a) SO_4 in the higher-resolution North American domain, (b) SO_4 in the Asian domain, (c) OA in the North American domain, and (d) OA in the Asian domain.

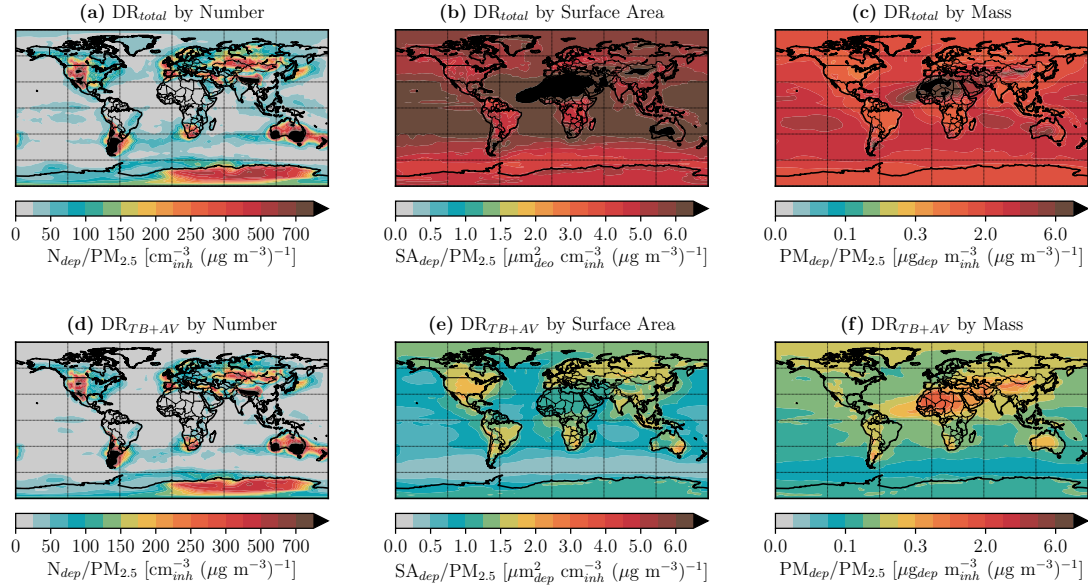


Figure 7.9: DR_{total} by (a) number (deposited number per ambient PM_{2.5} mass) and by (b) surface area (deposition dry surface area per ambient PM_{2.5} mass) and (c) mass (deposited mass per ambient PM_{2.5} mass) and DR_{TB+AV} by (d) number, (e) surface area, (f) mass.

7.3.4 Deposition ratios based on number and surface area

In addition to considering the health response due to different PM species, it has also been suggested that particle number and/or surface area may be key parameters influencing health response due to PM_{2.5} exposure (e.g., Breitner et al., 2011; Delfino et al., 2005; Peters et al., 1997, 2006; Valavanidis et al., 2008). To test the sensitivity to these other PM quantities, Figure 7.9a-c shows the DR_{total} based on (a) particle number concentration (total respiratory deposited number per unit ambient PM_{2.5} mass), (b) particle surface area concentration (total respiratory deposited dry surface area per unit ambient PM_{2.5} mass), and (c) particle mass concentration (total respiratory deposited mass per unit ambient PM_{2.5} mass). As seen in Figures 7.9a and b, DR_{total} based on number and surface area have substantially different geographic variability than the analogous DR_{total} based on mass (Figures 7.9c). The DR_{total} based on number has maxima in regions where new particle formation events are common but low overall PM_{2.5} mass concentration. This results in high concentrations of sub-50 nm particles, where the ICRP deposition curves have maximum

values (Figure 7.1). Such regions include the high-altitude regions of the Rocky Mountains and Himalayas, along with South Africa and South America. Maxima in DR_{total} by surface area and mass occur in desert regions where there is substantial coarse-mode mass at particle size with efficient deposition fractions in the head/nose region (Figure 7.1).

Similarly, in Figure 7.9d-f, we show the $DR_{\text{TB+AV}}$ based on **(d)** number, **(e)** surface area, **(f)** and mass. Figure 7.9f is identical to Figure 7.6a except with a different colorbar. Comparing DR_{total} to $DR_{\text{TB+AV}}$, much of the variability in respiratory deposition based on number is driven by deposition in the TB+AV. Conversely, much of the variability in deposition by surface area is driven by deposition in all respiratory regions (especially the head/nose regions). The spatial variability in $DR_{\text{TB+AV}}$ based on surface area seems to share features with $DR_{\text{TB+AV}}$ from both number (such as in the Rocky Mountains in the western US) and mass (such as in the Sahara). Deposition based on mass shows substantial variability for DR_{total} and $DR_{\text{TB+AV}}$, suggesting a high degree of variability due to ambient particle size distribution for each respiratory deposition site considered here. The spatial distributions present in Figure 7.9 demonstrate the potential variability in health response to $PM_{2.5}$ exposure if the health response to exposure is more strongly correlated to deposition by number, surface area, or mass. Given the $DR_{\text{TB+AV}}$ based on mass, surface area, and number show different spatial distributions, it is essential to understand what PM parameters control the health response to particle exposure.

7.3.5 Discussion and Conclusions

While studies consistently find a robust relationship with $PM_{2.5}$ exposure and negative health effects, variability in the health response to $PM_{2.5}$ exposure remains. The aim of this work is to motivate consideration of the role that particle size may play in determining the variability of the health response to $PM_{2.5}$ exposure. To explore this, we combine simulated aerosol size distributions from a chemical-transport model with a size-resolved particle dosimetry model to explore the geographic variability of deposited particle mass in the body. We find that on global scales, the ratio of deposited PM mass per unit ambient $PM_{2.5}$ mass in the tracheobronchial and alveolar regions

varies by 20-30% between different highly populated regions (e.g., eastern US vs. India) due to variability in ambient particle size distributions. This variability is also seen within countries using higher-resolution nested simulations. This variability is a reflection of local emissions and microphysical processes that affect ambient aerosol size distributions. In some regions, coarse-mode mass contributes a substantial portion of deposited PM mass in the tracheobronchial and alveolar regions. This mass is not included in ambient PM_{2.5} exposure measurements, resulting in variability up to a factor of 5 between regions dominated by fossil-fuel emissions (e.g., the eastern US and western Europe) and regions dominated by dust (e.g. North Africa).

To some degree, the variability in this deposition ratio is influenced by particle composition. While the ICRP model predicts deposition fractions of around 10% for particle diameters greater than 2.5 μm , the large mass concentration of coarse-mode dust in desert regions leads to high deposition ratios. This result further motivates the question of the toxicity of dust relative anthropogenic emitted species of sulfate, OA, and BC. We still find geographic variability on the order of 30% for sulfate and OA in the tracheobronchial and alveolar regions. As this spatial pattern is different than total PM mass, this further motivates understanding potential differential toxicity of PM chemical species. In addition to chemical composition, we also compared deposition ratios based on number and surface area and find the spatial variability is substantially different when based on number, surface area, or mass. These results show that regardless of the specific health impacts of individual PM species or parameters (number, surface area, mass), we may likely need to consider variability in the aerosol size distribution to fully connect exposure to dose and ultimately the health impacts.

A limitation of this work is the lack of observed aerosol size distributions. Long-term measurements of aerosol size distributions ranging from diameters of 1-10 nm to 5-10 μm are limited. Size distribution measurements in polluted regions sub-Saharan Africa, India, and China are especially limited. In this work, we use a sectional aerosol microphysical model (TOMAS) that has been shown to have skill in capturing the variability in long-term size-resolved aerosol measurements within size ranges commonly measured at sites in Europe and North America. Despite this skill, the coarse spatial and temporal resolution of the model reduces gradients in aerosol size distributions,

particularly in urban areas. This suggest that variability in aerosol size distributions at regional and continental scales may be greater than what is considered here. We also note here that there is likely substantial uncertainty in size-specific particle deposition fractions in various regions of the body. Despite these uncertainties, we know that particle deposition has a strong size dependence across several orders of magnitude in particle diameter, and geographic variability in aerosol size distributions has been commonly observed. The results of this work are a first step in exploring the geographic variability of respiratory particle deposition rates.

Chapter 8

Synthesis and future work

The scope of this dissertation sought to quantify estimates and identify key uncertainties in the climate and health impacts of atmospheric aerosol emitted from residential solid fuel use (SFU). We find that overall the aerosol radiative effects (the direct radiative effect and aerosol indirect effect) from residential SFU and trash combustion are largely uncertain and can range between positive and negative. Conversely, while major uncertainties remain in global mortality estimates, the global health burden is substantial and suggests that improving residential combustion sources in developing countries will likely greatly improve global health.

Limitations of SFU interventions due to nearby PM sources: The potential health benefits of improving air quality in developing countries through reducing residential SFU emissions are clear; however, important questions remain in the efficiency of certain emission mitigation plans. From a policy standpoint, a major source of uncertainty is whether to focus on household-level or village-level emission reduction plans. While intervention scenarios aimed at providing improved cookstoves or wood heaters may reduce indoor aerosol concentrations, there still may be major emissions at the village level that degrade air quality. These emissions may be from other combustion sources (such as trash fires) or household air pollution transported from other nearby homes. It is unclear to what degree mitigation programs need to focus on village-level ambient air quality compared to household-level air quality and if other non-SFU sources must also be reduced to gain substantial health benefits.

The importance of non-SFU sources in developing countries: In several chapters of this dissertation, we attempted to broaden the discussion above “household air pollution” to include other emission sources typical in developing countries. In quantifying the aerosol health impacts from residential trash fires, we can conclude that there are substantial emission sources affecting regional and global health not included in typical “household air pollution” inventories. Thus, even with

a successful household intervention program (such as providing cleaner-burning cookstoves to a village), there may still be substantial exposure from other combustion sources in the area.

Past cookstove intervention studies have suggested the influence on non-cookstove aerosol emission sources (such as trash fires) as a possible complexity in understanding changes in the observed health response from the intervention. Specifically, Mortimer et al. (2016) suggests trash fires and uncertainty in emission reductions from the improved cookstove as reasons for a null result in investigating the influence of a cookstove intervention on childhood pneumonia in rural Malawi. In calculating the combined exposure of household and ambient air pollution from all sources, we developed a framework that can be used in similar intervention studies to estimate health impacts from cookstove interventions while accounting for emissions from all other sources (such as trash fires) and uncertainties in the emissions of “improved” cookstoves. Use of the model developed in Chapter 4 for intervention programs is left for future work. Based on our initial results, we can generally conclude that while improvements to household emissions can provide a meaningful reduction in aerosol exposure, there will still be challenges (e.g., other emission sources) toward bringing air pollution exposure in developing countries to recommended guidelines (World Health Organization, 2006).

Impact of non-SFU PM on radiative effects of SFU PM: Aerosol emissions from other, non-SFU, sources may also significantly influence the aerosol-climate impacts attributed to residential SFU. Given the large emissions of black carbon (BC) in residential combustion sources, it is vital to understand the BC climate forcing to assess potential mitigation scenarios; however, the mixing state of BC remains a major uncertainty. Notably, our work constraining BC mixing state in the Arctic demonstrates the importance of non-BC aerosol in representing mixing state. Bias in representation of non-BC sources (including non-SFU sources) will impact the fraction of particles containing BC and the coating thickness around a BC core, leading to biased estimates of the direct radiative effect. Thus, it becomes important to not only quantify the BC emissions from residential SFU, but also the mixing between SFU particles and non-SFU particles through condensation and coagulation.

Climate and health impacts of near-source processing of aerosol properties: While the spatial resolution of global and regional climate models is increasing along with increasing computational resources, these models still lack sufficient spatial resolution to resolve aerosol impacts at the village level. Several of the chapters in this dissertation demonstrate the importance of representation of aerosol size distributions in investigating both aerosol climate and health impacts. Both the direct radiative effect and aerosol indirect effect from uncontrolled combustion of domestic waste are sensitive to emitted size distributions. We also found geographic variability in aerosol size distributions to impact BC mixing state and respiratory deposition. Currently, the horizontal resolution of global models cannot resolve microphysical processes that may be happening at length scales corresponding to villages and neighborhoods. It is unclear how emitted aerosol size distributions from residential SFU evolve from emissions near the combustion source, time spent indoors at high concentrations, and dilution at the village and regional levels. This evolution is likely impacted by surrounding emission sources (affecting coagulation, condensation, and nucleation rates). Notably, treatment of the volatility of organic aerosol from residential SFU in global and regional models is lacking in my work.

Aerosol sources will change in the future: While much of this dissertation focuses on emission sources typical in developing countries, the information presented here is useful in understanding future impacts of air pollution in developed countries. As increasing regulation and improving technology continues to reduce the highest anthropogenic aerosol sources in developed countries, there may be an increased contribution to ambient aerosol concentrations from biomass combustion sources. Cooking emissions in restaurants and biomass (especially wood) heaters and fireplaces in developed countries are already considered substantial aerosol sources in urban areas (Pandis et al., 2016). Additionally, biomass combustion in the form of wildfires has been increasing due to climate change (Westerling, 2016). As other emission sources decrease, the importance of understanding the climate and health impacts of biomass combustion becomes essential. Moreover, as regulation of many anthropogenic sources increases, it is becoming increasingly important to not only characterize the emission properties of aerosol, but also aerosol properties as they age.

The chemical components of organic aerosol may evolve as time spent in the atmosphere increases. It is possible that the health and climate relevant properties may evolve as chemical composition changes.

Mitigating household air pollution has the potential to substantially improve global health, particularly in developing countries where the mortality burden from air pollution is the highest. However, the results of this dissertation suggest that a more complex approach that considers all aerosol emission sources is needed better quantify aerosol climate and health impacts.

Bibliography

- P. Aalto, K. Hämeri, E. D. O. Becker, R. Weber, J. Salm, J. M. Mäkelä, C. Hoell, C. D. O'Dowd, H. Karlsson, H. Hansson, M. Väkevä, I. K. Koponen, G. Buzorius, and M. Kulmala. Physical characterization of aerosol particles during nucleation events. *Tellus, Series B: Chemical and Physical Meteorology*, 53(4):344–358, 2001. ISSN 02806509. doi: 10.1034/j.1600-0889.2001.d01-25.x.
- H. Abdul-Razzak and S. J. Ghan. A parameterization of aerosol activation 3. Sectional representation. *Journal of Geophysical Research*, 107(D3):4026, 2002. ISSN 0148-0227. doi: 10.1029/2001JD000483. URL <http://doi.wiley.com/10.1029/2001JD000483>.
- P. J. Adams and J. H. Seinfeld. Predicting global aerosol size distributions in general circulation models. *Journal of Geophysical Research*, 107(D19):4370, 2002. ISSN 0148-0227. doi: 10.1029/2001JD001010. URL <http://doi.wiley.com/10.1029/2001JD001010>.
- P. J. Adams and J. H. Seinfeld. Disproportionate impact of particulate emissions on global cloud condensation nuclei concentrations. *Geophysical Research Letters*, 30(5):n/a–n/a, mar 2003. ISSN 00948276. doi: 10.1029/2002GL016303. URL <http://onlinelibrary.wiley.com/doi/10.1029/2002GL016303/full>.
- A. Agarwal, K. Kirwa, M. N. Eliot, F. Alenezi, D. Menya, S. S. Mitter, E. J. Velazquez, R. Vedanthan, G. A. Wellenius, and G. S. Bloomfield. Household Air Pollution is Associated with Altered Cardiac Function Among Women in Kenya. *American Journal of Respiratory and Critical Care Medicine*, pages rccm.201704–0832LE, sep 2017. ISSN 1073-449X. doi: 10.1164/rccm.201704-0832LE. URL <http://www.atsjournals.org/doi/10.1164/rccm.201704-0832LE>.
- S. K. Akagi, R. J. Yokelson, C. Wiedinmyer, M. J. Alvarado, J. S. Reid, T. Karl, J. D. Crounse, and P. O. Wennberg. Emission factors for open and domestic biomass burning for use in atmospheric models. *Atmospheric Chemistry and Physics*, 11(9):4039–4072, may 2011. ISSN

- 1680-7324. doi: 10.5194/acp-11-4039-2011. URL <http://www.atmos-chem-phys.net/11/4039/2011/acp-11-4039-2011.html>.
- M. O. Andreae and A. Gelencsér. Black carbon or brown carbon? The nature of light-absorbing carbonaceous aerosols, 2006. ISSN 16807375.
- M. O. Andreae, C. D. Jones, and P. M. Cox. Strong present-day aerosol cooling implies a hot future. *Nature*, 435(7046):1187–1190, jun 2005. ISSN 0028-0836. URL <http://dx.doi.org/10.1038/nature03671>.
- S. C. Anenberg, L. W. Horowitz, D. Q. Tong, and J. J. West. An estimate of the global burden of anthropogenic ozone and fine particulate matter on premature human mortality using atmospheric modeling. *Environmental Health Perspectives*, 118(9):1189–1195, 2010. ISSN 00916765. doi: 10.1289/ehp.0901220.
- S. C. Anenberg, D. K. Henze, F. Lacey, A. Irfan, P. Kinney, G. Kleiman, and A. Pillarisetti. Air pollution-related health and climate benefits of clean cookstove programs in Mozambique. *Environmental Research Letters*, 12(2):025006, feb 2017. ISSN 1748-9326. doi: 10.1088/1748-9326/aa5557. URL <http://stacks.iop.org/1748-9326/12/i=2/a=025006?key=crossref.c7b27fa8078c16ed8d87df3fd856af87>.
- A. Anselm, T. Heibel, J. Gebhart, and G. Ferron. “In vivo”-studies of growth factors of sodium chloride particles in the human respiratory tract. *Journal of Aerosol Science*, 21:S427–S430, jan 1990. ISSN 0021-8502. doi: 10.1016/0021-8502(90)90272-Y. URL <https://www.sciencedirect.com/science/article/pii/002185029090272Y>.
- J. S. Apte, J. D. Marshall, A. J. Cohen, and M. Brauer. Addressing Global Mortality from Ambient PM_{2.5}. *Environmental Science & Technology*, 49(13):8057–8066, 2015. doi: 10.1021/acs.est.5b01236. URL <http://dx.doi.org/10.1021/acs.est.5b01236>.
- Arctic Monitoring and Assessment Programme. *AMAP Assessment 2015: Black carbon and ozone as Arctic climate forcers*. AMAP, 2015.

- K. Balakrishnan, S. Ghosh, B. Ganguli, S. Sambandam, N. Bruce, D. F. Barnes, and K. R. Smith. State and national household concentrations of PM_{2.5} from solid cookfuel use: Results from measurements and modeling in India for estimation of the global burden of disease. *Environmental Health*, 12(1):77, 2013. ISSN 1476-069X. doi: 10.1186/1476-069X-12-77. URL <http://dx.doi.org/10.1186/1476-069X-12-77>.
- G. A. Ban-Weiss, M. M. Lunden, T. W. Kirchstetter, and R. A. Harley. Size-resolved particle number and volume emission factors for on-road gasoline and diesel motor vehicles. *Journal of Aerosol Science*, 41:5–12, 2010. ISSN 00218502. doi: 10.1016/j.jaerosci.2009.08.001.
- J. T. Bates, R. J. Weber, J. Abrams, V. Verma, T. Fang, M. Klein, M. J. Strickland, S. E. Sarnat, H. H. Chang, J. A. Mulholland, P. E. Tolbert, and A. G. Russell. Reactive Oxygen Species Generation Linked to Sources of Atmospheric Particulate Matter and Cardiorespiratory Effects. *Environmental Science & Technology*, 49(22):13605–13612, nov 2015. ISSN 0013-936X. doi: 10.1021/acs.est.5b02967. URL <https://doi.org/10.1021/acs.est.5b02967>.
- S. E. Bauer, D. L. Wright, D. Koch, E. R. Lewis, R. McGraw, L.-S. Chang, S. E. Schwartz, and R. Ruedy. MATRIX (Multiconfiguration Aerosol TRacker of mIXing state): an aerosol microphysical module for global atmospheric models. *Atmospheric Chemistry and Physics*, 8(20):6003–6035, oct 2008. ISSN 1680-7324. doi: 10.5194/acp-8-6003-2008. URL <http://www.atmos-chem-phys.net/8/6003/2008/>.
- S. E. Bauer, S. Menon, D. Koch, T. C. Bond, and K. Tsigaridis. A global modeling study on carbonaceous aerosol microphysical characteristics and radiative effects. *Atmospheric Chemistry and Physics*, 10:7439–7456, 2010. ISSN 16807316. doi: 10.5194/acp-10-7439-2010.
- J. Baumgartner, J. J. Schauer, M. Ezzati, L. Lu, C. Cheng, J. Patz, and L. E. Bautista. Patterns and predictors of personal exposure to indoor air pollution from biomass combustion among women and children in rural China. *Indoor Air*, 21(6):479–488, dec 2011. ISSN 09056947. doi: 10.1111/j.1600-0668.2011.00730.x. URL <http://doi.wiley.com/10.1111/j.1600-0668.2011.00730.x>.

- R. Beelen, G. Hoek, P. A. van den Brandt, R. A. Goldbohm, P. Fischer, L. J. Schouten, M. Jerrett, E. Hughes, B. Armstrong, and B. Brunekreef. Long-Term Effects of Traffic-Related Air Pollution on Mortality in a Dutch Cohort (NLCS-AIR Study). *Environmental Health Perspectives*, 116(2): 196–202, feb 2008. ISSN 0091-6765. doi: 10.1289/ehp.10767. URL <http://www.ncbi.nlm.nih.gov/pmc/articles/PMC2235230/>.
- M. L. Bell, F. Dominici, K. Ebisu, S. L. Zeger, and J. M. Samet. Spatial and Temporal Variation in PM(2.5) Chemical Composition in the United States for Health Effects Studies. *Environmental Health Perspectives*, 115(7):989–995, jul 2007. ISSN 0091-6765. doi: 10.1289/ehp.9621. URL <http://www.ncbi.nlm.nih.gov/pmc/articles/PMC1913582/>.
- N. Bellouin, J. Rae, A. Jones, C. Johnson, J. Haywood, and O. Boucher. Aerosol forcing in the Climate Model Intercomparison Project (CMIP5) simulations by HadGEM2-ES and the role of ammonium nitrate. *Journal of Geophysical Research*, 116(D20):D20206, oct 2011. ISSN 0148-0227. doi: 10.1029/2011JD016074. URL <http://doi.wiley.com/10.1029/2011JD016074>.
- N. Bellouin, G. W. Mann, M. T. Woodhouse, C. Johnson, K. S. Carslaw, and M. Dalvi. Impact of the modal aerosol scheme GLOMAP-mode on aerosol forcing in the Hadley Centre Global Environmental Model. *Atmospheric Chemistry and Physics*, 13(6):3027–3044, mar 2013. ISSN 1680-7324. doi: 10.5194/acp-13-3027-2013. URL <http://www.atmos-chem-phys.net/13/3027/2013/acp-13-3027-2013.html>.
- I. Bey, D. J. Jacob, R. M. Yantosca, J. A. Logan, B. D. Field, A. M. Fiore, Q. Li, H. Y. Liu, L. J. Mickley, and M. G. Schultz. Global modeling of tropospheric chemistry with assimilated meteorology: Model description and evaluation. *Journal of Geophysical Research: Atmospheres*, 106(D19):23073–23095, oct 2001. ISSN 01480227. doi: 10.1029/2001JD000807. URL <http://doi.wiley.com/10.1029/2001JD000807>.
- Q. Bian, S. H. Jathar, J. K. Kodros, K. C. Barsanti, L. E. Hatch, A. A. May, S. M. Kreidenweis, and J. R. Pierce. Secondary organic aerosol formation in biomass-burning plumes: theoretical analysis

- of lab studies and ambient plumes. *Atmospheric Chemistry and Physics*, 17(8):5459–5475, apr 2017. ISSN 1680-7324. doi: 10.5194/acp-17-5459-2017. URL <http://www.atmos-chem-phys.net/17/5459/2017/>.
- F. S. Binkowski and U. Shankar. The Regional Particulate Matter Model: 1. Model description and preliminary results. *Journal of Geophysical Research*, 100(D12):26191, dec 1995. ISSN 0148-0227. doi: 10.1029/95JD02093. URL <http://onlinelibrary.wiley.com/doi/10.1029/95JD02093/abstract>.
- C. F. Bohren and D. R. Huffman. *Absorption and scattering of light by small particles*, volume 98. 1983. ISBN 047105772X. doi: 10.1038/ncomms1111. URL <http://adsabs.harvard.edu/abs/1983uaz..rept....B>.
- T. C. Bond and R. W. Bergstrom. Light Absorption by Carbonaceous Particles: An Investigative Review. *Aerosol Science and Technology*, 40(1):27–67, jan 2006. ISSN 0278-6826. doi: 10.1080/02786820500421521. URL <http://www.tandfonline.com/doi/abs/10.1080/02786820500421521>.
- T. C. Bond, D. G. Streets, K. F. Yarber, S. M. Nelson, J. H. Woo, and Z. Klimont. A technology-based global inventory of black and organic carbon emissions from combustion. *Journal of Geophysical Research*, 109(D14):D14203, 2004. ISSN 0148-0227. doi: 10.1029/2003JD003697. URL <http://doi.wiley.com/10.1029/2003JD003697>.
- T. C. Bond, G. Habib, and R. W. Bergstrom. Limitations in the enhancement of visible light absorption due to mixing state. *Journal of Geophysical Research*, 111(D20):D20211, oct 2006. ISSN 0148-0227. doi: 10.1029/2006JD007315. URL <http://doi.wiley.com/10.1029/2006JD007315>.
- T. C. Bond, E. Bhardwaj, R. Dong, R. Jogani, S. Jung, C. Roden, D. G. Streets, and N. M. Trautmann. Historical emissions of black and organic carbon aerosol from energy-related combustion, 1850-2000. *Global Biogeochemical Cycles*, 21(2), jun 2007. ISSN 08866236. doi: 10.1029/2006GB002840. URL <http://onlinelibrary.wiley.com/doi/10.1029/2006GB002840/full>.

- T. C. Bond, S. J. Doherty, D. W. Fahey, P. M. Forster, T. Berntsen, B. J. DeAngelo, M. G. Flanner, S. Ghan, B. Kärcher, D. Koch, S. Kinne, Y. Kondo, P. K. Quinn, M. C. Sarofim, M. G. Schultz, M. Schulz, C. Venkataraman, H. Zhang, S. Zhang, N. Bellouin, S. K. Guttikunda, P. K. Hopke, M. Z. Jacobson, J. W. Kaiser, Z. Klimont, U. Lohmann, J. P. Schwarz, D. Shindell, T. Storelvmo, S. G. Warren, and C. S. Zender. Bounding the role of black carbon in the climate system: A scientific assessment. *Journal of Geophysical Research: Atmospheres*, 118(11):5380–5552, jun 2013. ISSN 2169897X. doi: 10.1002/jgrd.50171. URL <http://doi.wiley.com/10.1002/jgrd.50171>.
- S. Bonjour, H. Adair-Rohani, J. Wolf, N. G. Bruce, S. Mehta, A. Prüss-Ustün, M. Lahiff, E. A. Rehfuess, V. Mishra, and K. R. Smith. Solid Fuel Use for Household Cooking: Country and Regional Estimates for 1980–2010. *Environmental Health Perspectives*, 121(7):784–790, jul 2013. ISSN 0091-6765. doi: 10.1289/ehp.1205987. URL <http://www.ncbi.nlm.nih.gov/pmc/articles/PMC3701999/>.
- O. Boucher, D. Randall, P. Artaxo, C. Bretherton, G. Feingold, P. Forster, V.-M. Kerminen, Y. Kondo, H. Liao, U. Lohmann, P. Rasch, S. Satheesh, S. Sherwood, B. Stevens, and X. Zhang. *Clouds and Aerosols. In: Climate Change 2013: The Physical Science Basis. Contribution of Working Group I to the Fifth Assessment Report of the Intergovernmental Panel on Climate Change*. Cambridge University Press, Cambridge, United Kingdom and New York, NY, USA, 2013.
- A. Bougiatioti, I. Stavroulas, E. Kostenidou, P. Zarnpas, C. Theodosi, G. Kouvarakis, F. Canonaco, A. S. H. Prévôt, A. Nenes, S. N. Pandis, and N. Mihalopoulos. Processing of biomass-burning aerosol in the eastern Mediterranean during summertime. *Atmospheric Chemistry and Physics*, 14(9):4793–4807, may 2014. ISSN 1680-7324. doi: 10.5194/acp-14-4793-2014. URL <http://www.atmos-chem-phys.net/14/4793/2014/>.
- M. Brauer, G. Hoek, P. Van Vliet, K. Meliefste, P. H. Fischer, A. Wijga, L. P. Koopman, H. J. Neijens, J. Gerritsen, M. Kerkhof, J. Heinrich, T. Bellander, and B. Brunekreef. Air Pollution from Traffic and the Development of Respiratory Infections and Asthmatic and Allergic Symptoms in Children. *American Journal of Respiratory and Critical Care Medicine*, 166(8):1092–1098, oct

2002. ISSN 1073-449X. doi: 10.1164/rccm.200108-007OC. URL <https://doi.org/10.1164/rccm.200108-007OC>.
- S. Breitner, L. Liu, J. Cyrus, I. Brüske, U. Franck, U. Schlink, A. M. Leitte, O. Herbarth, A. Wiedensohler, B. Wehner, M. Hu, X.-C. Pan, H.-E. Wichmann, and A. Peters. Sub-micrometer particulate air pollution and cardiovascular mortality in Beijing, China. *Science of The Total Environment*, 409(24):5196–5204, nov 2011. ISSN 0048-9697. doi: 10.1016/J.SCITOTENV.2011.08.023. URL <https://www.sciencedirect.com/science/article/pii/S0048969711008874>.
- J. F. Brewer, M. Bishop, M. Kelp, C. A. Keller, A. R. Ravishankara, and E. V. Fischer. A sensitivity analysis of key natural factors in the modeled global acetone budget. *Journal of Geophysical Research: Atmospheres*, 122(3):2043–2058, feb 2017. ISSN 2169897X. doi: 10.1002/2016JD025935. URL <http://doi.wiley.com/10.1002/2016JD025935>.
- C. A. Brock, J. Cozic, R. Bahreini, K. D. Froyd, A. M. Middlebrook, A. McComiskey, J. Brioude, O. R. Cooper, A. Stohl, K. C. Aikin, J. A. de Gouw, D. W. Fahey, R. A. Ferrare, R.-S. Gao, W. Gore, J. S. Holloway, G. Hübler, A. Jefferson, D. A. Lack, S. Lance, R. H. Moore, D. M. Murphy, A. Nenes, P. C. Novelli, J. B. Nowak, J. A. Ogren, J. Peischl, R. B. Pierce, P. Pilewskie, P. K. Quinn, T. B. Ryerson, K. S. Schmidt, J. P. Schwarz, H. Sodemann, J. R. Spackman, H. Stark, D. S. Thomson, T. Thornberry, P. Veres, L. A. Watts, C. Warneke, and A. G. Wollny. Characteristics, sources, and transport of aerosols measured in spring 2008 during the aerosol, radiation, and cloud processes affecting arctic climate (arcpac) project. *Atmospheric Chemistry and Physics*, 11(6):2423–2453, 2011.
- R. D. Brook, S. Rajagopalan, C. A. Pope, J. R. Brook, A. Bhatnagar, A. V. Diez-Roux, F. Holguin, Y. Hong, R. V. Luepker, M. A. Mittleman, A. Peters, D. Siscovick, S. C. Smith, L. Whitsel, and J. D. Kaufman. Particulate Matter Air Pollution and Cardiovascular Disease. *Circulation*, 121(21):2331 LP – 2378, jun 2010. URL <http://circ.ahajournals.org/content/121/21/2331.abstract>.
- J. Browse, K. S. Carslaw, S. R. Arnold, K. Pringle, and O. Boucher. The scavenging processes controlling the seasonal cycle in Arctic sulphate and black carbon aerosol. *Atmospheric Chemistry*

and Physics, 12(15):6775–6798, aug 2012. ISSN 1680-7324. doi: 10.5194/acp-12-6775-2012.
URL <http://www.atmos-chem-phys.net/12/6775/2012/>.

J. Burkart, M. D. Willis, H. Bozem, J. L. Thomas, K. Law, P. Hoor, A. A. Aliabadi, F. Köllner, J. Schneider, A. Herber, J. P. D. Abbatt, and W. R. Leaitch. Summertime observations of elevated levels of ultrafine particles in the high arctic marine boundary layer. *Atmospheric Chemistry and Physics*, 17(8):5515–5535, 2017.

R. T. Burnett, C. Arden Pope, M. Ezzati, C. Olives, S. S. Lim, S. Mehta, H. H. Shin, G. Singh, B. Hubbell, M. Brauer, H. Ross Anderson, K. R. Smith, J. R. Balmes, N. G. Bruce, H. Kan, F. Laden, A. Prüss-Ustün, M. C. Turner, S. M. Gapstur, W. R. Diver, and A. Cohen. An integrated risk function for estimating the global burden of disease attributable to ambient fine particulate matter exposure. *Environmental Health Perspectives*, 122(4):397–403, 2014. ISSN 15529924. doi: 10.1289/ehp.1307049.

E. W. Butt, A. Rap, A. Schmidt, C. E. Scott, K. J. Pringle, C. L. Reddington, N. A. D. Richards, M. T. Woodhouse, J. Ramirez-Villegas, H. Yang, V. Vakkari, E. A. Stone, M. Rupakheti, P. S. Praveen, P. G. van Zyl, J. P. Beukes, M. Josipovic, E. J. S. Mitchell, S. M. Sallu, P. M. Forster, and D. V. Spracklen. The impact of residential combustion emissions on atmospheric aerosol, human health, and climate. *Atmospheric Chemistry and Physics*, 16(2):873–905, jan 2016. ISSN 1680-7324. doi: 10.5194/acp-16-873-2016. URL <http://www.atmos-chem-phys.net/16/873/2016/>.

Y. Cai, D. C. Montague, W. Mooiweer-Bryan, and T. Deshler. Performance characteristics of the ultra high sensitivity aerosol spectrometer for particles between 55 and 800 nm: Laboratory and field studies. *Journal of aerosol science*, 39(9):759–769, 2008.

C. D. Cappa, T. B. Onasch, P. Massoli, D. R. Worsnop, T. S. Bates, E. S. Cross, P. Davidovits, J. Hakala, K. L. Hayden, B. T. Jobson, K. R. Kolesar, D. a. Lack, B. M. Lerner, S.-M. Li, D. Mellon, I. Nuaaman, J. S. Olfert, T. Petäjä, P. K. Quinn, C. Song, R. Subramanian, E. J. Williams, and R. a. Zaveri. Radiative absorption enhancements due to the mixing state of

- atmospheric black carbon. *Science (New York, N.Y.)*, 337(6098):1078–81, aug 2012. ISSN 1095-9203. doi: 10.1126/science.1223447. URL <http://www.ncbi.nlm.nih.gov/pubmed/22936774>.
- I. M. Carey, R. W. Atkinson, A. J. Kent, T. van Staa, D. G. Cook, and H. R. Anderson. Mortality Associations with Long-Term Exposure to Outdoor Air Pollution in a National English Cohort. *American Journal of Respiratory and Critical Care Medicine*, 187(11):1226–1233, apr 2013. ISSN 1073-449X. doi: 10.1164/rccm.201210-1758OC. URL <https://doi.org/10.1164/rccm.201210-1758OC>.
- C. M. Carrico, M. D. Petters, S. M. Kreidenweis, A. P. Sullivan, G. R. McMeeking, E. J. T. Levin, G. Engling, W. C. Malm, and J. L. Collett. Water uptake and chemical composition of fresh aerosols generated in open burning of biomass. *Atmospheric Chemistry and Physics*, 10(11):5165–5178, jun 2010. ISSN 1680-7324. doi: 10.5194/acp-10-5165-2010. URL <http://www.atmos-chem-phys.net/10/5165/2010/>.
- K. S. Carslaw, L. A. Lee, C. L. Reddington, K. J. Pringle, A. Rap, P. M. Forster, G. W. Mann, D. V. Spracklen, M. T. Woodhouse, L. A. Regayre, and J. R. Pierce. Large contribution of natural aerosols to uncertainty in indirect forcing. *Nature*, 503(7474):67–71, nov 2013. ISSN 0028-0836. URL <http://dx.doi.org/10.1038/nature12674>.
- G. Cesaroni, C. Badaloni, C. Gariazzo, M. Stafoggia, R. Sozzi, M. Davoli, and F. Forastiere. Long-Term Exposure to Urban Air Pollution and Mortality in a Cohort of More than a Million Adults in Rome. *Environmental Health Perspectives*, 121(3):324–331, mar 2013. ISSN 0091-6765. doi: 10.1289/ehp.1205862. URL <http://www.ncbi.nlm.nih.gov/pmc/articles/PMC3621202/>.
- Z. A. Chafe, M. Brauer, Z. Klimont, R. Van Dingenen, S. Mehta, S. Rao, K. Riahi, F. Dentener, and K. R. Smith. Household Cooking with Solid Fuels Contributes to Ambient PM(2.5) Air Pollution and the Burden of Disease, dec 2014. ISSN 0091-6765 (Print).

- R. J. Charlson, S. E. Schwartz, J. M. Hales, R. D. Cess, J. A. Coakley, J. E. Hansen, and D. J. Hofmann. Climate forcing by anthropogenic aerosols. *Science (New York, N.Y.)*, 255:423–430, 1992. ISSN 0036-8075. doi: 10.1126/science.255.5043.423.
- L. H. Chen, S. F. Knutsen, D. Shavlik, W. L. Beeson, F. Petersen, M. Ghamsary, and D. Abbey. The Association between Fatal Coronary Heart Disease and Ambient Particulate Air Pollution: Are Females at Greater Risk? *Environmental Health Perspectives*, 113(12):1723–1729, dec 2005. ISSN 0091-6765. doi: 10.1289/ehp.8190. URL <http://www.ncbi.nlm.nih.gov/pmc/articles/PMC1314912/>.
- Y. Chen and T. C. Bond. Light absorption by organic carbon from wood combustion. *Atmospheric Chemistry and Physics*, 10(4):1773–1787, feb 2010. ISSN 1680-7324. doi: 10.5194/acp-10-1773-2010. URL <http://www.atmos-chem-phys.net/10/1773/2010/acp-10-1773-2010.html>.
- S. Chowdhury and S. Dey. Cause-specific premature death from ambient PM_{2.5} exposure in India: Estimate adjusted for baseline mortality. *Environment International*, 91:283–290, 2016. ISSN 01604120. doi: 10.1016/j.envint.2016.03.004.
- T. J. Christian, R. J. Yokelson, B. Cárdenas, L. T. Molina, G. Engling, and S.-C. Hsu. Trace gas and particle emissions from domestic and industrial biofuel use and garbage burning in central Mexico. *Atmospheric Chemistry and Physics*, 10(2):565–584, jan 2010. ISSN 1680-7324. doi: 10.5194/acp-10-565-2010. URL <http://www.atmos-chem-phys.net/10/565/2010/acp-10-565-2010.html>.
- S. H. Chung and J. H. Seinfeld. Climate response of direct radiative forcing of anthropogenic black carbon. *Journal of Geophysical Research*, 110:D11102, 2005. ISSN 0148-0227. doi: 10.1029/2004JD005441. URL <http://www.agu.org/pubs/crossref/2005/2004JD005441.shtml>.
- M. Clark, S. J. Reynolds, J. B. Burch, S. Conway, A. M. Bachand, and J. L. Peel. Indoor air pollution, cookstove quality, and housing characteristics in two Honduran communities. *Environmental Research*, 110(1):12–18, 2010. ISSN 00139351. doi: 10.1016/j.envres.2009.10.008.

- M. Clark, A. M. Bachand, J. M. Heiderscheidt, S. A. Yoder, B. Luna, J. Volckens, K. A. Koehler, S. Conway, S. J. Reynolds, and J. L. Peel. Impact of a cleaner-burning cookstove intervention on blood pressure in Nicaraguan women. *Indoor Air*, 23(2):105–114, apr 2013. ISSN 09056947. doi: 10.1111/ina.12003. URL <http://doi.wiley.com/10.1111/ina.12003>.
- S. Clark, E. Carter, M. Shan, K. Ni, H. Niu, J. T. W. Tseng, S. K. Pattanayak, M. Jeuland, J. J. Schauer, M. Ezzati, C. Wiedinmyer, X. Yang, and J. Baumgartner. Adoption and use of a semi-gasifier cooking and water heating stove and fuel intervention in the Tibetan Plateau, China. *Environmental Research Letters*, 12(7):075004, jul 2017. ISSN 1748-9326. doi: 10.1088/1748-9326/aa751e. URL <http://stacks.iop.org/1748-9326/12/i=7/a=075004?key=crossref.04d09918c8dc46cd01c64ab0005e9144>.
- A. J. Cohen, M. Brauer, R. Burnett, H. R. Anderson, J. Frostad, K. Estep, K. Balakrishnan, B. Brunekreef, L. Dandona, R. Dandona, V. Feigin, G. Freedman, B. Hubbell, A. Jobling, H. Kan, L. Knibbs, Y. Liu, R. Martin, L. Morawska, C. A. Pope, H. Shin, K. Straif, G. Shaddick, M. Thomas, R. van Dingenen, A. van Donkelaar, T. Vos, C. J. L. Murray, and M. H. Forouzanfar. Estimates and 25-year trends of the global burden of disease attributable to ambient air pollution: an analysis of data from the Global Burden of Diseases Study 2015. *The Lancet*, 389(10082):1907–1918, may 2017. ISSN 01406736. doi: 10.1016/S0140-6736(17)30505-6. URL <http://linkinghub.elsevier.com/retrieve/pii/S0140673617305056>.
- W. J. Collins, N. Bellouin, M. Doutriaux-Boucher, N. Gedney, P. Halloran, T. Hinton, J. Hughes, C. D. Jones, M. Joshi, S. Liddicoat, G. Martin, F. O’Connor, J. Rae, C. Senior, S. Sitch, I. Totterdell, A. Wiltshire, and S. Woodward. Development and evaluation of an Earth-System model – HadGEM2. *Geoscientific Model Development*, 4(4):1051–1075, nov 2011. ISSN 1991-9603. doi: 10.5194/gmd-4-1051-2011. URL <http://www.geosci-model-dev.net/4/1051/2011/>.
- L. Conibear, E. W. Butt, C. Knote, S. R. Arnold, and D. V. Spracklen. Residential energy use emissions dominate health impacts from exposure to ambient particulate matter in India. *Nature*

- Communications*, 9(1):617, 2018. ISSN 2041-1723. doi: 10.1038/s41467-018-02986-7. URL <https://doi.org/10.1038/s41467-018-02986-7>.
- J. J. Corbett, J. J. Winebrake, E. H. Green, P. Kasibhatla, V. Eyring, and A. Lauer. Mortality from Ship Emissions: A Global Assessment. *Environmental Science & Technology*, 41(24):8512–8518, dec 2007. ISSN 0013-936X. doi: 10.1021/es071686z. URL <http://dx.doi.org/10.1021/es071686z>.
- B. Croft, U. Lohmann, and K. von Salzen. Black carbon ageing in the Canadian Centre for Climate modelling and analysis atmospheric general circulation model. *Atmospheric Chemistry and Physics*, 5(7):1931–1949, jul 2005. ISSN 1680-7324. doi: 10.5194/acp-5-1931-2005. URL <http://www.atmos-chem-phys.net/5/1931/2005/>.
- B. Croft, J. R. Pierce, R. V. Martin, C. Hoose, and U. Lohmann. Uncertainty associated with convective wet removal of entrained aerosols in a global climate model. *Atmospheric Chemistry and Physics*, 12(22):10725–10748, nov 2012. ISSN 1680-7324. doi: 10.5194/acp-12-10725-2012. URL <http://www.atmos-chem-phys.net/12/10725/2012/>.
- B. Croft, R. V. Martin, W. R. Leaitch, P. Tunved, T. J. Breider, S. D. D'Andrea, and J. R. Pierce. Processes controlling the annual cycle of Arctic aerosol number and size distributions. *Atmospheric Chemistry and Physics*, 16(6):3665–3682, mar 2016a. ISSN 1680-7324. doi: 10.5194/acp-16-3665-2016. URL <http://www.atmos-chem-phys.net/16/3665/2016/>.
- B. Croft, G. R. Wentworth, R. V. Martin, W. R. Leaitch, J. G. Murphy, B. N. Murphy, J. K. Kodros, J. P. D. Abbatt, and J. R. Pierce. Contribution of Arctic seabird-colony ammonia to atmospheric particles and cloud-albedo radiative effect. *Nature Communications*, 7:13444, nov 2016b. URL <http://dx.doi.org/10.1038/ncomms13444><http://10.0.4.14/ncomms13444><http://www.nature.com/articles/ncomms13444#supplementary-information>.
- D. L. Crouse, P. A. Peters, A. van Donkelaar, M. S. Goldberg, P. J. Villeneuve, O. Brion, S. Khan, D. O. Atari, M. Jerrett, C. A. Pope, M. Brauer, J. R. Brook, R. V. Martin, D. Stieb, and R. T. Burnett. Risk of Nonaccidental and Cardiovascular Mortality in Relation to Long-term

- Exposure to Low Concentrations of Fine Particulate Matter: A Canadian National-Level Cohort Study. *Environmental Health Perspectives*, 120(5):708–714, may 2012. ISSN 0091-6765. doi: 10.1289/ehp.1104049. URL <http://www.ncbi.nlm.nih.gov/pmc/articles/PMC3346774/>.
- S. D. D’Andrea, S. a. K. Häkkinen, D. M. Westervelt, C. Kuang, E. J. T. Levin, V. P. Kanawade, W. R. Leitch, D. V. Spracklen, I. Riipinen, and J. R. Pierce. Understanding global secondary organic aerosol amount and size-resolved condensational behavior. *Atmospheric Chemistry and Physics*, 13(22):11519–11534, nov 2013. ISSN 1680-7324. doi: 10.5194/acp-13-11519-2013. URL <http://www.atmos-chem-phys.net/13/11519/2013/>.
- S. D. D’Andrea, J. C. Acosta Navarro, S. C. Farina, C. E. Scott, A. Rap, D. K. Farmer, D. V. Spracklen, I. Riipinen, and J. R. Pierce. Aerosol size distribution and radiative forcing response to anthropogenically driven historical changes in biogenic secondary organic aerosol formation. *Atmospheric Chemistry and Physics*, 15(5):2247–2268, mar 2015. ISSN 1680-7324. doi: 10.5194/acp-15-2247-2015. URL <http://www.atmos-chem-phys.net/15/2247/2015/acp-15-2247-2015.html>.
- R. J. Delfino, C. Sioutas, and S. Malik. Potential Role of Ultrafine Particles in Associations between Airborne Particle Mass and Cardiovascular Health. *Environmental Health Perspectives*, 113(8): 934–946, aug 2005. ISSN 0091-6765. doi: 10.1289/ehp.7938. URL <http://www.ncbi.nlm.nih.gov/pmc/articles/PMC1280331/>.
- F. Dentener, J. Drevet, J. F. Lamarque, I. Bey, B. Eickhout, A. M. Fiore, D. Hauglustaine, L. W. Horowitz, M. Krol, U. C. Kulshrestha, M. Lawrence, C. Galy-Lacaux, S. Rast, D. Shindell, D. Stevenson, T. Van Noije, C. Atherton, N. Bell, D. Bergman, T. Butler, J. Cofala, B. Collins, R. Doherty, K. Ellingsen, J. Galloway, M. Gauss, V. Montanaro, J. F. Müller, G. Pitari, J. Rodriguez, M. Sanderson, F. Solmon, S. Strahan, M. Schultz, K. Sudo, S. Szopa, and O. Wild. Nitrogen and sulfur deposition on regional and global scales: A multimodel evaluation. *Global Biogeochemical Cycles*, 20(4):n/a–n/a, dec 2006. ISSN 08866236. doi: 10.1029/2005GB002672. URL <http://doi.wiley.com/10.1029/2005GB002672>.

- R. Detchon and R. V. Leeuwen. Bring sustainable energy to the developing world. *Nature Comment*, pages 5–7, 2011.
- D. W. Dockery, C. A. Pope, X. Xu, J. D. Spengler, J. H. Ware, M. E. Fay, B. G. Ferris, and F. E. Speizer. An Association between Air Pollution and Mortality in Six U.S. Cities. *New England Journal of Medicine*, 329(24):1753–1759, dec 1993. ISSN 0028-4793. doi: 10.1056/NEJM199312093292401. URL <http://dx.doi.org/10.1056/NEJM199312093292401>.
- L. J. Donner, B. L. Wyman, R. S. Hemler, L. W. Horowitz, Y. Ming, M. Zhao, J.-C. Golaz, P. Ginoux, S.-J. Lin, M. D. Schwarzkopf, J. Austin, G. Alaka, W. F. Cooke, T. L. Delworth, S. M. Freidenreich, C. T. Gordon, S. M. Griffies, I. M. Held, W. J. Hurlin, S. A. Klein, T. R. Knutson, A. R. Langenhorst, H.-C. Lee, Y. Lin, B. I. Magi, S. L. Malyshev, P. C. D. Milly, V. Naik, M. J. Nath, R. Pincus, J. J. Ploshay, V. Ramaswamy, C. J. Seman, E. Shevliakova, J. J. Sirutis, W. F. Stern, R. J. Stouffer, R. J. Wilson, M. Winton, A. T. Wittenberg, and F. Zeng. The Dynamical Core, Physical Parameterizations, and Basic Simulation Characteristics of the Atmospheric Component AM3 of the GFDL Global Coupled Model CM3. *Journal of Climate*, 24(13):3484–3519, jul 2011. ISSN 0894-8755. doi: 10.1175/2011JCLI3955.1. URL <http://journals.ametsoc.org/doi/abs/10.1175/2011JCLI3955.1{#}.V7GofL1zAYs.mendeley>.
- E. J. Dunlea, P. F. DeCarlo, A. C. Aiken, J. R. Kimmel, R. E. Peltier, R. J. Weber, J. Tomlinson, D. R. Collins, Y. Shinozuka, C. S. McNaughton, S. G. Howell, A. D. Clarke, L. K. Emmons, E. C. Apel, G. G. Pfister, A. van Donkelaar, R. V. Martin, D. B. Millet, C. L. Heald, and J. L. Jimenez. Evolution of Asian aerosols during transpacific transport in INTEX-B. *Atmospheric Chemistry and Physics*, 9(19):7257–7287, oct 2009. ISSN 1680-7324. doi: 10.5194/acp-9-7257-2009. URL <http://www.atmos-chem-phys.net/9/7257/2009/>.
- U. Dusek, G. P. Frank, L. Hildebrandt, J. Curtius, J. Schneider, S. Walter, D. Chand, F. Drewnick, S. Hings, D. Jung, S. Borrmann, and M. O. Andreae. Size matters more than chemistry for cloud-nucleating ability of aerosol particles. *Science (New York, N.Y.)*, 312(5778):1375–8, jun

2006. ISSN 1095-9203. doi: 10.1126/science.1125261. URL <http://science.sciencemag.org/content/312/5778/1375.abstract>.

J. Evans, A. van Donkelaar, R. V. Martin, R. Burnett, D. G. Rainham, N. J. Birkett, and D. Krewski. Estimates of global mortality attributable to particulate air pollution using satellite imagery. *Environmental research*, 120:33–42, jan 2013. ISSN 1096-0953. doi: 10.1016/j.envres.2012.08.005. URL <http://www.sciencedirect.com/science/article/pii/S001393511200240X>.

T. Fang, H. Guo, L. Zeng, V. Verma, A. Nenes, and R. J. Weber. Highly Acidic Ambient Particles, Soluble Metals, and Oxidative Potential: A Link between Sulfate and Aerosol Toxicity. *Environmental Science & Technology*, 51(5):2611–2620, mar 2017. ISSN 0013-936X. doi: 10.1021/acs.est.6b06151. URL <https://doi.org/10.1021/acs.est.6b06151>.

S. D. Fernandes, N. M. Trautmann, D. G. Streets, C. a. Roden, and T. C. Bond. Global biofuel use, 1850-2000. *Global Biogeochemical Cycles*, 21(2), jun 2007. ISSN 08866236. doi: 10.1029/2006GB002836. URL <http://doi.wiley.com/10.1029/2006GB002836>.

B. Ford and C. L. Heald. Exploring the uncertainty associated with satellite-based estimates of premature mortality due to exposure to fine particulate matter. *Atmospheric Chemistry and Physics*, 16(5):3499–3523, mar 2016. ISSN 1680-7324. doi: 10.5194/acp-16-3499-2016. URL <http://www.atmos-chem-phys.net/16/3499/2016/acp-16-3499-2016.html>.

M. H. Forouzanfar, A. Afshin, L. T. Alexander, H. R. Anderson, Z. A. Bhutta, S. Biryukov, M. Brauer, R. Burnett, K. Cercy, F. J. Charlson, A. J. Cohen, L. Dandona, K. Estep, A. J. Ferrari, J. J. Frostad, N. Fullman, P. W. Gething, W. W. Godwin, M. Griswold, S. I. Hay, Y. Kinfu, H. H. Kyu, H. J. Larson, X. Liang, S. S. Lim, P. Y. Liu, A. D. Lopez, R. Lozano, L. Marczak, G. A. Mensah, A. H. Mokdad, M. Moradi-Lakeh, M. Naghavi, B. Neal, M. B. Reitsma, G. A. Roth, J. A. Salomon, P. J. Sur, T. Vos, J. A. Wagner, H. Wang, Y. Zhao, M. Zhou, G. M. Aasvang, A. A. Abajobir, K. H. Abate, C. Abbafati, K. M. Abbas, F. Abd-Allah, A. M. Abdulle, S. F. Abera, B. Abraham, L. J. Abu-Raddad, G. Y. Abyu, A. O. Adebisi, I. A. Adedeji, Z. Ademi, A. K.

Adou, J. C. Adsuar, E. E. Agardh, A. Agarwal, A. Agrawal, A. A. Kiadaliri, O. N. Ajala, T. F. Akinyemiju, Z. Al-Aly, K. Alam, N. K. M. Alam, S. F. Aldahri, R. W. Aldridge, Z. A. Alemu, R. Ali, A. Alkerwi, F. Alla, P. Allebeck, U. Alsharif, K. A. Altirkawi, E. A. Martin, N. Alvis-Guzman, A. T. Amare, A. Amberbir, A. K. Amegah, H. Amini, W. Ammar, S. M. Amrock, H. H. Andersen, B. O. Anderson, C. A. T. Antonio, P. Anwari, J. Ärnlöv, A. Artaman, H. Asayesh, R. J. Asghar, R. Assadi, S. Atique, E. F. G. A. Avokpaho, A. Awasthi, B. P. A. Quintanilla, P. Azzopardi, U. Bacha, A. Badawi, M. C. Bahit, K. Balakrishnan, A. Barac, R. M. Barber, S. L. Barker-Collo, T. Bärnighausen, S. Barquera, L. Barregard, L. H. Barrero, S. Basu, C. Batis, S. Bazargan-Hejazi, J. Beardsley, N. Bedi, E. Beghi, B. Bell, M. L. Bell, A. K. Bello, D. A. Bennett, I. M. Bensor, A. Berhane, E. Bernabé, B. D. Betsu, A. S. Beyene, N. Bhala, A. Bhansali, S. Bhatt, S. Biadgilign, B. Bikbov, D. Bisanzio, E. Bjertness, J. D. Blore, R. Borschmann, S. Boufous, R. R. A. Bourne, M. Brainin, A. Brazinova, N. J. K. Breitborde, H. Brenner, D. M. Broday, T. S. Brugha, B. Brunekreef, Z. A. Butt, L. E. Cahill, B. Calabria, I. R. Campos-Nonato, R. Cárdenas, D. O. Carpenter, J. J. Carrero, D. C. Casey, C. A. Castañeda-Orjuela, J. C. Rivas, R. E. Castro, F. Catalá-López, J.-C. Chang, P. P.-C. Chiang, M. Chibalabala, O. Chimed-Ochir, V. H. Chisumpa, A. A. Chitheer, J.-Y. J. Choi, H. Christensen, D. J. Christopher, L. G. Ciobanu, M. M. Coates, S. M. Colquhoun, A. G. C. Manzano, L. T. Cooper, K. Cooperrider, L. Cornaby, M. Cortinovis, J. A. Crump, L. Cuevas-Nasu, A. Damasceno, R. Dandona, S. C. Darby, P. I. Dargan, J. das Neves, A. C. Davis, K. Davletov, E. F. de Castro, V. De la Cruz-Góngora, D. De Leo, L. Degenhardt, L. C. Del Gobbo, B. del Pozo-Cruz, R. P. Dellavalle, A. Deribew, D. C. D. Jarlais, S. D. Dharmaratne, P. K. Dhillon, C. Diaz-Torné, D. Dicker, E. L. Ding, E. R. Dorsey, K. E. Doyle, T. R. Driscoll, L. Duan, M. Dubey, B. B. Duncan, I. Elyazar, A. Y. Endries, S. P. Ermakov, H. E. Erskine, B. Eshrati, A. Esteghamati, S. Fahimi, E. J. A. Faraon, T. A. Farid, C. S. e. S. Farinha, A. Faro, M. S. Farvid, F. Farzadfar, V. L. Feigin, S.-M. Fereshtehnejad, J. G. Fernandes, F. Fischer, J. R. A. Fitchett, T. Fleming, N. Foigt, K. Foreman, F. G. R. Fowkes, R. C. Franklin, T. Fürst, N. D. Futran, E. Gakidou, A. L. Garcia-Basteiro, T. T. Gebrehiwot, A. T. Gebremedhin, J. M. Geleijnse, B. D. Gessner, A. Z. Giref, M. Giroud, M. D. Gishu, G. Giussani, S. Goenka, M. C. Gomez-Cabrera,

H. Gomez-Dantes, P. Gona, A. Goodridge, S. V. Gopalani, C. C. Gotay, A. Goto, H. N. Gouda, H. C. Gugnani, F. Guillemin, Y. Guo, R. Gupta, R. Gupta, R. A. Gutiérrez, J. A. Haagsma, N. Hafezi-Nejad, D. Haile, G. B. Hailu, Y. A. Halasa, R. R. Hamadeh, S. Hamidi, A. J. Handal, G. J. Hankey, Y. Hao, H. L. Harb, S. Harikrishnan, J. M. Haro, M. S. Hassanvand, T. A. Hassen, R. Havmoeller, I. B. Heredia-Pi, N. F. Hernández-Llanes, P. Heydarpour, H. W. Hoek, H. J. Hoffman, M. Horino, N. Horita, H. D. Hosgood, D. G. Hoy, M. Hsairi, A. S. Htet, G. Hu, J. J. Huang, A. Hussein, S. J. Hutchings, I. Huybrechts, K. M. Iburg, B. T. Idrisov, B. V. Ileanu, M. Inoue, T. A. Jacobs, K. H. Jacobsen, N. Jahanmehr, M. B. Jakovljevic, H. A. F. M. Jansen, S. K. Jassal, M. Javanbakht, S. P. Jayaraman, A. U. Jayatilleke, S. H. Jee, P. Jeemon, V. Jha, Y. Jiang, T. Jibat, Y. Jin, C. O. Johnson, J. B. Jonas, Z. Kabir, Y. Kalkonde, R. Kamal, H. Kan, A. Karch, C. K. Karema, C. Karimkhani, A. Kasaeian, A. Kaul, N. Kawakami, D. S. Kazi, P. N. Keiyoro, L. Kemmer, A. H. Kemp, A. P. Kengne, A. Keren, C. N. Kesavachandran, Y. S. Khader, A. R. Khan, E. A. Khan, G. Khan, Y.-H. Khang, S. Khatibzadeh, S. Khera, T. A. M. Khoja, J. Khubchandani, C. Kieling, C.-i. Kim, D. Kim, R. W. Kimokoti, N. Kisson, M. Kivipelto, L. D. Knibbs, Y. Kokubo, J. A. Kopec, P. A. Koul, A. Koyanagi, M. Kravchenko, H. Kromhout, H. Krueger, T. Ku, B. K. Defo, R. S. Kuchenbecker, B. K. Bicer, E. J. Kuipers, G. A. Kumar, G. F. Kwan, D. K. Lal, R. Laloo, T. Lallukka, Q. Lan, A. Larsson, A. A. Latif, A. E. B. Lawrynowicz, J. L. Leasher, J. Leigh, J. Leung, M. Levi, X. Li, Y. Li, J. Liang, S. Liu, B. K. Lloyd, G. Logroscino, P. A. Lotufo, R. Lunevicius, M. MacIntyre, M. Mahdavi, M. Majdan, A. Majeed, R. Malekzadeh, D. C. Malta, W. A. A. Manamo, C. C. Mapoma, W. Marcenes, R. V. Martin, J. Martinez-Raga, F. Masiye, K. Matsushita, R. Matzopoulos, B. M. Mayosi, J. J. McGrath, M. McKee, P. A. Meaney, C. Medina, A. Mehari, F. Mejia-Rodriguez, A. B. Mekonnen, Y. A. Melaku, Z. A. Memish, W. Mendoza, G. B. M. Mensink, A. Meretoja, T. J. Meretoja, Y. M. Mesfin, F. A. Mhimira, A. Millier, T. R. Miller, E. J. Mills, M. Mirarefin, A. Misganaw, C. N. Mock, A. Mohammadi, S. Mohammed, G. L. D. Mola, L. Monasta, J. C. M. Hernandez, M. Montico, L. Morawska, R. Mori, D. Mozaffarian, U. O. Mueller, E. Mullany, J. E. Mumford, G. V. S. Murthy, J. B. Nachega, A. Naheed, V. Nangia, N. Nassiri, J. N. Newton, M. Ng, Q. L. Nguyen, M. I. Nisar,

P. M. N. Pete, O. F. Norheim, R. E. Norman, B. Norrving, L. Nyakarahuka, C. M. Obermeyer, F. A. Ogbo, I.-H. Oh, O. Oladimeji, P. R. Olivares, H. Olsen, B. O. Olusanya, J. O. Olusanya, J. N. Opio, E. Oren, R. Orozco, A. Ortiz, E. Ota, M. PA, A. Pana, E.-K. Park, C. D. Parry, M. Parsaeian, T. Patel, A. J. P. Caicedo, S. T. Patil, S. B. Patten, G. C. Patton, N. Pearce, D. M. Pereira, N. Perico, K. Pesudovs, M. Petzold, M. R. Phillips, F. B. Piel, J. D. Pillay, D. Plass, S. Polinder, C. D. Pond, C. A. Pope, D. Pope, S. Popova, R. G. Poulton, F. Pourmalek, N. M. Prasad, M. Qorbani, R. H. S. Rabiee, A. Radfar, A. Rafay, V. Rahimi-Movaghar, M. Rahman, M. H. U. Rahman, S. U. Rahman, R. K. Rai, S. Rajsic, M. Raju, U. Ram, S. M. Rana, K. Ranganathan, P. Rao, C. A. R. García, A. H. Refaat, C. D. Rehm, J. Rehm, N. Reinig, G. Remuzzi, S. Resnikoff, A. L. Ribeiro, J. A. Rivera, H. S. Roba, A. Rodriguez, S. Rodriguez-Ramirez, D. Rojas-Rueda, Y. Roman, L. Ronfani, G. Roshandel, D. Rothenbacher, A. Roy, M. M. Saleh, J. R. Sanabria, L. Sanchez-Riera, M. D. Sanchez-Niño, T. G. Sánchez-Pimienta, L. Sandar, D. F. Santomauro, I. S. Santos, R. Sarmiento-Suarez, B. Sartorius, M. Satpathy, M. Savic, M. Sawhney, J. Schmidhuber, M. I. Schmidt, I. J. C. Schneider, B. Schöttker, A. E. Schutte, D. C. Schwebel, J. G. Scott, S. Seedat, S. G. Sepanlou, E. E. Servan-Mori, G. Shaddick, A. Shaheen, S. Shahraz, M. A. Shaikh, T. S. Levy, R. Sharma, J. She, S. Sheikhabaei, J. Shen, K. N. Sheth, P. Shi, K. Shibuya, M. Shigematsu, M.-J. Shin, R. Shiri, K. Shishani, I. Shiue, M. G. Shrimel, I. D. Sigfusdottir, D. A. S. Silva, D. G. A. Silveira, J. I. Silverberg, E. P. Simard, S. Sindi, A. Singh, J. A. Singh, P. K. Singh, E. L. Slepak, M. Soljak, S. Soneji, R. J. D. Sorensen, L. A. Sposato, C. T. Sreeramareddy, V. Stathopoulou, N. Steckling, N. Steel, D. J. Stein, M. B. Stein, H. Stöckl, S. Stranges, K. Stroumpoulis, B. F. Sunguya, S. Swaminathan, B. L. Sykes, C. E. I. Szoeki, R. Tabarés-Seisdedos, K. Takahashi, R. T. Talongwa, N. Tandon, D. Tanne, M. Tavakkoli, B. W. Taye, H. R. Taylor, B. A. Tedla, W. M. Tefera, T. K. Tegegne, D. Y. Tekle, A. S. Terkawi, J. S. Thakur, B. A. Thomas, M. L. Thomas, A. J. Thomson, A. L. Thorne-Lyman, A. G. Thrift, G. D. Thurston, T. Tillmann, R. Tobegai, M. Tobollik, R. Topor-Madry, F. Topouzis, J. A. Towbin, B. X. Tran, Z. T. Dimbuene, N. Tsilimparis, A. K. Tura, E. M. Tuzcu, S. Tyrovolas, K. N. Ukwaja, E. A. Undurraga, C. J. Uneke, O. A. Uthman, A. van Donkelaar, J. van Os, Y. Y. Varakin, T. Vasankari, J. L. Veerman,

- N. Venketasubramanian, F. S. Violante, S. E. Vollset, G. R. Wagner, S. G. Waller, J. L. Wang, L. Wang, Y. Wang, S. Weichenthal, E. Weiderpass, R. G. Weintraub, A. Werdecker, R. Westerman, H. A. Whiteford, T. Wijeratne, C. S. Wiysonge, C. D. A. Wolfe, S. Won, A. D. Woolf, M. Wubshet, D. Xavier, G. Xu, A. K. Yadav, B. Yakob, A. Z. Yalew, Y. Yano, M. Yaseri, P. Ye, P. Yip, N. Yonemoto, S.-J. Yoon, M. Z. Younis, C. Yu, Z. Zaidi, M. E. S. Zaki, J. Zhu, B. Zipkin, S. Zodpey, L. J. Zuhlke, and C. J. L. Murray. Global, regional, and national comparative risk assessment of 79 behavioural, environmental and occupational, and metabolic risks or clusters of risks, 1990–2015: a systematic analysis for the Global Burden of Disease Study 2015. *The Lancet*, 388(10053):1659–1724, oct 2016. ISSN 01406736. doi: 10.1016/S0140-6736(16)31679-8. URL <http://linkinghub.elsevier.com/retrieve/pii/S0140673616316798>.
- P. Forster, V. Ramaswamy, P. Artaxo, T. Berntsen, R. Betts, D. W. Fahey, J. Haywood, J. Lean, D. C. Lowe, G. Myhre, and Others. Changes in Atmospheric Constituents and in Radiative Forcing. In 'Climate Change 2007: The Physical Science Basis. Contribution of Working Group I to the Fourth Assessment Report of the Intergovernmental Panel on Climate Change'. (Eds S Solomon, D Qin, M Ma, 2007).
- R. W. Gan, B. Ford, W. Lassman, G. Pfister, A. Vaidyanathan, E. Fischer, J. Volckens, J. R. Pierce, and S. Magzamen. Comparison of wildfire smoke estimation methods and associations with cardiopulmonary-related hospital admissions. *GeoHealth*, 1(3):122–136, may 2017. ISSN 24711403. doi: 10.1002/2017GH000073. URL <http://doi.wiley.com/10.1002/2017GH000073>.
- W. Q. Gan, J. M. FitzGerald, C. Carlsten, M. Sadatsafavi, and M. Brauer. Associations of Ambient Air Pollution with Chronic Obstructive Pulmonary Disease Hospitalization and Mortality. *American Journal of Respiratory and Critical Care Medicine*, 187(7):721–727, feb 2013. ISSN 1073-449X. doi: 10.1164/rccm.201211-2004OC. URL <https://doi.org/10.1164/rccm.201211-2004OC>.
- R. S. Gao, J. P. Schwarz, K. K. Kelly, D. W. Fahey, L. A. Watts, T. L. Thompson, J. R. Spackman, J. G. Slowik, E. S. Cross, J.-H. Han, P. Davidovits, T. B. Onasch, and D. R. Worsnop. A Novel Method for Estimating Light-Scattering Properties of Soot Aerosols Using a Modified Single-

- Particle Soot Photometer. *Aerosol Science and Technology*, 41(2):125–135, feb 2007. ISSN 0278-6826. doi: 10.1080/02786820601118398. URL <http://www.tandfonline.com/doi/abs/10.1080/02786820601118398>.
- T. J. Garrett, S. Brattström, S. Sharma, D. E. J. Worthy, and P. Novelli. The role of scavenging in the seasonal transport of black carbon and sulfate to the Arctic. *Geophysical Research Letters*, 38(16), 2011. ISSN 00948276. doi: 10.1029/2011GL048221.
- S. J. Ghan, R. C. Easter, E. G. Chapman, H. Abdul-Razzak, Y. Zhang, L. R. Leung, N. S. Laulainen, R. D. Saylor, and R. A. Zaveri. A physically based estimate of radiative forcing by anthropogenic sulfate aerosol. *Journal of Geophysical Research: Atmospheres*, 106(D6):5279–5293, mar 2001. ISSN 01480227. doi: 10.1029/2000JD900503. URL <http://doi.wiley.com/10.1029/2000JD900503>.
- S. L. Gong. A parameterization of sea-salt aerosol source function for sub- and super-micron particles. *Global Biogeochemical Cycles*, 17(4):n/a–n/a, dec 2003. ISSN 08866236. doi: 10.1029/2003GB002079. URL <http://onlinelibrary.wiley.com/doi/10.1029/2003GB002079/full>.
- A. P. Grieshop, C. C. O. Reynolds, M. Kandlikar, and H. Dowlatabadi. A black-carbon mitigation wedge. 2:533–534, 2009. ISSN 1752-0894. doi: 10.1038/ngeo595.
- A. P. Grieshop, J. D. Marshall, and M. Kandlikar. Health and climate benefits of cookstove replacement options. *Energy Policy*, 39(12):7530–7542, dec 2011. ISSN 03014215. doi: 10.1016/j.enpol.2011.03.024. URL <http://linkinghub.elsevier.com/retrieve/pii/S0301421511002047>.
- G. M. W. Group. Burden of disease attributable to coal-burning and other major sources of air pollution in china. Technical report, Health Effects Institute, Boston, MA, 2016.
- M. Gysel, M. Laborde, J. S. Olfert, R. Subramanian, and A. J. Gröhn. Effective density of Aquadag and fullerene soot black carbon reference materials used for SP2 calibration. *Atmospheric Measurement Techniques*, 4(12):2851–2858, dec 2011. ISSN 1867-8548. doi: 10.5194/amt-4-2851-2011. URL <http://www.atmos-meas-tech.net/4/2851/2011/>.

- M. S. Hammer, R. V. Martin, A. van Donkelaar, V. Buchard, O. Torres, D. A. Ridley, and R. J. D. Spurr. Interpreting the ultraviolet aerosol index observed with the OMI satellite instrument to understand absorption by organic aerosols: implications for atmospheric oxidation and direct radiative effects. *Atmospheric Chemistry and Physics*, 16(4):2507–2523, mar 2016. ISSN 1680-7324. doi: 10.5194/acp-16-2507-2016. URL <http://www.atmos-chem-phys.net/16/2507/2016/>.
- C. He, Q. Li, K.-N. Liou, L. Qi, S. Tao, and J. P. Schwarz. Microphysics-based black carbon aging in a global CTM: constraints from HIPPO observations and implications for global black carbon budget. *Atmospheric Chemistry and Physics*, 16(5):3077–3098, mar 2016. ISSN 1680-7324. doi: 10.5194/acp-16-3077-2016. URL <http://www.atmos-chem-phys.net/16/3077/2016/>.
- C. L. Heald, D. A. Ridley, J. H. Kroll, S. R. H. Barrett, K. E. Cady-Pereira, M. J. Alvarado, and C. D. Holmes. Contrasting the direct radiative effect and direct radiative forcing of aerosols. *Atmospheric Chemistry and Physics*, 14(11):5513–5527, jun 2014. ISSN 1680-7324. doi: 10.5194/acp-14-5513-2014. URL <http://www.atmos-chem-phys.net/14/5513/2014/acp-14-5513-2014.html>.
- A. Herber, K. Dethloff, C. Haas, D. Steinhage, J. W. Strapp, J. Bottenheim, T. McElroy, and T. Yamanouchi. Polar 5—a new research aircraft for improved access to the arctic. *ISAR-1, Drastic Change under the Global Warming, Extended Abstract*, pages 54–57, 2008.
- A. B. Herber, C. Haas, R. S. Stone, J. W. Bottenheim, P. Liu, S.-M. Li, R. M. Staebler, J. W. Strapp, and K. Dethloff. Regular airborne surveys of arctic sea ice and atmosphere. *Eos, Transactions American Geophysical Union*, 93(4):41–42, 2012.
- I. Hertz-Picciotto, R. J. Baker, P.-S. Yap, M. Dostál, J. P. Joad, M. Lipsett, T. Greenfield, C. E. W. Herr, I. Beneš, R. H. Shumway, K. E. Pinkerton, and R. Šrám. Early Childhood Lower Respiratory Illness and Air Pollution. *Environmental Health Perspectives*, 115(10):1510–1518, oct 2007. ISSN 0091-6765. doi: 10.1289/ehp.9617. URL <http://www.ncbi.nlm.nih.gov/pmc/articles/PMC2022654/>.

- W. C. Hinds. *Aerosol technology: properties, behavior, and measurement of airborne particles*. A Wiley-Interscience Publication John Wiley & Sons, 1982.
- A. Hodshire, M. Lawler, J. Zhao, J. Ortega, C. Jen, T. Yli-Juuti, J. Brewer, J. Kodros, K. Barsanti, D. Hanson, P. McMurry, J. Smith, and J. Pierce. Multiple new-particle growth pathways observed at the US DOE Southern Great Plains field site. *Atmospheric Chemistry and Physics*, 16(14), 2016. ISSN 16807324. doi: 10.5194/acp-16-9321-2016.
- B. Holben, T. Eck, I. Slutsker, D. Tanré, J. Buis, A. Setzer, E. Vermote, J. Reagan, Y. Kaufman, T. Nakajima, F. Lavenu, I. Jankowiak, and A. Smirnov. AERONET—A Federated Instrument Network and Data Archive for Aerosol Characterization. *Remote Sensing of Environment*, 66(1):1–16, oct 1998. ISSN 00344257. doi: 10.1016/S0034-4257(98)00031-5. URL <http://www.sciencedirect.com/science/article/pii/S0034425798000315>.
- C. Hoose, J. E. Kristjánsson, T. Iversen, A. Kirkevåg, Ø. Seland, and A. Gettelman. Constraining cloud droplet number concentration in GCMs suppresses the aerosol indirect effect. *Geophysical Research Letters*, 36(12):L12807, jun 2009. ISSN 0094-8276. doi: 10.1029/2009GL038568. URL <http://onlinelibrary.wiley.com/doi/10.1029/2009GL038568/full>.
- W. Hoppel and G. Frick. Submicron aerosol size distributions measured over the tropical and South Pacific. *Atmospheric Environment. Part A. General Topics*, 24(3):645–659, jan 1990. ISSN 09601686. doi: 10.1016/0960-1686(90)90020-N. URL <http://linkinghub.elsevier.com/retrieve/pii/096016869090020N>.
- W. A. Hoppel, G. M. Frick, and R. E. Larson. Effect of nonprecipitating clouds on the aerosol size distribution in the marine boundary layer. *Geophysical Research Letters*, 13(2):125–128, feb 1986. ISSN 00948276. doi: 10.1029/GL013i002p00125. URL <http://onlinelibrary.wiley.com/doi/10.1029/GL013i002p00125/abstract>.
- T. Hussein, J. Löndahl, P. Paasonen, A. J. Koivisto, T. Petäjä, K. Hämeri, and M. Kulmala. Modeling regional deposited dose of submicron aerosol particles. *Science of The Total Environment*, 458-

- 460:140–149, aug 2013. ISSN 0048-9697. doi: 10.1016/J.SCITOTENV.2013.04.022. URL [#](https://www.sciencedirect.com/science/article/pii/S0048969713004439)f0010.
- P. Hystad, P. A. Demers, K. C. Johnson, R. M. Carpiano, and M. Brauer. Long-term Residential Exposure to Air Pollution and Lung Cancer Risk. *Epidemiology*, 24(5), 2013. ISSN 1044-3983. URL <https://journals.lww.com/epidem/Fulltext/2013/09000/Long{ }term{ }Residential{ }Exposure{ }to{ }Air{ }Pollution.18.aspx>.
- M. J. Iacono, J. S. Delamere, E. J. Mlawer, M. W. Shephard, S. A. Clough, and W. D. Collins. Radiative forcing by long-lived greenhouse gases: Calculations with the AER radiative transfer models. *Journal of Geophysical Research*, 113(D13):D13103, jul 2008. ISSN 0148-0227. doi: 10.1029/2008JD009944. URL <http://doi.wiley.com/10.1029/2008JD009944>.
- International Commission on Radiological Protection. *Human Respiratory Tract Model for Radiological Protection*, volume Publication 66 of 1-3. ICRP, Tarrytown, NY, 1994.
- International Energy Agency. Energy access outlook 2017: From poverty to prosperity. Technical report, International Energy Agency, Paris, France, 2017.
- M. Z. Jacobson. Strong radiative heating due to the mixing state of black carbon in atmospheric aerosols. *Nature*, 409(6821):695–7, feb 2001. ISSN 0028-0836. doi: 10.1038/35055518. URL <http://www.ncbi.nlm.nih.gov/pubmed/11217854>.
- L. Jaeglé, P. K. Quinn, T. S. Bates, B. Alexander, and J.-T. Lin. Global distribution of sea salt aerosols: new constraints from in situ and remote sensing observations. *Atmospheric Chemistry and Physics*, 11(7):3137–3157, apr 2011. ISSN 1680-7324. doi: 10.5194/acp-11-3137-2011. URL <http://www.atmos-chem-phys.net/11/3137/2011/>.
- R. Jaenicke. Chapter 1 Tropospheric Aerosols. *International Geophysics*, 54:1–31, jan 1993. ISSN 0074-6142. doi: 10.1016/S0074-6142(08)60210-7. URL <https://www.sciencedirect.com/science/article/pii/S0074614208602107>.

- S. Janhäll, Å. M. Jonsson, P. Molnár, E. A. Svensson, and M. Hallquist. Size resolved traffic emission factors of submicrometer particles. *Atmospheric Environment*, 38(26):4331–4340, aug 2004. ISSN 13522310. doi: 10.1016/j.atmosenv.2004.04.018. URL <http://www.sciencedirect.com/science/article/pii/S1352231004004170>.
- S. Janhäll, M. O. Andreae, and U. Pöschl. Biomass burning aerosol emissions from vegetation fires: particle number and mass emission factors and size distributions. *Atmospheric Chemistry and Physics*, 10(3):1427–1439, feb 2010. ISSN 1680-7324. doi: 10.5194/acp-10-1427-2010. URL <http://www.atmos-chem-phys.net/10/1427/2010/acp-10-1427-2010.html>.
- G. Janssens-Maenhout, A. M. R. Petrescu, M. Muntean, and V. Blujdea. Verifying greenhouse gas emissions: Methods to support international climate agreements. *Greenhouse Gas Measurement and Management*, 1(2):132–133, 06 2011. doi: 10.1080/20430779.2011.579358. URL <https://doi.org/10.1080/20430779.2011.579358>.
- G. Janssens-Maenhout, M. Crippa, D. Guizzardi, F. Dentener, M. Muntean, G. Pouliot, T. Keating, Q. Zhang, J. Kurokawa, R. Wankmüller, H. Denier van der Gon, J. J. P. Kuenen, Z. Klimont, G. Frost, S. Darras, B. Koffi, and M. Li. HTAP_v2.2: a mosaic of regional and global emission grid maps for 2008 and 2010 to study hemispheric transport of air pollution. *Atmospheric Chemistry and Physics*, 15(19):11411–11432, oct 2015. ISSN 1680-7324. doi: 10.5194/acp-15-11411-2015. URL <http://www.atmos-chem-phys.net/15/11411/2015/>.
- J. L. Jimenez, M. R. Canagaratna, N. M. Donahue, A. S. H. Prevot, Q. Zhang, J. H. Kroll, P. F. DeCarlo, J. D. Allan, H. Coe, N. L. Ng, A. C. Aiken, K. S. Docherty, I. M. Ulbrich, A. P. Grieshop, A. L. Robinson, J. Duplissy, J. D. Smith, K. R. Wilson, V. A. Lanz, C. Hueglin, Y. L. Sun, J. Tian, A. Laaksonen, T. Raatikainen, J. Rautiainen, P. Vaattovaara, M. Ehn, M. Kulmala, J. M. Tomlinson, D. R. Collins, M. J. Cubison, J. Dunlea, J. A. Huffman, T. B. Onasch, M. R. Alfarra, P. I. Williams, K. Bower, Y. Kondo, J. Schneider, F. Drewnick, S. Borrmann, S. Weimer, K. Demerjian, D. Salcedo, L. Cottrell, R. Griffin, A. Takami, T. Miyoshi, S. Hatakeyama, A. Shimono, J. Y. Sun, Y. M. Zhang, K. Dzepina, J. R. Kimmel, D. Sueper, J. T. Jayne, S. C. Herndon, A. M.

- Trimborn, L. R. Williams, E. C. Wood, A. M. Middlebrook, C. E. Kolb, U. Baltensperger, and D. R. Worsnop. Evolution of Organic Aerosols in the Atmosphere. *Science*, 326(5959):1525 LP – 1529, dec 2009. URL <http://science.sciencemag.org/content/326/5959/1525.abstract>.
- M. Johnson, R. Edwards, C. Alatorre Frenk, and O. Masera. In-field greenhouse gas emissions from cookstoves in rural Mexican households. *Atmospheric Environment*, 42:1206–1222, 2008. ISSN 13522310. doi: 10.1016/j.atmosenv.2007.10.034.
- M. Johnson, N. Lam, S. Brant, C. Gray, and D. Pennise. Modeling indoor air pollution from cookstove emissions in developing countries using a Monte Carlo single-box model. *Atmospheric Environment*, 45(19):3237–3243, 2011. ISSN 13522310. doi: 10.1016/j.atmosenv.2011.03.044.
- J. Jung, C. Fountoukis, P. J. Adams, and S. N. Pandis. Simulation of in situ ultrafine particle formation in the eastern United States using PMCAMx-UF. *Journal of Geophysical Research*, 115(D3):D03203, feb 2010. ISSN 0148-0227. doi: 10.1029/2009JD012313. URL <http://doi.wiley.com/10.1029/2009JD012313>.
- C. Karr, T. Lumley, A. Schreuder, R. Davis, T. Larson, B. Ritz, and J. Kaufman. Effects of Subchronic and Chronic Exposure to Ambient Air Pollutants on Infant Bronchiolitis. *American Journal of Epidemiology*, 165(5):553–560, mar 2007. ISSN 0002-9262. URL <http://dx.doi.org/10.1093/aje/kwk032>.
- C. J. Karr, C. B. Rudra, K. A. Miller, T. R. Gould, T. Larson, S. Sathyanarayana, and J. Q. Koenig. Infant exposure to fine particulate matter and traffic and risk of hospitalization for RSV bronchiolitis in a region with lower ambient air pollution. *Environmental Research*, 109(3):321–327, 2009. ISSN 0013-9351. doi: <https://doi.org/10.1016/j.envres.2008.11.006>. URL <http://www.sciencedirect.com/science/article/pii/S0013935108002570>.
- V. A. Karydis, P. Kumar, D. Barahona, I. N. Sokolik, and A. Nenes. On the effect of dust particles on global cloud condensation nuclei and cloud droplet number. *Journal of Geophysical Research*:

- Atmospheres*, 116(D23):n/a–n/a, dec 2011. ISSN 01480227. doi: 10.1029/2011JD016283. URL <http://onlinelibrary.wiley.com/doi/10.1029/2011JD016283/full>.
- V. A. Karydis, S. L. Capps, R. H. Moore, A. G. Russell, D. K. Henze, and A. Nenes. Using a global aerosol model adjoint to unravel the footprint of spatially-distributed emissions on cloud droplet number and cloud albedo. *Geophysical Research Letters*, 39(24):n/a–n/a, dec 2012. ISSN 00948276. doi: 10.1029/2012GL053346. URL <http://onlinelibrary.wiley.com/doi/10.1029/2012GL053346/full>.
- Z. Klimont, K. Kupiainen, C. Heyes, P. Purohit, J. Cofala, P. Rafaj, J. Borken-Kleefeld, and W. Schöpp. Global anthropogenic emissions of particulate matter including black carbon. *Atmospheric Chemistry and Physics*, 17(14):8681–8723, jul 2017. ISSN 1680-7324. doi: 10.5194/acp-17-8681-2017. URL <https://www.atmos-chem-phys.net/17/8681/2017/>.
- J. K. Kodros and J. R. Pierce. Important global and regional differences in aerosol cloud-albedo effect estimates between simulations with and without prognostic aerosol microphysics. *Journal of Geophysical Research: Atmospheres*, 2017. ISSN 2169897X. doi: 10.1002/2016JD025886. URL <http://doi.wiley.com/10.1002/2016JD025886>.
- J. K. Kodros, C. E. Scott, S. C. Farina, Y. H. Lee, C. L'Orange, J. Volckens, and J. R. Pierce. Uncertainties in global aerosols and climate effects due to biofuel emissions. *Atmospheric Chemistry and Physics*, 15(15):8577–8596, aug 2015. ISSN 1680-7324. doi: 10.5194/acp-15-8577-2015. URL <http://www.atmos-chem-phys.net/15/8577/2015/acp-15-8577-2015.html>.
- J. K. Kodros, R. Cucinotta, D. A. Ridley, C. Wiedinmyer, and J. R. Pierce. The aerosol radiative effects of uncontrolled combustion of domestic waste. *Atmospheric Chemistry and Physics*, 16(11):6771–6784, jun 2016a. ISSN 1680-7324. doi: 10.5194/acp-16-6771-2016. URL <http://www.atmos-chem-phys.net/16/6771/2016/acp-16-6771-2016-metrics.html>.
- J. K. Kodros, C. Wiedinmyer, B. Ford, R. Cucinotta, R. Gan, S. Magzamen, and J. R. Pierce. Global burden of mortalities due to chronic exposure to ambient PM 2.5 from open combustion

- of domestic waste. *Environmental Research Letters*, 11(12):124022, dec 2016b. ISSN 1748-9326. doi: 10.1088/1748-9326/11/12/124022. URL <http://stacks.iop.org/1748-9326/11/i=12/a=124022?key=crossref.31d7056d432849d89ef6481c4995bd5e>.
- P. Koepke, M. Hess, I. Schult, and E. Shettle. Global aerosol data set. *MPI Meteorologie Hamburg Rep*, 243(44):7017–7039, 1997.
- J. F. Kok. A scaling theory for the size distribution of emitted dust aerosols suggests climate models underestimate the size of the global dust cycle. *Proceedings of the National Academy of Sciences of the United States of America*, 108(3):1016–21, jan 2011. ISSN 1091-6490. doi: 10.1073/pnas.1014798108. URL <http://www.ncbi.nlm.nih.gov/pubmed/21189304><http://www.pubmedcentral.nih.gov/articlerender.fcgi?artid=PMC3024662>.
- Y. Kondo, H. Matsui, N. Moteki, L. Sahu, N. Takegawa, M. Kajino, Y. Zhao, M. J. Cubison, J. L. Jimenez, S. Vay, G. S. Diskin, B. Anderson, A. Wisthaler, T. Mikoviny, H. E. Fuelberg, D. R. Blake, G. Huey, A. J. Weinheimer, D. J. Knapp, and W. H. Brune. Emissions of black carbon, organic, and inorganic aerosols from biomass burning in North America and Asia in 2008. *Journal of Geophysical Research*, 116(D8):D08204, apr 2011. ISSN 0148-0227. doi: 10.1029/2010JD015152. URL <http://doi.wiley.com/10.1029/2010JD015152>.
- D. Krewski, M. Jerrett, R. T. Burnett, R. Ma, E. Hughes, Y. Shi, M. C. Turner, C. A. Pope, G. Thurston, E. E. Calle, M. J. Thun, B. Beckerman, P. DeLuca, N. Finkelstein, K. Ito, D. K. Moore, K. B. Newbold, T. Ramsay, Z. Ross, H. Shin, and B. Tempalski. Extended follow-up and spatial analysis of the American Cancer Society study linking particulate air pollution and mortality. *Research report (Health Effects Institute)*, (140):5–114; discussion 115–136, 2009. ISSN 1041-5505.
- M. Krzyżanowski, B. Kuna-Dibbert, and J. Schneider. *Health effects of transport-related air pollution*. WHO Regional Office Europe, 2005.

- H. Kuhns, E. M. Knipping, and J. M. Vukovich. Development of a United States–Mexico Emissions Inventory for the Big Bend Regional Aerosol and Visibility Observational (BRAVO) Study. *Journal of the Air & Waste Management Association*, 55(5):677–692, may 2005. ISSN 1096-2247. doi: 10.1080/10473289.2005.10464648. URL <http://www.tandfonline.com/doi/abs/10.1080/10473289.2005.10464648>{#}.VnHeMcYEEtU.mendeley.
- A. Kupc, C. Williamson, N. L. Wagner, M. Richardson, and C. A. Brock. Modification, calibration, and performance of the ultra-high sensitivity aerosol spectrometer for particle size distribution and volatility measurements during the atmospheric tomography mission (atom) airborne campaign. *Atmospheric Measurement Techniques*, 11(1):369–383, 2018.
- M. Laborde, P. Mertes, P. Zieger, J. Dommen, U. Baltensperger, and M. Gysel. Sensitivity of the Single Particle Soot Photometer to different black carbon types. *Atmospheric Measurement Techniques*, 5(5):1031–1043, may 2012. ISSN 1867-8548. doi: 10.5194/amt-5-1031-2012. URL <http://www.atmos-meas-tech.net/5/1031/2012/>.
- F. Lacey and D. Henze. Global climate impacts of country-level primary carbonaceous aerosol from solid-fuel cookstove emissions. *Environmental Research Letters*, 10(11):114003, 2015.
- F. G. Lacey, D. K. Henze, C. J. Lee, A. van Donkelaar, and R. V. Martin. Transient climate and ambient health impacts due to national solid fuel cookstove emissions. *Proceedings of the National Academy of Sciences of the United States of America*, 114(6):1269–1274, feb 2017. ISSN 1091-6490. doi: 10.1073/pnas.1612430114. URL <http://www.ncbi.nlm.nih.gov/pubmed/28115698><http://www.pubmedcentral.nih.gov/articlerender.fcgi?artid=PMC5307449>.
- D. A. Lack and C. D. Cappa. Impact of brown and clear carbon on light absorption enhancement, single scatter albedo and absorption wavelength dependence of black carbon. *Atmospheric Chemistry and Physics*, 10(9):4207–4220, may 2010. ISSN 1680-7324. doi: 10.5194/acp-10-4207-2010. URL <http://www.atmos-chem-phys.net/10/4207/2010/>.

- F. Laden, J. Schwartz, F. E. Speizer, and D. W. Dockery. Reduction in fine particulate air pollution and mortality: Extended follow-up of the Harvard Six Cities study. *American journal of respiratory and critical care medicine*, 173(6):667–72, mar 2006. ISSN 1073-449X. doi: 10.1164/rccm.200503-443OC. URL <http://www.atsjournals.org/doi/abs/10.1164/rccm.200503-443OC>{#}.Vms8T9E13nI.mendeley.
- J.-F. Lamarque, L. K. Emmons, P. G. Hess, D. E. Kinnison, S. Tilmes, F. Vitt, C. L. Heald, E. A. Holland, P. H. Lauritzen, J. Neu, J. J. Orlando, P. J. Rasch, and G. K. Tyndall. CAM-chem: description and evaluation of interactive atmospheric chemistry in the Community Earth System Model. *Geoscientific Model Development*, 5(2):369–411, mar 2012. ISSN 1991-9603. doi: 10.5194/gmd-5-369-2012. URL <http://www.geosci-model-dev.net/5/369/2012/>.
- J.-F. Lamarque, D. T. Shindell, B. Josse, P. J. Young, I. Cionni, V. Eyring, D. Bergmann, P. Cameron-Smith, W. J. Collins, R. Doherty, S. Dalsoren, G. Faluvegi, G. Folberth, S. J. Ghan, L. W. Horowitz, Y. H. Lee, I. A. MacKenzie, T. Nagashima, V. Naik, D. Plummer, M. Righi, S. T. Rumbold, M. Schulz, R. B. Skeie, D. S. Stevenson, S. Strode, K. Sudo, S. Szopa, A. Voulgarakis, and G. Zeng. The Atmospheric Chemistry and Climate Model Intercomparison Project (ACCMIP): overview and description of models, simulations and climate diagnostics. *Geoscientific Model Development*, 6(1):179–206, feb 2013. ISSN 1991-9603. doi: 10.5194/gmd-6-179-2013. URL <http://www.geosci-model-dev.net/6/179/2013/>.
- W. R. Leaitch, S. Sharma, L. Huang, D. Toom-Sauntry, A. Chivulescu, A. M. Macdonald, K. von Salzen, J. R. Pierce, A. K. Bertram, J. C. Schroder, N. C. Shantz, R. Y.-W. Chang, and A.-L. Norman. Dimethyl sulfide control of the clean summertime Arctic aerosol and cloud. *Elementa: Science of the Anthropocene*, 2013. ISSN 2325-1026. doi: 10.12952/journal.elementa.000017.
- W. R. Leaitch, A. Korolev, A. A. Aliabadi, J. Burkart, M. D. Willis, J. P. D. Abbatt, H. Bozem, P. Hoor, F. Köllner, J. Schneider, A. Herber, C. Konrad, and R. Brauner. Effects of 20–100 nm particles on liquid clouds in the clean summertime arctic. *Atmospheric Chemistry and Physics*, 16(17):11107–11124, 2016.

- W. R. Leaitch, L. M. Russell, J. Liu, F. Kolonjari, D. Toom, L. Huang, S. Sharma, A. Chivulescu, D. Veber, and W. Zhang. Organic Functional Groups in the Submicron Aerosol at 82.5°N from 2012 to 2014. *Atmospheric Chemistry and Physics Discussions*, pages 1–38, aug 2017. ISSN 1680-7375. doi: 10.5194/acp-2017-511. URL <https://www.atmos-chem-phys-discuss.net/acp-2017-511/>.
- H. J. J. Lee, P. K. Aiona, A. Laskin, J. Laskin, and S. A. Nizkorodov. Effect of solar radiation on the optical properties and molecular composition of laboratory proxies of atmospheric brown carbon. *Environmental science & technology*, 48(17):10217–26, sep 2014. ISSN 1520-5851. doi: 10.1021/es502515r. URL <http://pubs.acs.org/doi/abs/10.1021/es502515r>{#}.Vpg0F4sppaM.mendeley.
- Y. H. Lee and P. J. Adams. A Fast and Efficient Version of the Two-Moment Aerosol Sectional (TOMAS) Global Aerosol Microphysics Model. *Aerosol Science and Technology*, 46(6):678–689, jun 2012. ISSN 0278-6826. doi: 10.1080/02786826.2011.643259. URL <http://www.tandfonline.com/doi/abs/10.1080/02786826.2011.643259>.
- L. Lee, K. J. Pringle, C. L. Reddington, G. W. Mann, P. Stier, D. V. Spracklen, J. R. Pierce, and K. S. Carslaw. The magnitude and causes of uncertainty in global model simulations of cloud condensation nuclei. *Atmospheric Chemistry and Physics*, 13(17):8879–8914, sep 2013. ISSN 1680-7324. doi: 10.5194/acp-13-8879-2013. URL <http://www.atmos-chem-phys.net/13/8879/2013/>.
- Y. H. Lee, J. R. Pierce, and P. J. Adams. Representation of nucleation mode microphysics in a global aerosol model with sectional microphysics. *Geoscientific Model Development*, 6:1221–1232, 2013. ISSN 1991959X. doi: 10.5194/gmd-6-1221-2013.
- J. Lelieveld, C. Barlas, D. Giannadaki, and A. Pozzer. Model calculated global, regional and megacity premature mortality due to air pollution. *Atmospheric Chemistry and Physics*, 13(14):7023–7037, jul 2013. ISSN 1680-7324. doi: 10.5194/acp-13-7023-2013. URL <http://www.atmos-chem-phys.net/13/7023/2013/acp-13-7023-2013.html>.

- J. Lelieveld, J. S. Evans, M. Fnais, D. Giannadaki, and A. Pozzer. The contribution of outdoor air pollution sources to premature mortality on a global scale. *Nature*, 525(7569):367–371, sep 2015. ISSN 0028-0836. URL <http://dx.doi.org/10.1038/nature15371>.
- J. Lepeule, F. Laden, D. Dockery, and J. Schwartz. Chronic Exposure to Fine Particles and Mortality: An Extended Follow-up of the Harvard Six Cities Study from 1974 to 2009. *Environmental Health Perspectives*, 120(7):965–970, jul 2012. ISSN 0091-6765. doi: 10.1289/ehp.1104660. URL <http://www.ncbi.nlm.nih.gov/pmc/articles/PMC3404667/>.
- S. S. Lim, T. Vos, A. D. Flaxman, G. Danaei, K. Shibuya, H. Adair-Rohani, M. Amann, H. R. Anderson, K. G. Andrews, M. Aryee, C. Atkinson, L. J. Bacchus, A. N. Bahalim, K. Balakrishnan, J. Balmes, S. Barker-Collo, A. Baxter, M. L. Bell, J. D. Blore, F. Blyth, C. Bonner, G. Borges, R. Bourne, M. Boussinesq, M. Brauer, P. Brooks, N. G. Bruce, B. Brunekreef, C. Bryan-Hancock, C. Bucello, R. Buchbinder, F. Bull, R. T. Burnett, T. E. Byers, B. Calabria, J. Carapetis, E. Carnahan, Z. Chafe, F. Charlson, H. Chen, J. S. Chen, A. T.-A. Cheng, J. C. Child, A. Cohen, K. E. Colson, B. C. Cowie, S. Darby, S. Darling, A. Davis, L. Degenhardt, F. Dentener, D. C. Des Jarlais, K. Devries, M. Dherani, E. L. Ding, E. R. Dorsey, T. Driscoll, K. Edmond, S. E. Ali, R. E. Engell, P. J. Erwin, S. Fahimi, G. Falder, F. Farzadfar, A. Ferrari, M. M. Finucane, S. Flaxman, F. G. R. Fowkes, G. Freedman, M. K. Freeman, E. Gakidou, S. Ghosh, E. Giovannucci, G. Gmel, K. Graham, R. Grainger, B. Grant, D. Gunnell, H. R. Gutierrez, W. Hall, H. W. Hoek, A. Hogan, H. D. Hosgood, D. Hoy, H. Hu, B. J. Hubbell, S. J. Hutchings, S. E. Ibeanusi, G. L. Jacklyn, R. Jasrasaria, J. B. Jonas, H. Kan, J. a. Kanis, N. Kassebaum, N. Kawakami, Y.-H. Khang, S. Khatibzadeh, J.-P. Khoo, C. Kok, F. Laden, R. Lalloo, Q. Lan, T. Lathlean, J. L. Leasher, J. Leigh, Y. Li, J. K. Lin, S. E. Lipshultz, S. London, R. Lozano, Y. Lu, J. Mak, R. Malekzadeh, L. Mallinger, W. Marcenes, L. March, R. Marks, R. Martin, P. McGale, J. McGrath, S. Mehta, G. a. Mensah, T. R. Merriman, R. Micha, C. Michaud, V. Mishra, K. Mohd Hanafiah, A. a. Mokdad, L. Morawska, D. Mozaffarian, T. Murphy, M. Naghavi, B. Neal, P. K. Nelson, J. M. Nolla, R. Norman, C. Olives, S. B. Omer, J. Orchard, R. Osborne, B. Ostro, A. Page, K. D. Pandey, C. D. H. Parry, E. Passmore, J. Patra, N. Pearce, P. M. Pelizzari, M. Petzold, M. R.

- Phillips, D. Pope, C. A. Pope, J. Powles, M. Rao, H. Razavi, E. a. Rehfuss, J. T. Rehm, B. Ritz, F. P. Rivara, T. Roberts, C. Robinson, J. a. Rodriguez-Portales, I. Romieu, R. Room, L. C. Rosenfeld, A. Roy, L. Rushton, J. a. Salomon, U. Sampson, L. Sanchez-Riera, E. Sanman, A. Sapkota, S. Seedat, P. Shi, K. Shield, R. Shivakoti, G. M. Singh, D. a. Sleet, E. Smith, K. R. Smith, N. J. C. Stapelberg, K. Steenland, H. Stöckl, L. J. Stovner, K. Straif, L. Straney, G. D. Thurston, J. H. Tran, R. Van Dingenen, A. van Donkelaar, J. L. Veerman, L. Vijayakumar, R. Weintraub, M. M. Weissman, R. a. White, H. Whiteford, S. T. Wiersma, J. D. Wilkinson, H. C. Williams, W. Williams, N. Wilson, A. D. Woolf, P. Yip, J. M. Zielinski, A. D. Lopez, C. J. L. Murray, M. Ezzati, M. a. AlMazroa, and Z. a. Memish. A comparative risk assessment of burden of disease and injury attributable to 67 risk factors and risk factor clusters in 21 regions, 1990-2010: a systematic analysis for the Global Burden of Disease Study 2010. *Lancet*, 380 (9859):2224–60, dec 2012. ISSN 1474-547X. doi: 10.1016/S0140-6736(12)61766-8. URL <http://www.ncbi.nlm.nih.gov/pubmed/23245609>.
- M. J. Lipsett, B. D. Ostro, P. Reynolds, D. Goldberg, A. Hertz, M. Jerrett, D. F. Smith, C. Garcia, E. T. Chang, and L. Bernstein. Long-Term Exposure to Air Pollution and Cardiorespiratory Disease in the California Teachers Study Cohort. *American Journal of Respiratory and Critical Care Medicine*, 184(7):828–835, oct 2011. ISSN 1073-449X. doi: 10.1164/rccm.201012-2082OC. URL <https://doi.org/10.1164/rccm.201012-2082OC>.
- D. Liu, B. Quennehen, E. Darbyshire, J. D. Allan, P. I. Williams, J. W. Taylor, S. J.-B. Bauguitte, M. J. Flynn, D. Lowe, M. W. Gallagher, K. N. Bower, T. W. Choularton, and H. Coe. The importance of Asia as a source of black carbon to the European Arctic during springtime 2013. *Atmospheric Chemistry and Physics*, 15(20):11537–11555, oct 2015. ISSN 1680-7324. doi: 10.5194/acp-15-11537-2015. URL <http://www.atmos-chem-phys.net/15/11537/2015/>.
- X. Liu. Global modeling of aerosol dynamics: Model description, evaluation, and interactions between sulfate and nonsulfate aerosols. *Journal of Geophysical Research*, 110(D18):D18206,

2005. ISSN 0148-0227. doi: 10.1029/2004JD005674. URL <http://doi.wiley.com/10.1029/2004JD005674>.

X. Liu, R. C. Easter, S. J. Ghan, R. Zaveri, P. Rasch, X. Shi, J.-F. Lamarque, A. Gettelman, H. Morrison, F. Vitt, A. Conley, S. Park, R. Neale, C. Hannay, A. M. L. Ekman, P. Hess, N. Mahowald, W. Collins, M. J. Iacono, C. S. Bretherton, M. G. Flanner, and D. Mitchell. Toward a minimal representation of aerosols in climate models: description and evaluation in the Community Atmosphere Model CAM5. *Geoscientific Model Development*, 5(3):709–739, may 2012. ISSN 1991-9603. doi: 10.5194/gmd-5-709-2012. URL <http://www.geosci-model-dev.net/5/709/2012/>.

J. Löndahl, A. Massling, J. Pagels, E. Swietlicki, E. Vaclavik, and S. Loft. Size-Resolved Respiratory-Tract Deposition of Fine and Ultrafine Hydrophobic and Hygroscopic Aerosol Particles During Rest and Exercise. *Inhalation Toxicology*, 19(2):109–116, jan 2007. ISSN 0895-8378. doi: 10.1080/08958370601051677. URL <http://www.tandfonline.com/doi/full/10.1080/08958370601051677>.

J. Löndahl, A. Massling, E. Swietlicki, E. V. Bräuner, M. Ketzler, J. Pagels, and S. Loft. Experimentally Determined Human Respiratory Tract Deposition of Airborne Particles at a Busy Street. *Environmental Science & Technology*, 43(13):4659–4664, jul 2009. ISSN 0013-936X. doi: 10.1021/es803029b. URL <http://pubs.acs.org/doi/abs/10.1021/es803029b>.

N. Mahowald, S. Albani, J. F. Kok, S. Engelstaeder, R. Scanza, D. S. Ward, and M. G. Flanner. The size distribution of desert dust aerosols and its impact on the Earth system. *Aeolian Research*, 15:53–71, dec 2014. ISSN 1875-9637. doi: 10.1016/J.AEOLIA.2013.09.002. URL <https://www.sciencedirect.com/science/article/pii/S1875963713000736{#}b0230>.

G. W. Mann, K. S. Carslaw, D. V. Spracklen, D. A. Ridley, P. T. Manktelow, M. P. Chipperfield, S. J. Pickering, and C. E. Johnson. Description and evaluation of GLOMAP-mode: a modal global aerosol microphysics model for the UKCA composition-climate model. *Geoscientific Model*

- Development*, 3(2):519–551, oct 2010. ISSN 1991-9603. doi: 10.5194/gmd-3-519-2010. URL <http://www.geosci-model-dev.net/3/519/2010/gmd-3-519-2010.html>.
- G. W. Mann, K. S. Carslaw, D. A. Ridley, D. V. Spracklen, K. J. Pringle, J. Merikanto, H. Korhonen, J. P. Schwarz, L. A. Lee, P. T. Manktelow, M. T. Woodhouse, A. Schmidt, T. J. Breider, K. M. Emmerson, C. L. Reddington, M. P. Chipperfield, and S. J. Pickering. Intercomparison of modal and sectional aerosol microphysics representations within the same 3-D global chemical transport model. *Atmospheric Chemistry and Physics*, 12(10):4449–4476, may 2012. ISSN 1680-7324. doi: 10.5194/acp-12-4449-2012. URL <http://www.atmos-chem-phys.net/12/4449/2012/>.
- P. Massoli, T. B. Onasch, C. D. Cappa, I. Nuumaan, J. Hakala, K. Hayden, S.-M. Li, D. T. Sueper, T. S. Bates, P. K. Quinn, J. T. Jayne, and D. R. Worsnop. Characterization of black carbon-containing particles from soot particle aerosol mass spectrometer measurements on the R/V *Atlantis* during CalNex 2010. *Journal of Geophysical Research: Atmospheres*, 120(6):2575–2593, mar 2015. ISSN 2169897X. doi: 10.1002/2014JD022834. URL <http://doi.wiley.com/10.1002/2014JD022834>.
- B. C. McDonald, J. A. de Gouw, J. B. Gilman, S. H. Jathar, A. Akherati, C. D. Cappa, J. L. Jimenez, J. Lee-Taylor, P. L. Hayes, S. A. McKeen, Y. Y. Cui, S.-W. Kim, D. R. Gentner, G. Isaacman-VanWertz, A. H. Goldstein, R. A. Harley, G. J. Frost, J. M. Roberts, T. B. Ryerson, and M. Trainer. Volatile chemical products emerging as largest petrochemical source of urban organic emissions. *Science*, 359(6377):760 LP – 764, feb 2018. URL <http://science.sciencemag.org/content/359/6377/760.abstract>.
- G. R. McMeeking, W. T. Morgan, M. Flynn, E. J. Highwood, K. Turnbull, J. Haywood, and H. Coe. Black carbon aerosol mixing state, organic aerosols and aerosol optical properties over the United Kingdom. *Atmospheric Chemistry and Physics*, 11(17):9037–9052, sep 2011. ISSN 1680-7324. doi: 10.5194/acp-11-9037-2011. URL <http://www.atmos-chem-phys.net/11/9037/2011/>.
- G. R. McMeeking, E. Fortner, T. B. Onasch, J. W. Taylor, M. Flynn, H. Coe, and S. M. Kreidenweis. Impacts of nonrefractory material on light absorption by aerosols emitted from biomass burning.

- Journal of Geophysical Research: Atmospheres*, 119(21):12,272–12,286, nov 2014. ISSN 2169897X. doi: 10.1002/2014JD021750. URL <http://doi.wiley.com/10.1002/2014JD021750>.
- J. Merikanto, D. V. Spracklen, G. W. Mann, S. J. Pickering, and K. S. Carslaw. Impact of nucleation on global ccn. *Atmospheric Chemistry and Physics*, 9(21):8601–8616, 2009.
- F. J. Miller, B. Asgharian, J. D. Schroeter, and O. Price. Improvements and additions to the Multiple Path Particle Dosimetry model. *Journal of Aerosol Science*, 99:14–26, sep 2016. ISSN 0021-8502. doi: 10.1016/J.JAEROSCI.2016.01.018. URL <https://www.sciencedirect.com/science/article/pii/S0021850215300860>.
- K. A. Miller, D. S. Siscovick, L. Sheppard, K. Shepherd, J. H. Sullivan, G. L. Anderson, and J. D. Kaufman. Long-Term Exposure to Air Pollution and Incidence of Cardiovascular Events in Women. *New England Journal of Medicine*, 356(5):447–458, feb 2007. ISSN 0028-4793. doi: 10.1056/NEJMoa054409. URL <https://doi.org/10.1056/NEJMoa054409>.
- S. S. Mitter, R. Vedanthan, F. Islami, A. Pourshams, H. Khademi, F. Kamangar, C. C. Abnet, S. M. Dawsey, P. D. Pharoah, P. Brennan, V. Fuster, P. Boffetta, and R. Malekzadeh. Household Fuel Use and Cardiovascular Disease Mortality: Golestan Cohort Study. *Circulation*, 133(24): 2360–2369, jun 2016. ISSN 0009-7322. doi: 10.1161/CIRCULATIONAHA.115.020288. URL <http://www.ncbi.nlm.nih.gov/pmc/articles/PMC4910632/>.
- C. Mohr, J. A. Huffman, M. J. Cubison, A. C. Aiken, K. S. Docherty, J. R. Kimmel, I. M. Ulbrich, M. Hannigan, and J. L. Jimenez. Characterization of Primary Organic Aerosol Emissions from Meat Cooking, Trash Burning, and Motor Vehicles with High-Resolution Aerosol Mass Spectrometry and Comparison with Ambient and Chamber Observations. *Environmental Science & Technology*, 43(7):2443–2449, apr 2009. ISSN 0013-936X. doi: 10.1021/es8011518. URL <http://pubs.acs.org/doi/abs/10.1021/es8011518{#}.Vp57PQsbRCU.mendeley>.
- K. Mortimer, C. B. Ndamala, A. W. Naunje, J. Malava, C. Katundu, W. Weston, D. Havens, D. Pope, N. G. Bruce, M. Nyirenda, D. Wang, A. Crampin, J. Grigg, J. Balmes, and S. B. Gordon. A

- cleaner burning biomass-fuelled cookstove intervention to prevent pneumonia in children under 5 years old in rural Malawi (the Cooking and Pneumonia Study): a cluster randomised controlled trial. *Lancet (London, England)*, 389(10065):167–175, dec 2016. ISSN 1474-547X. doi: 10.1016/S0140-6736(16)32507-7. URL <http://www.thelancet.com/article/S0140673616325077/fulltext>.
- N. Moteki and Y. Kondo. Effects of Mixing State on Black Carbon Measurements by Laser-Induced Incandescence. *Aerosol Science and Technology*, 41(4):398–417, mar 2007. ISSN 0278-6826. doi: 10.1080/02786820701199728. URL <http://www.tandfonline.com/doi/abs/10.1080/02786820701199728>.
- N. Moteki, Y. Kondo, and S.-i. Nakamura. Method to measure refractive indices of small nonspherical particles: Application to black carbon particles. *Journal of Aerosol Science*, 41(5):513–521, may 2010. ISSN 00218502. doi: 10.1016/j.jaerosci.2010.02.013. URL <http://linkinghub.elsevier.com/retrieve/pii/S0021850210000467>.
- G. Myhre, B. H. Samset, M. Schulz, Y. Balkanski, S. Bauer, T. K. Berntsen, H. Bian, N. Bellouin, M. Chin, T. Diehl, R. C. Easter, J. Feichter, S. J. Ghan, D. Hauglustaine, T. Iversen, S. Kinne, A. Kirkevåg, J.-F. Lamarque, G. Lin, X. Liu, M. T. Lund, G. Luo, X. Ma, T. van Noije, J. E. Penner, P. J. Rasch, A. Ruiz, Ø. Seland, R. B. Skeie, P. Stier, T. Takemura, K. Tsigaridis, P. Wang, Z. Wang, L. Xu, H. Yu, F. Yu, J.-H. Yoon, K. Zhang, H. Zhang, and C. Zhou. Radiative forcing of the direct aerosol effect from aerocom phase ii simulations. *Atmospheric Chemistry and Physics*, 13(4):1853–1877, 2013.
- L. P. Naeher, M. Brauer, M. Lipsett, J. T. Zelikoff, C. D. Simpson, J. Q. Koenig, and K. R. Smith. Woodsmoke Health Effects: A Review. *Inhalation Toxicology*, 19(1):67–106, jan 2007. ISSN 0895-8378. doi: 10.1080/08958370600985875. URL <http://dx.doi.org/10.1080/08958370600985875>.
- M. Naghavi, H. Wang, R. Lozano, A. Davis, X. Liang, M. Zhou, S. E. Vollset, A. A. Ozgoren, S. Abdalla, F. Abd-Allah, M. I. A. Aziz, S. F. Abera, V. Aboyans, B. Abraham, J. P. Abraham,

K. E. Abuabara, I. Abubakar, L. J. Abu-Raddad, N. M. E. Abu-Rmeileh, T. Achoki, A. Adelekan, Z. N. Ademi, K. Adofo, A. K. Adou, J. C. Adsuar, J. Aernlov, E. E. Agardh, D. Akena, M. J. Al Khabouri, D. Alasfoor, M. Albittar, M. A. Alegretti, A. V. Aleman, Z. A. Alemu, R. Alfonso-Cristancho, S. Alhabib, M. K. Ali, R. Ali, F. Alla, F. Al Lami, P. Allebeck, M. A. AlMazroa, R. A.-S. Salman, U. Alsharif, E. Alvarez, N. Alviz-Guzman, A. A. Amankwaa, A. T. Amare, O. Ameli, H. Amini, W. Ammar, H. R. Anderson, B. O. Anderson, C. A. T. Antonio, P. Anwari, H. Apfel, S. A. Cunningham, V. S. A. Arsenijevic, A. Artaman, M. M. Asad, R. J. Asghar, R. Assadi, L. S. Atkins, C. Atkinson, A. Badawi, M. C. Bahit, T. Bakfalouni, K. Balakrishnan, S. Balalla, A. Banerjee, R. M. Barber, S. L. Barker-Collo, S. Barquera, L. Barregard, L. H. Barrero, T. Barrientos-Gutierrez, A. Basu, S. Basu, M. O. Basulaiman, J. Beardsley, N. Bedi, E. Beghi, T. Bekele, M. L. Bell, C. Benjet, D. A. Bennett, I. M. Bensenor, H. Benzian, A. Bertozzi-Villa, T. J. Beyene, N. Bhala, A. Bhalla, Z. A. Bhutta, B. Bikbov, A. Bin Abdulhak, S. Biryukov, J. D. Blore, F. M. Blyth, M. A. Bohensky, G. Borges, D. Bose, S. Boufous, R. R. Bourne, L. N. Boyers, M. Brainin, M. Brauer, C. E. G. Brayne, A. Brazinova, N. Breitborde, H. Brenner, A. D. M. Briggs, J. C. Brown, T. S. Brugha, G. C. Buckle, L. N. Bui, G. Bukhman, M. Burch, I. R. C. Nonato, H. Carabin, R. Cardenas, J. Carapetis, D. O. Carpenter, V. Caso, C. A. Castaneda-Orjuela, R. E. Castro, F. Catala-Lopez, F. Cavalleri, J.-C. Chang, F. C. Charlson, X. Che, H. Chen, Y. Chen, J. S. Chen, Z. Chen, P. P.-C. Chiang, O. Chimed-Ochir, R. Chowdhury, H. Christensen, C. A. Christophi, T.-W. Chuang, S. S. Chugh, M. Cirillo, M. M. Coates, L. E. Coffeng, M. S. Coggeshall, A. Cohen, V. Colistro, S. M. Colquhoun, M. Colomar, L. T. Cooper, C. Cooper, L. M. Coppola, M. Cortinovis, K. Courville, B. C. Cowie, M. H. Criqui, J. A. Crump, L. Cuevas-Nasu, I. d. C. Leite, K. C. Dabhadkar, L. Dandona, R. Dandona, E. Dansereau, P. I. Dargan, A. Dayama, V. la Cruz-Gongora, S. F. de la Vega, D. De Leo, L. Degenhardt, B. del Pozo-Cruz, R. P. Dellavalle, K. Deribe, D. C. D. Jarlais, M. Dessalegn, G. A. DeVeber, S. D. Dharmaratne, M. Dherani, J.-L. Diaz-Ortega, C. Diaz-Torne, D. Dicker, E. L. Ding, K. Dokova, E. R. Dorsey, T. R. Driscoll, L. Duan, H. C. Duber, A. M. Durrani, B. E. Ebel, K. M. Edmond, R. G. Ellenbogen, Y. Elshrek, S. P. Ermakov, H. E. Erskine, B. Eshrati, A. Esteghamati, K. Estep, T. Fuerst, S. Fahimi, A. S.

Fahrion, E. J. A. Faraon, F. Farzadfar, D. F. J. Fay, A. B. Feigl, V. L. Feigin, M. M. Felicio, S.-M. Fereshtehnejad, J. G. Fernandes, A. J. Ferrari, T. D. Fleming, N. Foigt, K. Foreman, M. H. Forouzanfar, F. G. R. Fowkes, U. Fra Paleo, R. C. Franklin, N. D. Futran, L. Gaffikin, K. Gambashidze, F. G. Gankpe, F. A. Garcia-Guerra, A. C. Garcia, J. M. Geleijnse, B. D. Gessner, K. B. Gibney, R. F. Gillum, S. Gilmour, I. Abdelmageem, M. Ginawi, M. Giroud, E. L. Glaser, S. Goenka, H. G. Dantes, P. Gona, D. Gonzalez-Medina, C. Guinovart, R. Gupta, R. Gupta, R. A. Gosselin, C. C. Gotay, A. Goto, H. N. Gowda, N. Graetz, K. F. Greenwell, H. C. Gugrani, D. Gunnell, R. A. Gutierrez, J. Haagsma, N. Hafezi-Nejad, H. Hagan, M. Hagstromer, Y. A. Halasa, R. R. Hamadeh, H. Hamavid, M. Hammami, J. Hancock, G. J. Hankey, G. M. Hansen, H. L. Harb, H. Harewood, J. M. Haro, R. Havmoeller, R. J. Hay, S. I. Hay, M. T. Hedayati, I. B. H. Pi, K. R. Heuton, P. Heydarpour, H. Higashi, M. Hijar, H. W. Hoek, H. J. Hoffman, J. C. Hornberger, H. D. Hosgood, M. Hossain, P. J. Hotez, D. G. Hoy, M. Hsairi, G. Hu, J. J. Huang, M. D. Huffman, A. J. Hughes, A. Hussein, C. Huynh, M. Iannarone, K. M. Iburg, B. T. Idrisov, N. Ikeda, K. Innos, M. Inoue, F. Islami, S. Ismayilova, K. H. Jacobsen, S. Jassal, S. P. Jayaraman, P. N. Jensen, V. Jha, G. Jiang, Y. Jiang, J. B. Jonas, J. Joseph, K. Juel, E. K. Kabagambe, H. Kan, A. Karch, C. Karimkhani, G. Karthikeyan, N. Kassebaum, A. Kaul, N. Kawakami, K. Kazanjan, D. S. Kazi, A. H. Kemp, A. P. Kengne, A. Keren, M. Kereselidze, Y. S. Khader, S. E. A. H. Khalifa, E. A. Khan, G. Khan, Y.-H. Khang, C. Kieling, Y. Kinfu, J. M. Kinge, D. Kim, S. Kim, M. Kivipelto, L. Knibbs, A. K. Knudsen, Y. Kokubo, S. Kosen, M. Kotagal, M. A. Kravchenko, S. Krishnaswami, H. Krueger, B. K. Defo, E. J. Kuipers, B. K. Bicer, C. Kulkarni, V. S. Kulkarni, K. Kumar, R. B. Kumar, G. F. Kwan, H. Kyu, T. Lai, A. L. Balaji, R. Lalloo, T. Lallukka, H. Lam, Q. Lan, V. C. Lansingh, H. J. Larson, A. Larsson, P. M. Lavados, A. E. B. Lawrynowicz, J. L. Leasher, J.-T. Lee, J. Leigh, M. Leinsalu, R. Leung, C. Levitz, B. Li, Y. Li, Y. Li, C. Liddell, S. S. Lim, G. M. F. de Lima, M. L. Lind, S. E. Lipshultz, S. Liu, Y. Liu, B. K. Lloyd, K. T. Lofgren, G. Logroscino, S. J. London, J. Lortet-Tieulent, P. A. Lotufo, R. M. Lucas, R. Lunevicius, R. A. Lyons, S. Ma, V. M. P. Machado, M. F. MacIntyre, M. T. Mackay, J. H. MacLachlan, C. Magis-Rodriguez, A. A. Mahdi, M. Majdan, R. Malekzadeh, S. Mangalam, C. C. Mapoma, M. Marape,

W. Marcenes, C. Margono, G. B. Marks, M. B. Marzan, J. R. Masci, M. T. Q. Mashal, F. Masiye, A. J. Mason-Jones, R. Matzopolous, B. M. Mayosi, T. T. Mazorodze, J. J. McGrath, A. C. Mckay, M. Mckee, A. McLain, P. A. Meaney, M. M. Mehndiratta, F. Mejia-Rodriguez, Y. A. Melaku, M. Meltzer, Z. A. Memish, W. Mendoza, G. A. Mensah, A. Meretoja, F. A. Mhimbira, T. R. Miller, E. J. Mills, A. Misganaw, S. K. Mishra, C. N. Mock, T. E. Moffitt, N. M. Ibrahim, K. A. Mohammad, A. H. Mokdad, G. L. Mola, L. Monasta, J. d. I. C. Monis, J. C. M. Hernandez, M. Montico, T. J. Montine, M. D. Mooney, A. R. Moore, M. Moradi-Lakeh, A. E. Moran, R. Mori, J. Moschandreas, W. N. Moturi, M. L. Moyer, D. Mozaffarian, U. O. Mueller, M. Mukaigawara, E. C. Mullany, J. Murray, A. Mustapha, P. Naghavi, A. Naheed, K. S. Naidoo, L. Naldi, D. Nand, V. Nangia, K. M. V. Narayan, D. Nash, J. Nasher, C. Nejjari, R. G. Nelson, M. Neuhouser, S. P. Neupane, P. A. Newcomb, L. Newman, C. R. Newton, M. Ng, F. N. Ngalesoni, G. Nguyen, N. Thi Trang Nguyen, M. I. Nisar, S. Nolte, O. F. Norheim, R. E. Norman, B. Norrving, L. Nyakarahuka, S. Odell, M. O'Donnell, T. Ohkubo, S. L. Ohno, B. O. Olusanya, S. B. Omer, J. N. Opio, O. E. Orisakwe, K. F. Ortblad, A. Ortiz, M. L. K. Otayza, A. W. Pain, J. D. Pandian, C. I. Panelo, J. Panniyammakal, C. Papachristou, A. J. Paternina Caicedo, S. B. Patten, G. C. Patton, V. K. Paul, B. Pavlin, N. Pearce, C. A. Pellegrini, D. M. Pereira, S. C. Peresson, R. Perez-Padilla, F. P. Perez-Ruiz, N. Perico, A. Pervaiz, K. Pesudovs, C. B. Peterson, M. Petzold, B. K. Phillips, D. E. Phillips, M. R. Phillips, D. Plass, F. B. Piel, D. Poenaru, S. Polinder, S. Popova, R. G. Poulton, F. Pourmalek, D. Prabhakaran, D. Qato, A. D. Quezada, D. A. Quistberg, F. Rabito, A. Rafay, K. Rahimi, V. Rahimi-Movaghar, S. U. R. Rahman, M. Raju, I. Rakovac, S. M. Rana, A. Refaat, G. Remuzzi, A. L. Ribeiro, S. Ricci, P. M. Riccio, L. Richardson, J. H. Richardus, B. Roberts, D. A. Roberts, M. Robinson, A. Roca, A. Rodriguez, D. Rojas-Rueda, L. Ronfani, R. Room, G. A. Roth, D. Rothenbacher, D. H. Rothstein, J. T. Rowley, N. Roy, G. M. Ruhago, L. Rushton, S. Sambandam, K. Soreide, M. Y. Saeedi, S. Saha, R. Sahathevan, M. A. Sahraian, B. W. Sahle, J. A. Salomon, D. Salvo, G. M. J. Samonte, U. Sampson, J. R. Sanabria, L. Sandar, I. S. Santos, M. Satpathy, M. Sawhney, M. Saylan, P. Scarborough, B. Schoettker, J. C. Schmidt, I. J. C. Schneider, A. E. Schumacher, D. C. Schwebel, J. G. Scott, S. G. Sepanlou, E. E. Servan-

Mori, K. Shackelford, A. Shaheen, S. Shahraz, M. Shakh-Nazarova, S. Shangguan, J. She, S. Sheikhabaei, D. S. Shepard, K. Shibuya, Y. Shinohara, K. Shishani, I. Shiue, R. Shivakoti, M. G. Shrimel, I. D. Sigfusdottir, D. H. Silberberg, A. P. Silva, E. P. Simard, S. Sindi, J. A. Singh, L. Singh, E. Sioson, V. Skirbekk, K. Sliwa, S. So, M. Soljak, S. Soneji, S. S. Soshnikov, L. A. Sposato, C. T. Sreeramareddy, J. R. D. Stanaway, V. K. Stathopoulou, K. Steenland, C. Stein, C. Steiner, A. Stevens, H. Stoeckl, K. Straif, K. Stroumpoulis, L. Sturua, B. F. Sunguya, S. Swaminathan, M. Swaroop, B. L. Sykes, K. M. Tabb, K. Takahashi, R. T. Talongwa, F. Tan, D. Tanne, M. Tanner, M. Tavakkoli, B. T. Ao, C. M. Teixeira, T. Templin, E. Y. Tenkorang, A. S. Terkawi, B. A. Thomas, A. L. Thorne-Lyman, A. G. Thrift, G. D. Thurston, T. Tillmann, D. L. Tirschwell, I. M. Tleyjeh, M. Tonelli, F. Topouzis, J. A. Towbin, H. Toyoshima, J. Traebert, B. X. Tran, T. Truelsen, U. Trujillo, M. Trillini, Z. T. Dimbuene, M. Tsilimbaris, E. M. Tuzcu, C. Ubeda, U. S. Uchendu, K. N. Ukwaja, E. A. Undurraga, A. J. Vallely, S. van de Vijver, C. H. van Gool, Y. Y. Varakin, T. J. Vasankari, A. M. N. Vasconcelos, M. S. Vavilala, N. Venketasubramanian, L. Vijayakumar, S. Villalpando, F. S. Violante, V. V. Vlassov, G. R. Wagner, S. G. Waller, J. Wang, L. Wang, X. Wang, Y. Wang, T. S. Warouw, S. Weichenthal, E. Weiderpass, R. G. Weintraub, W. Wenzhi, A. Werdecker, K. R. R. Wessells, R. Westerman, H. A. Whiteford, J. D. Wilkinson, T. N. Williams, S. M. Woldeyohannes, C. D. A. Wolfe, T. M. Wolock, A. D. Woolf, J. Q. Wong, J. L. Wright, S. Wulf, B. Wurtz, G. Xu, Y. C. Yang, Y. Yano, H. Yatsuya, P. Yip, N. Yonemoto, S.-J. Yoon, M. Younis, C. Yu, K. Y. Jin, M. E. S. Zaki, M. F. Zamakhshary, H. Zeeb, Y. Zhang, Y. Zhao, Y. Zheng, J. Zhu, S. Zhu, D. Zonies, X. N. Zou, J. R. Zunt, T. Vos, A. D. Lopez, and C. J. L. Murray. Global, regional, and national age-sex specific all-cause and cause-specific mortality for 240 causes of death, 1990-2013: a systematic analysis for the Global Burden of Disease Study 2013. *The Lancet*, 385(9963):117–171, 2015. ISSN 0140-6736. URL [http://dx.doi.org/10.1016/S0140-6736\(14\)61682-2](http://dx.doi.org/10.1016/S0140-6736(14)61682-2).

I. Napari, M. Kulmala, and H. Vehkamäki. Ternary nucleation of inorganic acids, ammonia, and water. *Journal of Chemical Physics*, 117:8418–8425, 2002. ISSN 00219606. doi: 10.1063/1.1511722.

- A. Nenes and J. H. Seinfeld. Parameterization of cloud droplet formation in global climate models. *Journal of Geophysical Research: Atmospheres*, 108(D14), 2018/04/09 2003. doi: 10.1029/2002JD002911. URL <https://doi.org/10.1029/2002JD002911>.
- K. Ni, E. Carter, J. Schauer, M. Ezzati, Y. Zhang, H. Niu, A. Lai, M. Shan, Y. Wang, X. Yang, and J. Baumgartner. Seasonal variation in outdoor, indoor, and personal air pollution exposures of women using wood stoves in the Tibetan Plateau: Baseline assessment for an energy intervention study. *Environment International*, 94:449–457, sep 2016. ISSN 0160-4120. doi: 10.1016/J.ENVINT.2016.05.029. URL <http://www.sciencedirect.com/science/article/pii/S0160412016302136>.
- B. Ostro, R. Broadwin, S. Green, W.-Y. Feng, and M. Lipsett. Fine Particulate Air Pollution and Mortality in Nine California Counties: Results from CALFINE. *Environmental Health Perspectives*, 114(1):29–33, jan 2006. ISSN 0091-6765. doi: 10.1289/ehp.8335. URL <http://www.ncbi.nlm.nih.gov/pmc/articles/PMC1332652/>.
- S. N. Pandis, K. Skyllakou, K. Florou, E. Kostenidou, C. Kaltsonoudis, E. Hasa, and A. A. Presto. Urban particulate matter pollution: a tale of five cities. *Faraday Discussions*, 189(0):277–290, 2016. ISSN 1359-6640. doi: 10.1039/C5FD00212E. URL <http://dx.doi.org/10.1039/C5FD00212E>.
- R. Park, D. JACOB, N. KUMAR, and R. YANTOSCA. Regional visibility statistics in the United States: Natural and transboundary pollution influences, and implications for the Regional Haze Rule. *Atmospheric Environment*, 40(28):5405–5423, sep 2006. ISSN 13522310. doi: 10.1016/j.atmosenv.2006.04.059. URL <http://www.sciencedirect.com/science/article/pii/S1352231006004316>.
- A. Peters, D. W. Dockery, J. Heinrich, and H. E. Wichmann. Short-term effects of particulate air pollution on respiratory morbidity in asthmatic children. *Eur Respir J*, 10, 1997.

- A. Peters, B. Veronesi, L. Calderon-Garciduenas, P. Gehr, L. C. Chen, M. Geiser, W. Reed, B. Rothen-Rutishauser, S. Schurch, and H. Schulz. Translocation and potential neurological effects of fine and ultrafine particles a critical update. *Part Fibre Toxicol*, 3, 2006. doi: 10.1186/1743-8977-3-13. URL <https://doi.org/10.1186/1743-8977-3-13>.
- M. D. Petters and S. M. Kreidenweis. A single parameter representation of hygroscopic growth and cloud condensation nucleus activity. *Atmospheric Chemistry and Physics*, 7(8):1961–1971, apr 2007. ISSN 1680-7324. doi: 10.5194/acp-7-1961-2007. URL <http://www.atmos-chem-phys.net/7/1961/2007/>.
- A. Petzold, J. A. Ogren, M. Fiebig, P. Laj, S.-M. Li, U. Baltensperger, T. Holzer-Popp, S. Kinne, G. Pappalardo, N. Sugimoto, C. Wehrli, A. Wiedensohler, and X.-Y. Zhang. Recommendations for reporting "black carbon" measurements. *Atmospheric Chemistry and Physics*, 13(16):8365–8379, aug 2013. ISSN 1680-7324. doi: 10.5194/acp-13-8365-2013. URL <http://www.atmos-chem-phys.net/13/8365/2013/>.
- S. Philip, R. V. Martin, J. R. Pierce, J. L. Jimenez, Q. Zhang, M. R. Canagaratna, D. V. Spracklen, C. R. Nowlan, L. N. Lamsal, M. J. Cooper, and N. A. Krotkov. Spatially and seasonally resolved estimate of the ratio of organic mass to organic carbon. *Atmospheric Environment*, 87:34–40, 2014. ISSN 1352-2310. doi: <https://doi.org/10.1016/j.atmosenv.2013.11.065>. URL <http://www.sciencedirect.com/science/article/pii/S1352231013009151>.
- R. Piedrahita, K. L. Dickinson, E. Kanyomse, E. Coffey, R. Alirigia, Y. Hagar, I. Rivera, A. Oduro, V. Dukic, C. Wiedinmyer, and M. Hannigan. Assessment of cookstove stacking in Northern Ghana using surveys and stove use monitors. *Energy for Sustainable Development*, 34:67–76, 2016. ISSN 09730826. doi: 10.1016/j.esd.2016.07.007. URL <http://www.sciencedirect.com/science/article/pii/S0973082616302137>.
- J. R. Pierce and P. J. Adams. Uncertainty in global CCN concentrations from uncertain aerosol nucleation and primary emission rates. *Atmospheric Chemistry and Physics*, 9(4):1339–1356,

- feb 2009. ISSN 1680-7324. doi: 10.5194/acp-9-1339-2009. URL <http://www.atmos-chem-phys.net/9/1339/2009/acp-9-1339-2009.html>.
- J. R. Pierce, K. Chen, and P. J. Adams. Contribution of primary carbonaceous aerosol to cloud condensation nuclei: processes and uncertainties evaluated with a global aerosol microphysics model. *Atmospheric Chemistry and Physics*, 7(20):5447–5466, oct 2007. ISSN 1680-7324. doi: 10.5194/acp-7-5447-2007. URL <http://www.atmos-chem-phys.net/7/5447/2007/>.
- J. R. Pierce, B. Croft, J. K. Kodros, S. D. D’Andrea, and R. V. Martin. The importance of interstitial particle scavenging by cloud droplets in shaping the remote aerosol size distribution and global aerosol-climate effects. *Atmospheric Chemistry and Physics*, 15(11):6147–6158, jun 2015. ISSN 1680-7324. doi: 10.5194/acp-15-6147-2015. URL <http://www.atmos-chem-phys.net/15/6147/2015/acp-15-6147-2015.html>.
- L. Pinault, M. Tjepkema, D. L. Crouse, S. Weichenthal, A. van Donkelaar, R. V. Martin, M. Brauer, H. Chen, and R. T. Burnett. Risk estimates of mortality attributed to low concentrations of ambient fine particulate matter in the Canadian community health survey cohort. *Environmental Health*, 15(1):18, 2016. ISSN 1476-069X. doi: 10.1186/s12940-016-0111-6. URL <https://doi.org/10.1186/s12940-016-0111-6>.
- R. Pincus, H. W. Barker, and J.-J. Morcrette. A fast, flexible, approximate technique for computing radiative transfer in inhomogeneous cloud fields. *Journal of Geophysical Research: Atmospheres*, 108(D13):n/a–n/a, jul 2003. ISSN 01480227. doi: 10.1029/2002JD003322. URL <http://onlinelibrary.wiley.com/doi/10.1029/2002JD003322/full>.
- C. A. Pope and D. W. Dockery. Health effects of fine particulate air pollution: lines that connect. *Journal of the Air & Waste Management Association (1995)*, 56:709–742, 2006. ISSN 1096-2247.
- C. A. Pope, R. T. Burnett, M. J. Thun, E. E. Calle, D. Krewski, K. Ito, and G. D. Thurston. Lung cancer, cardiopulmonary mortality, and long-term exposure to fine particulate air pollution. *JAMA*

- : *the journal of the American Medical Association*, 287(9):1132–1141, 2002. ISSN 0098-7484. doi: 10.1016/j.scitotenv.2011.03.017.
- K. J. Pringle, K. S. Carslaw, D. V. Spracklen, G. M. Mann, and M. P. Chipperfield. The relationship between aerosol and cloud drop number concentrations in a global aerosol microphysics model. *Atmospheric Chemistry and Physics*, 9(12):4131–4144, jun 2009. ISSN 1680-7324. doi: 10.5194/acp-9-4131-2009. URL <http://www.atmos-chem-phys.org/9/4131/2009/acp-9-4131-2009.html>.
- R. C. Puett, J. E. Hart, J. D. Yanosky, C. Paciorek, J. Schwartz, H. Suh, F. E. Speizer, and F. Laden. Chronic Fine and Coarse Particulate Exposure, Mortality, and Coronary Heart Disease in the Nurses' Health Study. *Environmental Health Perspectives*, 117(11):1697–1701, nov 2009. ISSN 0091-6765. doi: 10.1289/ehp.0900572. URL <http://www.ncbi.nlm.nih.gov/pmc/articles/PMC2801178/>.
- E. Pungler and J. West. The effect of grid resolution on estimates of the burden of ozone and fine particulate matter on premature mortality in the USA. *Air Quality, Atmosphere & Health*, 6(3): 563–573, 2013. ISSN 1873-9318. doi: 10.1007/s11869-013-0197-8. URL <http://dx.doi.org/10.1007/s11869-013-0197-8>.
- P. Quinn, G. Shaw, E. Andrews, E. Dutton, T. Ruoho-Airola, and S. Gong. Arctic haze: current trends and knowledge gaps. *Tellus B*, 59(1):99–114, 2007.
- T. Raatikainen, D. Brus, A.-P. Hyvärinen, J. Svensson, E. Asmi, and H. Lihavainen. Black carbon concentrations and mixing state in the Finnish Arctic. *Atmospheric Chemistry and Physics*, 15(17):10057–10070, sep 2015. ISSN 1680-7324. doi: 10.5194/acp-15-10057-2015. URL <http://www.atmos-chem-phys.net/15/10057/2015/>.
- A. Rap, C. E. Scott, D. V. Spracklen, N. Bellouin, P. M. Forster, K. S. Carslaw, A. Schmidt, and G. Mann. Natural aerosol direct and indirect radiative effects. *Geophysical Research Letters*, 40: 3297–3301, 2013. ISSN 00948276. doi: 10.1002/grl.50441.

- D. K. Rogalsky, P. Mendola, T. A. Metts, and W. J. Martin. Estimating the Number of Low-Income Americans Exposed to Household Air Pollution from Burning Solid Fuels. *Environmental Health Perspectives*, 122(8):806–810, aug 2014. ISSN 0091-6765. doi: 10.1289/ehp.1306709. URL <http://www.ncbi.nlm.nih.gov/pmc/articles/PMC4123020/>.
- L. D. Rotstayn, S. J. Jeffrey, M. A. Collier, S. M. Dravitzki, A. C. Hirst, J. I. Syktus, and K. K. Wong. Aerosol- and greenhouse gas-induced changes in summer rainfall and circulation in the Australasian region: a study using single-forcing climate simulations. *Atmospheric Chemistry and Physics*, 12(14):6377–6404, jul 2012. ISSN 1680-7324. doi: 10.5194/acp-12-6377-2012. URL <http://www.atmos-chem-phys.net/12/6377/2012/>.
- I. Ruiz-Mercado, O. Masera, H. Zamora, and K. R. Smith. Adoption and sustained use of improved cookstoves. *Energy Policy*, 39(12):7557–7566, dec 2011. ISSN 03014215. doi: 10.1016/j.enpol.2011.03.028. URL <http://linkinghub.elsevier.com/retrieve/pii/S0301421511002084>.
- K. M. Sakamoto, J. D. Allan, H. Coe, J. W. Taylor, T. J. Duck, and J. R. Pierce. Aged boreal biomass-burning aerosol size distributions from BORTAS 2011. *Atmospheric Chemistry and Physics*, 15(4):1633–1646, feb 2015. ISSN 1680-7324. doi: 10.5194/acp-15-1633-2015. URL <http://www.atmos-chem-phys.net/15/1633/2015/acp-15-1633-2015.html>.
- K. M. Sakamoto, J. R. Laing, R. G. Stevens, D. A. Jaffe, and J. R. Pierce. The evolution of biomass-burning aerosol size distributions due to coagulation: dependence on fire and meteorological details and parameterization. *Atmospheric Chemistry and Physics*, 16(12):7709–7724, jun 2016. ISSN 1680-7324. doi: 10.5194/acp-16-7709-2016. URL <http://www.atmos-chem-phys.net/16/7709/2016/>.
- R. Saleh, C. J. Hennigan, G. R. McMeeking, W. K. Chuang, E. S. Robinson, H. Coe, N. M. Donahue, and a. L. Robinson. Absorptivity of brown carbon in fresh and photo-chemically aged biomass-burning emissions. *Atmospheric Chemistry and Physics*, 13(15):7683–7693, aug 2013. ISSN 1680-7324. doi: 10.5194/acp-13-7683-2013. URL <http://www.atmos-chem-phys.net/13/7683/2013/>.

- R. Saleh, E. S. Robinson, D. S. Tkacik, A. T. Ahern, S. Liu, A. C. Aiken, R. C. Sullivan, A. A. Presto, M. K. Dubey, R. J. Yokelson, N. M. Donahue, and A. L. Robinson. Brownness of organics in aerosols from biomass burning linked to their black carbon content. *Nature Geoscience*, 7 (August):647–650, 2014. doi: 10.1038/NGEO2220.
- A. Saltelli, S. Tarantola, and K. P.-S. Chan. A Quantitative Model-Independent Method for Global Sensitivity Analysis of Model Output. *Technometrics*, 41(1):39–56, feb 1999. ISSN 0040-1706. doi: 10.1080/00401706.1999.10485594. URL <http://www.tandfonline.com/doi/abs/10.1080/00401706.1999.10485594>.
- A. Saltelli, M. Ratto, T. Andres, F. Campolongo, J. Cariboni, D. Gatelli, M. Saisana, and S. Tarantola. Introduction to Sensitivity Analysis. In *Global Sensitivity Analysis. The Primer*, pages 1–51. John Wiley & Sons, Ltd, 2007. ISBN 9780470725184. doi: 10.1002/9780470725184.ch1. URL <http://dx.doi.org/10.1002/9780470725184.ch1>.
- A. Saltelli, P. Annoni, I. Azzini, F. Campolongo, M. Ratto, and S. Tarantola. Variance based sensitivity analysis of model output. Design and estimator for the total sensitivity index. *Computer Physics Communications*, 181(2):259–270, feb 2010. ISSN 00104655. doi: 10.1016/j.cpc.2009.09.018. URL <http://linkinghub.elsevier.com/retrieve/pii/S0010465509003087>.
- M. Schnaiter, H. Horvath, O. Möhler, K. H. Naumann, H. Saathoff, and O. W. Schöck. UV-VIS-NIR spectral optical properties of soot and soot-containing aerosols. *Journal of Aerosol Science*, 34: 1421–1444, 2003. ISSN 00218502. doi: 10.1016/S0021-8502(03)00361-6.
- M. Schnaiter, C. Linke, O. Möhler, K. H. Naumann, H. Saathoff, R. Wagner, U. Schurath, and B. Wehner. Absorption amplification of black carbon internally mixed with secondary organic aerosol. *Journal of Geophysical Research D: Atmospheres*, 110:1–11, 2005. ISSN 01480227. doi: 10.1029/2005JD006046.
- J. P. Schwarz, R. S. Gao, J. R. Spackman, L. A. Watts, D. S. Thomson, D. W. Fahey, T. B. Ryerson, J. Peischl, J. S. Holloway, M. Trainer, G. J. Frost, T. Baynard, D. A. Lack, J. A. de Gouw,

- C. Warneke, and L. A. Del Negro. Measurement of the mixing state, mass, and optical size of individual black carbon particles in urban and biomass burning emissions. *Geophysical Research Letters*, 35(13):L13810, jul 2008a. ISSN 0094-8276. doi: 10.1029/2008GL033968. URL <http://doi.wiley.com/10.1029/2008GL033968>.
- J. P. Schwarz, J. R. Spackman, D. W. Fahey, R. S. Gao, U. Lohmann, P. Stier, L. A. Watts, D. S. Thomson, D. A. Lack, L. Pfister, M. J. Mahoney, D. Baumgardner, J. C. Wilson, and J. M. Reeves. Coatings and their enhancement of black carbon light absorption in the tropical atmosphere. *Journal of Geophysical Research*, 113(D3):D03203, feb 2008b. ISSN 0148-0227. doi: 10.1029/2007JD009042. URL <http://doi.wiley.com/10.1029/2007JD009042>.
- C. E. Scott, a. Rap, D. V. Spracklen, P. M. Forster, K. S. Carslaw, G. W. Mann, K. J. Pringle, N. Kivekäs, M. Kulmala, H. Lihavainen, and P. Tunved. The direct and indirect radiative effects of biogenic secondary organic aerosol. *Atmospheric Chemistry and Physics*, 14(1):447–470, jan 2014. ISSN 1680-7324. doi: 10.5194/acp-14-447-2014. URL <http://www.atmos-chem-phys.net/14/447/2014/>.
- G. A. Sehmel. Particle and gas dry deposition: A review. *Atmospheric Environment (1967)*, 14(9):983–1011, jan 1980. ISSN 0004-6981. doi: 10.1016/0004-6981(80)90031-1. URL <https://www.sciencedirect.com/science/article/pii/0004698180900311>.
- J. H. Seinfeld and S. N. Pandis. *Atmospheric chemistry and physics: from air pollution to climate change*. John Wiley & Sons, 2012.
- G. Shaddick, M. L. Thomas, A. Green, M. Brauer, A. van Donkelaar, R. Burnett, H. H. Chang, A. Cohen, R. V. Dingenen, C. Dora, S. Gumy, Y. Liu, R. Martin, L. A. Waller, J. West, J. V. Zidek, and A. Prüss-Ustün. Data integration model for air quality: a hierarchical approach to the global estimation of exposures to ambient air pollution. *Journal of the Royal Statistical Society: Series C (Applied Statistics)*, jun 2017. ISSN 00359254. doi: 10.1111/rssc.12227. URL <http://doi.wiley.com/10.1111/rssc.12227>.

- S. Sharma, W. R. Leaitch, L. Huang, D. Veber, F. Kolonjari, W. Zhang, S. J. Hanna, A. K. Bertram, and J. A. Ogren. An Evaluation of three methods for measuring black carbon at Alert, Canada. *Atmospheric Chemistry and Physics Discussions*, pages 1–42, may 2017. ISSN 1680-7375. doi: 10.5194/acp-2017-339. URL <https://www.atmos-chem-phys-discuss.net/acp-2017-339/>.
- D. Shindell, J. C. I. Kuylenstierna, E. Vignati, R. van Dingenen, M. Amann, Z. Klimont, S. C. Anenberg, N. Muller, G. Janssens-Maenhout, F. Raes, J. Schwartz, G. Faluvegi, L. Pozzoli, K. Kupiainen, L. Höglund-Isaksson, L. Emberson, D. Streets, V. Ramanathan, K. Hicks, N. T. K. Oanh, G. Milly, M. Williams, V. Demkine, and D. Fowler. Simultaneously mitigating near-term climate change and improving human health and food security. *Science (New York, N.Y.)*, 335: 183–9, 2012. ISSN 1095-9203. doi: 10.1126/science.1210026. URL <http://www.ncbi.nlm.nih.gov/pubmed/22246768>.
- D. T. Shindell, J.-F. Lamarque, M. Schulz, M. Flanner, C. Jiao, M. Chin, P. J. Young, Y. H. Lee, L. Rotstayn, N. Mahowald, G. Milly, G. Faluvegi, Y. Balkanski, W. J. Collins, A. J. Conley, S. Dalsoren, R. Easter, S. Ghan, L. Horowitz, X. Liu, G. Myhre, T. Nagashima, V. Naik, S. T. Rumbold, R. Skeie, K. Sudo, S. Szopa, T. Takemura, A. Voulgarakis, J.-H. Yoon, and F. Lo. Radiative forcing in the ACCMIP historical and future climate simulations. *Atmospheric Chemistry and Physics*, 13(6):2939–2974, mar 2013a. ISSN 1680-7324. doi: 10.5194/acp-13-2939-2013. URL <http://www.atmos-chem-phys.net/13/2939/2013/>.
- D. T. Shindell, O. Pechony, A. Voulgarakis, G. Faluvegi, L. Nazarenko, J.-F. Lamarque, K. Bowman, G. Milly, B. Kovari, R. Ruedy, and G. A. Schmidt. Interactive ozone and methane chemistry in GISS-E2 historical and future climate simulations. *Atmospheric Chemistry and Physics*, 13(5):2653–2689, mar 2013b. ISSN 1680-7324. doi: 10.5194/acp-13-2653-2013. URL <http://www.atmos-chem-phys.net/13/2653/2013/>.
- R. B. Skeie, T. K. Berntsen, G. Myhre, K. Tanaka, M. M. Kvalevåg, and C. R. Hoyle. Anthropogenic radiative forcing time series from pre-industrial times until 2010. *Atmospheric Chemistry and*

- Physics*, 11(22):11827–11857, nov 2011. ISSN 1680-7324. doi: 10.5194/acp-11-11827-2011. URL <http://www.atmos-chem-phys.net/11/11827/2011/>.
- J. G. Slowik, E. S. Cross, J.-H. Han, P. Davidovits, T. B. Onasch, J. T. Jayne, L. R. Williams, M. R. Canagaratna, D. R. Worsnop, R. K. Chakrabarty, H. Moosmüller, W. P. Arnott, J. P. Schwarz, R.-S. Gao, D. W. Fahey, G. L. Kok, and A. Petzold. An Inter-Comparison of Instruments Measuring Black Carbon Content of Soot Particles. *Aerosol Science and Technology*, 41(3):295–314, apr 2007. ISSN 0278-6826. doi: 10.1080/02786820701197078. URL <http://www.tandfonline.com/doi/abs/10.1080/02786820701197078>.
- K. R. Smith, N. Bruce, K. Balakrishnan, H. Adair-Rohani, J. Balmes, Z. Chafe, M. Dherani, H. D. Hosgood, S. Mehta, D. Pope, and E. Rehfuss. Millions dead: how do we know and what does it mean? Methods used in the comparative risk assessment of household air pollution. *Annual review of public health*, 35:185–206, 2014. ISSN 1545-2093. doi: 10.1146/annurev-publhealth-032013-182356. URL <http://www.ncbi.nlm.nih.gov/pubmed/24641558>.
- D. V. Spracklen, K. J. Pringle, K. S. Carslaw, M. P. Chipperfield, and G. W. Mann. A global off-line model of size-resolved aerosol microphysics: I. Model development and prediction of aerosol properties. *Atmospheric Chemistry and Physics*, 5(8):2227–2252, aug 2005. ISSN 1680-7324. doi: 10.5194/acp-5-2227-2005. URL <http://www.atmos-chem-phys.org/5/2227/2005/acp-5-2227-2005.html>.
- D. V. Spracklen, J. L. Jimenez, K. S. Carslaw, D. R. Worsnop, M. J. Evans, G. W. Mann, Q. Zhang, M. R. Canagaratna, J. Allan, H. Coe, G. McFiggans, A. Rap, and P. Forster. Aerosol mass spectrometer constraint on the global secondary organic aerosol budget. *Atmospheric Chemistry and Physics*, 11:12109–12136, 2011. ISSN 16807316. doi: 10.5194/acp-11-12109-2011.
- D. G. Streets, T. Bond, G. R. Carmichael, S. Fernandes, Q. Fu, D. He, Z. Klimont, S. Nelson, N. Y. Tsai, M. Wang, J.-H. Woo, and K. Yarber. An inventory of gaseous and primary aerosol emissions in Asia in the year 2000. *Journal of Geophysical Research*, 108(D21):8809, 2003. ISSN 0148-0227. doi: 10.1029/2002JD003093. URL <http://doi.wiley.com/10.1029/2002JD003093>.

- R. Subramanian, G. L. Kok, D. Baumgardner, A. Clarke, Y. Shinozuka, T. L. Campos, C. G. Heizer, B. B. Stephens, B. de Foy, P. B. Voss, and R. A. Zaveri. Black carbon over Mexico: the effect of atmospheric transport on mixing state, mass absorption cross-section, and BC/CO ratios. *Atmospheric Chemistry and Physics*, 10(1):219–237, jan 2010. ISSN 1680-7324. doi: 10.5194/acp-10-219-2010. URL <http://www.atmos-chem-phys.net/10/219/2010/>.
- S. Szopa, Y. Balkanski, M. Schulz, S. Bekki, D. Cugnet, A. Fortems-Cheiney, S. Turquety, A. Cozic, C. Déandreis, D. Hauglustaine, A. Idelkadi, J. Lathière, F. Lefevre, M. Marchand, R. Vuolo, N. Yan, and J.-L. Dufresne. Aerosol and ozone changes as forcing for climate evolution between 1850 and 2100. *Climate Dynamics*, 40(9):2223–2250, 2013. ISSN 1432-0894. doi: 10.1007/s00382-012-1408-y. URL <http://dx.doi.org/10.1007/s00382-012-1408-y>.
- T. M. Thompson and N. E. Selin. Influence of air quality model resolution on uncertainty associated with health impacts. *Atmospheric Chemistry and Physics*, 12(20):9753–9762, oct 2012. ISSN 1680-7324. doi: 10.5194/acp-12-9753-2012. URL <http://www.atmos-chem-phys.net/12/9753/2012/>.
- G. D. Thurston, J. Ahn, K. R. Cromar, Y. Shao, H. R. Reynolds, M. Jerrett, C. C. Lim, R. Shanley, Y. Park, and R. B. Hayes. Ambient Particulate Matter Air Pollution Exposure and Mortality in the NIH-AARP Diet and Health Cohort. *Environmental Health Perspectives*, 124(4):484–490, apr 2016. ISSN 0091-6765. doi: 10.1289/ehp.1509676. URL <http://www.ncbi.nlm.nih.gov/pmc/articles/PMC4829984/>.
- J. Tröstl, W. K. Chuang, H. Gordon, M. Heinritzi, C. Yan, U. Molteni, L. Ahlm, C. Frege, F. Bianchi, R. Wagner, M. Simon, K. Lehtipalo, C. Williamson, J. S. Craven, J. Duplissy, A. Adamov, J. Almeida, A.-K. Bernhammer, M. Breitenlechner, S. Brilke, A. Dias, S. Ehrhart, R. C. Flagan, A. Franchin, C. Fuchs, R. Guida, M. Gysel, A. Hansel, C. R. Hoyle, T. Jokinen, H. Junninen, J. Kangasluoma, H. Keskinen, J. Kim, M. Krapf, A. Kürten, A. Laaksonen, M. Lawler, M. Leiminger, S. Mathot, O. Möhler, T. Nieminen, A. Onnela, T. Petäjä, F. M. Piel, P. Miettinen, M. P. Rissanen, L. Rondo, N. Sarnela, S. Schobesberger, K. Sengupta, M. Sipilä, J. N. Smith,

- G. Steiner, A. Tomè, A. Virtanen, A. C. Wagner, E. Weingartner, D. Wimmer, P. M. Winkler, P. Ye, K. S. Carslaw, J. Curtius, J. Dommen, J. Kirkby, M. Kulmala, I. Riipinen, D. R. Worsnop, N. M. Donahue, and U. Baltensperger. The role of low-volatility organic compounds in initial particle growth in the atmosphere. *Nature*, 533(7604):527–531, may 2016. ISSN 0028-0836. URL <http://dx.doi.org/10.1038/nature18271><http://10.0.4.14/nature18271>.
- P. Tunved, J. Ström, and R. Krejci. Arctic aerosol life cycle: linking aerosol size distributions observed between 2000 and 2010 with air mass transport and precipitation at zeppelin station, ny-å. . . lesund, svalbard. *Atmospheric Chemistry and Physics*, 13(7):3643–3660, 2013.
- S. Twomey. Pollution and the planetary albedo. *Atmospheric Environment (1967)*, 8(12):1251–1256, 1974. URL <http://www.sciencedirect.com/science/article/pii/0004698174900043>.
- S. Twomey. Aerosols, clouds and radiation. *Atmospheric Environment. Part A. General Topics*, 25(11):2435–2442, jan 1991. ISSN 09601686. doi: 10.1016/0960-1686(91)90159-5. URL <http://linkinghub.elsevier.com/retrieve/pii/0960168691901595>.
- A. Valavanidis, K. FIOTAKIS, and T. VLACHOGIANNI. Airborne Particulate Matter and Human Health: Toxicological Assessment and Importance of Size and Composition of Particles for Oxidative Damage and Carcinogenic Mechanisms. *Journal of Environmental Science and Health, Part C*, 26(4):339–362, dec 2008. ISSN 1059-0501. doi: 10.1080/10590500802494538. URL <https://doi.org/10.1080/10590500802494538>.
- G. R. Van Der Werf, J. T. Randerson, L. Giglio, G. J. Collatz, M. Mu, P. S. Kasibhatla, D. C. Morton, R. S. Defries, Y. Jin, and T. T. Van Leeuwen. Global fire emissions and the contribution of deforestation, savanna, forest, agricultural, and peat fires (1997-2009). *Atmospheric Chemistry and Physics*, 10:11707–11735, 2010. ISSN 16807316. doi: 10.5194/acp-10-11707-2010.
- A. van Donkelaar, R. V. Martin, M. Brauer, R. Kahn, R. Levy, C. Verduzco, and P. J. Villeneuve. Global estimates of ambient fine particulate matter concentrations from satellite-based aerosol optical depth: development and application. *Environmental health perspectives*, 118(6):847–55,

- jun 2010. ISSN 1552-9924. doi: 10.1289/ehp.0901623. URL <http://www.pubmedcentral.nih.gov/articlerender.fcgi?artid=2898863&tool=pmcentrez&rendertype=abstract>.
- A. van Donkelaar, R. V. Martin, M. Brauer, and B. L. Boys. Use of satellite observations for long-term exposure assessment of global concentrations of fine particulate matter. *Environmental health perspectives*, 123(2):135–43, 2015. ISSN 1552-9924. doi: 10.1289/ehp.1408646. URL <http://www.pubmedcentral.nih.gov/articlerender.fcgi?artid=4314252&tool=pmcentrez&rendertype=abstract>.
- H. Vehkamäki. An improved parameterization for sulfuric acid–water nucleation rates for tropospheric and stratospheric conditions. *Journal of Geophysical Research*, 107(D22):4622, 2002. ISSN 0148-0227. doi: 10.1029/2002JD002184. URL <http://doi.wiley.com/10.1029/2002JD002184>.
- V. Verma, T. Fang, L. Xu, R. E. Peltier, A. G. Russell, N. L. Ng, and R. J. Weber. Organic Aerosols Associated with the Generation of Reactive Oxygen Species (ROS) by Water-Soluble PM _{2.5}. *Environmental Science & Technology*, 49(7):4646–4656, apr 2015. ISSN 0013-936X. doi: 10.1021/es505577w. URL <http://pubs.acs.org/doi/10.1021/es505577w>.
- V. Vestreng, L. Ntziachristos, A. Semb, S. Reis, I. S. A. Isaksen, and L. Tarrasón. Evolution of NO_x emissions in Europe with focus on road transport control measures. *Atmospheric Chemistry and Physics*, 9(4):1503–1520, feb 2009. ISSN 1680-7324. doi: 10.5194/acp-9-1503-2009. URL <http://www.atmos-chem-phys.net/9/1503/2009/acp-9-1503-2009.html>.
- P. J. Villeneuve, S. A. Weichenthal, D. Crouse, A. B. Miller, T. To, R. V. Martin, A. van Donkelaar, C. Wall, and R. T. Burnett. Long-term Exposure to Fine Particulate Matter Air Pollution and Mortality Among Canadian Women. *Epidemiology*, 26(4), 2015. ISSN 1044-3983. URL <https://journals.lww.com/epidem/Fulltext/2015/07000/Long-term-Exposure-to-Fine-Particulate-Matter-Air.14.aspx>.

- S. C. Wang and R. C. Flagan. Scanning Electrical Mobility Spectrometer. *Aerosol Science and Technology*, 13(2):230–240, jan 1990. ISSN 0278-6826. doi: 10.1080/02786829008959441. URL <http://www.tandfonline.com/doi/abs/10.1080/02786829008959441{#}.V6jkX9oIVPY.mendeley>.
- Q. Wang, R.-J. Huang, J. Cao, Y. Han, G. Wang, G. Li, Y. Wang, W. Dai, R. Zhang, and Y. Zhou. Mixing State of Black Carbon Aerosol in a Heavily Polluted Urban Area of China: Implications for Light Absorption Enhancement. *Aerosol Science and Technology*, 48(7):689–697, may 2014. ISSN 0278-6826. doi: 10.1080/02786826.2014.917758. URL <http://www.tandfonline.com/doi/abs/10.1080/02786826.2014.917758>.
- X. Wang, C. L. Heald, D. a. Ridley, J. P. Schwarz, J. R. Spackman, a. E. Perring, H. Coe, D. Liu, and a. D. Clarke. Exploiting simultaneous observational constraints on mass and absorption to estimate the global direct radiative forcing of black carbon and brown carbon. *Atmospheric Chemistry and Physics*, 14(20):10989–11010, oct 2014. ISSN 1680-7324. doi: 10.5194/acp-14-10989-2014. URL <http://www.atmos-chem-phys.net/14/10989/2014/>.
- S. Watanabe, T. Hajima, K. Sudo, T. Nagashima, T. Takemura, H. Okajima, T. Nozawa, H. Kawase, M. Abe, T. Yokohata, T. Ise, H. Sato, E. Kato, K. Takata, S. Emori, and M. Kawamiya. MIROC-ESM 2010: model description and basic results of CMIP5-20c3m experiments. *Geoscientific Model Development*, 4(4):845–872, oct 2011. ISSN 1991-9603. doi: 10.5194/gmd-4-845-2011. URL <http://www.geosci-model-dev.net/4/845/2011/>.
- G. R. Wentworth, J. G. Murphy, B. Croft, R. V. Martin, J. R. Pierce, J.-S. Côté, I. Courchesne, J.-É. Tremblay, J. Gagnon, J. L. Thomas, S. Sharma, D. Toom-Sauntry, A. Chivulescu, M. Levasseur, and J. P. D. Abbatt. Ammonia in the summertime Arctic marine boundary layer: sources, sinks, and implications. *Atmospheric Chemistry and Physics*, 16(4):1937–1953, feb 2016. ISSN 1680-7324. doi: 10.5194/acp-16-1937-2016. URL <http://www.atmos-chem-phys.net/16/1937/2016/>.
- A. L. Westerling. Increasing western US forest wildfire activity: sensitivity to changes in the timing of spring. *Philosophical Transactions of the Royal Society B: Biological Sciences*, 371(1696), jun 2016. URL <http://rspb.royalsocietypublishing.org/content/371/1696/20150178.abstract>.

- D. M. Westervelt, J. R. Pierce, I. Riipinen, W. Trivitayanurak, A. Hamed, M. Kulmala, A. Laaksonen, S. Decesari, and P. J. Adams. Formation and growth of nucleated particles into cloud condensation nuclei: model–measurement comparison. *Atmospheric Chemistry and Physics*, 13(15):7645–7663, aug 2013. ISSN 1680-7324. doi: 10.5194/acp-13-7645-2013. URL <http://www.atmos-chem-phys.net/13/7645/2013/acp-13-7645-2013.html>.
- D. M. Westervelt, J. R. Pierce, and P. J. Adams. Analysis of feedbacks between nucleation rate, survival probability and cloud condensation nuclei formation. *Atmospheric Chemistry and Physics*, 14(11):5577–5597, jun 2014. ISSN 1680-7324. doi: 10.5194/acp-14-5577-2014. URL <http://www.atmos-chem-phys.net/14/5577/2014/acp-14-5577-2014.html>.
- D. L. Westphal and O. B. Toon. Simulations of microphysical, radiative, and dynamical processes in a continental-scale forest fire smoke plume. *Journal of Geophysical Research*, 96(D12):22379, 1991. ISSN 0148-0227. doi: 10.1029/91JD01956. URL <http://doi.wiley.com/10.1029/91JD01956>.
- K. T. Whitby. The physical characteristics of sulfur aerosols. *Atmospheric Environment (1967)*, 12(1):135–159, 1978. ISSN 00046981. doi: 10.1016/0004-6981(78)90196-8.
- C. Wiedinmyer, S. K. Akagi, R. J. Yokelson, L. K. Emmons, J. A. Al-Saadi, J. J. Orlando, and A. J. Soja. The Fire INventory from NCAR (FINN): a high resolution global model to estimate the emissions from open burning. *Geoscientific Model Development*, 4(3):625–641, jul 2011. ISSN 1991-9603. doi: 10.5194/gmd-4-625-2011. URL <http://www.geosci-model-dev.net/4/625/2011/>.
- C. Wiedinmyer, R. J. Yokelson, and B. K. Gullett. Global emissions of trace gases, particulate matter, and hazardous air pollutants from open burning of domestic waste. *Environmental science & technology*, 48(16):9523–30, 2014. ISSN 1520-5851. doi: 10.1021/es502250z. URL <http://www.ncbi.nlm.nih.gov/pubmed/25019173>.
- M. D. Willis, J. Burkart, J. L. Thomas, F. Köllner, J. Schneider, H. Bozem, P. M. Hoor, A. A. Aliabadi, H. Schulz, A. B. Herber, W. R. Leaitch, and J. P. D. Abbatt. Growth of nucleation mode particles in the summertime Arctic: a case study. *Atmospheric Chemistry and Physics*,

- 16(12):7663–7679, jun 2016. ISSN 1680-7324. doi: 10.5194/acp-16-7663-2016. URL <http://www.atmos-chem-phys.net/16/7663/2016/>.
- E. Winijkul, F. Yan, Z. Lu, D. G. Streets, T. C. Bond, and Y. Zhao. Size-resolved global emission inventory of primary particulate matter from energy-related combustion sources. *Atmospheric Environment*, 107:137–147, 2015. ISSN 1352-2310. doi: <https://doi.org/10.1016/j.atmosenv.2015.02.037>. URL <http://www.sciencedirect.com/science/article/pii/S1352231015001569>.
- World Bank. *The Cost of Air Pollution: Strengthening the Economic Case for Action*. World Bank, Washington, D.C., 2016.
- World Health Organization. *Air quality guidelines: global update 2005*. World Health Organization, 2006.
- World Health Organization. *Burden of disease from Household Air Pollution for 2012*. World Health Organization, Geneva Switzerland, 2014.
- J. Xu, R. V. Martin, A. Morrow, S. Sharma, L. Huang, W. R. Leitch, J. Burkart, H. Schulz, M. Zanatta, M. D. Willis, D. K. Henze, C. J. Lee, A. B. Herber, and J. P. D. Abbatt. Source attribution of Arctic black carbon constrained by aircraft and surface measurements. *Atmospheric Chemistry and Physics Discussions*, pages 1–45, mar 2017. ISSN 1680-7375. doi: 10.5194/acp-2017-236. URL <http://www.atmos-chem-phys-discuss.net/acp-2017-236/>.
- C. S. Zender. Mineral Dust Entrainment and Deposition (DEAD) model: Description and 1990s dust climatology. *Journal of Geophysical Research*, 108(D14):4416, jul 2003. ISSN 0148-0227. doi: 10.1029/2002JD002775. URL <http://onlinelibrary.wiley.com/doi/10.1029/2002JD002775/full>.
- L. Zhang, S. Gong, J. Padro, and L. Barrie. A size-segregated particle dry deposition scheme for an atmospheric aerosol module. *Atmospheric Environment*, 35(3):549–560, jan 2001. ISSN 1352-2310. doi: 10.1016/S1352-2310(00)00326-5. URL <https://www.sciencedirect.com/science/article/pii/S1352231000003265>.

- R. Zhang, A. F. Khalizov, J. Pagels, D. Zhang, H. Xue, and P. H. McMurry. Variability in morphology, hygroscopicity, and optical properties of soot aerosols during atmospheric processing. *Proceedings of the National Academy of Sciences of the United States of America*, 105:10291–10296, 2008. ISSN 0027-8424. doi: 10.1073/pnas.0804860105.
- Y. Zhang, R. C. Easter, S. J. Ghan, and H. Abdul-Razzak. Impact of aerosol size representation on modeling aerosol-cloud interactions. *Journal of Geophysical Research: Atmospheres*, 107 (D21):AAC 4–1–AAC 4–17, nov 2002. ISSN 01480227. doi: 10.1029/2001JD001549. URL <http://doi.wiley.com/10.1029/2001JD001549>.
- R. Zhao, A. K. Y. Lee, L. Huang, X. Li, F. Yang, and J. P. D. Abbatt. Photochemical processing of aqueous atmospheric brown carbon. *Atmospheric Chemistry and Physics*, 15(11):6087–6100, jun 2015. ISSN 1680-7324. doi: 10.5194/acp-15-6087-2015. URL <http://www.atmos-chem-phys.net/15/6087/2015/>.

Appendix A

Supplemental to Global burden of mortalities due to chronic exposure to ambient PM_{2.5} from open combustion of domestic waste

A.1 Details of the GEOS-Chem chemical transport model

The chemical-transport model, GEOS-Chem (<http://geos-chem.org>), uses re-analysis meteorological data to predict concentrations of aerosols and gaseous species. In this study, we use GEOS-Chem version 10.01 with GEOS-5 meteorological fields (<http://gmao.gsfc.nasa.gov>) to predict surface level PM_{2.5}. Aerosol species in GEOS-Chem include sulfate, ammonium, nitrate, primary hydrophilic and hydrophobic black and organic carbon, secondary organic aerosol, accumulation and coarse mode sea salt, and size-resolved dust.

The simulations in this study use black and organic carbon emissions for biofuel and fossil-fuel sources from Bond et al. (2007) and biomass burning from Global Fire Emissions Database version 3 (GFED3; van der Werf et al., 2010) with three-hourly scale factors. Globally, anthropogenic emissions from fossil-fuel combustion are from the Emissions Database for Global Atmospheric Research (EDGAR) (Janssens-Maenhout et al., 2011) version 4. EDGAR emissions are overwritten in the United States by the Environmental Protection Agency 2011 National Emissions Inventory (NEI2011; <http://www3.epa.gov/ttn/chief/>), in Canada by Criteria Air Contaminants (CAC; <http://www.ec.gc.ca/inrp-npri/>), in Mexico and the southwestern US by Big Bend Regional Aerosol and Visibility Study (BRAVO) (Kuhns et al., 2005), in Europe by the Cooperative Programme for Monitoring and Evaluation of the Long-Range Transmission of Air Pollutants in Europe (EMEP) (Vestreng et al., 2009), and in Asia by the Streets inventory (Streets et al., 2003).

A.2 Total adult mortalities due to exposure to ambient PM_{2.5}

Figure A.1 shows total premature adult mortalities due to chronic exposure to ambient PM_{2.5} in the year 2010 in the 2°x2.5°-resolution simulation. We estimate 2.7 million (95% CI: 2.10-3.25 million) annual deaths, which is of similar magnitude to, yet slightly lower than, recent estimates from other studies (e.g., Lelieveld et al., 2015; Lim et al., 2012, which estimated 3.1 million deaths per year). We attribute part of this difference to the coarser model resolution.

A.3 Waste-combustion emissions

Emissions inventories currently in the standard GEOS-Chem setup do not include estimates of waste combustion. In our simulation with waste-combustion emissions, we add the Wiedinmyer et al. (2014) domestic-waste-combustion emissions inventory to the standard setup. Figure A.2 shows waste-combustion emissions of primary black carbon (a), primary organic carbon (b), gas-phase NH₃ (c), and gas-phase SO₂. In the model, 1% of gas-phase SO₂ is emitted as SO₄ aerosol (Stevens and Pierce, 2013). This inventory also includes emissions of nitrogen oxides and non-methane organic compounds, which together with NH₃ and SO₂ may increase aerosol mass through formation of nitrate, sulfuric acid and secondary organic aerosol; however, these emissions are relatively minor, and the PM_{2.5} increase due to these secondary processes is much smaller than through primary emissions of organic and black carbon aerosol.

A.4 Model evaluation

GEOS-Chem aerosol estimates of PM_{2.5} mass have been evaluated in several studies (Park et al., 2006; van Donkelaar et al., 2010). van Donkelaar et al. (2010) compares global GEOS-Chem simulated PM_{2.5} to ground based measurements and finds a slope of 0.54, bias of 8.89 $\mu\text{g m}^{-3}$, and a correlation coefficient of 0.63 (Supplemental Table S2). Global PM_{2.5} measurements are limited, especially in developing countries where waste combustion is common. To compare global aerosol loading in the model in regions where waste burning exists, we compare model aerosol optical depth (AOD) to Aerosol Robotic Network (AERONET) measurements as there are more AERONET

measurements available in these regions than surface $\text{PM}_{2.5}$ monitors. AOD measures the optical extinction of radiation along a path length (in this case the atmosphere). While AOD is a common metric to determine aerosol loading, we note that it does not directly yield information on surface level aerosol concentrations. To compare to AERONET, we output GEOS-Chem AOD at three-hour intervals. AOD is calculated online in GEOS-Chem using modeled aerosol mass concentrations and refractive indices from the Global Aerosol Data Set (GADS) (Koepke et al., 1997). We restrict model AOD to be greater than 0.01 as this is the uncertainty limit of AERONET AOD measurements. AERONET sites attempt to measure AOD every 15 minutes. We average AERONET measurements at each site to 3-hour intervals only if there are greater than 6 measurements, thus removing time intervals where measurements were not possible due to clouds or instrument error. Figure A.3 shows comparisons of annually averaged modeled AOD to AERONET measurements at all available AERONET sites for the simulation with waste combustion (BASE) and without (WASTE_OFF). In both simulations, the model captures the variability (slope = 0.98; log mean bias = -0.22). Given the coarse spatial resolution of the model, the large variability is expected ($r^2=0.59$). On a global scale, including waste-combustion emissions leads to slight improvements in each of the three metrics: slope, model bias, and r^2 .

A.5 Country-level mortalities

Table S1 of the online version of Kodros et al. (2016a) lists mortalities per capita for each country as well as World Bank (WB) income level, population, and mass of waste generated per capita. The WB considers high-income countries (HIC) to be developed while upper-middle income (UMI), lower-middle income (LMI), and low income (LI) to be developing. Of the countries affected by waste-combustion- $\text{PM}_{2.5}$ exposure, mortality rates per capita in developing countries are an order of magnitude greater than in developed countries; however, this difference decreases when considering countries that have no mortalities due to waste-combustion $\text{PM}_{2.5}$ (either through low $\text{PM}_{2.5}$ exposure or concentrations in the country are below the minimum threshold concentration in our concentration-response function).

S4 shows box and whisker plots organized by WBO income level for (top) kg of waste generated per capita, (middle) mortalities from waste-generation $PM_{2.5}$ per capita multiplied by 10^6 , and (bottom) mortalities per Tg of waste generated. A number of countries in each income level have zero deaths from waste combustion emissions due, in part, from $PM_{2.5}$ concentrations being below the minimum threshold for health impacts in our concentration-response function. On average (denoted by stars), developing countries tend to generate less waste and have higher mortality rates per capita and per waste generated than in developed countries.

A.6 Sensitivity simulations

There are large uncertainties in the particulate emission mass from waste combustion. To address this, we introduce a factor-of-2 uncertainty in waste-combustion $PM_{2.5}$. The factor of 2 is chosen because it is similar to uncertainties reported in emission factors from Akagi et al. (2011). Figure A.5 shows the mortalities per 10^4 km² per year for the doubled ('HIGHMASS') and halved ('LOWMASS') emission simulations at the $2^\circ \times 2.5^\circ$ resolution.

Figure A.6 shows waste-combustion adult mortalities per 10^4 km² per year at the $2^\circ \times 2.5^\circ$ resolution using the “subtraction” method. Alternatively to “attributing” present-day mortalities from waste-combustion, this method estimates the number of premature deaths avoided due to a complete removal of waste-combustion emissions.

A.7 Mortalities at different resolutions

To explore the dependence of mortality estimates on model resolution, we perform global simulations at $4^\circ \times 5^\circ$ and $2^\circ \times 2.5^\circ$, as well as a $0.5^\circ \times 0.666^\circ$ simulation over Asia. Figure A.7 shows the spatial pattern of mortalities per 10^4 km² per year at the $4^\circ \times 5^\circ$ global simulation (and Figure 3.2 in the main text shows the mortalities at the finer $2^\circ \times 2.5^\circ$ resolution). Mortalities at this coarser resolution are lower than at the $2^\circ \times 2.5^\circ$ resolution due to averaging $PM_{2.5}$ concentrations over a larger area. This reduces the model ability to co-locate high $PM_{2.5}$ gradients with dense populations.

In addition, $PM_{2.5}$ spread over a larger area may decrease concentrations in the gridcell below the minimum concentration threshold for health impacts.

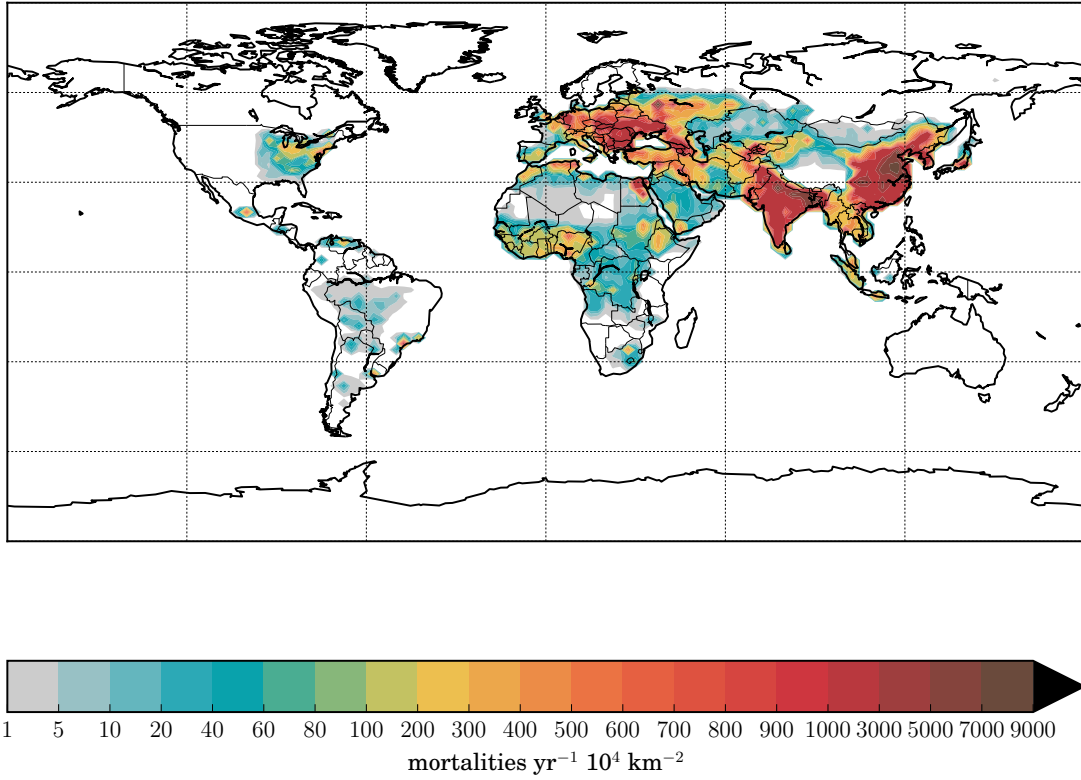


Figure A.1: Total adult premature mortalities due to chronic exposure to ambient PM_{2.5} in the year 2010 in the 2°x2.5°-resolution simulation.

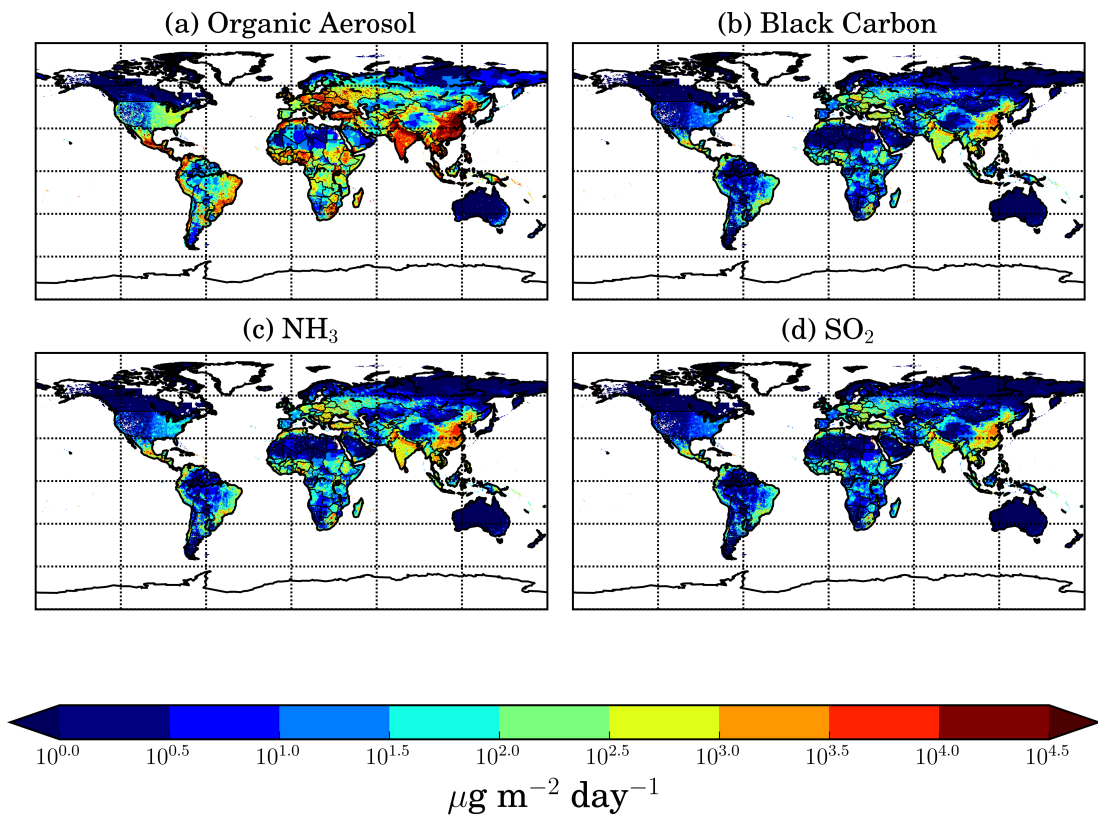


Figure A.2: Waste-combustion emissions flux of (a) organic aerosol (OA), (b) black carbon (BC), (c) NH_3 , and (d) SO_2 in $\mu\text{g m}^{-2} \text{day}^{-1}$ from Wiedinmyer et al, 2014.

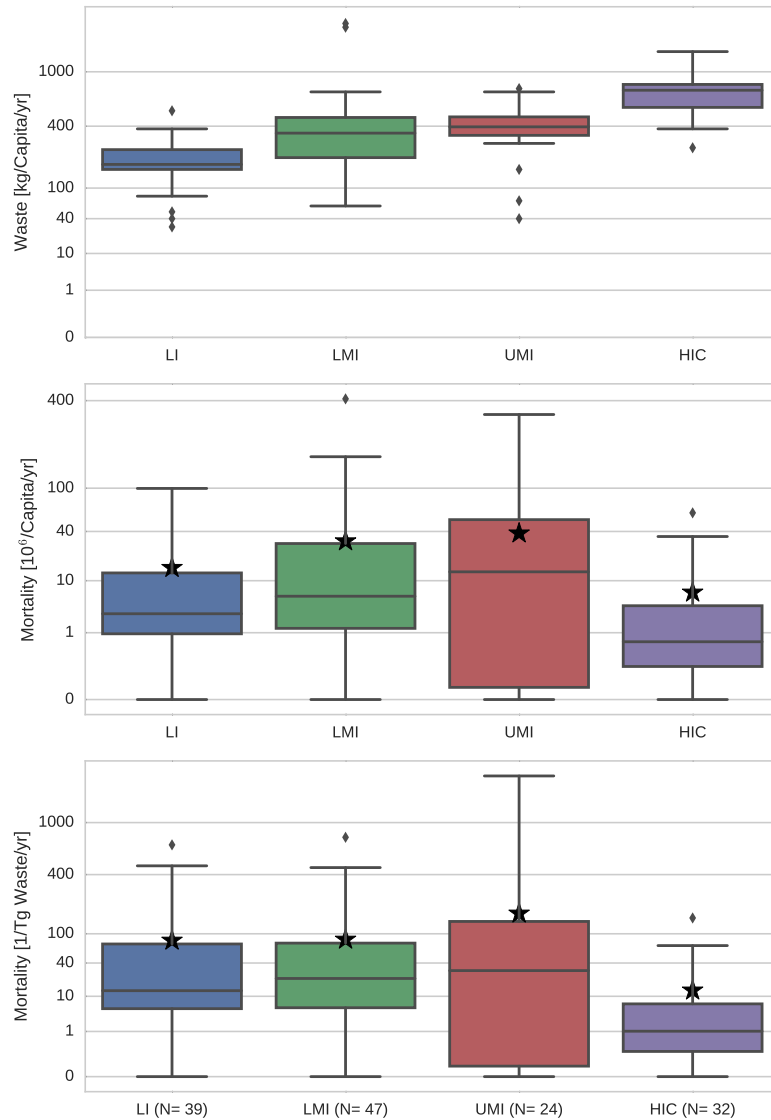


Figure A.4: Box-and-whisker plots (with stars denoting the mean) for countries organized into four WBO income levels for **(top)** annual mass of waste generated, **(middle)** mortalities from waste-generation $PM_{2.5}$ per capita multiplied by 10^6 , and **(bottom)** mortalities per Tg of waste generated. “LI” refers to “Low Income”, “LMI” to “Low Middle Income”, “UMI” to “Upper Middle Income”, and “HIC” to “High Income Countries”. The y-axis is non-linear and scales with the 4th root of the y value (this scale is chosen to both show the spread in the non-Gaussian distribution as well as extend to a value of 0, which a log y axis would not). Mean values are denoted by stars, median values are denoted by black horizontal lines in the middle of the colored boxes, 25th and 75th percentiles are the bottom and top of the colored boxes. The whiskers extend to 1.5x the interquartile range (in 4th root space) or the max value, whatever is smaller. Outliers are denoted by black diamonds.

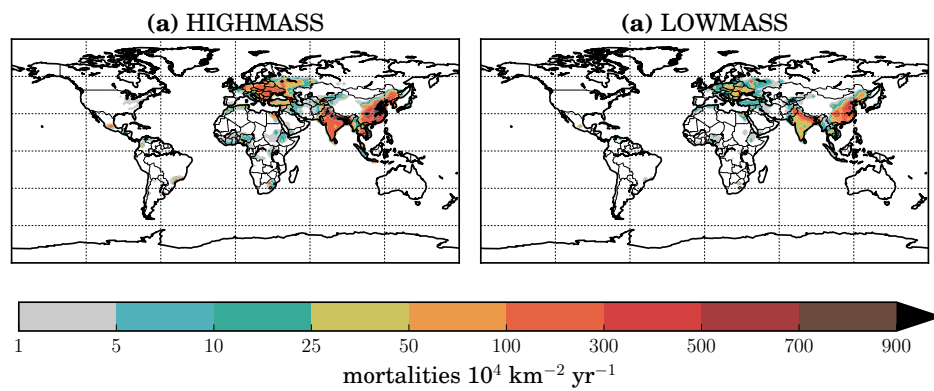


Figure A.5: Annual premature adult mortalities per 10^4 km^2 due to exposure to waste-combustion $\text{PM}_{2.5}$ at the global $2^\circ \times 2.5^\circ$ model resolution when waste-combustion emission mass is doubled **(a)** and halved **(b)**

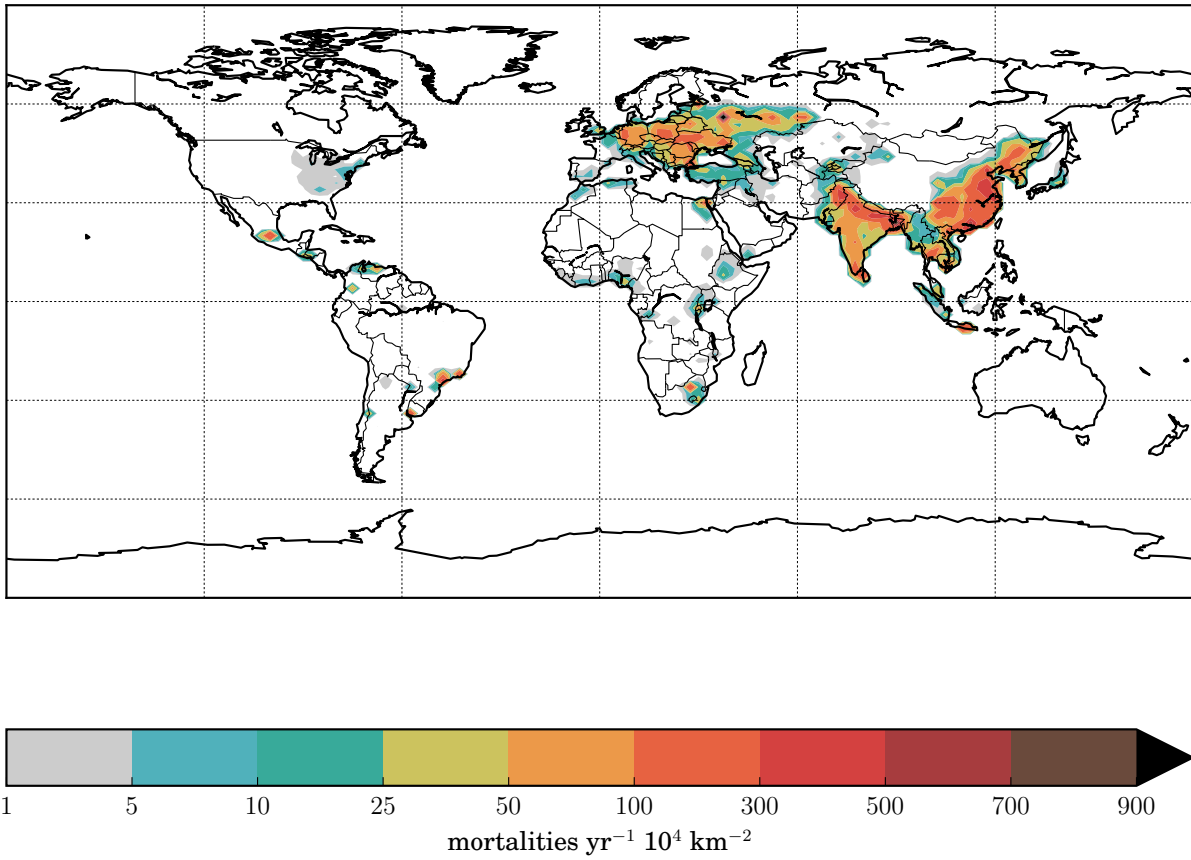


Figure A.6: Annual premature adult mortalities per 10⁴ km² estimated using the “subtraction” method (i.e. a complete removal of waste-combustion emissions).

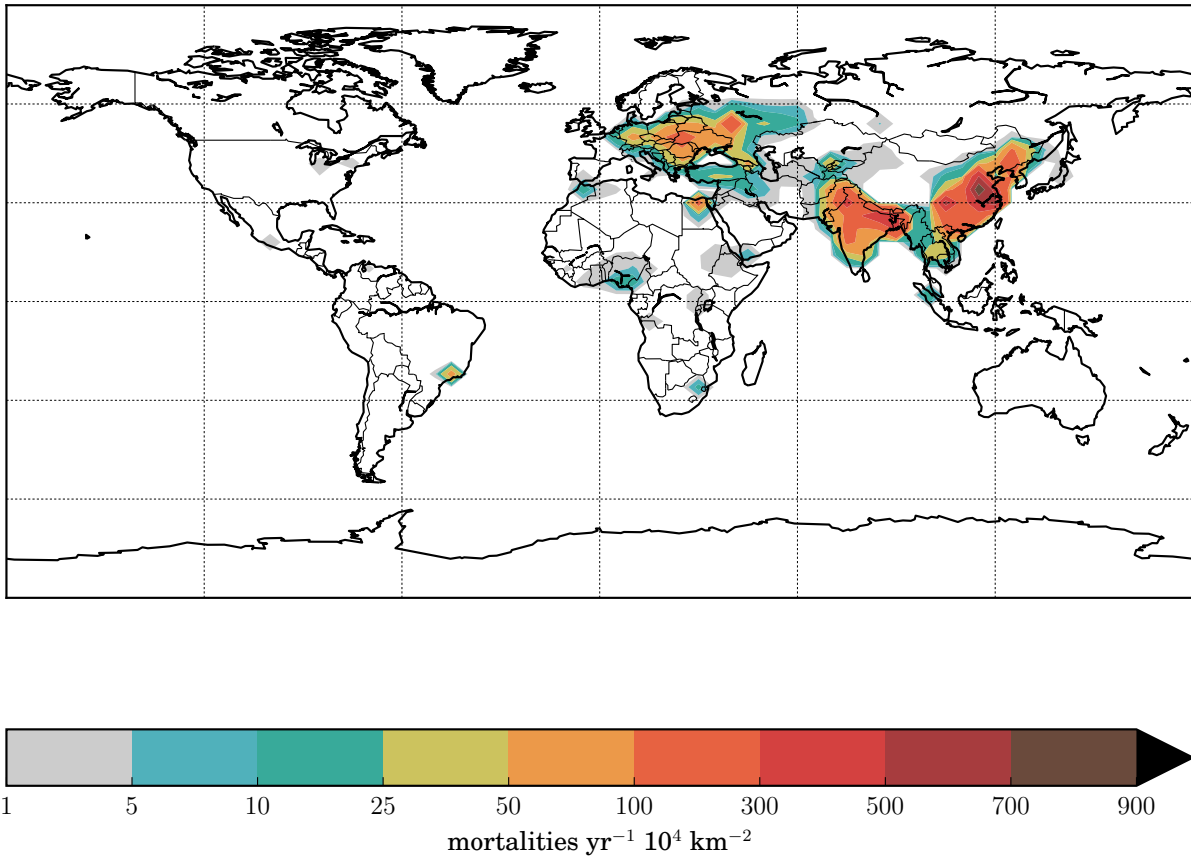


Figure A.7: Annual premature adult mortalities due to waste-combustion PM_{2.5} per 10⁴ km² at the global 4°x5° model resolution.

Appendix B

Supporting Information for Quantifying the contribution to uncertainty in mortality attributed to household, ambient, and joint exposure to PM_{2.5} from residential solid-fuel use

B.1 GEOS-Chem model setup

We simulate the fraction of ambient PM_{2.5} originating from SFU emissions using the Goddard Earth Observing System chemical-transport model (GEOS-Chem) version 10.01 (Bey et al., 2001; <http://acmg.seas.harvard.edu/geos/>). GEOS-Chem is driven by GEOS-5 assimilated meteorology fields (<http://gmao.gsfc.nasa.gov>), and includes PM tracers for black carbon, organic aerosol, dust, sea salt, sulfate, nitrate, and ammonium in addition to 52 gas-phase species. Global aerosol emissions are derived from The Emissions Database for Global Atmospheric Research (EDGAR) Hemispheric Transport of Air Pollution (HTAP) version 2.2 (Janssens-Maenhout et al., 2015). We simulate the year 2010 with and without emissions from the residential sector in order to estimate the fraction of total population-weighted PM_{2.5} in a country originating from SFU.

B.2 Calculating lognormal parameters

All input parameters (with the exception of the concentration-response function) are published with mean and 95% confidence bounds. As the underlying uncertainty distribution itself is not explicitly provided, we assume a lognormal uncertainty distribution in the main text of this study (and consider a uniform distribution below). To describe the lognormal distribution, we calculate the standard deviation using the relationship that the ratio of the width of the 95% confidence interval to the standard deviation is a factor of 3.92. This assumes that the confidence interval is

symmetric about the median (a factor of 1.96 of the standard deviation on each side). While the input parameters are not all symmetric about the median, this asymmetry is generally small and we do not feel it greatly impacts our results.

B.3 Sensitivity analysis results with a lognormal uncertainty distribution and restricting input parameters to 2.5 to 97.5 percentile range

Figure B.1 shows the results of the sensitivity analysis for the J-SFU calculation assuming a lognormal uncertainty distribution for all input parameters (except for the concentration-response function, as defined in the main text), but restricting the sampling to values within the 95% confidence interval. This restriction reduces the summed total effect to 118-130% across all four regions.

B.4 Sensitivity analysis results with uniform uncertainty distributions (where the endpoints are the 2.5 to 97.5 percentiles)

Figure B.2 shows the results of the sensitivity analysis for the J-SFU calculation assuming a uniform uncertainty distribution for all input parameters (except for the concentration-response function, as defined in the main text). The uniform distribution is truncated at the 95% confidence interval. This restriction reduces the summed total effect to 108-110% across all four regions.

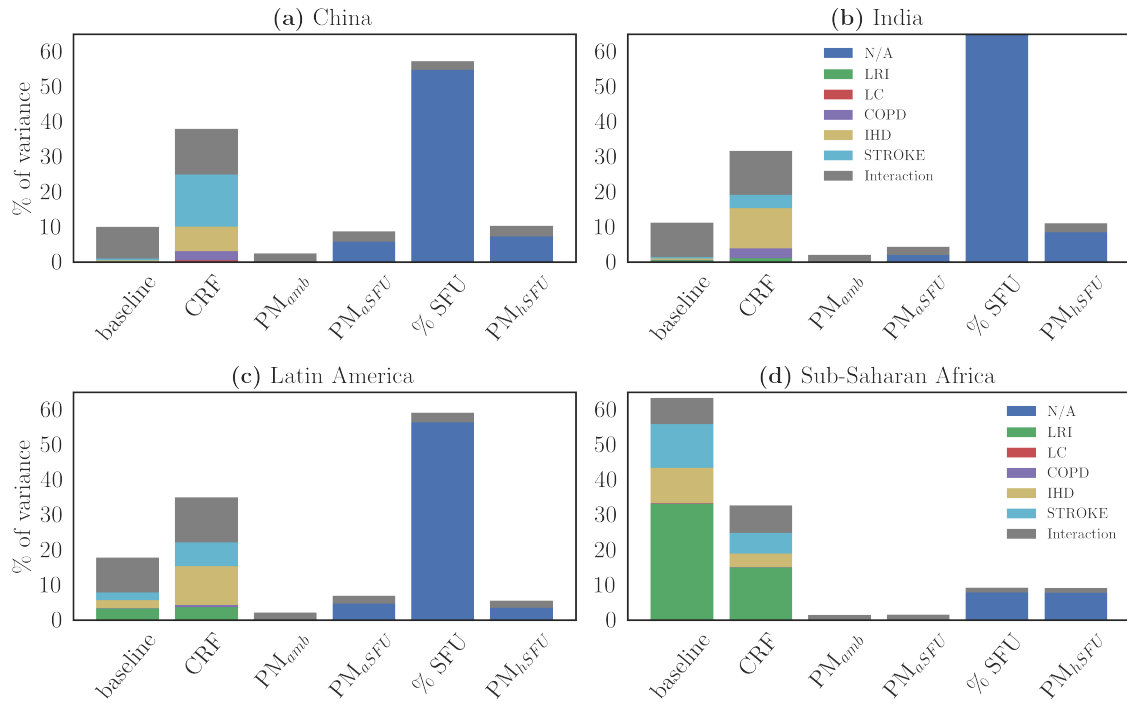


Figure B.1: Contribution to overall variance by each parameter to the uncertainty in the joint-effect mortality calculation in China (a) and India (b) as well as regional averages weighted by cookstove mortalities for countries in Latin America (c) and Sub-Saharan Africa (d). Figure B.1 is similar to Figure 4.6 of the main text, but restricting sampling to the 95% confidence interval.

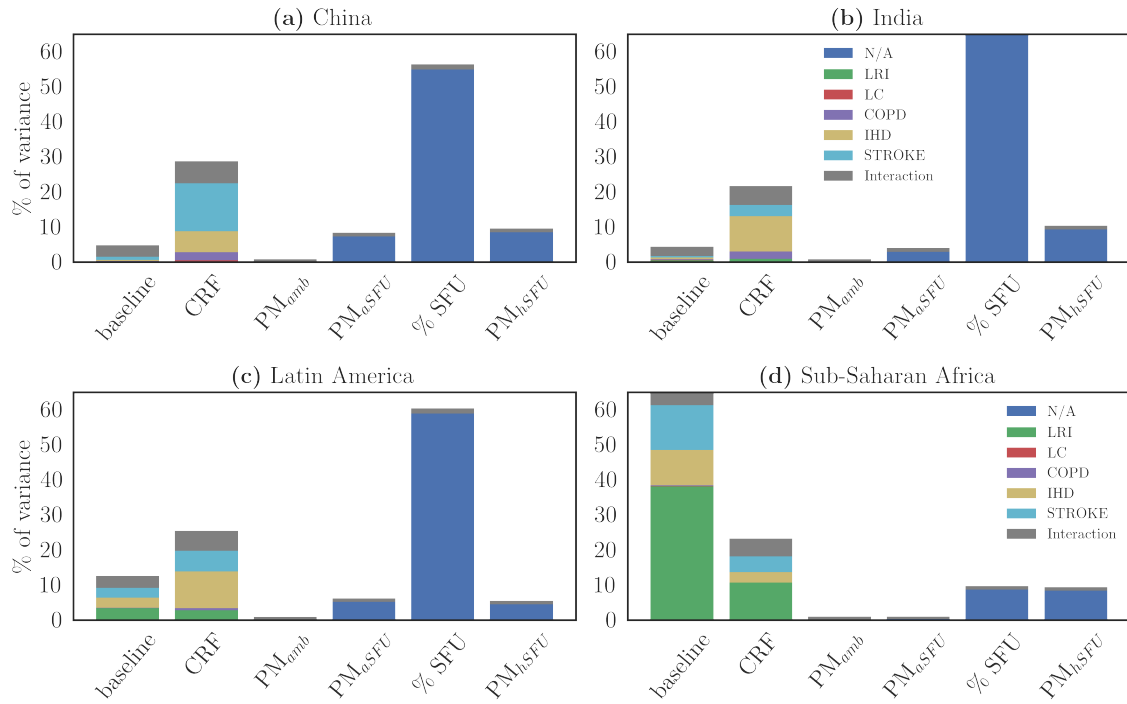


Figure B.2: Contribution to overall variance by each parameter to the uncertainty in the joint-effect mortality calculation in China (a) and India (b) as well as regional averages weighted by cookstove mortalities for countries in Latin America (c) and Sub-Saharan Africa (d). Figure B.2 is similar to Figure 6 of the main text, but with a uniform uncertainty distribution truncated at the 95% confidence interval.

Appendix C

Supplemental Material to Size-resolved mixing state of black carbon in the Canadian high Arctic and implications for simulated direct radiative effect

C.1 Bounding cases of coating thickness for rBC cores less than 140 nm and resulting direct radiative effect

To determine the coating thickness as a function of rBC core diameter (as shown in Figure 6.2) the rBC cores were binned in 5 nm intervals and the median coating thickness across all flights and measurements was calculated for each bin. However, since there is a known bias toward thicker coatings at smaller rBC cores sizes, this median value is not accurate for rBC core diameters less than 140 nm. This is due in large part to the fact that small particles with thin or no coatings do not produce a detectable elastic scattering signal and therefore cannot have a coating thickness determined for them. To overcome this, conservative minimum and maximum coating thickness were also calculated for each bin. We estimated minimum coating thicknesses by assuming that all particles for which a coating thickness could not be determined were bare rBC particles. We estimated maximum coating thicknesses by assuming that all particles for which a coating thickness could not be determined had the median coating thickness from the successful fits. For bins where >90% of all particles could be successfully assigned a coating thickness, the minimum, maximum, and median were very similar. For smaller particles, where <90% could be assigned a coating thickness, the differences were significant. In order to overcome the known biases in the median for these cases, we used the minimum and maximum coating values as bounding values. The median coating value for bins with <90% successful fits was set as the overall median coating thickness from bins where the LEO success rate was 90% or greater. For rBC core diameters larger than 220

nm, the median value for a 220 nm particle was used. The results from this are shown in Figure C.1. This process was carried out separately for each flight and the average of all flights (black line in Figure C.1) was used for the GEOS-Chem simulations.

Table C.1 presents the resulting direct radiative effect (DRE) for the r_{shell} -constrained and f_{BC} -constrained mixing states considering the minimum, median, and maximum coating assumptions. Overall there is not a large difference in DRE across the minimum and maximum assumptions. This is due to most of the optical extinction taking place at particle diameters greater than 140 nm.

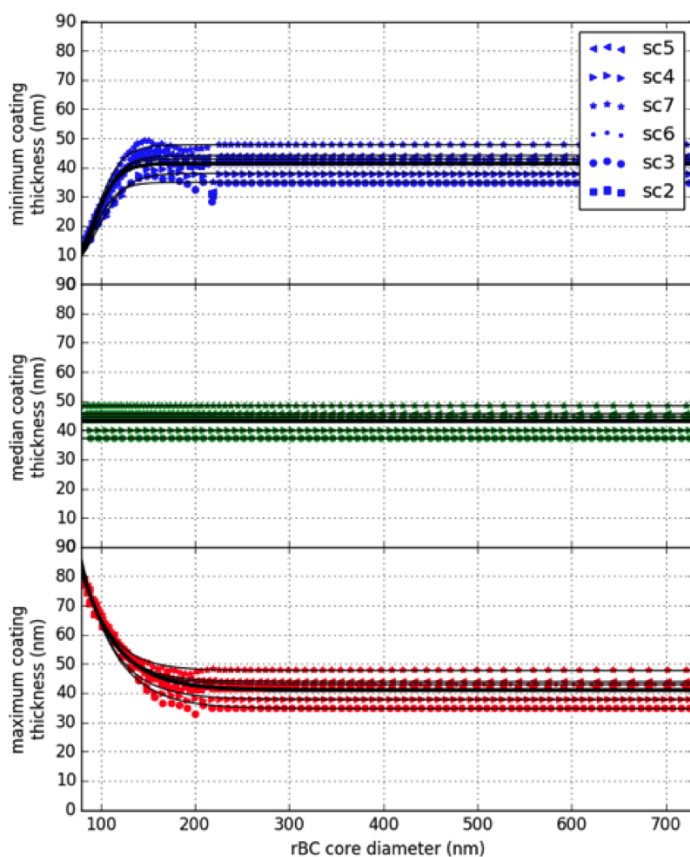


Figure C.1: Minimum, median, and maximum possible coating thicknesses as a function of rBC core diameter. In each scenario, there are separate symbols and a fit line for each flight, and there is a heavy black line which is the fit to all flights combined.

Table C.1: The DRE for measurement-constrained mixing states using the minimum, median, and maximum assumptions.

Simulation	Assumption	DRE [W m^{-2}]
fBC-constrained	min	-1.462
	med	-1.454
	max	-1.455
r _{shell} -constrained	min	-1.593
	med	-1.591
	max	-1.588

C.2 April mean albedo

Figure C.2 shows April climatological mean albedo in the Arctic. Albedo climatology is derived from MODIS retrievals from years 2002-2007 and described in Heald et al. (2014). Ocean albedo is held constant at a value of 0.07; however, sea ice alters the spatial distribution of albedo. Estimates of DRE are likely sensitive to albedo climatology.

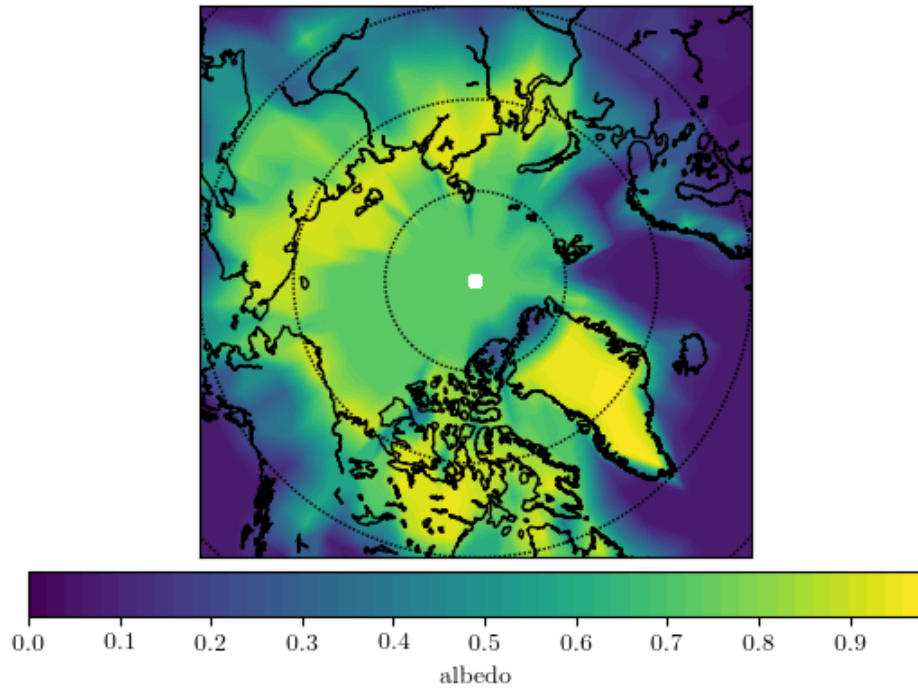


Figure C.2: April mean albedo for visible wavelengths.

Appendix D

Supplemental Information for The role of inter-regional variability in aerosol size distributions on respiratory deposition of particulate matter

D.1 Sensitivity to particle dosimetry model: ICRP versus MPPD

Two commonly referenced models of size-resolved particle deposition in the respiratory tract include the International Commission on Radiological Protection (ICRP) model (ICRP, 1995) and the Multiple Pathway Particle Dosimetry (MPPD) model (Miller et al., 2016). In the main text, we present results with the ICRP model average across breathing rates using equations in Hinds, 1999. Here we explore the sensitivity of size-resolved particle deposition in the respiratory tract to choice of dosimetry model. Figure D.1 shows deposition fractions for the ICRP and MPPD models for all respiratory regions, the head and nose region, the tracheobronchial region, and the pulmonary/alveolar region (following terminology used in each model, respectively). Generally, deposition in all respiratory regions and the head/nose regions are similar between models. The largest difference in total respiratory deposition is the minimum occurs at smaller particle diameters in the ICRP model with lower deposition fractions. There are some differences between the two models for deposition in the tracheobronchial and pulmonary/alveolar regions. Figure D.2 compares the ICRP and MPPD models for the sum of the tracheobronchial and alveolar regions (TB+AV). The TB+AV deposition fraction curves generally follow a similar shape, with the ICRP model showing more efficient deposition at the maximum for ultrafine particles and less efficient deposition in the minimum. The minimum for accumulation-mode particles is at a smaller particle diameter in the ICRP model. Conversely, the MPPD model predicts more efficient coarse-mode deposition.

We explore the implication of differences in deposition fraction between the ICRP and MPPD models in Figure D.3. Figure D.3 shows the ratio of the deposition mass in the TB+AV regions

between the ICRP and MPPD models. The largest difference in deposition occurs in the desert regions (e.g. North Africa and the Middle East) where the ICRP model predicts around 50% less deposited mass than the MPPD model. This corresponds to deposition fractions between 1-10 μm . The two models are most similar in biomass burning regions (South America and Central Africa). The lower deposition efficiency of coarse-mode mass in the ICRP model suggests the $DR_{\text{TB+AV}}$ (Figure 7.4 in the main text) would exhibit a higher spatial variability if we use the MPPD model.

Given the large uncertainties in particle deposition models and aerosol microphysical models (that simulate ambient size distributions), we feel we are justified in using a single particle deposition model. Using the MPPD model would not substantially alter our general discussion and conclusions.

D.2 Size-resolved particle growth due to water uptake in the lung

Particles may take up liquid water due to an increase in relative humidity, thus increasing diameter. Aerosol water uptake in the ambient atmosphere is accounted for online in GEOS-Chem-TOMAS. This section describes swelling of aerosol particles due to water uptake in the lung. We assume that air in the lung and associated airways has a relative humidity (RH) of 99.5% and a temperature of 37° C (Anselm et al., 1990). This constant value of RH is used in other particle deposition studies (e.g. Londahl et al., 2007; Londhal et al., 2009; Hussein et al., 2013); however, is likely a simplification. We estimate the equilibrium particle diameter due to water uptake in the lung using the hygroscopicity parameter, kappa, and Equation D.1:

$$D_{p,\text{equilibrium}} = \left(1 + \kappa \frac{\text{RH}}{1 - \text{RH}}\right)^{1/3} D_{p,\text{ambient}} \quad (\text{D.1})$$

where $D_{p,\text{equilibrium}}$ is the equilibrium particle diameter in the lung, $D_{p,\text{ambient}}$ is the ambient particle diameter, RH is the relative humidity (in this case 99.5%), and κ is the hygroscopicity parameter (Petters and Kreidenweis, 2007). GEOS-Chem-TOMAS treats particles as internally mixed within each size bin, and so we calculate the total particle κ as the volume-weighted average

of the individual chemical components. Equation D.1 calculates the particle diameter in the lung under ideal conditions assuming the particle remains in the lung long enough to reach the equilibrium diameter. We also assume the inhaled air mass instantly reaches the relative humidity and temperature in the lung.

We approximate the timescale for particles to reach equilibrium due to condensation of water in the lung with Equation D.2:

$$\tau = \frac{D_{p,lung} - D_{p,ambient}}{4D_g\beta M(c_\infty - c_s)(1/D_{p,ambient}\rho)} \quad (D.2)$$

where D_g is the diffusivity of water vapor, β is the Danheke correction factor, M is the molar mass of water vapor, c_{inf} is the water vapor concentration in the lung, c_s is the water vapor concentration at the particle surface, $D_{p,ambient}$ is the initial ambient diameter, and ρ is the particle density. The numerator of Equation D.2 is the maximum growth of the particle due to water uptake in the lung if the particle is allowed to reach equilibrium. The denominator of Equation D.2 is the diameter growth velocity due to condensation and is a function of particle diameter. Here, we approximate the timescale as dependent on only the initial particle diameter. The condensation rate slows as the particle takes up water and C_s increases, which is not captured in this approximation.

We compare the approximate equilibrium timescale with an assumed particle residence time in the lung of 2.5 seconds (Miller et al., 2016). Equation D.3 compares the equilibrium timescale to the lung-residence timescale:

$$f = \frac{\tau}{\tau + \tau_{lung}} \quad (D.3)$$

where τ_{lung} is the residence timescale in the lung (2.5 seconds). This factor f is used to interpolate between initial ambient diameter and the diameter in the lung:

$$D_{p,lung} = f \times D_{p,ambient} + (1 - f)D_{p,lung} \quad (D.4)$$

where $D_{p,\text{lung}}$ is the particle diameter in the lung. Ambient particle diameters up to around $10\ \mu\text{m}$ are able to grow to the equilibrium size.

Finally, we calculate the particle diameter relevant for deposition in the body, $D_{p,\text{deposition}}$, as the aerodynamic diameter after accounting for water uptake in the lung:

$$D_{p,\text{deposition}} = D_{p,\text{lung}} \times (\rho_{\text{particle}}/\rho_{\text{water}})^{1/2} \quad (\text{D.5})$$

where ρ_{particle} is the density of the particle and ρ_{water} is the density of water. This approximation of hygroscopic growth due to the relative humidity in the lung is likely an upper bound. First we assume the inhaled air mass containing particles instantly acquires the temperature and relative humidity in the body. Second, we calculate the condensation rate of the particles based on the initial ambient diameter, but this rate will decrease as particle sizes grow. Both of these factors will contribute to the growth timescale being longer than what we calculated here, and hence we expect particles to be somewhat smaller than what we approximated. The approach taken here to account for hygroscopic growth in the lung is simplistic. We test the sensitivity of particle deposition along the respiratory tract assuming no particle growth and growth based on RH of 98% and 99.5% in Figure D.4.

Figure D.4 shows $\text{DR}_{\text{TB+AV}}$ assuming no growth in the lung or growth based on RH of 98% and 99.5%. Assuming no growth leads to the largest geographic variability in $\text{DR}_{\text{TB+AV}}$. This is because accumulation-mode particles (largely from anthropogenic emissions) tend to be centered near the minimum in deposition in the ICRP deposition fraction curve. Growth based on an RH of 98% grows particle diameters out of this minimum. Growth based on an RH of 99.5% grows particles even further out of this minimum (and closer to the local maximum at $2\ \mu\text{m}$), thus increasing the $\text{DR}_{\text{TB+AV}}$ in fossil fuel dominated regions. Conversely, as deposition efficiency decreases from $2\ \mu\text{m}$ and larger, growth of coarse-mode particles leads to decreasing $\text{DR}_{\text{TB+AV}}$. The net result is more water uptake in the lung leads to less geographic variability of $\text{DR}_{\text{TB+AV}}$ as accumulation-mode particles grow to sizes that deposit more efficiently and coarse-mode particles grow to sizes that deposit less efficiently.

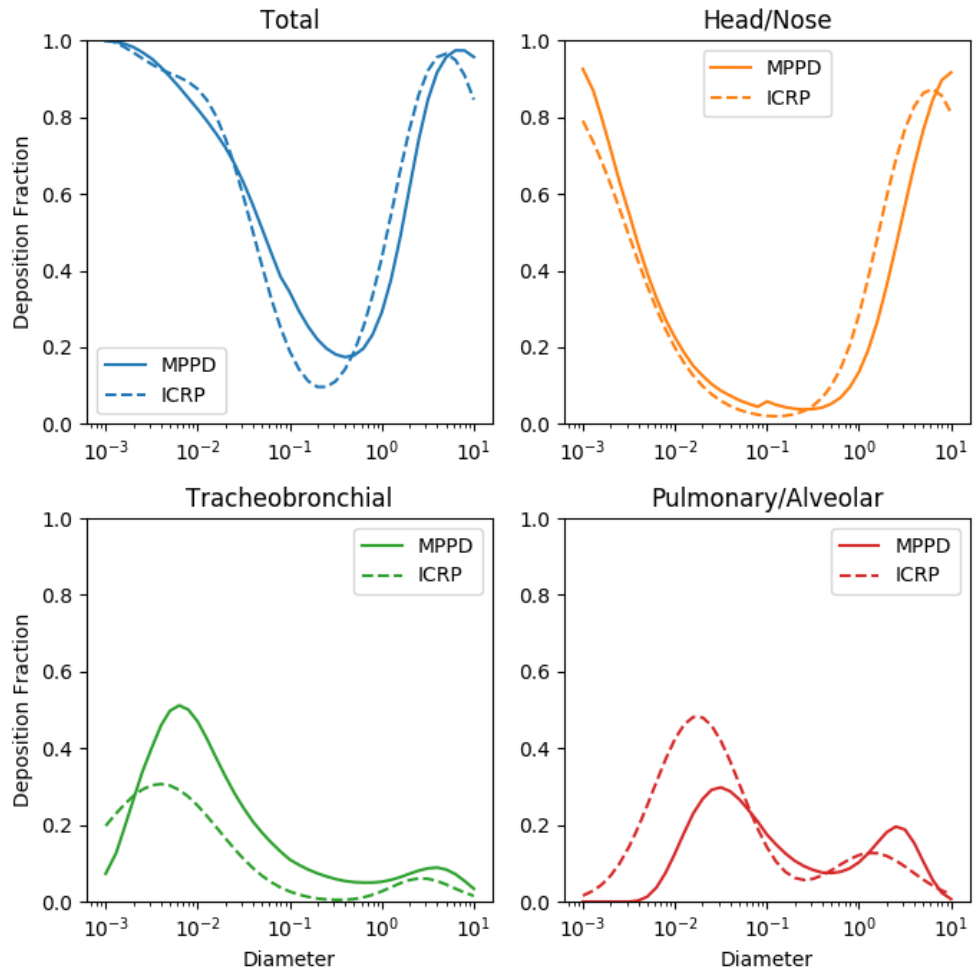


Figure D.1: Deposition fractions in the ICRP and MPPD models in (a) all respiratory regions, (b) head/nose region, (c) tracheobronchial region, (d) pulmonary/alveolar region.

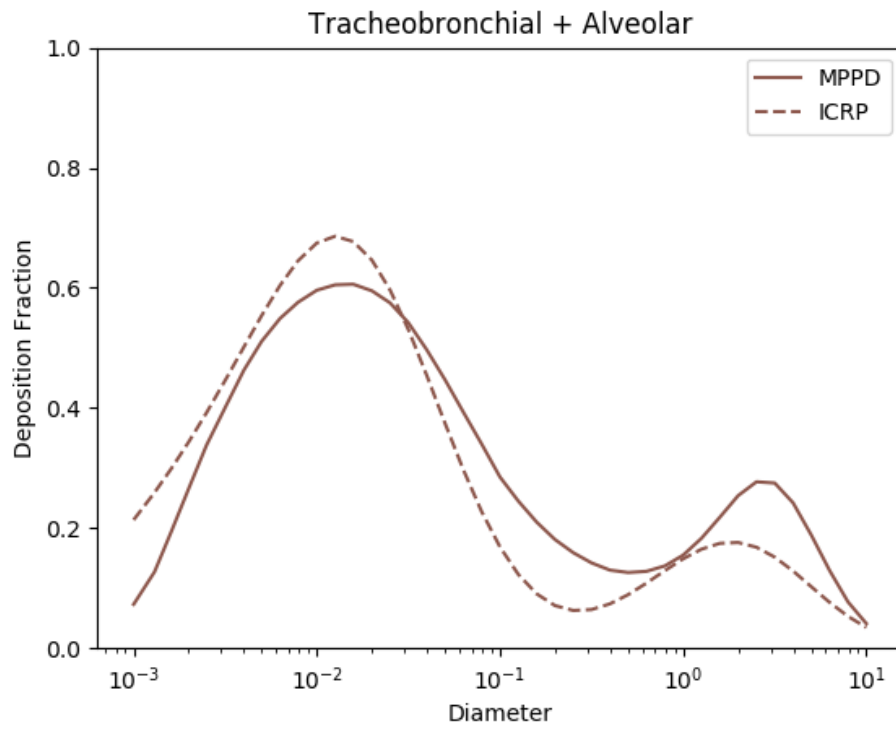


Figure D.2: Deposition fractions in the ICRP and MPPD models for the sum of tracheobronchial and alveolar regions.

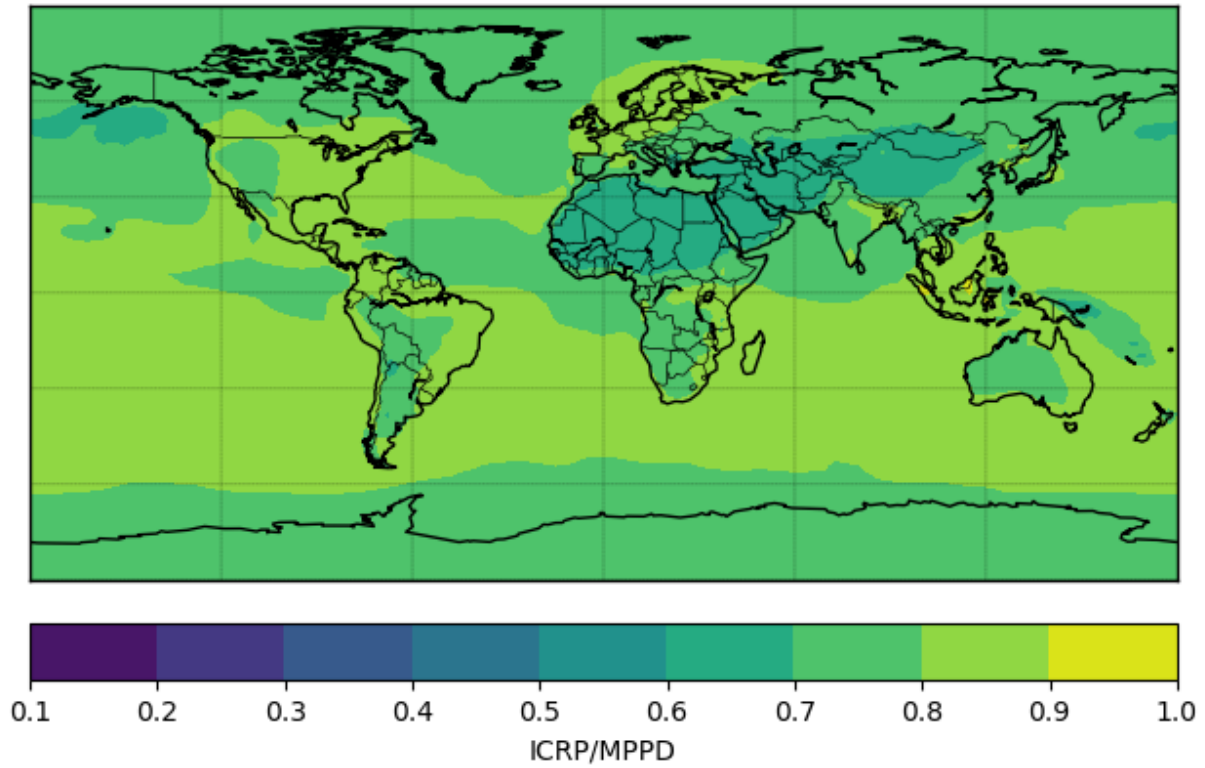


Figure D.3: The ratio of ICRP deposited mass and MPPD deposited mass in the TB+AV regions (with ambient PM mass simulated by GEOS-Chem-TOMAS).

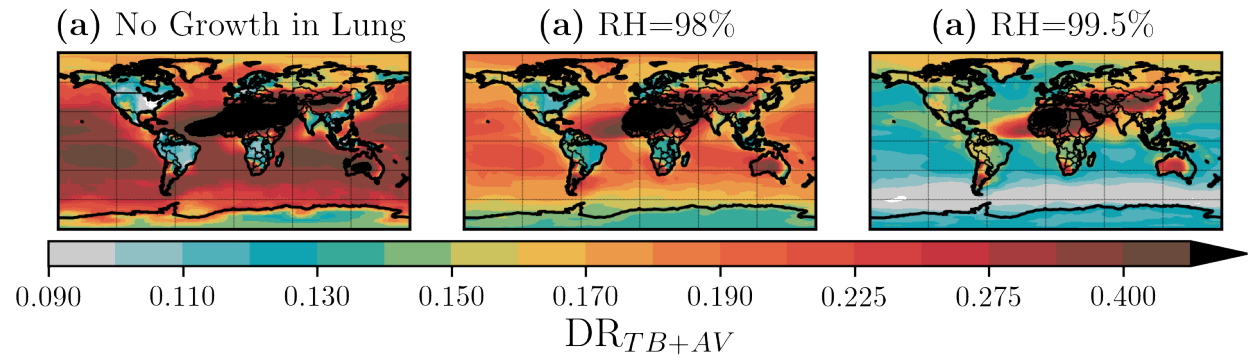


Figure D.4: DR_{TB+AV} assuming (a) no growth in the lung, (b) growth with an RH of 98%, (c) growth with an RH of 99.5% (as in the main text).